CURRENT AND FLUX DISTRIBUTIONS, FORCES AND STIFFNESSES IN LINEAR INDUCTION MACHINES

by

Som Nath Mahendra, M.Sc.(Eng.)

A thesis submitted for the degree of Doctor of Philosphy of The City University, London.

Electrical and Electronic Engineering Department

The City University

London

July, 1977

CONTENTS

CHAPTER 5

TEST, CORRELATION AND DISCUSSION OF RESULTS

CHAPTER 6

MOTION OF A THICKER CONDUCTING PLATE WITH ITS BACKING IRON CARRYING EDDY CURRENTS

ABSTRACT

The thesis deals with a study of the transverse flux linear induction machine under motoring and braking conditions, with a view to estimating flux densities and forces produced. These machines have discontinuities in all three directions and therefore the field, in and around the device, has been derived by solving numerically in three dimensions Poisson's and Laplace's equations by using the magnetic scalar potential as the field parameter.

The approach has been applied and experimentally verified on a novel test rig - called the "Basic Transverse Flux Circular Motor" - devised primarily for testing the transverse flux linear induction machine under dynamic conditions and eliminating entry and exit effects for initial simplifications. The calculated and measured flux densities and forces have been compared and the correlation has been shown to be reasonably good. The computed flux density in the air gap and the current density in the secondary conducting sheet have been plotted in two and three dimensions to show their distribution along the length of the machine.

Suggestions for further work (aimed ultimately at design methods) are made.

ACKNOWLEDGEMENTS

A deep sense of gratitude is expressed to Professor A.J. Ellison for continuous encouragement, invaluable guidance and generous facilities provided in the Department throughout the work and in the preparation of this thesis. The author also wishes to acknowledge with thanks the work and papers of [redacted] which have been a constant source of inspiration and guidance.

The author is indebted to many friends and members of the Department of Electrical and Electronic Engineering and of the Department of Mechanical Engineering at The City University and at Imperial College, especially to [redacted] for helpful discussions and advice.

Thanks are due to [redacted] and his colleagues for their skilful construction of the test rig and to [redacted] for his assistance during the experimental work. The dedicated and sincere assistance of [redacted] has been very helpful and the author wishes to offer him his special thanks. He is also grateful to [redacted] for encouragement and useful comments.

The author is very much indebted to [redacted] and [redacted] for so kindly typing the manuscript with interest and care in a very short time.

Thanks are also due to the [redacted], for the National Scholarship which enabled the author to carry out the work.

LIST OF SYMBOLS

$\overline{A}$	Magnetic vector potential, Wb/m
$\overline{B}$	Flux density vector, T
C_m	Magnetic capacitance, H
C_s	Current sheet distribution, At
d	Depth of penetration for the conducting sheet material at frequency (f) defined by eqn. 3.7, m
$\overline{E}$	Electric field intensity, V/m
$\overline{e}^N$	Error vector
$\overline{F}$	Force vector, N
$\overline{F}_s$	Flux sheet distribution, Wb
F_x, F_y, F_z	Components of force vector $\overline{F}$, N
F_G, F_x	Lateral guidance force, N
F_T, F_y	Propulsive force, N
F_L, F_z	Normal force between primary and secondary member, N
f	Frequency of operation, Hz
f_x, f_y, f_z	Components of stress tensor vector lying along Z-axis, N/m^2
G_m	Magnetic admittance, Ω
h	Intermode spacing, m
$\overline{J}$	Current density vector, A/m^2
K	A constant defined by eqn. 3.6
K_v	A constant defined by eqn. 3.25
R_o	Residual defined by eqn. 2.9
s	Per unit slip
T^m	Maxwell's second stress tensor
t	Thickness of conducting sheet, m
U	Magnetic scalar potential, A
ΔU	MSP drop across the plate, A
$\overline{v}$	Velocity vector, m/s
$\overline{v}_s$	Synchronous velocity of the magnetic field travelling wave in the air gap, m/s
v_y	Velocity along the y-axis, m/s
α	Acceleration factor
α_b	Optimum acceleration factor
ε	Error
ε_a	Absolute error
ε_r	Relative error

μ	Relative permeability of the medium
μ_0	Permeability of free space, H/m
ρ	Resistivity of the conducting sheet, Ω.m
σ	Conductivity of the conducting sheet, S/m
τ_p	Pole pitch of the stator winding,m
Φ	Flux source of a node,Wb
Φ_1	A source function
ψ	A potential
ψ_{new}	New potential
ψ_{old}	Old potential
ω	Angular velocity ($=2\pi$ f), rad/s
$\mathcal{R}_n$	Internode reluctance between node'o' and the surrounding node 'n',H^{-1}
$\bar{T}$	Electric vector potential defined by eqn. $3.15^{(a)}$,A/m
Z_p, Z_{ma}	Magnetic impedance of the alminium conducting sheet,S
Z_i, Z_{mi}	Surface magnetic impedance of the solid backing iron, S
$\bar{K}$	Surface current density, A/m

LIST OF ABBREVIATIONS

AFM	Axial flux machine
HSGT	High speed ground transport
LIM	Linear induction motor
MSP	Magnetic scalar potential
MVP	Magnetic vector potential
SEC1	Secondary member as shown in Fig.5.1
SEC2	Secondary member as shown in Fig.5.2
SLIM	Single sided linear induction motor
TFM	Transverse flux machine
BTFCM	Basic transverse flux circular motor
BI1, BI2, BI3	Backing iron described in Fig.6.5

CHAPTER 1

CHAPTER 1 GENERAL INTRODUCTION

1.1 THE PROBLEM

The electromagnetic transformation of energy for the production of forces, i.e., electromechanical energy conversion, has certain outstanding features when compared with the hydraulic, thermal or aerodynamic types of energy transformation. In the electromechanical energy converter:

(a) It is not necessary for the member receiving the energy for the production of forces, to have a mechanical contact with its source.

(b) Because of (a), the losses and problems associated with mechanical friction can be reduced to a minimum.

(c) The medium surrounding the moving member transmits the energy from the source to the moving member without loss - a feature quite distinct from that in fluidodynamics. Thus losses due to the movement of the surrounding medium are zero.

(d) The noise level associated with this system is much lower than that of any fluidodynamic system.

(e) For transportation, electromagnetism can be used to produce the necessary driving force by induction by fixing to the track a secondary member consisting of an aluminium sheet backed by steel. The maintenance of such a track will be negligible when compared with the conventional railway track which requires frequent maintenance partly as a result of the high stress concentration due to a small area of contact between the wheel and the rail. A hover vehicle would also require a reasonably maintained track.

(f) From (a) and (b) above, it follows that adhesion is no longer the factor deciding the maximum velocity of the vehicles discussed in (e).

However, the relative merits of various methods of force production depend on the application, restrictions, limitations and possible compromises necessary.

Our interest is restricted to a problem where it is desired to move the moving member in a straight line at a high speed without any physical contact between the moving and stationary parts. The direct application of this technology is in the high speed ground transport (HSGT) and similar applications where it is necessary that the moving member follow a pre-defined path without touching its source or surroundings. In brief the desired features of the device can be summarised as follows:

(a) it should 'float' in air, along a given route, without any mechanical friction (except that of air);

(b) it should maintain a desired height which can be kept within limits between no-load and full-load conditions;

(c) it should produce lateral guidance force (to keep the device on the track) - the forces being sufficiently effective to cope with normal irregularities due to man, nature or both;

(d) it should have alternative controls and effective landing pads to meet the most critical condition of power failure (at both full-load and no-load conditions).

In the present work emphasis has been given to features (a), (b) and (c), and Fig.1.1 shows the device with the necessary forces to take care of these features. Also Fig.1.2 shows the desired characteristics of these forces.

The force/speed characteristic is similar to that of a conventional 3-phase induction motor having high resistance in the rotor circuit. This is desirable for HSGT because the device has to start from rest at full load to accelerate, and once it is moving at full speed on its electromagnetic cushion it will require power to overcome the aerodynamic drag. The variation of lift-force (F_L) with respect to speed has been studied [1] in some detail. It has been shown that the force varies from one end of the linear induction motor to the other at different speeds. The lateral guidance force (F_G) is responsible for keeping the device on the track and it is a function of the displacement of the longitudinal axis of the moving member from that of the fixed member. In a stable system the lateral guidance force tends to restore the moving member to its central position. The lateral guidance force is also dependent, as are the other forces, on the speed of the moving member.

1.2 INVERTED PERFORMANCE FUNCTION APPROACH

After understanding the requirements of the device and the desired characteristics of the forces, the next desired step would be to deduce the necessary flux density distribution around the moving member followed by design, fabrication and testing of the electromagnetic circuits. However, the inversion of the force equations to obtain a suitable flux density distribution is neither an easy nor a practical proposition even for very simple electromagnetic problems.

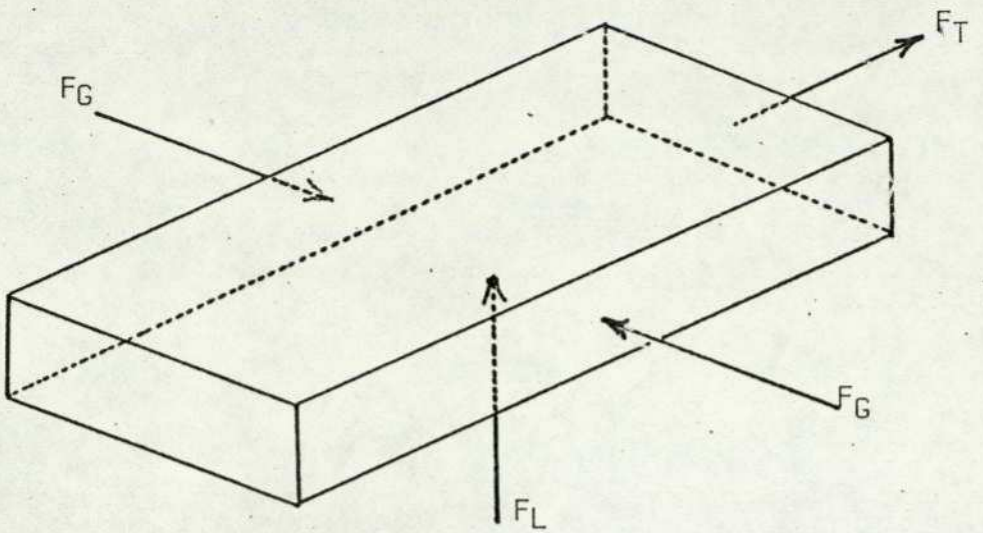

Fig.1.1 Device with its forces

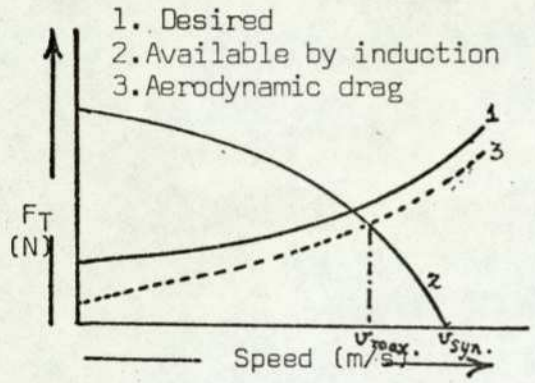

(a) Tractive force (F_T)

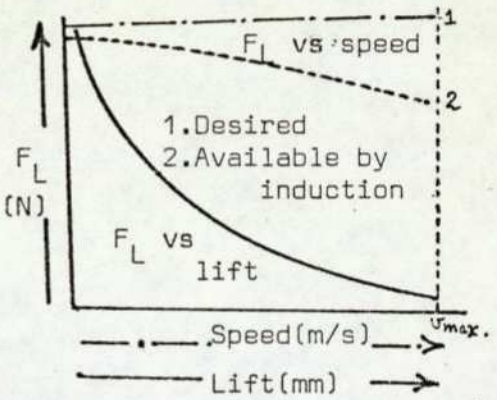

(b) Lift force (F_L)

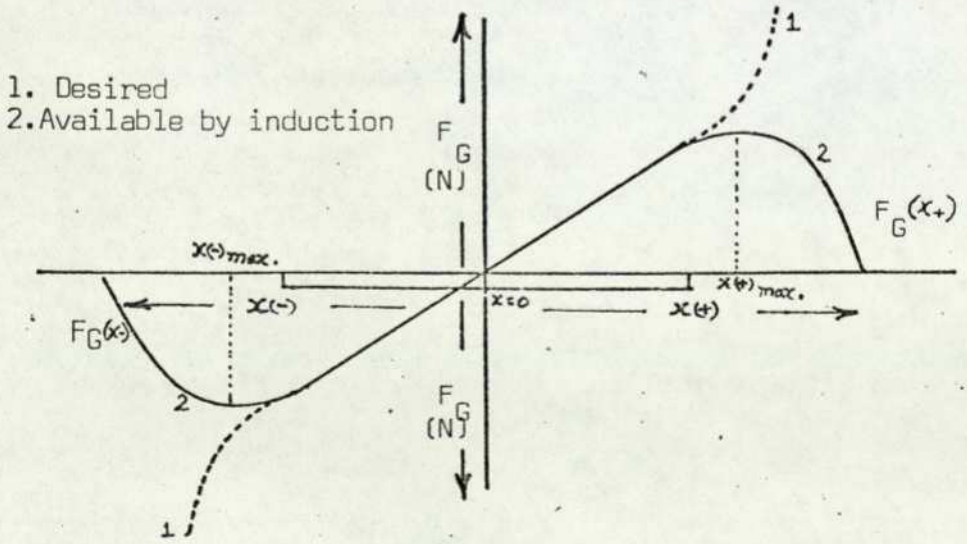

(c) Lateral guidance force (F_G)

Fig.1.2 Desired force characteristics of the device

Similarly, the design of the magnetic and electric circuits and the deduction of the design parameters are equally difficult. This is primarily because the number of equations defining the problem is much smaller than the number of design variables. A possible remedy is to make use of a 'hybrid' technique of design wherein some of the variables are defined from past experience and previous test results, and the remainder are obtained by making use of these defined design variables and the desired force characteristics.

In the present thesis, the theoretical and experimental approaches have been developed to assist a designer in building up the necessary experience and understanding of special purpose electromagnetic devices from first principles. This will be followed by their application in the hybrid technique of design and in the development of suitable equivalent circuits for analysing the device. Optimisation can then be made possible by a suitable interaction between the designer on the console and the computer with the library of programmes to design and analyse the electromagnetic device. Fig.1.3 summarises the complete research programme, and shows alternative paths it is possible to take as results and experience grow .

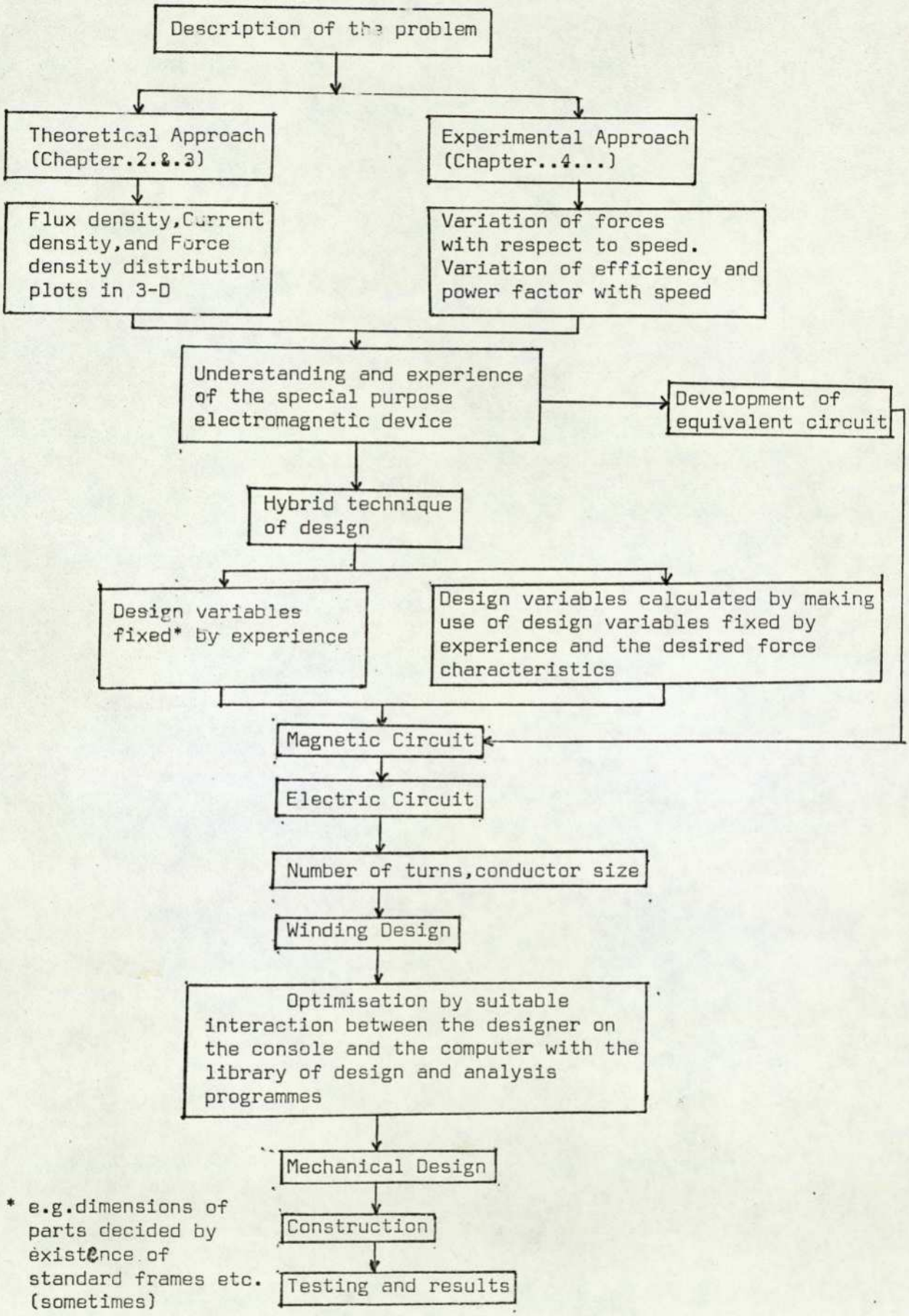

Fig.1.3 Summary of the Research Programme

1.3 PROBLEM OF HSGT

When we refer to high-speed ground transport we imply speeds of the order of 400 km/h. The wheel-rail system has long served the combined purposes of propulsion, suspension and guidance, but it has now been established[2] that the system will be neither feasible nor economical for high speeds of this order. The main reasons are the existence of severe problems of adhesion and wear and tear, and higher noise levels. Speeds of 300 km/h, possibly even higher have been reported [3] feasible without adequate test experience and data on noise levels. Hence, the need for a contact-free system comprising a suspension sub-system, a sideways guidance sub-system and a propulsion sub-system, remains undisputed for high speeds. The detailed analyses[4] and comparison[5,6] of the various types of each of these sub-systems are being carried out in several countries.

In the following sections the state of the art regarding two distinct but interdependent sub-systems, viz those for suspension and guidance and for propulsion of HSGT are discussed.

1.3.1 Suspension and guidance sub-system

The suspension of a vehicle on a track can be accomplished in one or more of the following ways.

(a) by air cushion;

(b) by the force of attraction between two magnetised bodies

(c) by the force of repulsion

(i) between two magnets of the same polarity

(ii) between a high-field magnet and a conducting sheet in which eddy currents are induced

(ii) continued

due to a high relative speed between the magnet and the conducting sheet or

(iii) between a linear induction motor and an aluminium track with or without backing iron.

The air-cushion type of suspension sub-system[7] has a 'natural' stability as it settles down by itself in the event of any changes in the weight or speed. It does not require any cryogenics or complicated control system as an essential element for maintaining the suspension of the vehicle. Earlier, this type of suspension was considered with all types of propulsion system. Tracked Hovercraft Ltd., in the United Kingdom, used air pads for suspension and guidance, and the single-sided linear induction motor for propulsion. The French Aerotrain used an air- cushion suspension and employed a double-sided linear induction motor for propulsion on a track of inverted-T cross-section.

Further researches into air-cushion suspension have shown that this type of suspension sub-system has a high noise-level, relatively high power requirements, a low operating air-gap, low lift-force to drag-force ratio, low lift-pressure, and is difficult to operate in long tunnels. These, unfortunately, appear to make the sub-system unsuitable for HSGT.

The suspension sub-system based on the principle of attraction between an electromagnetic and a ferromagnetic body[8] is the most developed of the contact-free suspension sub-systems yet devised, and is in an advanced stage in the U.K. under Professor Jayawant, at the University of Sussex, and in Germany by Transrapid - a joint company formed by Messerschmitt-Bolkow-Blohm (MBB) and Krauss-Maffei (KM) at the initiation of the German government - and at the British Rail Research Division. The suspension force produced in this type of sub-system is very large, but the system is inherently unstable and hence requires a continuous feed-back control, involving a suitable injection of positive or negative pulses of current, to maintain a constant air-gap (10 to 20 mm). The static power consumption of the servo-controlled suspension sub-system is very low (about 0.1 W/N), but the dynamic requirements would clearly be much greater. Thus, for high speed and, therefore, larger air gaps the power requirement, and consequently the rating, the weight and the cost of the solid-state feed-back amplifiers would be very much greater.

The suspension sub-system based on the principle of repulsion between high coercivity permanent magnets as rails under the vehicle and on the track[9,10] has distinct advantages of neither requiring any power along the track for vehicle suspension nor of producing any drag. However, the system is inherently unstable and needs additional mechanical or powered guidance. The consideration of this type of suspension sub-system for high speed transport is still dependent on further developments in magnetic materials and hence the cost of laying a permanent magnet track cannot be estimated accurately.

A force of repulsion between a magnet and a conducting plate[11,12] is produced when the clearance between them is appropriately small and the relative speed is sufficiently high, due to the interaction between the eddy currents induced in the plate and the magnetic field of the magnet. The force thus produced is too small for transportation purposes. However, a substantial lift-force with a considerable length of airgap can be obtained by replacing the permanent magnets by superconducting magnets wherein supercooled coils are made to carry very large currents. At low speed the eddy current drag-force in such a cryogenic suspension sub-system increases with speed in a manner similar to that of the aerodynamic force of an aerofoil. But whereas the drag force in the former reaches a maximum and then falls off sharply at higher speeds, that in the latter(aerofoil) continues rising with speed.
A disadvantage with the cryogenic suspension sub-system is that no lift-force is produced at stand-still and a minimum speed is necessary for 'lift-off'. Thus an additional auxiliary suspension sub-system becomes essential. Japan appears to be leading the world in the cryogenic suspension sub-system and her engineers have been the first to demonstrate this type of suspension using a reduced scale vehicle powered by a double-sided linear induction motor. At present this sytem is being studied also in the U.K. (Warwick University), the U.S.A., Canada and Germany.

It has also been proposed to obtain a stable magnetic suspension by using a 'mixed' system[13] comprising superconducting coils and screens mounted on the vehicle and a passive iron track (which may be the existing rails). The underlying principle[14,15,16] is based on the findings[15] of Braunbeck, according to which a dielectric or a magnetic body may be stably suspended only if the permittivity or permeability of the system is somewhat less than that of free space'. Work on this type of suspension system is in its initial stages at the Rutherford and Culham laboratories and comparison with the other suspension systems cannot be made.

Yet another(and perhaps the most promising) way of obtaining suspension by repulsion is by making use of a suitably designed linear motor under the vehicle and an aluminium track with or without backing iron. Incidentally this type of suspension sub-system, in contrast to others discussed earlier, does not require an additional propulsion system for propelling the vehicle. The next section discusses the problems of the propulsion sub-system. It also deals in detail with the problems associated with the LIM suspension-cum-propulsion system and with their solution.

1.3.2. Propulsion Sybsystem

The most natural propulsion system for a magnetically levitated vehicle is by a linear motor that produces magnetic forces to produce thrust. There are many types of linear motor, as there are rotary motors, but the linear induction motor is the one that has reached the most advanced stage by receiving the maximum amount of study, analysis and testing.

The linear induction motor is often described as an unrolled rotary induction motor (as shown in Fig.1.4); but, in reality, it is the linear version that is the most basic machine and the rotary version is a special case.

Since the invention of the induction motor by Tesla in 1888 the attention of electrical engineers has been continually focused on it, almost the whole of this attention being on the rotary induction motor.

This configuration of the induction motor has been developed and improved because of the fact that a very good and reliable performance can be obtained from configurations with closed electric and magnetic circuits. Designers know now that parameters like power-to-weight ratio, efficiency, power factor, air-gap flux, speed and many others can be easily controlled to yield induction motor designs which may be the best compromise between ideal performance and cost. The same detailed knowledge of linear machines does not exist: they were considered for many years to be 'bad'machines and hence ignored.

Nevertheless, interesting and invaluable contributions by Professor E.R.Laithwaite since the late forties, and the need for a high speed ground transport system, having contact-free, comfortable suspension, noiseless and pollution-free,have,with other factors, provided an effective impetus towards the development of the large linear machine.

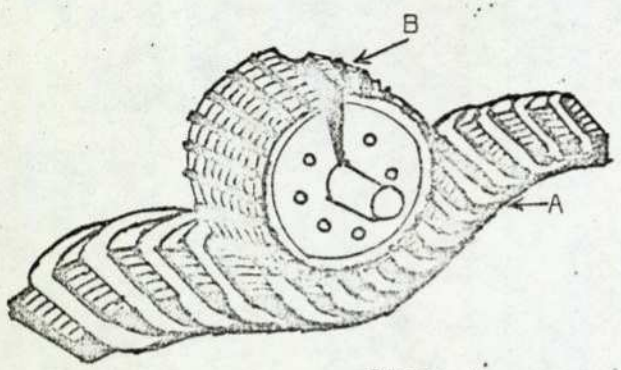

Stage 1

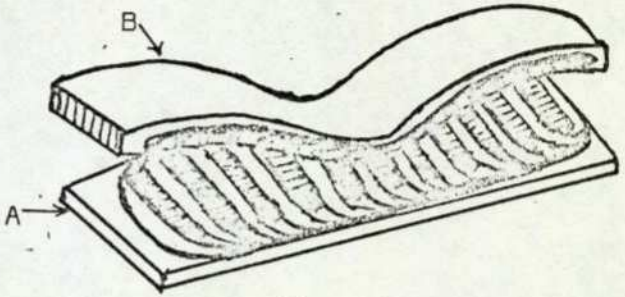

Stage 2

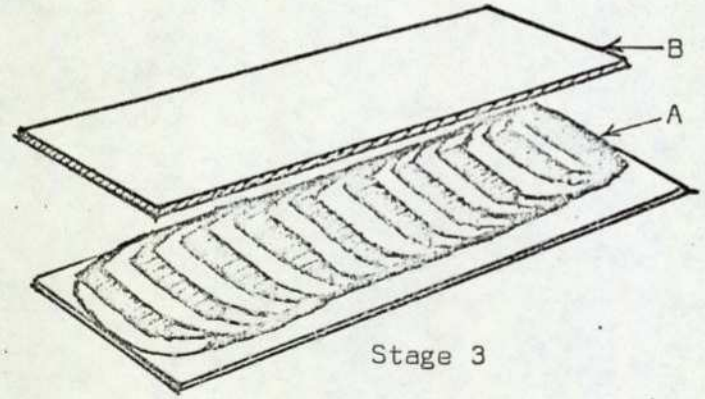

Stage 3

A Primary member

B Secondary member

Fig.1.4 Evolution of linear induction motor

During the early stages of work on HSGT, it was suggested that for maximum efficiency and the elimination of unbalanced forces the LIM's should be of the double-sided configuration. However, later it was realised that although for efficient operation the LIM should operate at relatively small air-gap lengths, yet for speeds of the order of 400km/h the air-gap must be sufficiently long for a safe mechanical clearance. Alternatively, the vertical secondary member must be constructed to impossibly fine tolerances, while keeping in view the buckling of the secondary member due to the normal ambient temperature variations. Furthermore, the construction should be able to cope with the large vehicle forces without unacceptable distortion. In view of these practical problems, it has been now decided almost generally to use the single-sided linear induction motor (SLIM) having its secondary conductor firmly bolted flush with the track.

The synchronous velocity of a linear induction motor is given by the product of the supply frequency and the double pole-pitch of the machine. Therefore, for high speed operation it is obvious that either the supply frequency has to be increased or the pole pitch has to be made large. Unfortunately, the weight and the cost of electronic frequency changing equipment is high and therefore the pole-pitch has to be made large.

For a 50Hz supply and a synchronous velocity of 400km/h, the length of pole-pitch is more than a metre. The large pole-pitch gives rise to a corresponding increase in the length of the overhang winding and hence the ohmic loss.

The core depth, behind the stator teeth and behind the reaction rail, also has to be increased to accommodate (in the worst case) the pole flux. (In rotary induction motor the core has to carry only half of the pole flux.) The net result is that the motor is heavy; its leakage inductance is large and the efficiency low.

There might be some saving in copper and the corresponding ohmic loss by arranging a Gramme-type, instead of surface winding. But, apart from increase in leakage flux, there is no saving in core depths behind stator teeth and the reaction rail for the core flux is still a function of pole-pitch.

One more choice is to change the flux path from planes parallel to the direction of motion to the planes perpendicular to the direction of motion. The former arrangement is called axial flux and the latter transverse flux. Fig.1.5 shows the constructional and flux path differences between the surface wound and the Gramme-type axial flux LIM and the surface wound transverse flux LIM. It is evident that in the surface wound TFM the winding overhang is still a function of the pole pitch of the primary winding, similar to that in the surface wound AFM. The end windings and the end rings increase the cost of the track conductor, the weight carried and the primary leakage flux. Nevertheless, the reduction in the magnetic core made possible by the transverse flux configuration compensates for additional electric circuit weight.

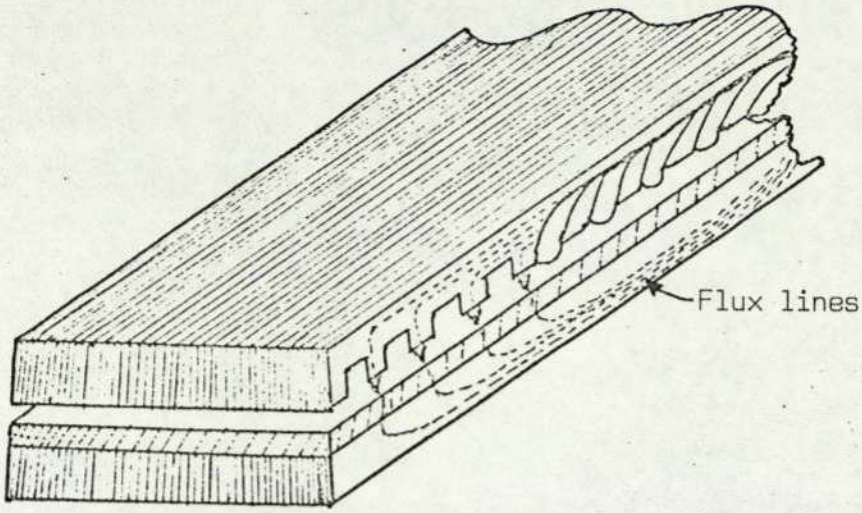

(a) Surface-wound axial flux linear induction motor

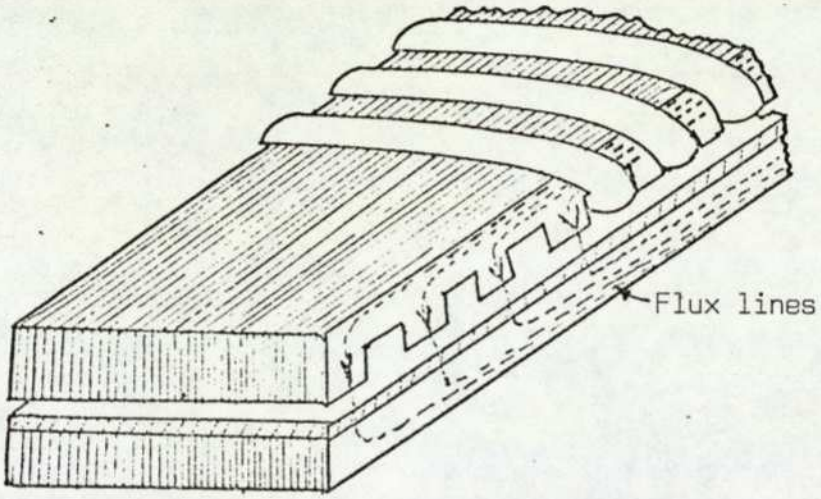

(b) Gramme-ring type axial flux linear induction motor

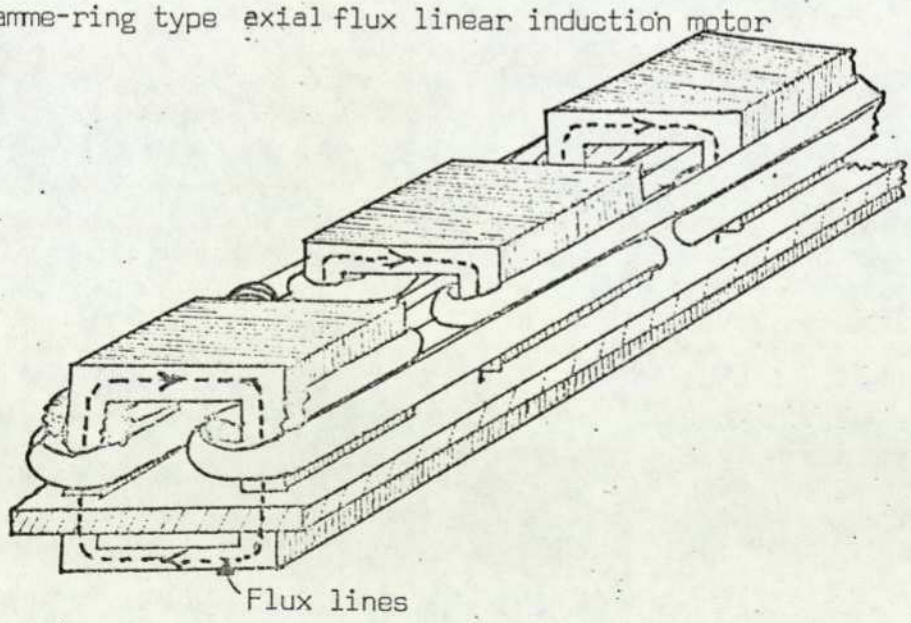

(c) Surface wound transverse flux linear induction motor

Fig.1.5 Axial flux versus transverse flux linear induction motor

1.4 HISTORY OF THE TFM

The transverse flux motors have a history as old as that of the longitudinal flux motors. In fact, at the middle of the nineteenth century, most of the alternative shapes tried for the improvement of d.c.motor performance were based on the transverse flux principle[17]. The TFM's took the lead in the induction mode as well, the first transverse flux induction machine being energy meters having the C-core type magnetic circuit.

The earliest reference to transverse flux applied to linear machines may be traced back to the patent[18] taken out by Andre in 1904: this motor was excited by doubly-excited C-cores. In 1938,Kemper[19] published a patent describing an E-core electromagnetic suspension system with a note that motoring action is possible if the single-phase winding is replaced by a polyphase one. In the late sixties Laithwaite and others[20,21,22] revived the interest in the transverse flux linear induction motor by inventing the 'magnetic river'.[63,64]

A reference to transverse flux machines was also made in 1966 in an M.I.T. group report[23].

In 1971,Bolton[24] made a significant contribution towards the development of transverse flux linear induction motor by devising suitable design techniques and a method of predicting its performance (based on an equivalent circuit approach). Further work in this direction is in progress at the Imperial College of Science and Technology (University of London) under Professor Laithwaite, at the City University in London

under Professor Ellison and at the University of Aberdeen under Professor Eastham.

The transverse flux linear induction motor, when suitably designed, can behave as a 'magnetic-river' and develop lift force for suspension, tractive force for propulsion together with lateral guidance force, and may replace the wheel-rail system for high speed ground transport. Although the advantages of the transverse flux linear induction motor have been realised and there is little doubt about their practicality, yet a rigorous treatment leading to an independent analysis and understanding of TFM's is not yet published and is now necessary for their further development and application. The treatment must involve the estimation of the three forces and associated stiffness and also include the effects of the three other asymmetries in the air-gap due to roll, pitch and yaw of the vehicle with respect to the track. The effects of all these on the others must also be considered. When this understanding has been achieved such machines can be designed and their performance and cost calculated.

An approach towards this end, as discussed in this thesis, has been made both theoretically and experimentally. In the theoretical model the magnetic scalar potential has been used as the field parameter to obtain the 3-dimensional distribution of flux-density, current density in the secondary member and the forces produced. For the experimental approach a novel test rig called the Basic Transverse Flux Circular Motor (BTFCM) has been made. This test rig, if cut along a radial line and straightened out would result in a transverse

flux linear motor. The test rig in its basic form does not exhibit the entry and exit effects of the linear motor, but it does have provision for carrying our studies involving these effects(by omitting a section). The test rig in itself is a useful research machine for carrying out a detailed study of the transverse flux linear electric motor.

1.5 AXIAL FLUX LIM VERSUS TRANSVERSE FLUX LIM

The transverse flux linear induction motor has certain outstanding features. It also has a number of advantages over its counterpart the longitudinal flux linear induction motor for HSGT application.

1.5.1 Depth of iron required

In the transverse flux LIM the depth of iron in the stator core and the thickness of the backing iron on the secondary side can be kept very small[20]. This is primarily because in the transverse flux LIM the core has to carry only that flux which is produced by the corresponding limbs of the U-core or E-core, and not the pole-flux as in the axial flux LIM. Thus the TFM design leads to a very large saving in iron required for the track and hence a correspondingly large reduction in cost in comparison with the axial-flux machine.

1.5.2 Entry and exit effects

The open ends of the axial flux LIM give rise to the well-known end-effects due to the magnetic discontinuity. However, in the case of the transverse flux-LIM the absence of magnetic discontinuity reduces these end-effects. This,according to Chahal[25], will lead to a corresponding reduction of entry and exit edge losses.

1.5.3 Overhang winding leakage flux

A part of the overhang winding flux in the transverse flux LIM reacts with the secondary aluminium track to produce levitation forces. Also, when appropriately designed, the transverse flux linear induction motor produces guidance forces at each side which tend to keep the vehicle centred on the track when it is displaced sideways. Since these forces are a function of displacement from the centre line, the system becomes independent of external controls and complete in itself. This feature of the transverse flux LIM is in contradistinction to that of the axial flux LIM where the forces in the two sides of the motor resulting from sideways displacement have a tendency to displace the primary member further.

1.5.4 Speed control of linear motors

The synchronous speed of an axial flux LIM is fixed by the length of the pole-pitch of the motor and can be controlled only by altering the supply frequency. The transverse flux LIM has an additional facility for controlling the synchronous speed. The cores of the primary member can be separately wound and the distances between them can be altered mechanically[26] to result in a change of the length of pole-pitch and hence of the synchronous speed. The output-to-weight ratio of the motor alone with this arrangement will be made worse but, nevertheless, it should still be better than the overall output-to-weight ratio of a normal transverse flux-LIM together with the necessary frequency conversion equipment. The arrangement will be also comparable with pole-changing speed control where the synchronous speed will be changing in discrete steps - perhaps not so very desirable from the point of view of passenger comfort.

1.6 OUTLINE OF THE THESIS

The aim of the work reported in the ensuing chapters is to develop a numerical method for predicting flux density, current density and forces in transverse flux machines followed by the correlation of calculated flux densities and forces with those measured on the basic transverse flux circular motor.

Transverse flux machines have discontinuities in all three axes and they produce tractive, normal and lateral forces. These features make the three dimensional analysis mandatory for their development. In the past, electromagnetic scale modelling of the device has been suggested for predicting its performance by making use of suitable scaling parameters[57]. This requires measurement of the flux density and forces for every modification made in the model and it assumes the validity of the scaling parameters for any rating. Moreover, the approach requires a considerable amount of workshop skill for constructing small models which may have to be constructed afresh to include certain major modifications.

The standard analytical treatments from first principles, discussed in Chap.2, have two serious limitations. First, the number of boundaries (which are present in all the three axes) results in great complexity[43]. This is because linear machines have to operate with relatively large air gaps for mechanical reasons and they have entry and exit effects due to one of the members being much shorter than the other. This results in end effects and currents in the secondary member not guided in the ways they would be in rotary machines.

Secondly, having analysed a device it is generally difficult to suggest, from the results of analysis, means for improving its performance further. Taking these factors into consideration, it has been shown in Chap.2 that owing to the discontinuities in the device and the rectangular geometry of linear machines, the finite difference formulation of the field equations is the best choice.

In Chap.3 a numerical model of the basic transverse flux circular motor has been constructed such that modifications made in its geometry, anywhere and in any direction, can be easily accounted for. The primary magnetomotive force in the BTFCM has been defined by current sheets on the primary iron surfaces and flux sheets on the boundaries of the winding. The secondary conducting sheet backed by laminated iron has been represented by a thin sheet model. The formulation thus considers the features of the device in stages and, therefore, accounts for the existing discontinuities in the machine during the initial stages of the formulation of the problem. The necessary finite difference equations have been discussed to obtain the magnetic scalar potential distribution in and around the device during standstill, motoring and braking conditions. This potential distribution has then been used to define the flux densities and the forces produced.

Chapter 4 looks into the problems associated with the testing of linear electric machines and describes in detail a new test rig - the Basic Transverse Flux Circular Motor.

The arrangements made for the measurement of forces and flux densities under standstill and dynamic conditions are also discussed.

In Chapter 5 the results of numerical analysis, as discussed in Chap.3, and those obtained by measurements on the BTFCM, described in Chap.4, are compared. The correlation of flux densities and forces at standstill, motoring and braking conditions are discussed. Also two and three dimensional plots of computed flux density and current density are presented to show their distribution along the length of the machine.

In Chapter 6 the numerical analysis discussed in Chapter 3 has been further extended to predict the performance of the BTFCM when the secondary consists of thick conducting sheet backed by a partially saturated backing iron. The thick conducting sheet has been divided into thin 'slices' and each slice has been represented by a split-node model described in Chapter 3. The backing iron is assumed to have a fixed degree of saturation and the corresponding magnetic impedance has been defined and used in the numerical formulation.

The approach discussed in this thesis can be supplemented to account for the three dimensional heat flow in the machine and the results of final analysis might then be used to derive suitable equivalent circuits for use in design offices for designing and costing larger machines in a conventional way. These aspects, together with suggestions for further work and the conclusions drawn from the research reported in this thesis, are discussed in Chap.7.

CHAPTER 2

2. ANALYSIS OF ELECTROMAGNETIC DEVICES

2.1 INTRODUCTION

The design of magnets, and electromagnetic devices, even of simple form, poses many problems. These are associated principally with non-linearity, geometric complications, particularly in 3-dimensions, and eddy currents. In magnetostatic applications the current flow paths are defined, but the flux paths are not, while in eddy current problems, neither is, and the interactions are controlled only by the material properties. This complex arrangement of conducting, insulating and magnetic materials has led to a very marked dichotomy in the traditional methods of analysis. The more familiar method is based on a lumped-parameter model, in which only a few parameters suffice because of the relatively effective physical separation of the current and flux paths in the machine. This combined with the energy conversion principle enables the machine to be treated virtually as a 'black-box' thereby accounting for the mechanical power in terms of the electrical terminal quantities only. However, when we need to delve more deeply into the energy conversion process, and predict the parameters, more than one force (desired or undesired) and losses, it becomes necessary to go back to the basic electromagnetic principles of the field theory on which the operation of the machine depends.

Rotary electric motors have axial symmetry and neglecting the leakage flux of the slot, zig-zag and overhang windings, the machine can be analysed by considering a plane normal to the axis.

The air-gap is usually very small and hence the main flux in the air-gap can be safely assumed to be radial. This simplifies the theoretical model and the machine can therefore be analysed and its performance predicted fairly accurately by using a one-dimensional analytical approach. To simplify the treatment still further, the number of slots per pole per phase is assumed sufficiently large and the turns per coil are varied, to permit the harmonic content to be neglected. The rotor if slotted, is replaced by a sheet rotor such that it has the same effective resistance and leakage reactance as the original.

The problem, however, becomes two/three dimensional as the rotary electric motor is transformed topologically to yield the corresponding linear motor. This is primarily because:

(a) the length of air-gap is for mechanical reasons no longer small, and hence the flux lines in the gap can no longer be assumed to remain normal to the primary iron surface along the whole of their length. This implies that there are no planes equivalent to those normal to the axis of rotary machines where the flux patterns are identical. This is particularly true of the single-sided linear machine.

(b) Apart from the driving force, normal and lateral forces are also produced and for a large normal levitation force (due to repulsion) it becomes necessary to use wide slots and narrow teeth (contrary to rotary motors). This increases the high order (slot) harmonic content

of the primary mmf waveform but the large air gap reduces the corresponding flux distribution harmonics.

In the last decade or two, many researchers have looked into the problem of analysing linear electric motors. Their approaches can be broadly classified under two headings:

(a) the equivalent circuit approach and

(b) the electromagnetic field approach.

The equivalent circuit approach is very useful in practice for it does give efficiency of design effort and makes easier the task of testing, fault finding and repair. But when the linear electric motor is considered as a 'black-box', more attention is given to the performance than to the functional details. In the electromagnetic field approach, the emphasis shifts to the latter and therefore gives a better understanding of the internal properties and their effect on the performance of the device. The latter approach is useful, particularly during the development stages when it becomes necessary to account fully for topological or any other modifications made in the device.

In the following section the electromagnetic field approach and methods of solving field equations are briefly reviewed.

2.2. ELECTROMAGNETIC FIELD APPROACH

An accurate knowledge of the magnetic field in electrical machines, particularly in the special purpose types, is an essential pre-requisite to their design. Fortunately the associated magnetic field in an electrical machine is contained within a closed region and boundary conditions are prescribed around the entire boundary. The problem, therefore, is of a boundary value

type and its governing field equation has a form

$$\nabla^2 \psi = \Phi_1(x,y,z) \qquad 2.1$$

where ψ is a potential, ∇^2 is the Laplace's operator defined in Cartesian coordinate as

$$\nabla^2 \equiv \frac{\partial^2}{\partial x^2} + \frac{\partial^2}{\partial y^2} + \frac{\partial^2}{\partial z^2} \qquad 2.2$$

and Φ_1 is the source function.

The eqn. 2.1 is elliptic (Appendix A) and is referred to as Poisson's equation. In a particular form when $\Phi_1 = 0$ it becomes Laplace's equation

$$\nabla^2 \psi = 0 \qquad 2.3$$

Strictly speaking, these equations describe all stationary electric and magnetic fields in a uniform medium. However, fields varying with time can also be described with a high accuracy provided the rate of variation is sufficiently low, such that the effect of the resulting displacement current and eddy current due to frequency is negligible. Poisson's equation is applied within regions of distributed current or charge and Laplace's equation is applied in all other regions of the field. The solution of Poisson's equation, in general, is more difficult compared with that for Laplace's equation. However, when the field in a Poissonian region is of little interest the region can be replaced by an equivalent filament [27] or sheet so making the

whole field a Laplacian one. This, therefore, reduces the problem to the solving of Laplace's equation.

There are several techniques for obtaining solutions to eqn. 2.3 in different co-ordinate systems. These techniques can be broadly classified under the following headings :

(a) graphical,

(b) analogue,

(c) analytical and,

(d) numerical.

The graphical solution of eqn. 2.3 can be obtained by a trial-and-error process[28]. This is one of the earliest methods of solving two-dimensional field problems and works quite satisfactorily in current-free simple regions. However, in electric machines, where it is necessary to deal with regions carrying current and often geometries which are complex, this method finds little use.

Analogue methods[28] are useful when the direct measurement of the flux distribution presents experimental difficulties. The more common techniques are

(a) conducting sheet analogue (e.g. electrolytic tank),

(b) impedance network analogue,

(c) membrane analogue, and

(d) fluid mapper

As with the graphical method, these have limitations but are nevertheless useful for the simpler types of problem. This leaves us with the analytical and the numerical methods which are discussed in the following sections.

2.3 ANALYTICAL METHODS OF SOLVING FIELD EQUATIONS

Analytical solutions of eqns. 2.1 and 2.3 can be obtained by introducing suitable mathematical functions that satisfy the differential equation, but the problem is to obtain that solution which satisfies the boundary conditions. Moreover, none of the analytical techniques is perfectly general, since the practical problem imposes restrictions which, at times, make it extremely difficult to apply an analytical method for its complete solution.

Separation of the variables[29] is practicable only if the boundary surfaces coincide with the natural surfaces in a co-ordinate system in which Laplace's equation is separable. When it is appropriate the method usually yields an infinite series whose physical meaning is difficult to visualise.

The method of complex variables[28] gives the result only in two dimensions and that only if one is able to find the appropriate analytic function. Similarly, the method of images[28] is suitable only when a simple charge distribution that establishes the correct equipotentials is known, ab initio.

On the basis of the foregoing discussions, numerical methods seem to be eminently suitable for solving eqns. 2.1 and 2.3 to obtain fields and forces in linear electrical machines. Some suitable methods applicable to the present problem are discussed in detail in the following sections.

2.4 NUMERICAL METHODS OF SOLVING FIELD EQUATIONS

The restrictions and limitations of the analytical approaches, discussed in Sec.2.3, can be quite conveniently dealt with by employing numerical methods for solving partial differential equations. These methods are very powerful and can be applied equally to steady state and transient problems, linear and non-linear, with or without regular boundary shapes and conditions.

The solutions obtained numerically are, however, always approximate, but a desired accuracy can be achieved by extending the computation for a sufficient length of time and by suitably increasing the number of nodes. Also, as in other numerical methods, if a separate solution is required for each set of parameters of a problem some computer time may be saved by obtaining an approximate solution with one set of parameters, and using this as a starting point for obtaining a solution with the new set of parameters. This is more likely to be so when a tendency to instability arises during the iteration process, and a progression towards a final solution can be obtained in this way by incrementally increasing one of the parameters (e.g. speed) at each stage. The relative merits of analytical and numerical methods depend solely on the problem in hand. When the problem can be solved both numerically and analytically, it is the complexity of the solution that decides which one to adopt. Analytical methods will be preferred except when they involve many lengthy manipulations, with or without lengthy computations. Numerical methods will then

be found more convenient and certainly more economical when a suitable computer programme - requiring only data defining the boundary shape and conditions - is available.

The principal numerical techniques applied to the solution of field problems are

(a) the finite element method, and

(b) the finite difference method.

In each approach the field region of interest is divided into a grid of meshes. Potential (or other field variable) values are assigned at each node and these are related to the values at the surrounding nodes by a series of approximate relationships based on Maxwell's equations.

The basic difference between these two techniques is that the latter is applied to the governing partial difference equation, e.g., eqns. 2.1 and 2.3, and the former is more often formulated directly from the physical arguments used to derive such equations (although the knowledge of the type of problem - harmonic or biharmonic - is useful during the finite element formulation). The finite element method gives an additional advantage when the geometry is complex and does not conform easily to one of the standard co-ordinate systems. The derivative boundary conditions are usually easier to handle using the finite element method and so also are the inhomogeneous solution domains involving abrupt changes of material properties. However, the application of the finite-element method for solving eddy current problems is found difficult

when compared to the finite difference method formulation because, in the former, the dissipation of energy effects the variational formulation.[30]

In linear electric motors the geometry often fits into the Cartesion co-ordinate system so that the grid lines can be conveniently considered parallel to the co-ordinate axes and the rows of nodes can be terminated on the boundary. These advantages, together with the ease with which suitable fine meshes can be adopted in regions where the variables change rapidly, make the finite difference method relatively more suitable than the finite element method for solving field problems in linear electric motors.

In the following section the finite difference equation is derived for Laplace's equation and the more common methods of solving it are discussed.

2.5 FINITE DIFFERENCE EQUATION AND METHODS OF SOLUTION

In the finite difference method Laplace's partial differential equation is replaced by finite difference equations which connect the values at surrounding nodes to those at the node under consideration. The mesh of nodes can be constructed as square, equilateral-triangular or equilangular-hexagonal. The most common of these is the square mesh which is a special case of rectangular node spacing.

In Cartesian coordinate system eqn.2.3 can be expanded as

$$\frac{\partial^2 \psi}{\partial x^2} + \frac{\partial^2 \psi}{\partial y^2} + \frac{\partial^2 \psi}{\partial z^2} = 0 \qquad 2.4$$

and in difference equation form, from Taylor's expansion (Appendix B), eqn. 2.4 for uniform internode spacing is

$$\sum_{n=1}^{6}(\psi_n - \psi_0) = 0 \qquad 2.5$$

where ψ_n is the potential surrounding nodes (n). Further, for Poisson's equation, when the right hand side of eqn. 2.4 is equal to $\Phi_1(x,y,z)$ instead of zero, eqn. 2.5 is modified as

$$\sum_{n=1}^{6}\psi_n - \psi_0 = h^2\Phi_1(x,y,z) \qquad 2.6$$

where 'h' is the internode spacing.

Depending upon whether the node lies in a current-free or a current-carrying region, its potential can be defined by eqns. 2.5 and 2.6 respectively and the solution of the field can be obtained by solving all these simultaneous equations. But the number of these simultaneous equations is always so large that it becomes unreasonable to solve them using methods involving elimination, determinants or matrix inversion. Instead the following methods are used. They are :

(a) Relaxation;

(b) Iteration; and

(c) Monte-Carlo.

The relaxation method[31] is basically a method for hand computation and is extremely flexible. Its effectiveness, however, depends upon the experience and skill of the user.
In contrast, the iteration method is based upon an entirely

automatic cycle of operations suitably planned for execution on a high speed computing machine. In both these methods the final solution is obtained by gradually reducing the error to a preset value, and the process is called the convergence of the solution. The convergence criterion and the methods of accelerating the convergence are discussed in Sec. 2.6.

The Monte-Carlo method[32] is a statistical method for approximating to the solutions of Poisson's and Laplace's equations. It is extremely simple to apply but since the calculation is very long its use requires comparatively longer computing time than does the iteration method. Moreover, the solution is obtained, at a time, for one point only and the convergence rate is much slower when compared with that of the other methods.

From the discussions in this section, it is seen to be clear that the iteration method is the best of the three methods for solving the finite difference equations to obtain the field in linear electric motors. This is primarily because of the existing complexities, discontinuities and the number of nodes in the linear electric motor model. In the following section the computational aspects of the iteration method are discussed.

2.6 COMPUTATIONAL ASPECTS

In the iterative method an automatic cycle of operations is performed on a high speed digital computer such that the difference of new and old potentials at all the nodes goes on

decreasing with the successive number of iterations. The process is called 'convergence' and the difference between the new and old values at a node is termed the 'residual'. Thus, if the node under consideration '0' is surrounded by equidistant nodes 1,2,3,4,5 and 6 in a current free region, the new value of potential at node '0' is

$$\psi_{new} = (\psi_1+\psi_2+\psi_3+\psi_4+\psi_5+\psi_6)/6.0 \qquad 2.7$$

and the residual is,

$$R_0 = \psi_{new} - \psi_{old} \qquad 2.8$$

Combining eqns. 2.7 and 2.8

$$R_0 = \frac{\psi_1+\psi_2+\psi_3+\psi_4+\psi_5+\psi_6}{6.0} - \psi_{old} \qquad 2.9$$

The new value of potential at '0' is found from eqn.2.8 rearranged as

$$\psi_{new} = \psi_{old} + R_0 \qquad 2.10$$

In eqn. 2.10 the addition of Ro to ψ_{old} affects the potential of the surrounding nodes as well. This decreases the convergence rate of the solution and, at times, when ψ is complex and the concerned nodes lie in the eddy current region, the solution may even diverge. Many powerful techniques have been devised to speed up the process. In essence they involve a factor α by which the residual in eqn 2.10 is altered. Thus eqn. 2.10 becomes $\psi_{new} = \psi_{old} - \alpha R_0$ 2.11

Here α is known as the acceleration factor and, depending upon whether it is less than or greater than unity, the

process is called under-[33] or over-[34] relaxation. It is difficult to quote specific situations where one or the other will be advantageous[27]; however, it will suffice to indicate the general circumstances and the rest must be left to the experience of the user. In simple problems where hand relaxation is possible, over-relaxation assists in convergence when a residual is surrounded by residuals of like sign. In a similar way under relaxation is found useful in situations when the surrounding residuals have opposite sign. However, when iterating towards a final solution after first initialising the iteration matrix to zero, it is always preferable to over-relax (e.g. $\alpha > 1.0$) since the residuals will not be greatly dissimilar for nodes in close proximity.

Considerable work[35] has been done for predicting the best acceleration factor to apply in the iteration process when solving Laplace's and Poisson's equations in electrostatic and magnetostatic field problems. However, when the field quantities are complex, a real acceleration factor, which was earlier suitable for a similar electrostatic and magnetostatic field problem, is not the best choice. Ehrenborg and Sigdell[36] have found that a complex acceleration factor is better than a real acceleration factor, although the imaginary part is quite small. The determination of an optimum acceleration factor is difficult, especially of the imaginary part. Experience shows that the real part of the optimum acceleration factor lies between 1 and 2 and the imaginary part within say $\pm$ 0.03.[37]

In the present work no attempt has been made to predict theoretically the optimum acceleration factor. However, during the execution of the computer programme, after a set number of iterations, the error or residual is integrated over the iteration matrix for two successive iterations. The ratio of these two integrals is used for estimating the optimum acceleration factor (see Appendix C). The new value of the real part of the acceleration factor for the next set of iterations, is generally modified according to a modification factor as in eqn. C.12. At times, the modification of the imaginary part of the acceleration factor also helps.

The technique has been found to work satisfactorily for the initial investigations described in this thesis. It is very simple to apply and can be easily modified by trial-and-error method to suit a particular problem.

One of the most difficult features of these trial-and-error methods is the derivation of a criterion to study their overall effect on the iteration process. One method is to plot the real and imaginary parts of the greatest residual (Ro), in the iteration matrix, against the number of iterations (as shown in Fig.2.1). However, when the values of the real and imaginary parts change rapidly in apparently random manner, it becomes difficult to examine the effect of a modification in the iteration process on the overall convergence rate of the programme. An alternative[38] is to plot the imaginary part against the real part of the greatest value of Ro for each

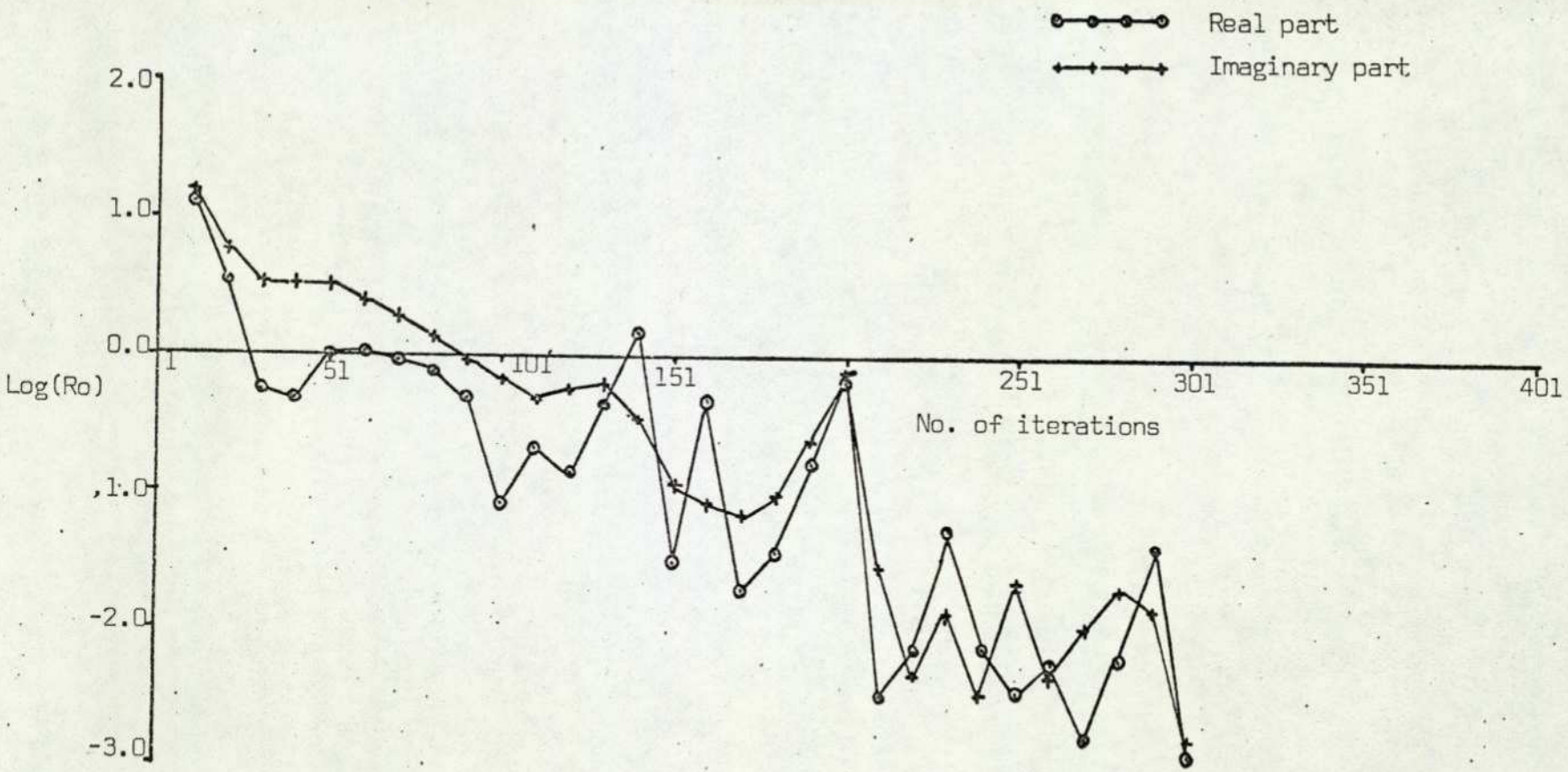

Fig.2.1 Convergence example having variation of log of real and imaginary parts of highest residual in the iteration matrix, with respect to the number of iterations.

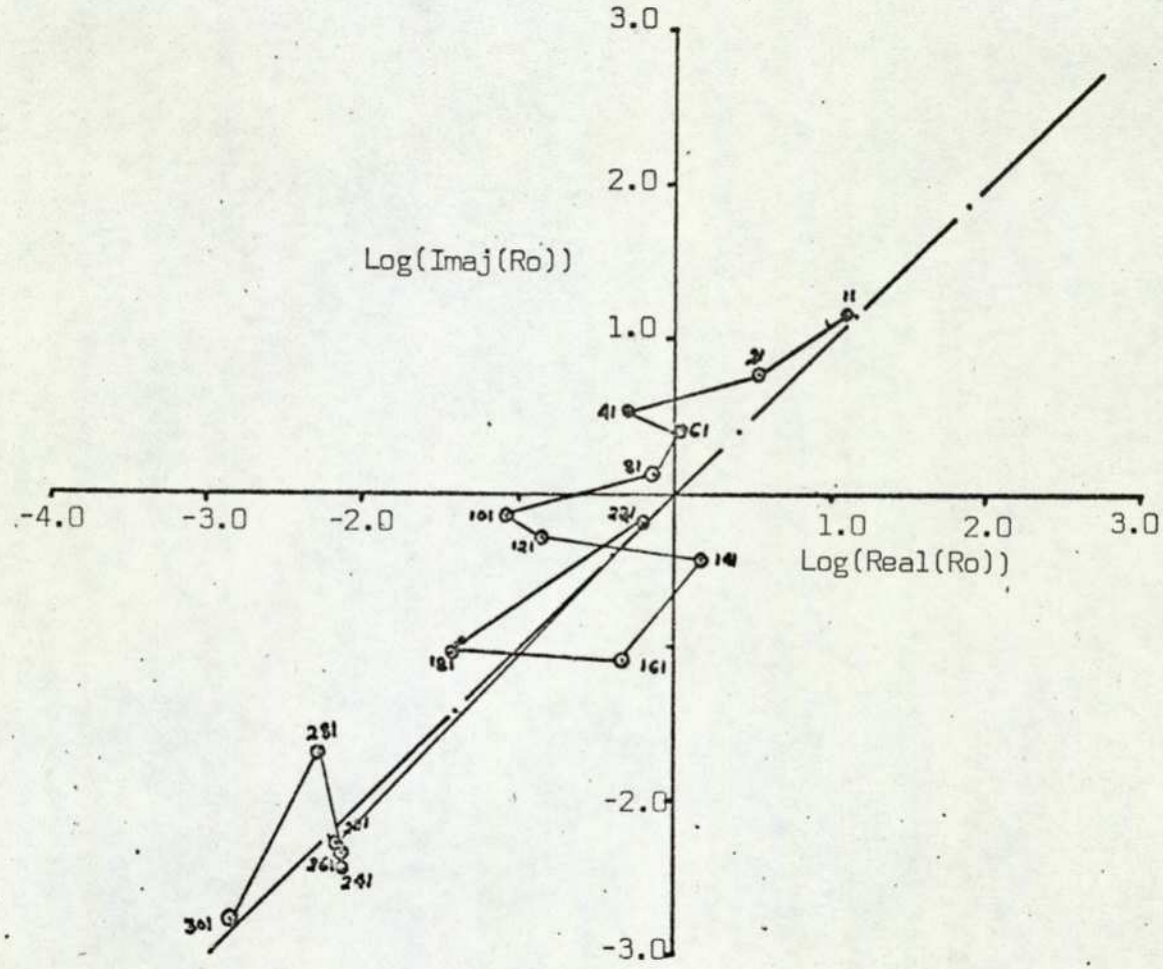

Fig.2.2 Convergence example showing variation of the Log of real part against that of the imaginary part of the greatest residual in the iteration matrix.

iteration cycle. For an ideal and well defined problem, the locus of these points should lie on the 45^{o} axis, as shown in Fig.2.2. The aim of all the modifications made in the iteration procedure, therefore, should be to keep this locus, as near as possible to the 45^{o} axis. Fig.2.3 shows an example where the trial-and-error modifications were made to improve the convergence rate. Each plot is a locus of greatest residuals corresponding to modifications listed in Table 2.1, after a set number of iterations as indicated on each curve.

It is difficult to draw general guidelines for improving the rate of convergence of the iteration process from these plots. This is primarily because they vary considerably from problem to problem. Nevertheless, the trial-and-error technique (discussed for tackling the problem of convergence) is very useful, especially when it involves eddy currents with or without speed effects, and it has been used in the present work with advantage.

TABLE 2.1

Plot Symbol	Starting acceleration factor (ACCL)	Residual after 301 iterations	Remarks
A	(1.6,0.03)	$(1.0X10^{-3}, 6.46X10^{-3})$	ACCL altered after every 10 iterations
B	(1.6,0.005)	$(1.09X10^{-3}, 6.45X10^{-3})$	Ditto
C	(1.7,0.05)	$(8.96X10^{-4}, 6.14X10^{-3})$	Ditto
D	(1.8,0.1)	$(7.56X10^{-4}, 5.76X10^{-3})$	Ditto
E	(1.8,0.1)	$(8.09X10^{-4}, 3.26X10^{-3})$	ACCL altered after every 20 iterations. First alteration after 40th.
F	(1.8,0.3)	$(2.5X10^{-3}, 1.45X10^{-3})$	Ditto
G	(1.8,0.2)	$(5.74X10^{-4}, 2.52X10^{-3}$	Ditto
H	(1.8,0.25)	$(1.21X10^{-3}, 1.90X10^{-3})$	Ditto

Largest potential in the iteration matrix = 636

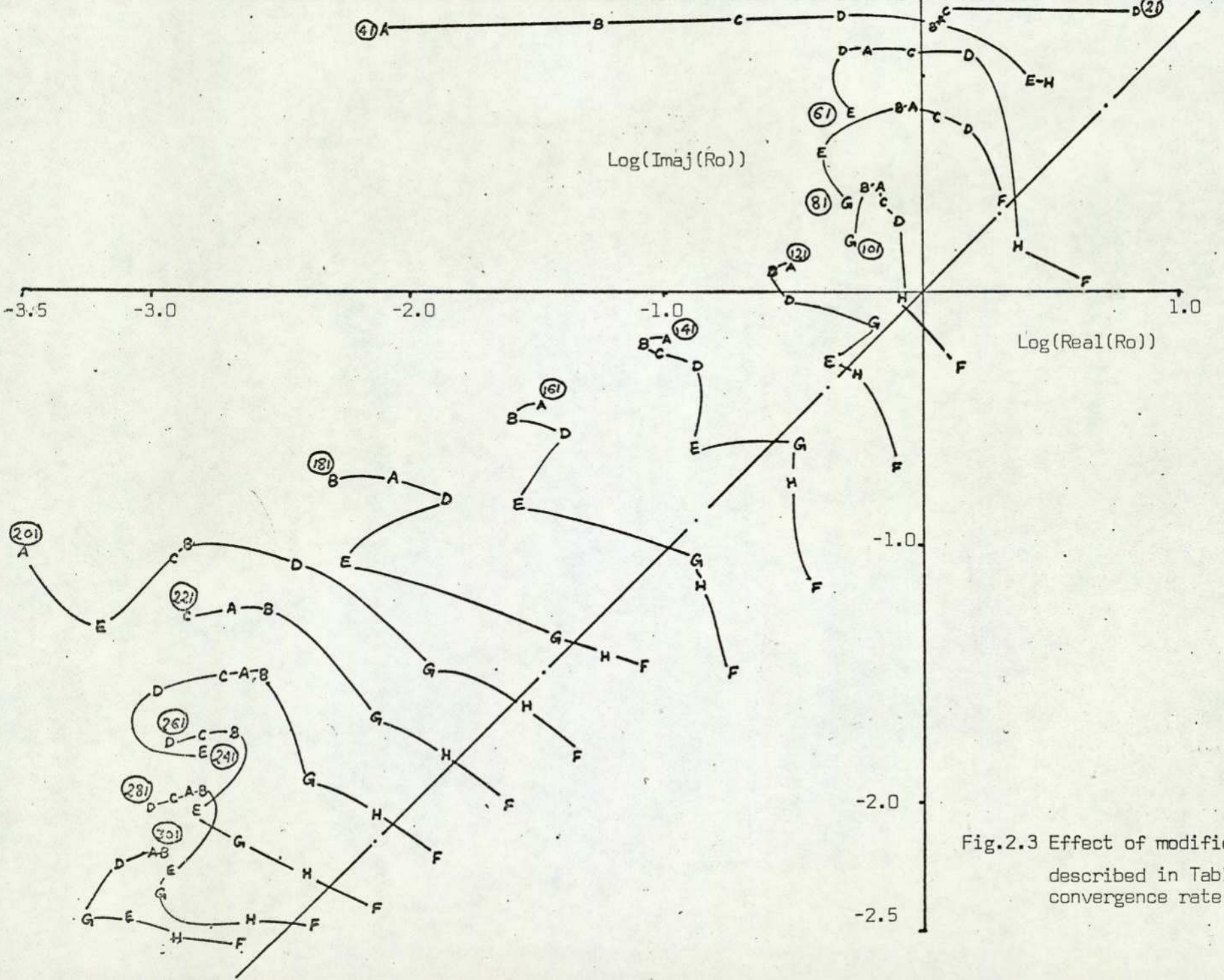

Fig.2.3 Effect of modifications described in Table 2.1 on the convergence rate.

2.6.1 Convergence Criterion

The solution obtained by iterative methods is not accurate and involves a certain degree of error which may be defined according to the accuracy desired. If U_0 is the final value at a node, the absolute error after (m+1) iterations is

$$\varepsilon_a = U_0 - U_{m+1} \qquad 2.12$$

and the relative error is

$$\varepsilon_r = \frac{\varepsilon_a}{U_0} \qquad 2.13$$

But, U_0 is always unknown and hence the following test has to be applied:

$$\varepsilon_r = \left| \frac{U_{m+1} - U_m}{U_{m+1}} \right| < \varepsilon \qquad 2.14$$

where ε is the error which gives the desired accuracy in the solution.

A possible way of considering the situation at all the nodes simultaneously is to use:

$$\varepsilon_r = \sum_{i=1}^{n} \left| \frac{\delta U_i}{U_i^m} \right| < \varepsilon \qquad 2.15$$

where $\delta U_i = U_i^m - U_i^{m-1}$

and the superscript m indicates the value after m^{th} iteration. This is, obviously, a poor choice of convergence criterion for it becomes misleading when U_i is very small or zero. A much better criterion will be

$$\varepsilon_r = \frac{\sum_{i=1}^{n} |\delta U_i|}{\sum_{i=1}^{n} |U_i^m|} < \varepsilon \qquad 2.16$$

A disadvantage with the above test is that it is difficult to notice divergence of the process if the U_i tend to infinity. However, after the first few iterations a test for divergence can be made by testing to see whether $\varepsilon_r > 1$. If $\varepsilon_r > 1$ there is no 'rapid' divergence. Unfortunately, even this method will fail to detect a slow divergence.

The convergence criterion, used in the present work, is that the error at every node should be less than a fixed value, given by

$$\delta U_i^m < \varepsilon \left| \sum_{i=1}^{n} \right. \qquad 2.17$$

and ε has been defined as 10^{-7} of the highest potential in the iteration matrix. In addition to this, a comparison between the calculated and the measured values of the flux density in the air-gap, has been used as a final check for convergence.

CHAPTER 3

3.0 NUMERICAL MODEL IN TERMS OF MAGNETIC SCALAR POTENTIAL FOR THE FIELD ANALYSIS

3.1 INTRODUCTION

In Chapter 2 it was decided to solve field equations numerically. This, essentially, requires some form of lumping, i.e., the use of discrete circuit elements. This can be done effectively by dividing the electromagnetic device into a number of simple elements. The field conditions can then be approximated closely by using the circuit approach applied to the magnetic field for defining these elements and the boundary conditions[45]. The network model thus obtained can be solved directly by a computer. Further, this approach also provides a means of visualising and gaining insight into the underlying interaction, especially in the analysis of special purpose electromagnetic devices where the approach lends facilities by virtue of which the effect of novel modifications in the device can be studied theoretically with ease.

The choice of field parameter for calculation purposes depends upon the problem in hand. The use of the magnetic vector potential (MVP) for two-dimensional problems is found useful because it requires only two components of $\overline{B}$ and one of $\overline{J}$. However, when the problem is three-dimensional, the MVP formulation[43] requires solving for all the three components of $\overline{A}$ at each node together with the possibility of an electric scalar potential V for nodes lying at the irregular boundaries of the conducting sheet. By using the magnetic scalar potential (MSP) as the field quantity, however, solving is required for only one component at each node. The current flow in a flat conducting sheet is assumed as two-dimensional and the magnetic

potential difference at any point on the conducting sheet is defined as the current flow integrated up to that point.[44,45]

The MSP formulation also offers computational advantages over the MVP, particularly when solved iteratively. This is primarily due to a fundamental difference between the boundary conditions that have to be met, in each case, on the iron surfaces: Dirichlet boundaries, in the MSP formulation, absorb the residual, whereas, Neumann's boundary in MVP formulation reflects back into the iteration matrix thereby slowing the convergence rate of the iteration process.

In the following sections the network model approach for analysing an electromagnetic device numerically has been developed, as an example, for the basic transverse flux circular motor by using the magnetic scalar potential as the field parameter. The example under consideration has all the possible discontinuities, except those at entry and exit, present in the transverse flux linear induction machine. This, however, can be taken into consideration at a later stage, and thus the approach may be also extended for analysing longitudinal and transverse flux types of linear and rotary electrical machines.

3.2. DESCRIPTION OF THE MODEL

Figure 3.1 gives the schematic diagram of the transverse flux circular motor, drawn for the purpose of formulating a theoretical model suitable for numerical analysis. It shows the location of U-cores, the coils in the primary member, and the secondary aluminium plate with its backing iron. The

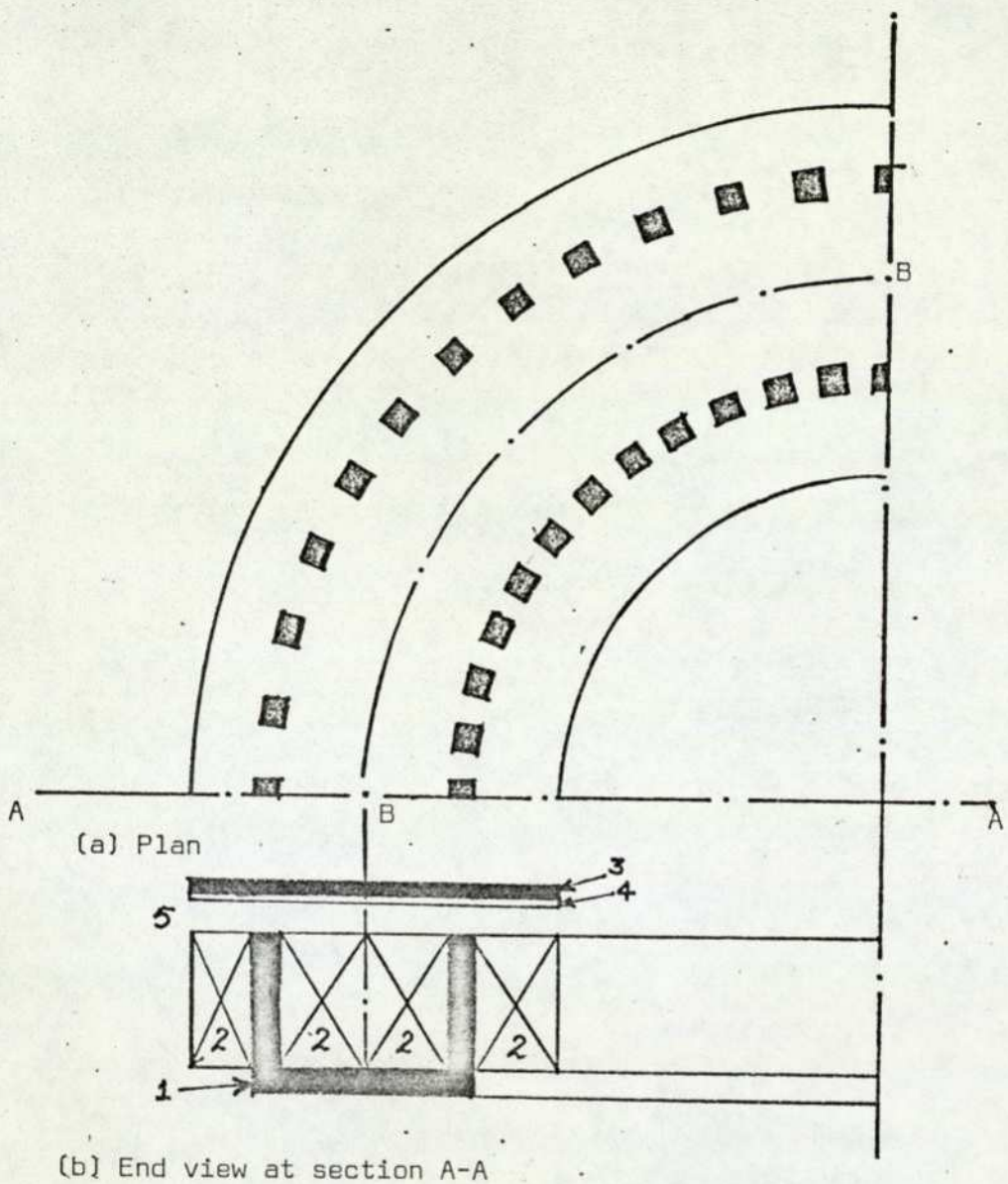

Fig.3.1 Schematic diagram of transverse flux circular motor

primary member has a double-layer, 2 slots per pole per phase, 3-phase winding having a coil span of 1 to 5 slots. This gives rise to two layers of coils in between U-cores and four layers on the overhangs. For the purpose of convenience a cross-section at A-A has been divided into five suitable regions as shown in Fig.3.1(b).

Region 1 constitutes radially laminated U-cores which are laid in the primary member, along a circle as shown in Fig.4.3 (Chapter 4). In linear machines the overhang winding plays an important role and the method of its inclusion in the primary forcing function has been discussed in Appendix D. In Fig.3.1(b) the stator overhang winding has been shown by region 2.

In the secondary member the iron core behind the secondary conducting plate also has its laminations laid radially along the circle. This forms region 3. Region 4 is the secondary conducting plate which is responsible for the forces produced due to the induction phenomena, and region 5 defines the space surrounding regions 1 to 4.

In Fig.3.1(a) the vertical plane through B-B is a plane of symmetry for the case when the secondary member is placed symmetrically above the primary U-cores. For this case, therefore, one can consider only half of the machine (widthwise) and one pole pitch circumferentially. Fig.3.2 shows two planes of the numerical model to define the location of regions 1 to 5 and the nodes lying at the corners of the model defined for the analysis.

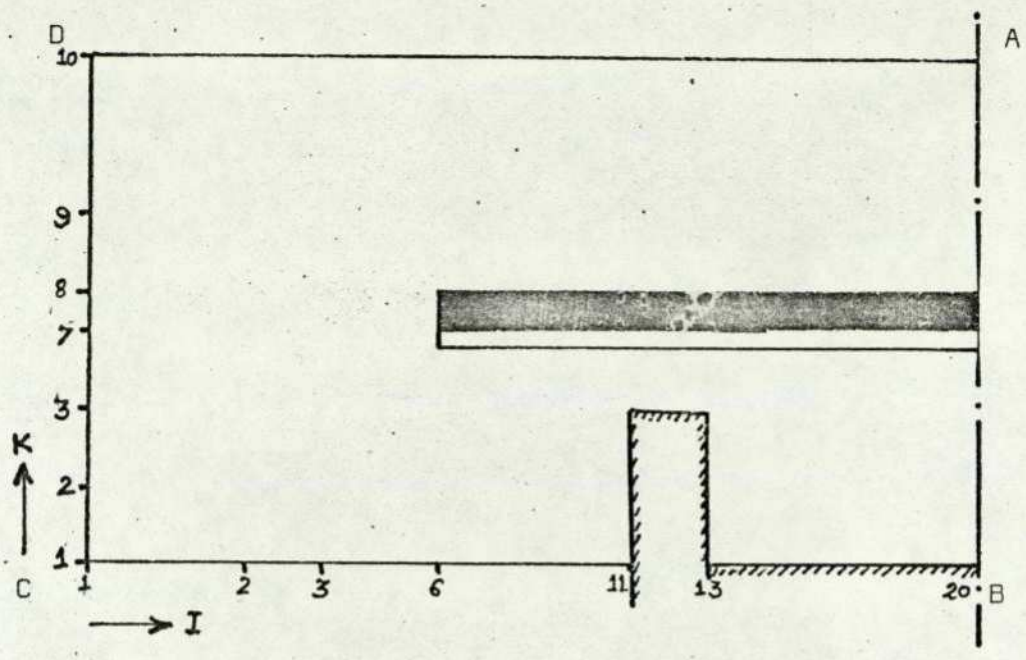

(a) I-K plane at J=1

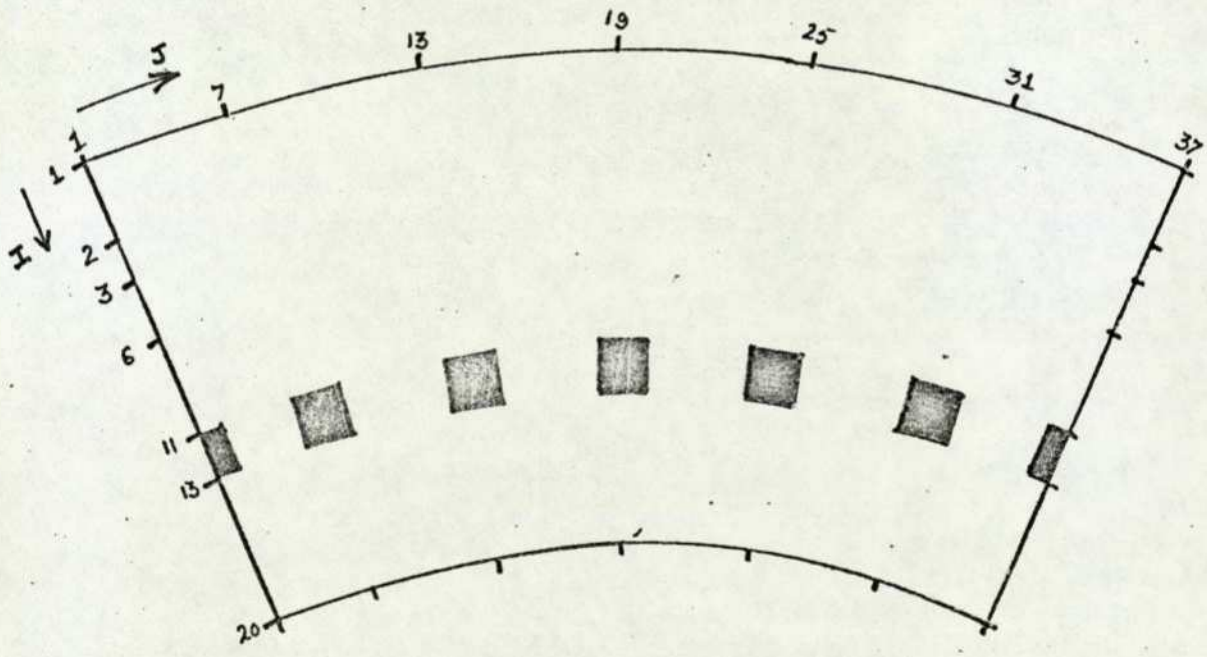

(b) I-J plane at K=3

Fig.3.2 Sections of the numerical model

3.3 ASSUMPTIONS MADE

In the present approach certain realistic assumptions have been made. The saturation of the ferromagnetic material has been neglected. This is justified because the 'entrefer' in the linear induction machines is large. The laminations in the primary and the secondary members are laid in the X -Z plane and,therefore, the iron can be assumed to have negligible conductivity in the Y-direction. This means that, as compared to air, the iron behind the secondary conducting plate has a very high permeability and, therefore, negligible reluctance and magnetic potential drop. Also, the laminated backing iron lies in between two limbs of the stator U-core which are a source of equal and opposite forcing functions and, therefore, it is justified to set the potential on the backing iron at zero. However, when saturation exists, the potential throughout the backing iron can no longer be assumed to be zero. Instead, the potential in region 3 will have to be evaluated in a manner similar to that used for region 4. The effect of saturation will be small and, therefore, can be neglected as a first approximation.

The physical constants of the materials have been assumed to be constant, i.e,the materials are assumed homogeneous, isotropic and linear (although the approach has provision for dealing with materials having physical properties otherwise). The secondary conducting plate is assumed to be thin enough for the eddy currents to lie in the plane of the plate. The

movement of the secondary member has been assumed to be in the y-direction only (although the movement in any other direction or directions can be considered at later stages).

The time variation has been considered as sinusoidal. This is usually the case, so long as we are not working near the saturation zone of the B/H characteristics.

3.4 REPRESENTATION OF THIN CONDUCTING SHEET BY MAGNETIC SCALAR POTENTIAL MODEL

In Appendix D it has been shown that an electromagnet coil can be replaced by its equivalent flux sheet (for solving Poisson's equations in the current carrying region) when currents in the coil are known. In conducting sheets, however, the eddy currents are not known, and the problem, therefore, involves not only the solution of the magnetic network but also the simultaneous solution of the electric network[50].

In linear induction machines where a flat conducting sheet is used, the current flow is essentially two-dimensional and therefore one component of the current density vector $\overline{J}$ may be assumed to be zero. This is reasonable because the current flow is confined by insulation, viz. the space surrounding the conducting sheet region. The magnetic field, however, pervades the device in all directions and hence it requires a three-dimensional description.

Under these circumstances, for an isolated conducting sheet lying in an alternating magnetic field, the magnetic potential U_0 and U_0' (Fig.3.3) may be expressed[47] in terms of the magnetic

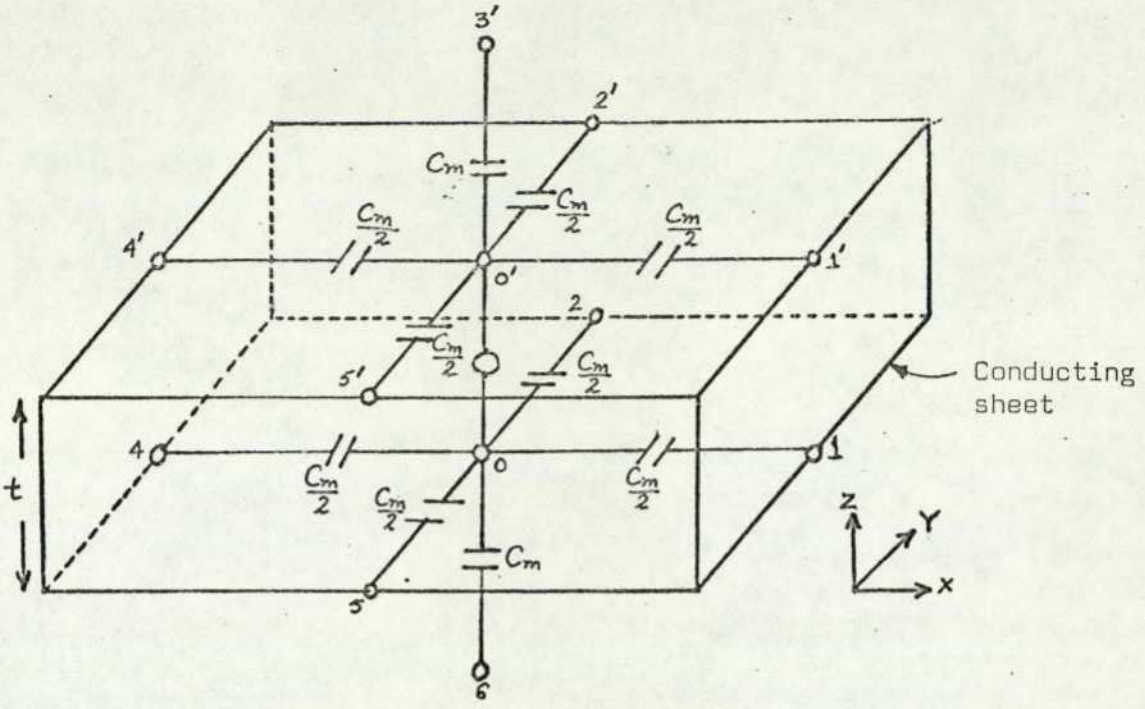

(a) Magnetic network

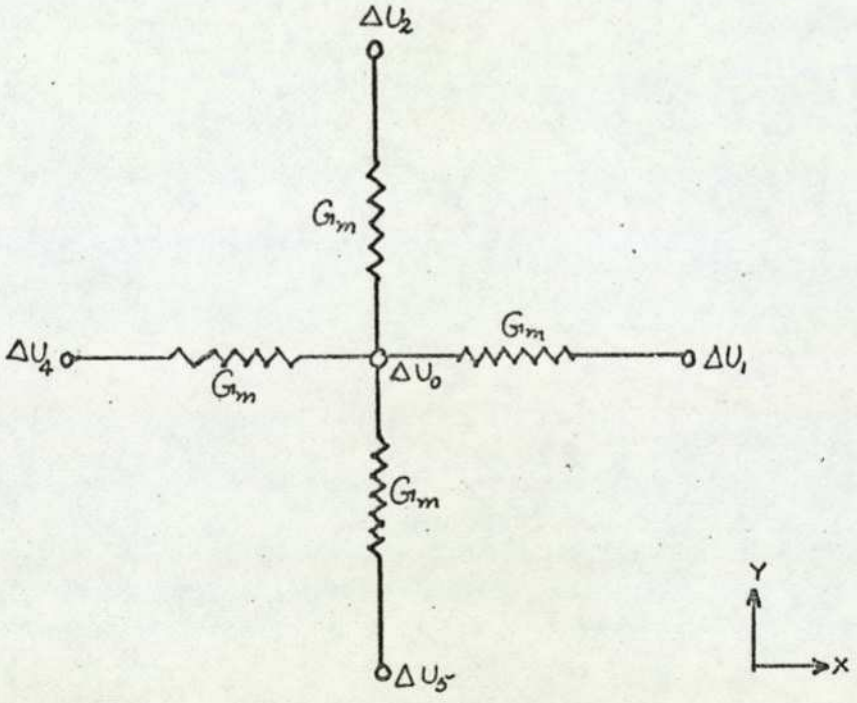

(b) Electric network

Fig.3.3 Split node model

potential of the surrounding nodes and the properties of the surrounding materials as follows:-

$$U_0 = \frac{(\frac{5}{3} + jK)(U_1 + U_2 + U_4 + U_5) + (\frac{4}{3} + j2K)U_6 - \frac{1}{3}(U'_1 + U'_2 + U'_4 + U'_5) + \frac{4}{3}U'_3}{(8 + j6K)} \quad 3.1$$

and

$$U'_0 = \frac{(\frac{5}{3} + jK)(U'_1 + U'_2 + U'_4 + U'_5) + (\frac{4}{3} + j2K)U'_3 - \frac{1}{3}(U_1 + U_2 + U_4 + U_5) + \frac{4}{3}U_6}{(8 + j6K)} \quad 3.2$$

where $K = \frac{\omega}{2} \cdot \frac{C_m}{G_m}$ 3.3

and, for a uniform node spacing 'h',

$$C_m = \mu\mu_0 h \quad 3.4$$

$$G_m = \frac{1}{\sigma t} \quad 3.5$$

also, $\omega = 2\pi f$ (f = frequency of operation)

μ_0 = permeability of free space,

μ = relative permeability of the medium

t = thickness of the conducting sheet

σ = conductivity of the conducting sheet,

$$K = \frac{ht}{d^2} \quad 3.6$$

where $d = \sqrt{\frac{2}{\omega\sigma\mu\mu_0}}$ 3.7

= depth of penetration for the conducting plate material at frequency (f).

However, when the conducting sheet is backed by an unsaturated iron surface the nodes on the iron surface have the same potential, which is zero in the present model (Sec.3.3). In Fig.3.3(a), consider the unsaturated iron surface to be in contact with nodes 0',1',2',3',4' and 5', so that,

$$U'_1 = U'_2 = U'_3 = U'_4 = U'_5 = U'_0 = 0 \quad 3.8$$

Therefore, the potential U at a node on the conduction sheet may be similarly expressed as

$$U_0 = \frac{(1+jK)(U_1+U_2+U_4+U_5)+(j2K)U_6}{(4+j6K)} \qquad 3.9$$

where K is given by eqn. 3.6

Eqn.3.9 is for a uniform internode spacing and requires simple modifications for dealing with non-uniform internode spacing.

3.5 REPRESENTATION OF SPEED EFFECT IN CONDUCTING PLATE (BACKED BY UNSATURATED IRON)

The assumptions made in this analysis are similar to those stated in Sec.3.3. In addition, it is also assumed that the conducting plate, together with its backing iron, is moving at a constant velocity v_y along the y-direction only.

From these assumptions it follows that in the plate,

$$\bar{B} = \bar{a}_z B_z \qquad 3.10$$

$$\bar{J} = \bar{a}_x J_x + \bar{a}_y J_y \qquad 3.11$$

$$\bar{v} = \bar{a}_y v_y \qquad 3.12$$

the current density vector in a moving conducting plate is given by

$$\bar{J} = \sigma (\bar{E} + \bar{v} \times \bar{B}) \qquad 3.13$$

Taking curl both sides and assuming σ to be constant,

$$\nabla \times \bar{J} = \sigma (\nabla \times \bar{E} + \nabla \times \bar{v} \times \bar{B}) \qquad 3.14$$

An electric vector potential $\bar{T}$ (analogous to magnetic vector potential $\bar{A}$) may be defined in the conductor interior such that

$$\text{curl } \bar{T} = \bar{J} \qquad 3.15(a)$$

where $\bar{T}$ has only a z-component. (This is so because the current density distribution in the conducting sheet is in the x-y plane as assumed in eqn.3.11.) Thus,

$$\bar{T} = \bar{a}_z T_z \qquad 3.15(b)$$

The electric vector potential can be interpreted as a potential discontinuity due to the presence of the conducting sheet, such that,

if ΔU is the magnetic scalar potential difference across the thickness (t) of the conducting sheet,

$$T_z . t = \Delta U \qquad 3.15(c)$$

From eqns. 3.14 and 3.15 (a and b),

$$\nabla \times \bar{J} = \nabla \times \nabla \times (\bar{a}_z T_z) = \nabla^2 (\bar{a}_z T_z) \qquad 3.15(d)$$

Also, from Maxwell's equation for sinusoidal variation of flux density with respect to time

$$\nabla \times \bar{E} = j\omega \bar{B} \qquad 3.16$$

Solving $\nabla x\bar{v}x\bar{B}$ with the help of eqns.3.10 to 3.12 yields,

$$\nabla x\bar{v}x\bar{B} = -\bar{a}_z v_y \frac{\partial B_y}{\partial y} \qquad 3.17$$

where v_y is the velocity at which the conducting plate is moving, and in terms of synchronous velocity (v_s)

$$v_y = (1-s)v_s = (1-s)\frac{\tau_p}{\pi}\omega \qquad 3.18$$

where $s = \text{slip} = \dfrac{v_s - v_y}{v_s}$

Assuming that the variation of B_z with respect to y follows a square law,

$$\frac{\partial B_z}{\partial y} \simeq \frac{B_{z2} - B_{z5}}{2h} \qquad 3.19$$

at the node 0. At a later stage to improve the accuracy, eqn.3.19 may be re-defined using cubic or higher order law. From eqns. 3.14,3.15 and 3.19, after simplification, we have

$$\nabla^2(T_z) = \sigma t\{j\omega B_{z0} + (1-s)\frac{\tau_p}{2h\pi}(\omega B_{z2} - \omega B_{z5})\} \qquad 3.20$$

Flux normal to the conducting plate at a node, in terms of the surrounding magnetic scalar potentials is given by eqn.3.21 with respect to Fig.3.4

$$j\omega\Phi_0 = j\frac{1}{2}\omega C_m(U_1+U_2+U_4+U_5+2U_6-6U_0) \qquad 3.21$$

Also from eqn.3.10

$$B_0 = \frac{\Phi_0}{h^2} \qquad 3.22$$

where h is the internode spacing in x-y plane and, h^2 is the shaded area shown in Fig.3.4.

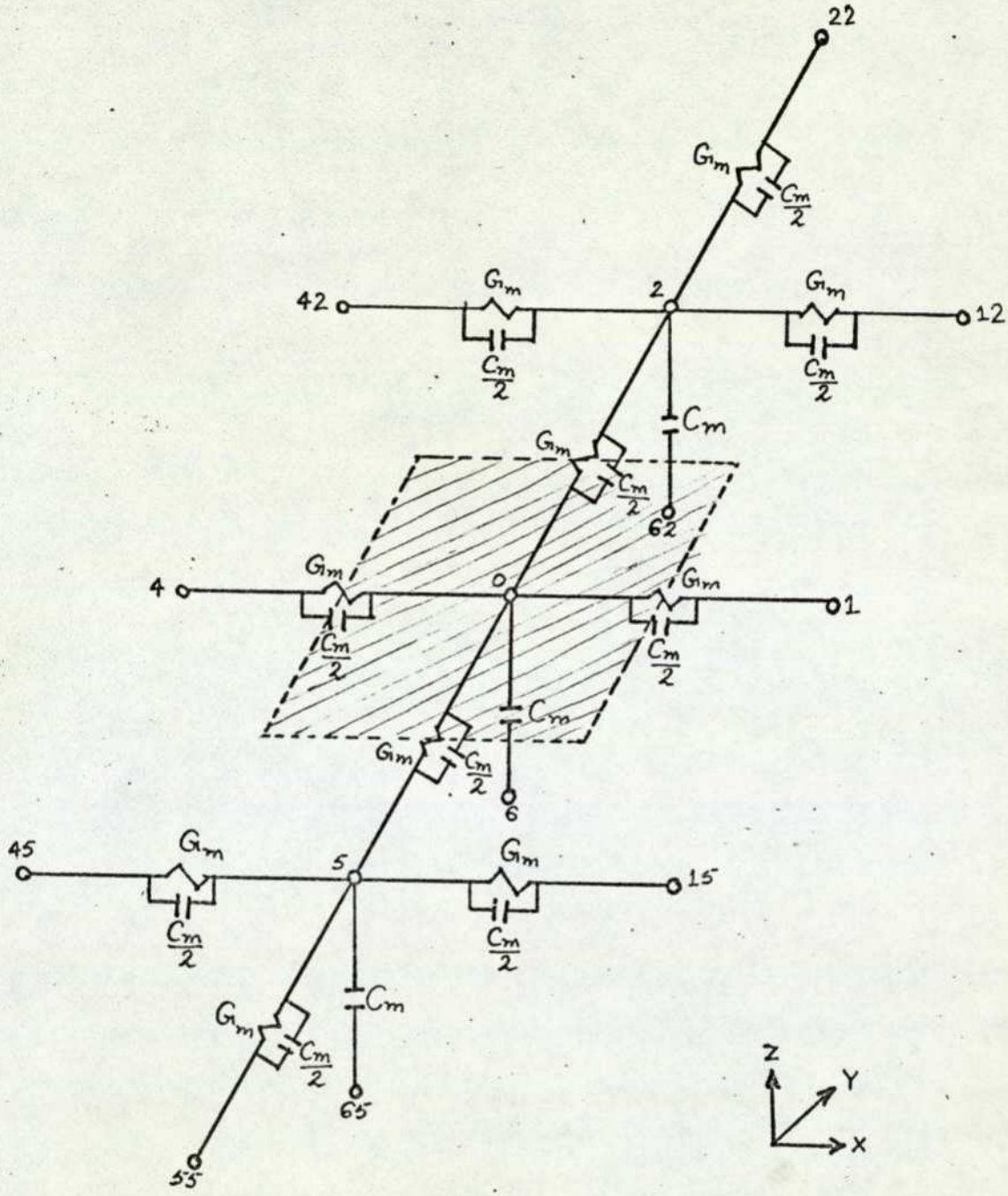

Fig.3.4 Network model for node '0' surrounded by other nodes lying on a conducting plate backed by unsaturated iron and moving at slip 's' in the direction of the moving field

It follows that for a two dimensional current density distribution in the conducting sheet,

$$\nabla^2(T_Z) = \frac{U_1 + U_2 + U_4 + U_5 - 4U_o}{h^2} \qquad 3.23$$

Thus, from eqns. 3.20 to 3.23 after solving for U_o we have,

$$\begin{aligned}(4 + j6K)U_o = {} & (1+jK)(U_1 + U_2 + U_4 + U_5) + (j2K)U_6 \\ & + (1-S)K_v \left\{(U_{15} - U_{12}) + (U_{45} - U_{42}) + (U_{55} - U_{22})\right. \\ & \left. +2(U_{65} - U_{62}) - 6\,(U_5 - U_2)\right\}\end{aligned} \qquad 3.24$$

where K is defined by eqn. 3.6

and $K_v = (1-S)\,\frac{(\text{number of nodes per pole pitch})_K}{2\pi}$

Therefore, using eqn. 3.24 the magnetic scalar potential of a node in a moving plate can be deduced from those of the surrounding nodes. It is interesting to note that in eqn. 3.24, whereas K accounts for the flux-linkage due to the flux-pulsation, K_v accounts for that due to the motion of the conducting sheet in the electromagnetic field and for s=1, case corresponding to standstill conditions, eqn. 3.24 takes the form of eqn. 3.9.

3.6 GOVERNING EQUATIONS FOR THE MODEL

In Sec.3.2 the model was divided into suitable inter-dependent regions. The division has been done such that only one finite difference equation is required for nodes lying in the same region. In the model, the Dirichlet's boundary conditions are satisfied on the plane through AB (Fig.3.2(a)) and, at the iron surfaces of the primary and the secondary members, because of the existing symmetry and the assumption made in Sec.3.3 respectively. Also, the Neumann boundary conditions are assumed on planes passing through line CD and DA in Fig.3.2(a). This has been made possible, by considering these boundaries so far away from the potential source that the variation in U with respect to the X- and Z- axes, respectively, can be neglected.

The magnetic scalar potential of nodes situated in the stator U-cores (i.e. Region 1) has been defined by a current sheet in Appendix D, and for nodes in Region 3, from Sec.3.3, the magnetic scalar potential has been set at zero. The potential of nodes in Regions 1 and 3 do not alter during the iteration since they lie on the Dirichlet's boundary. The problem, therefore, is reduced to the solving of finite difference equations, at nodes lying in Regions 2,4 and 5, to obtain the magnetic scalar potential distribution in and around the electromagnetic device.

Region 5 is a Laplacian space as it does not contain any current source and, therefore, the potential at a general node is given by eqn.B.11. In terms of magnetic scalar potential we have:

$$\sum_{n=1}^{6} \frac{U_n - U_o}{\mathcal{R}_n} = 0 \qquad 3.26$$

where U is the magnetic scalar potential,

o is the node under consideration,

n = 1 to 6 are the surrounding nodes.

$\mathcal{R}_n$ is the internode reluctance between the node o and the surrounding node n.

At Neumann boundaries CD and DA in Fig.3.2(a)

$U_4 = U_1$, and,

$U_3 = U6$

respectively. 3.27

In Region 2, the nodes are surrounded by current sources. In Appendix D these current sources have been replaced by equivalent flux sources Φ_0 at each node. The finite difference equation for this region, therefore, becomes

$$\sum_{n=1}^{6} \frac{U_n - U_o}{\mathcal{R}_n} + \Phi_0 = 0 \qquad 3.28$$

The finite difference equation for Region 4 is the most difficult to obtain because the currents in the secondary conducting plate are not known. In Sec.3.4 the network-approach formulations of the finite difference equation, for nodes lying in Region 4, has been discussed. It has been shown that a conducting sheet whose thickness is small compared to the depth of penetration, and which is backed by unsaturated iron, can be replaced by an infinitely thin plating on the

surface of the backing iron. The effective conductivity of this 'plating' and the internode conductance, however, is made equivalent to that of the original conducting sheet. This argument in effect justifies the assumption that the normal component of the current density vector in the conducting plate is zero. The finite difference equation for nodes lying in Region 4 can, therefore, be given by eqn.3.9 as

$$U_o = \frac{(1 + jK)(U_1 + U_2 + U_4 + U_5) + (j2K)U6}{(4 + j6K)} \qquad 3.29$$

where K is defined by eqn.3.6

Eqn.3.29 is for the case when the conducting plate is stationary and it requires a major modification to account for the induction in the plate due to motion. In Sec.3.5 a finite difference equation has been obtained to account for the speed effect as well. This is given by eqn.3.24 from which we have

$$U_o = \frac{(1 + jK)(U_1 + U_2 + U_4 + U_5) + (j2K)U_6}{(4 + j6K)} + \frac{(1-s)Kv}{(4 + j6K)} \{(U_{15} - U_{12}) + (U_{45} - U_{42}) + (U_{55} - U_{22}) + 2(U_{65} - U_{62}) - 6(U_5 - U_2)\} \qquad 3.30$$

where K is defined by eqn.3.6 and K_v by eqn.3.25

Thus, using eqns.3.25,3.28,3.29 and 3.30, the magnetic scalar potential distribution can be obtained for model shown in Fig.3.2 and the flow diagram of the computer programme developed for this purpose is shown in Fig.3.5. The calculation of flux

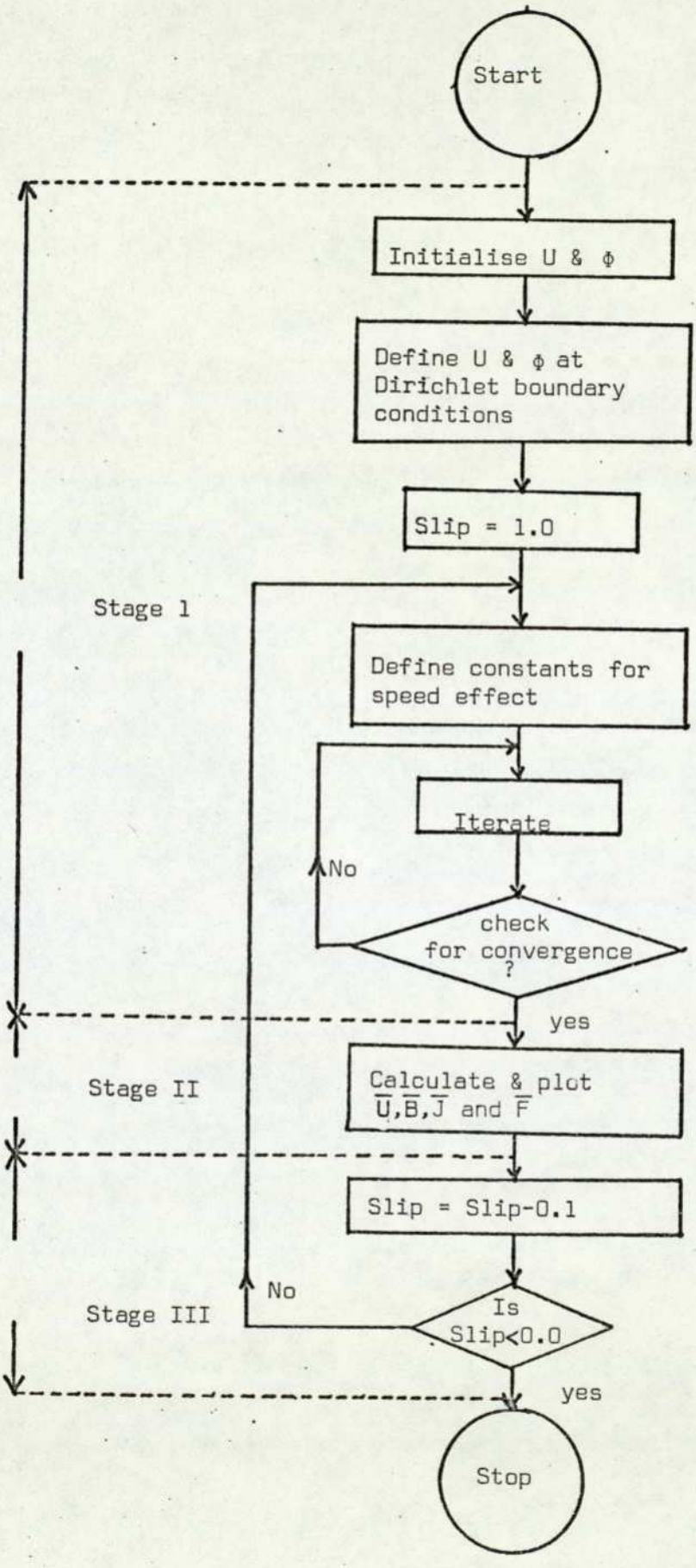

Fig.3.5 Computer Programme Flow Diagram (for details please see Sec.3.6 and 3.7)

densities and forces from the results of this programme are explained in the following section.

3.7 FLUX DENSITY AND FORCES

The magnetic scalar potential distribution obtained in Sec.3.6 only replaced the electromagnetic device by a field quantity U from which the characteristics of the device, as viewed from the electrical and mechanical 'terminals', can be obtained. As regards the verification of the potential distribution, the best way is to correlate the flux densities as obtained from measurements with those calculated from the potential distribution. This correlation has been done in Chapter 5. In this section the calculation of flux densities and forces has been discussed.

3.7.1 Flux-density

Its calculation follows directly from the definition of magnetic field intensity ($\overline{H}$) in terms of MSP U, i.e,

$$\overline{H} = - \text{grad } U \qquad 3.31$$

and therefore,

$$\overline{B} = \mu\mu_0 \overline{H} = -\mu\mu_0 \text{grad } U \qquad 3.32$$

where $\overline{B} = \overline{a}_x B_x + \overline{a}_y B_y + \overline{a}_z B_z$ 3.33

and $\mu\mu_0$ = permeability of the medium.

The gradient of U in eqns. 3.31 and 3.32 may be expressed as,

$$\text{grad } U = \overline{a}_x \frac{\partial U}{\partial x} + \overline{a}_y \frac{\partial U}{\partial y} + \overline{a}_z \frac{\partial U}{\partial z} \qquad 3.34$$

where it requires differentiation of U with respect to the three axes. Each differentiation may be performed numerically (on the assumption that the distribution of U is at the most linear, quadratic or even higher) by using two-, three- or more number - point formulation.[48] The use of greater number of

points along each axis reduces the trunctation error, although this reduction is at the cost of corresponding increase in the computation and the complexity in formulation. Thus as a first approximation eqn. 3.33 may be re-written, for node (l ,m,n)Fig.3.6, by using three-point formula as,

$$\bar{B} = \frac{\mu\mu_o}{2h}\{\bar{a}_x(U_{l-1}-U_{l+1}) + \bar{a}_y(U_{m-1}-U_{m+1}) + \bar{a}_z(U_{n-1}-U_{n+1})\} \quad 3.35$$

where -1 and +1 indicate a node before and after node (l,m,n) respectively along that axis.

3.7.2 Forces

In principle the mechanical forces can be calculated in a number of ways, but when the field equations are solved numerically it is often convenient to calculate forces by surface integration of Maxwell's second stress tensor [49] in air over any surface enclosing the part in which the force is produced. The choice of surface is quite arbitrary (so long as it encloses the part or parts on which the force is produced) because there can be no power loss in the air regions surrounding the secondary member[51]. For this reason, therefore, a surface can be chosen avoiding the discontinuities and the iron surfaces. It is essential to note, however, that the force density (or stress) distribution is associated with the particular surface, and the only way to examine the stress on the body is to choose a surface which lies just outside the body and follows its shape. This is generally inconvenient and, therefore, so long as only the total force is desired a surface which makes the calculation simple is chosen[44].

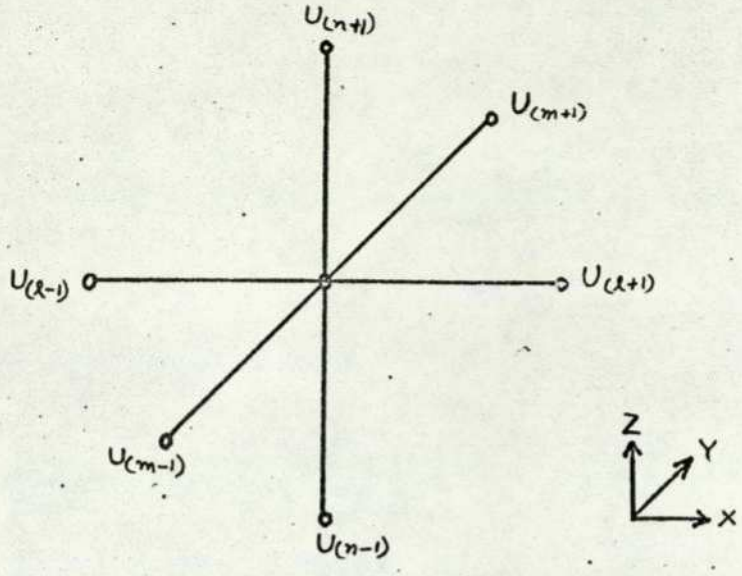

Fig.3.6 Node molecule for calculating $\overline{B}$

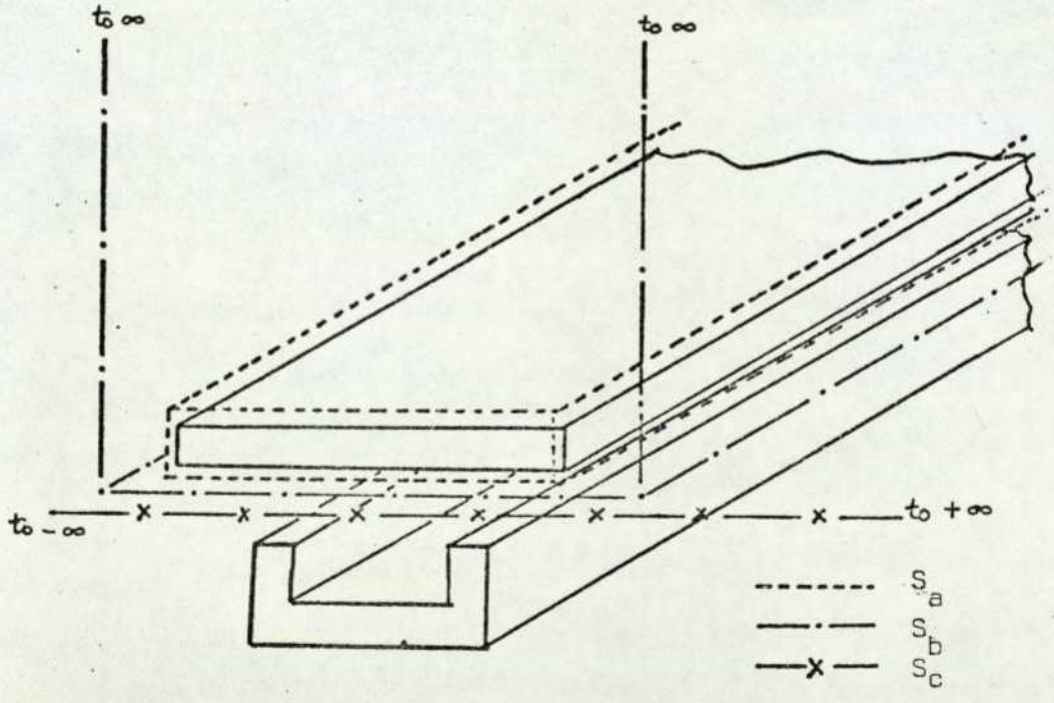

Fig.3.7 Choice of surface for evaluating the Maxwell's stress tensor(T^m)

Mathematically speaking the underlying philosophy may be expressed as,

$$\bar{F} = \iint (T^m \cdot \bar{n})\, da \qquad 3.36$$

where $\bar{n}$ is a unit vector normal to the surface on which the force $\bar{F}$ is being calculated,

and T^m is the Maxwell's second stress tensor, which has been defined in Appendix E by eqn.E.10, in terms of the components of the magnetic flux density vector in the air.

In the case of a linear electric machine, the estimation of force by this method has an additional advantage, particularly when it is used in conjunction with a numerical approach. Fig.3.7 shows the surfaces which will yield the same total force when the stress tensor is integrated over any one of them. With surface Sc the flux density diminishes along the x-axis beyond the 'rotor', and effectively remains zero (up to plus and minus infinity) on either side of it. The force vector components $\bar{F}x$ and $\bar{F}y$ (which would be required for surfaces Sa and S_b) can, therefore, be neglected. This simplifies the computation because only the z-component of the magnetic stress tensor is required for determining the force produced. The equation to be solved, therefore, reduces to

$$\bar{F}_z = \int_{-\infty}^{\infty}\int_{-\infty}^{\infty} T^m_z \, dxdy \qquad 3.37$$

where $\bar{T}_z = \bar{a}_x f_{xz} + \bar{a}_y f_{yz} + \bar{a}_z f_{zz}$ 3.38

and, f_{xz}, f_{yz} and f_{zz} are the components of the stress vector in the x,y and z directions respectively.

From eqns.3.37 and 3.38, total forces acting along the three axes may be expressed as

$$F_x = \int_{-\infty}^{\infty}\int_{-\infty}^{\infty} f_{xz}\,dydx \qquad 3.39$$

$$F_y = \int_{-\infty}^{\infty}\int_{-\infty}^{\infty} f_{yz}\,dydx \qquad 3.40$$

$$F_z = \int_{-\infty}^{\infty}\int_{-\infty}^{\infty} f_{zz}\,dydx \qquad 3.41$$

Substituting from Appendix E, eqn.E.10, for f_{xz}, f_{yz} and f_{zz}, eqns.3.39 to 3.41 may be re-written as

$$F_x = \frac{1}{\mu}\int_{-\infty}^{\infty}\int_{-\infty}^{\infty} B_x B_z\,dydx \qquad 3.42$$

$$F_y = \frac{1}{\mu}\int_{-\infty}^{\infty}\int_{-\infty}^{\infty} B_y B_z\,dydx \qquad 3.43$$

$$F_z = \frac{1}{\mu}\int_{-\infty}^{\infty}\int_{-\infty}^{\infty} \left(B_z^2 - \frac{1}{2}|B|^2\right)dydx \qquad 3.44$$

where $$|B|^2 = B_x^2 + B_y^2 + B_z^2 \qquad 3.45$$

Eqns.3.42 to 3.45 give instantaneous forces which, for a field varying sinusoidally with respect to time, may be modified to yield time average forces as given by the following expressions

$$F_{x(av)} = \frac{\mu}{2}\int_{-\infty}^{\infty}\int_{-\infty}^{\infty} \mathrm{Re}(H_z H_x^*)\,dydx \qquad 3.46$$

$$F_{y(av)} = \frac{\mu}{2}\int_{-\infty}^{\infty}\int_{-\infty}^{\infty} \mathrm{Re}(H_z H_y^*)\,dydx \qquad 3.47$$

$$F_{z(av)} = \frac{\mu}{2}\int_{-\infty}^{\infty}\int_{-\infty}^{\infty} \left(H_z^2 - \frac{1}{2}|H|^2\right)dydx \qquad 3.48$$

where 'Re' denotes the real part of the expressions and H,Hx,Hy and Hz are the peak values. Also the asterisk(*) indicates a complex conjugate.

Thus, using eqns.3.36 and 3.46 to 3.48 the three components of the total force produced on the secondary member can be computed from the magnetic scalar potential distribution obtained in Sec.3.6. It is evident from eqns.3.46 and 3.47 that, apart from the z- component of the flux density, there must be an x - component (i.e.Bx) for the lateral guidance force (Fx), and a y - component (i.e.,By) for the tractive

force (Fy). Also, from eq.3.48 for the normal force (Fz) to be repulsive $(Bz)^2$ should be less than $\frac{1}{2}|B|^2$.

CHAPTER 4

4.1 INTRODUCTION

The purpose of conducting tests on special purpose electric machines is primarily to understand and to verify the mathematical models proposed for their analyses. The tests include steady state and transient load characteristics, the measurement of flux densities at various parts of the machine, the electrical terminal quantities and the mechanical forces produced. These tests when conducted on a linear electric machine give rise to problems which are, normally, not present in the corresponding rotary machine. For example, to facilitate measurements in the case of a linear motor one requires a continuous motion which can be made possible only by constructing a long or a closed-loop continuous track. The cost involved in constructing either type, especially the former, for the testing of a reasonable size of linear electric motor, is high. The major research centres, involved in linear electric machine research have (depending upon the finances available to them) one or more of the following testing facilities with the necessary instrumentation:

(a) Static test rig

(b) Moving-belt test rig

(c) Circular motor test rig

(d) Disc test rig

(e) Drum test rig

(f) Circular/linear test track

Of these, the circular motor test rig (referred to as the BTFCM earlier) is new. It was constructed for the purpose of conducting tests on transverse flux machines under dynamic conditions. In the present chapter the BTFCM test rig and the facilities it provides for measuing the flux densities and the forces produced, are discussed.

4.2 BASIC TRANSVERSE FLUX CIRCULAR MOTOR

A basic transverse flux circular motor is, in principle, similar to the well known transverse flux linear induction motor[18,20,22,24], the main difference being that in the former the U-shaped stamping-stacks have been laid along a circle as shown in Fig.4.1. The purpose of the shape, design and construction of the basic transverse flux circular motor is to obtain dynamic test results (such as the effect of speed on the forces and the flux densities in the various parts of the machine) in the laboratory while taking into account the limitations of workshop, laboratory space and overall cost.

The fully assembled test rig is shown in Fig.4.2. It has been made small (outer diameter of the disc 'D' about 600 mm) to facilitate the carrying out of modifications in the test rig for a particular study. For example a comparative study of induction, synchronous and relultance types of linear motor can be made with the same stator by using suitable secondary members. The moving member rotates about a vertical axis and produces normal levitation forces similar to those in HSGT applications. These forces are measured in the test rig

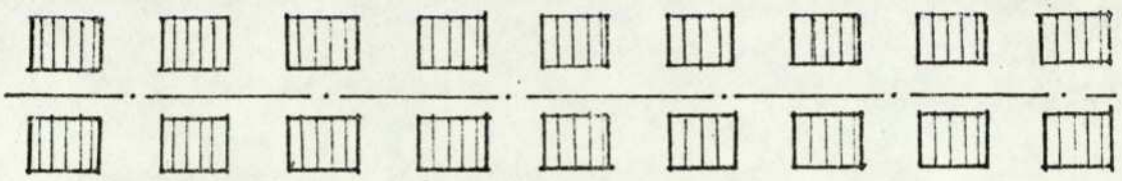

Transverse flux linear motor

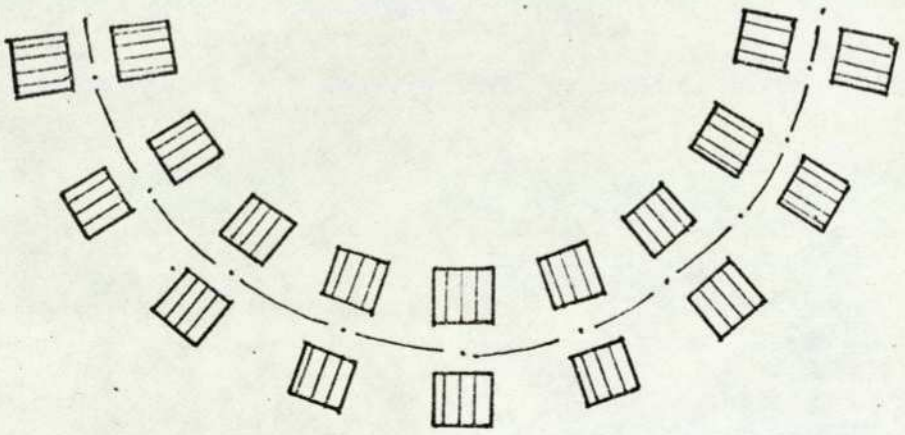

Transverse flux arched motor

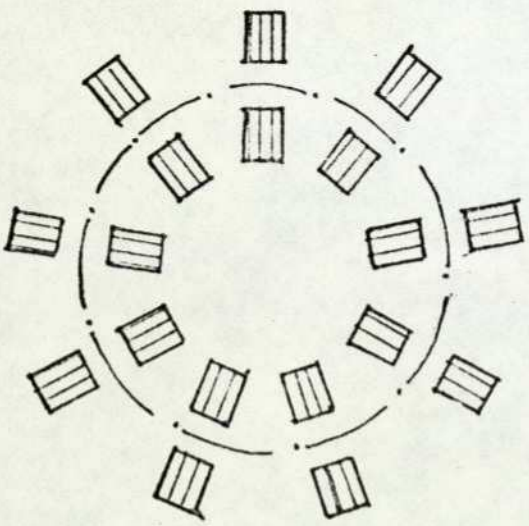

Transverse flux circular motor

Fig.4.1 Evolution of transverse flux circular motor

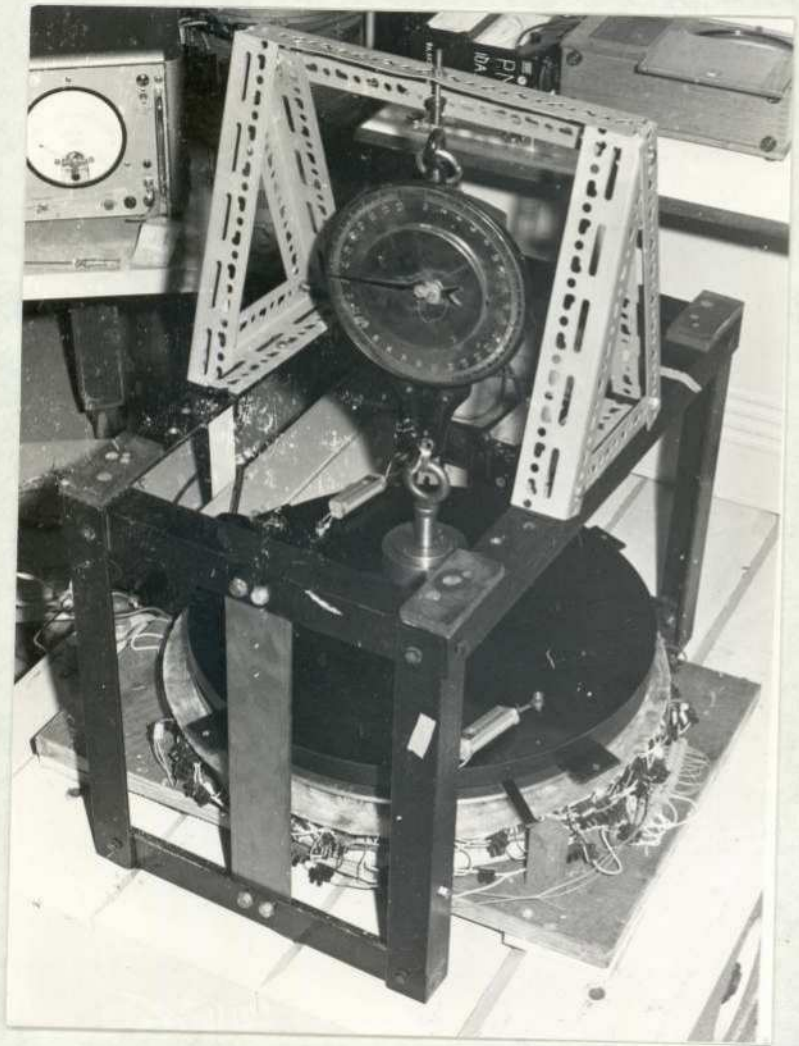

(a) Initial rig arrangement

(b) Final rig arrangement

Fig.4.2 The Test Rig

by a suitably arranged disc carrying strain gauges below the primary member.

In a practical application of a linear electric motor, entry- and exit-end effects exist due to one of the members being short. In the BTFCM, because of a continuous winding in the primary member and a continuous annular conducting ring used as the secondary member, the aforesaid effects become zero. These effects can, however, be re-introduced by removing a part of the primary or secondary member. This feature, incidentally gives far more insight into the entry and exit effect phenomena than would be possible with any other of the test rigs listed in Sec.4.1.

In the BTFCM (as in all the test rigs except (f) in Sec.4.1) the secondary plate temperature changes with time during a 'run' and hence so does the secondary resistance. The experimental arrangement therefore differs considerably from the actual case where the primary member will be continuously faced by a new cool secondary member throughout its 'run'. However, this test rig does eliminate the need for a very long continuous track during the initial stages of research involving dynamic tests on such linear electric motors. It also narrows the area of research for a particular application (especially in HSGT).

In the remaining section some of the parts of the BTFCM test rig are discussed in detail.

4.2.1. The Stationary Member and its Attachments

This consists of a primary member, a lift force measuring attachment and an arrangement for altering the 'entrefer'.

The primary member is also called the stator for it remains stationary in the present arrangement. As stated earlier, it has a circular geometry and the U-cores are laid along a circle. Fig.4.3 shows an individual U-core and also the complete set laid in a wooden frame, before the insertion of the coils into the slots. Incidentally, Fig.4.3(b) illustrates the form of the magnetic circuit of the primary member.

The inner and the outer limbs of the U-core in the stator each have an eight-pole, 3-phase star-connected double layer winding. It has two slots per pole per phase, 60^{o} phase spread, and a coil-pitch of 1-5. The choice of coil shape, coil pitch and slots per pole per phase was made on the basis of past experience and the available U-core stacks [52]. Fig.4.4 gives the main dimensions of the stator and Fig.4.5 shows the completely assembled stator.

The speed at which the secondary member moves has a direct effect on the lift force produced and if the secondary member is allowed to move under the influence of the lift force this leads to a corresponding change in the 'entrefer'. The new 'entrefer' creates new conditions in the machine, thereby resulting in a new tractive force, a new speed and hence a new lift force which gives rise to yet another new 'entrefer'. The whole operation has been summarised in Fig.4.6. This,

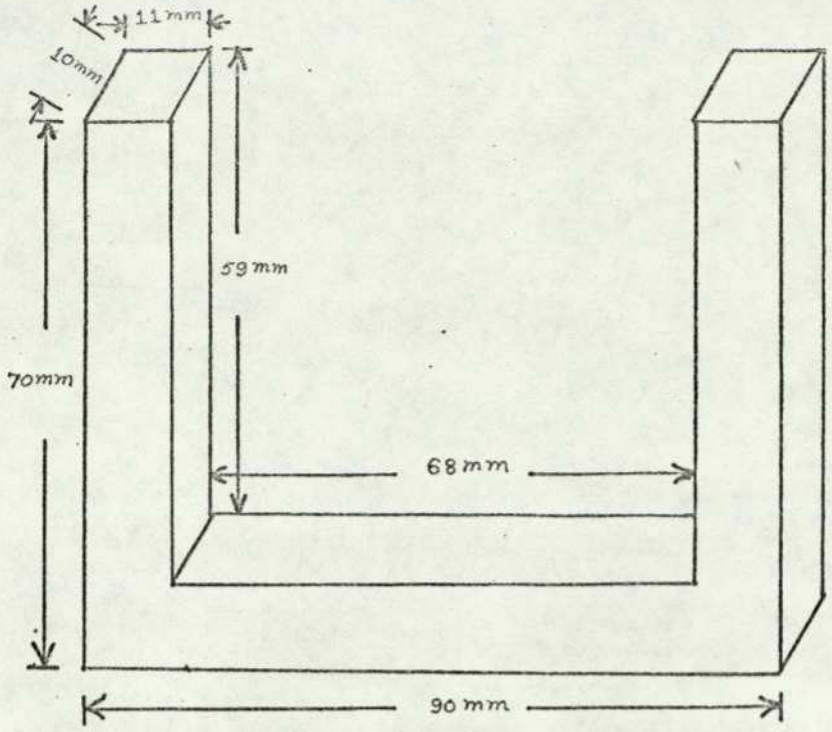

(a) The U-core

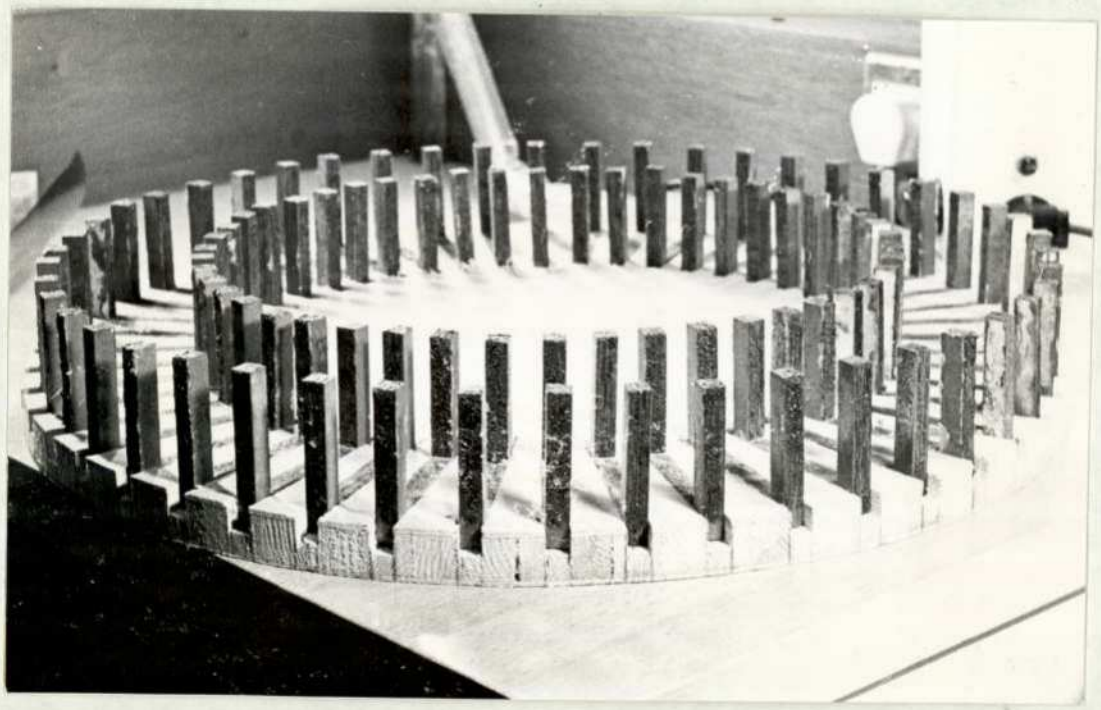

(b) The U-cores in the stator

Fig.4.3 the stator without winding

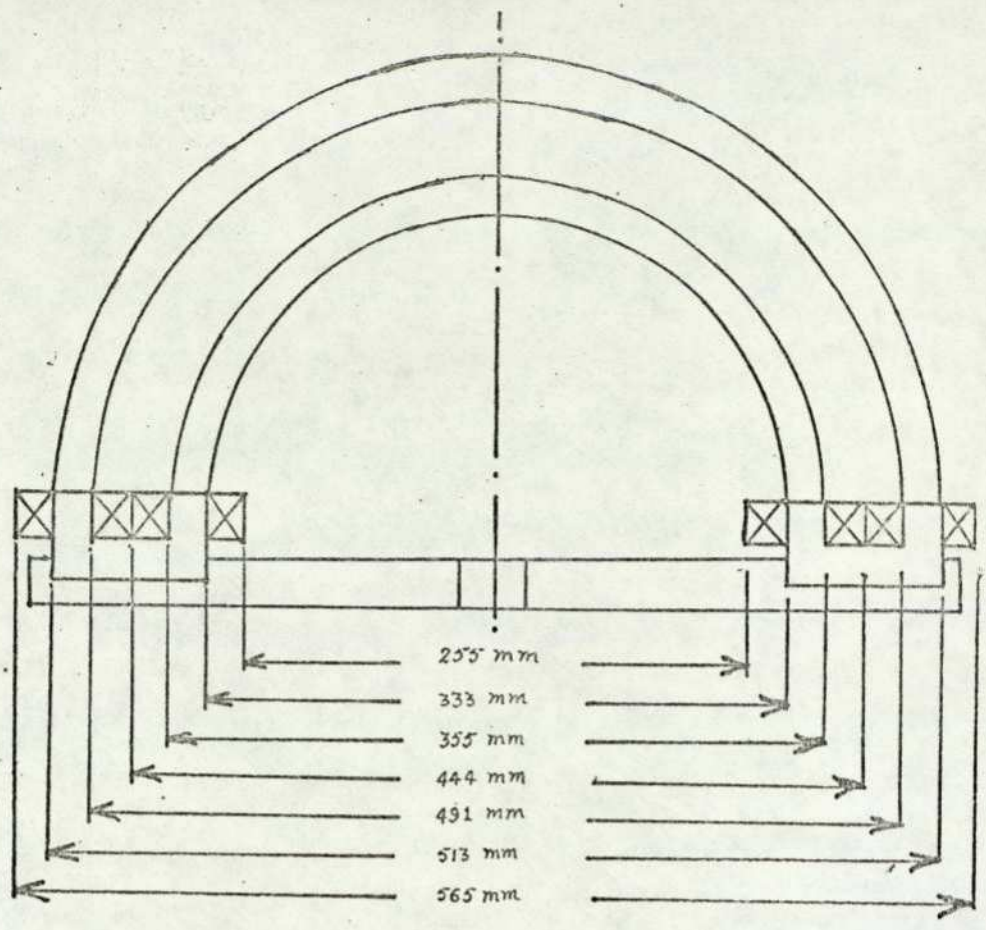

Fig.4.4 Main dimensions of the stator

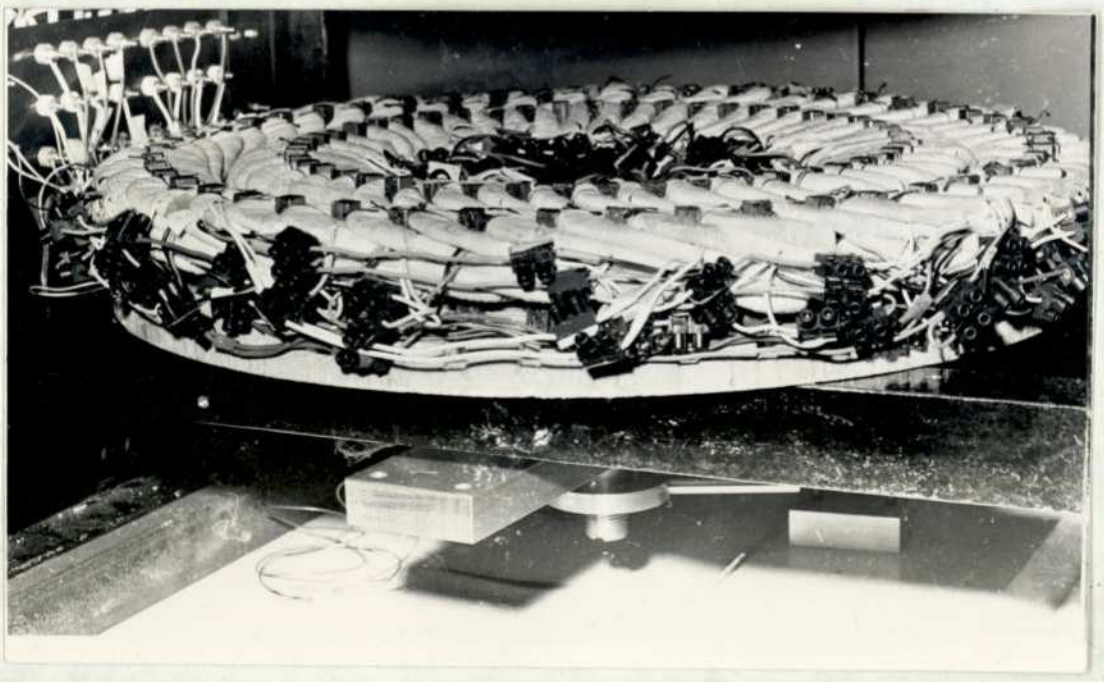

Fig.4.5 The stator

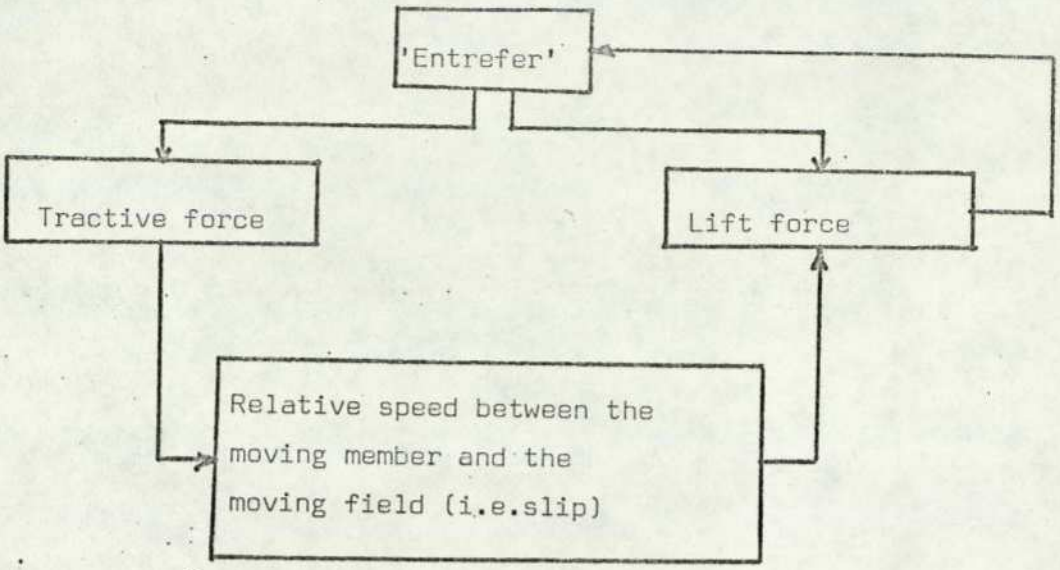

Fig.4.6 Interdependence of speed, lift-force, tractive force and 'entrefer'.

Fig.4.7 The load cell

however, dies down in due course since the 'entrefer' alters the magnetising reactance and the excitation current for a constant voltage operation. The problem of measuring four variables (levitation force, tractive force, speed and 'entrefer')remains.

This problem can, however, be simplified by measuring the lift force at constant 'entrefer' by constraining the movement of the secondary member under the influence of lift force, as discussed in Sec.4.2.2. Thus, in brief, the measuring device:

(a) should be able to measure a force the magnitude of which changes with speed,

(b) should cause only a negligible change in the 'entrefer' while measuring the normal lift force, and,

(c) can be raised and lowered with the complete stator assembly for changing the 'entrefer' and the secondary members.

These factors rule out the possibility of using a spring balance or dead weight type of force measuring device. A piezo-electric transducer also cannot be used because of two limitations.

First, it is relatively insensitive at low forces (minimum range of pressure acting on it should be of the order of 100 kN/m^2); and secondly, it cannot be used for the measurement of static pressures [53]. This leaves the strain gauge system for the lift force measurement. For the present test rig a load cell [54], incorporating the aforesaid features, was made and used. Fig.4.7 shows the location of the strain gauges on the load cell .

The attachment devised for adjusting the 'entrefer' is shown in Fig.4.8, and Fig.4.9 shows the attachment fixed to the load cell. The measurement of 'entrefer' is difficult, especially when the stator U-cores are not laid completely uniformly. It, therefore, becomes necessary to average 'entrefer' in the machine, and Fig.4.10 shows the arrangement made for a quick and easy determination of average 'entrefer'.

4.2.2 The Moving Member and its Attachments

The moving member consists of an annular conducting plate (with or without backing iron) fixed to a Paxolin disc (about 25 mm thick). This assembly is attached to a pair of 'angle-contact' thrust bearings (55) : used to restrict to a minimum the vertical movement of the shaft assembly (due to the normal forces produced), and, therefore, a constant average 'entrefer' can be maintained during the experiment. The shaft also carries a slip ring assembly to which search coils can be attached for the measurement of flux density in the secondary member under dynamic conditions. A dynamometer (with a strain gauge attachment) was coupled to the same shaft for loading the test rig and for the measurement of torque produced. The speed measurement is made by making use of a photo pick-up and equispaced black and white strips on the circumference of the Paxolin disc.

The measurement of flux density in the test rig was effected by using suitable search coils. These are discussed in detail in Sec.4.3.

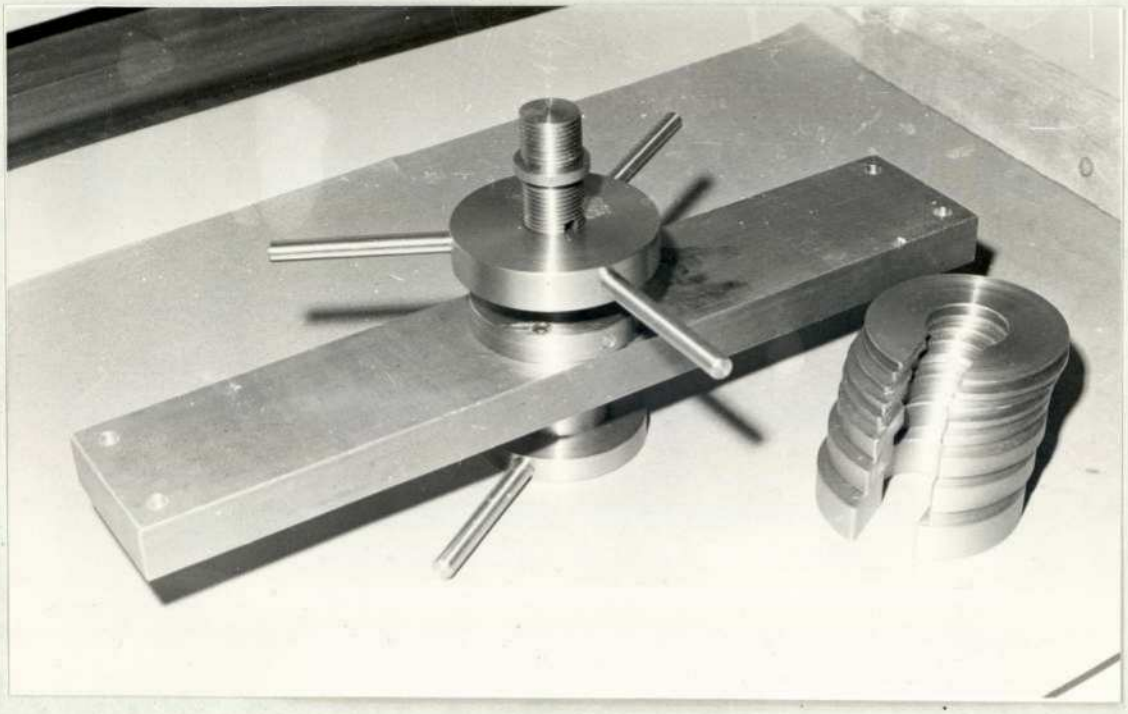

Fig.4.8 Attachment for moving the stator in the vertical direction to alter 'entrefer'

Fig.4.9 Load cell with the arrangement for altering 'entrefer'

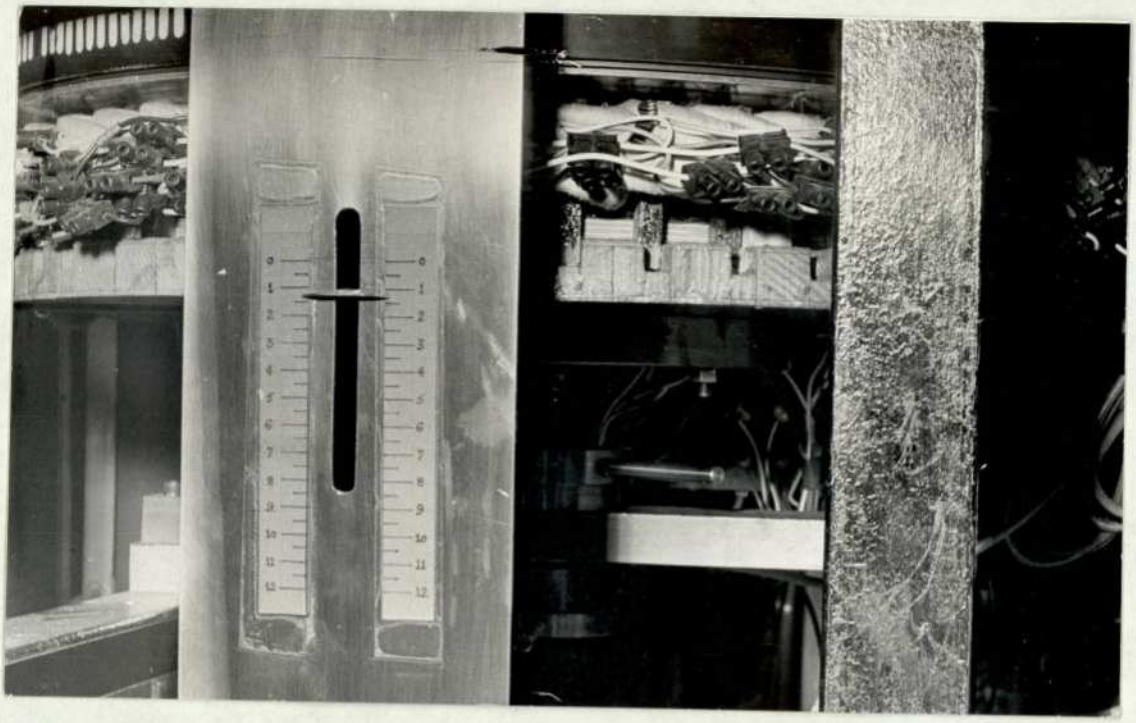

Fig.4.10 Arrangement to determine average 'entrefer'

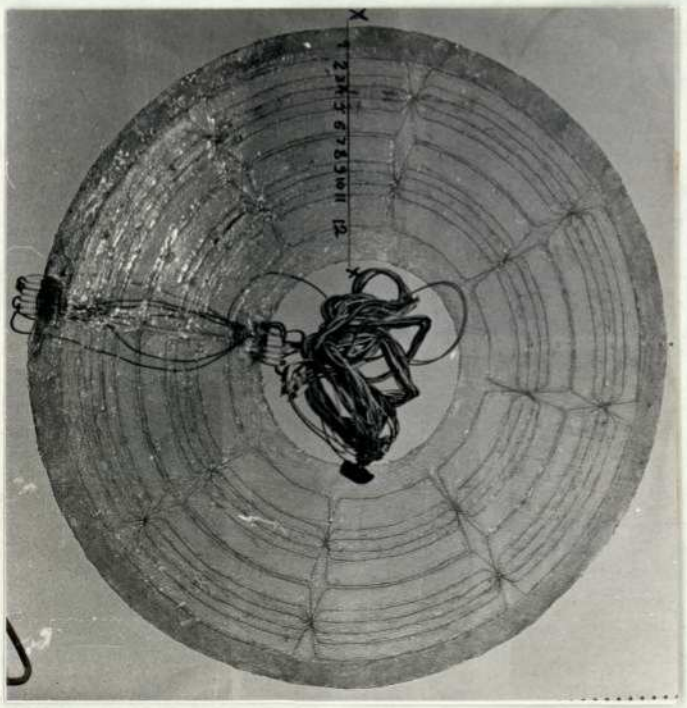

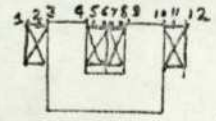

(a) Section at x-x

Fig.4.11 The circular search-coils

4.3 FLUX DENSITY MEASUREMENT

The measurement of magnetic flux density in and around the device is necessary for estimating useful and leakage fluxes. These measurements also reveal the high and low flux density regions in the device. The high flux density regions give rise to heavy additional losses and the low flux density regions lower the output to weight (or cost) ratio. Above all, the measurement of flux density assists in the verification of the theoretical models devised for analysing the device. In the following paragraphs, the discussion of the flux density measurements is based on the above objectives.

The usual method of measuring flux density in a.c. systems, is by employing suitable search coils in the region or path of interest in conjunction with an integrating instrument to measure and integrate the e.m.f.s induced in the search coils due to the changing fluxes. For the purpose of estimating the useful and leakage fluxes in the device large circular search coils were made. They were cast in fibre-glass to keep their thickness to a minimum and for their easy and compact movement in the air gap under standstill and dynamic conditions. Fig.4.11 shows the search coils with their leads and the six-way double-pole switch. The cross-section along x-x, in Fig.4.11(a) shows the location of each search coil with respect to a stator U-core. As is evident, the search coil assembly is appropriate for measuring the flux transferred, from one limb of a U-core to the other, between cores numbered as follows (Fig.4.11):

(a) 3-4 and 9-10

(b) 2-5 and 8-11, and,

(c) 1-6 and 7-12

in the air gap. The measurements made with these search coils are useful particularly in analysing the device by making use of the equivalent circuit approach [24]. The induced e.m.f. across 1 and 6, and 7 and 12 is proportional to the voltage across the magnetising reactance(X_m) in the T-equivalent circuit and therefore, its measurement assists in determining the parameters of the T-equivalent circuit and hence in predicting the performance.

The philosophy behind the construction and placing the search coils and the corresponding measurements of flux density become different, however, when they are to be used for the verification of theoretical models (especially the numerical type) devised to analyse the device. The problem becomes exceedingly difficult, in practice, when the region of interest has sharp discontinuities such that the change in flux density with respect to the spatial co-ordinates is high. This is because the measured flux density is the average of the flux density in the region occupied by the search coil and it is, therefore, difficult to obtain the maxima or minima of the flux density. The possible solution then is to use a very small search coil such that small movements along the three co-ordinate axes result in an inappreciable change in the measured induced e.m.f. This, however, gives rise to two problems: (a) the construction and (b) the measurement of

e.m.f. induced (which is proportional to the amount of flux passing through it).

In the present work, the former difficulty has been overcome by skillfully constructing small search coils having a small dimension on the axis along which the rate of change of flux density is high and relatively large dimensions along the other axes. Further, the problem of measurement has been solved by introducing an operational amplifier between the search coil and the measuring equipment, suitably screened from noise and other stray signals.

The measurement of flux density, like any other measurement, is associated with a number of sources of error giving rise to an uncertainty factor. The possible sources of error are:

(a) in the measurement of the search coil dimensions,

(b) in the measuring equipment and the linearity of the operational amplifier used (together with the presence of noise and stray signals),

(c) in locating exactly the location of the search coil in space because of the irregularities in the electromagnetic device, especially in the shape and height of the U-core limbs which are non-uniform throughout the machine, and,

(d) in the experience and the limitations of the experimenter.

It is not easy to estimate or remove all the sources of error listed above. However, attempts have been made to minimise them. For instance, the search coil has been calibrated by making use

of a source of uniform flux and a standard search coil. This eliminates the need for finding the exact dimensions of the search coil. Similarly, the gain of the operational amplifier has been derived by using standard equipment, and the leads between the search coil and the amplifier have been carefully screened against stray signals and surrounding noise. Also, suitable attachments have been devised to find the location of the search coil as accurately as possible. The location error, however, is also a function of the irregularities in the stator U-core and hence to minimise the error, due to sources (c) and (d) listed above, the measurements have been repeated at several locations.

In Chapter 5 results of the numerical analysis for the BTFCM (as discussed in Chap.3) are presented and compared with the experimental values.

4.4 CONCLUSION

In this Chapter, emphasis has been given to the testing of linear electric motors during the process of their development. This is because the secondaries of these motors in their applications are the tracks and therefore they become a part of the surroundings in which they are installed. For this reason, linear electric motors must normally be specially designed for their applications with due regard to compatibility, practicability, utility, convenience and cost.

The research programme can also provide results useful in electromagnetic scaling. Scaled down models of all the test rigs, listed in Sec.4.1, can be made at relatively lower cost for the verification of the predicted scaling factors (which are not linear)[51].

On long tracks, linear motors have to be tested during acceleration, a short run at constant speed, and a deceleration to stop. These tests can be conducted at

(a) constant terminal-voltage-to-frequency ratio,

or(b) constant rated current to the motor.

In practice, however, it is always difficult to maintain either of these conditions for the complete duration of the test and, therefore, it is always better to repeat the test under similar conditions. During the test the vehicle will be moving and hence all these necessary measurements have to be made via sensors, converted from analogue to digital quantities and telemetered to the ground control room for real time recording and later processing

by computer. The accuracy of the test results is a function of the accuracy of calibration and hence all data channels from end-to-end should be calibrated immediately before and after each test run.

CHAPTER 5

5. TESTS, CORRELATION AND DISCUSSION OF RESULTS

5.1. INTRODUCTION

In Chapter 3 a numerical approach for analysing the BTFCM has been discussed in detail. A computer programme, based on these discussions, has been developed to predict flux densities and forces in the BTFCM. As an example the programme has been tested for secondary members, each consisting of an aluminium plate with backing iron. The correlation of predicted and measured results, both under standstill and dynamic conditions, is shown in this chapter. The computed results are also presented in the form of two- and three-dimensional plots to show the variation of flux densities, current densities and force densities along the length of the machine.

5.2 DESCRIPTION OF THE SECONDARY MEMBERS USED FOR TESTING THE COMPUTER PROGRAMME

The computer programme developed on the lines of discussions of Chap.3 has been used to calculate flux densities and forces with the following secondary members. First, the programme was 'run' with no secondary member, i.e, with open boundary conditions. This was done primarily to check the discontinuities in the primary member. Next, a secondary member, as described by Fig.5.1, was used. The width of this secondary member was taken as equal to the width of the U-cores. The width of secondary member was then extended beyond the width of the U-cores as shown in Fig.5.2. This was done to reduce the current-density concentration at the edges of the disc, and this point will be discussed in Sec.5.5, the relevant diagrams being those in Figs. 5.15 and 5.16. This in fact was an example to show

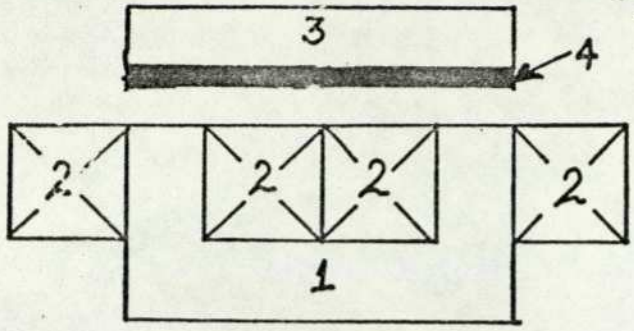

1. U-core 3.Laminated backing iron

2. Winding 4. 2.68 mm thick aluminium plate ($\rho = 2.8 \times 10^{-8}$ Ωm)

Fig.5.1 Secondary SEC1

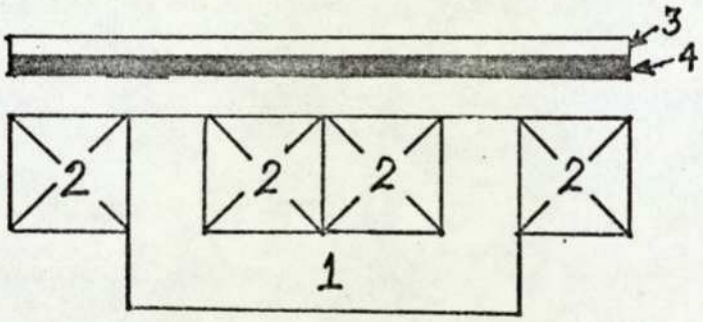

1. U-core 3.Solid backing iron

2. Winding 4. 2.68 mm thick aluminium plate ($\rho = 2.8 \times 10^{-8}$ Ωm)

Fig.5.2 Secondary SEC2

how with a slight modification in the computer programme various secondary members can be easily analysed. In the following section some results are presented to show the correlation of results obtained from the computer programme and the measurements made on the BTFCM.

5.3 FLUX DENSITIES

In Fig.5.3 the variation of flux density 5mm above and along a half U-core with no secondary member has been plotted. The correlation is reasonable throughout except at nodes numbered 12,6 to 8 and 16 to 18 in Fig.5.3. The discrepancy at nodes numbered 16 to 18 is most likely due to the shape of coils which in the model have been assumed flat and horizontal whereas in the BTFCM they are slanted. This leads to an error which can be resolved by using a finer mesh to describe the windings. Similarly for node No.12, the problem can be resolved by using a finer mesh interval along and above the U-core limbs. However, a moderate alteration, such as an addition of two nodes on the U-core limb, two close to the U-core limb and two along the length of air-gap, would increase the number of nodes in the X-Z plane from 200 to 288 (i.e. by 44 per cent), and need (as mentioned in Chap.2) a corresponding increase in the computation requirements. Fig.5.4 shows how the dip in flux density, at node No.12, diminishes with increasing distance from the pole surface. (This is expected because, with the increasing distance from the pole surface, the flux lines bend around the U-core limb and therefore reduce the vertical components of flux at its corners.)

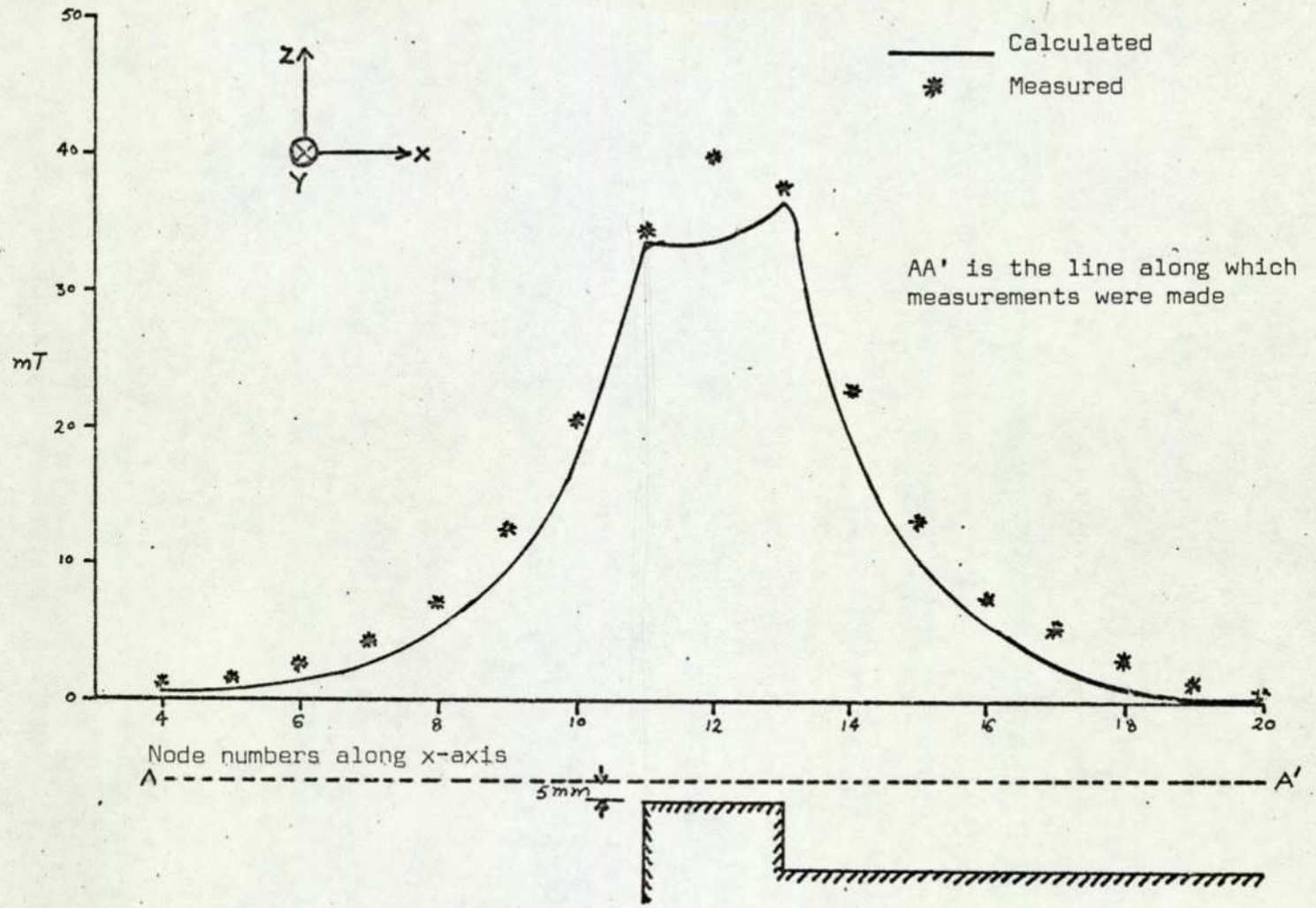

Fig.5.3 Vertical component of flux density (B_z) along x-axis

Case: No secondary member

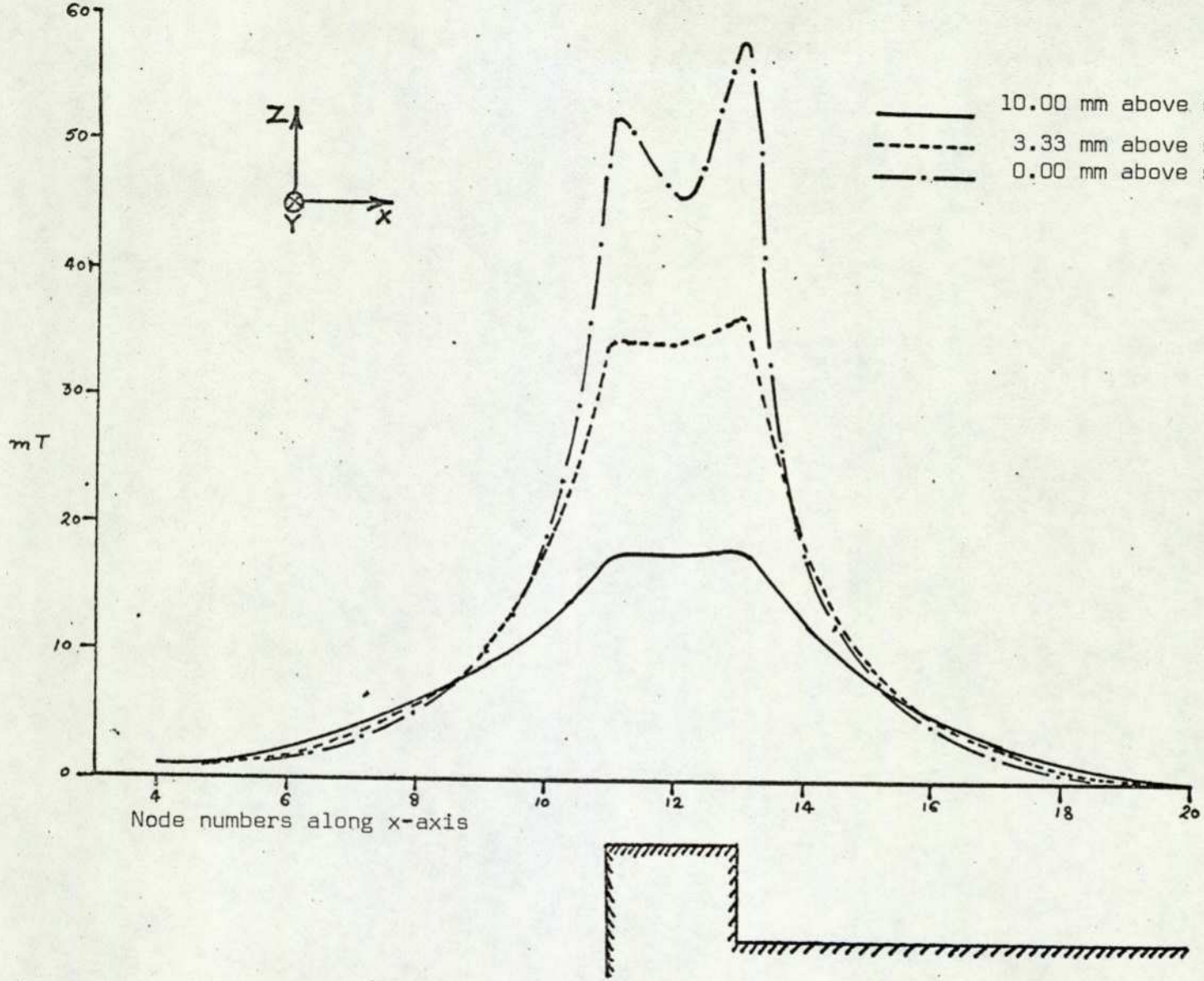

Fig.5.4 Variation in the vertical component of flux density (B_z) along x-axis with distance from the stator
Case: No secondary member

Fig.5.5 shows the variation of flux density 3mm above and along a half U-core for the secondary member SEC1. The 'entrefer' was kept at 7.68mm total, which represents 5mm mechanical clearance between primary and secondary members, and 2.68mm thickness of the aluminium plate. The correlation is worse, this time, at node No.11. The possible reason is that the potential at nodes lying on the outer edge of the conducting plate have been fixed at zero (to satisfy the condition that the iron is infinitely permeable and that the current paths do not lie in space). This results in a very high vertical potential gradient at node No.11 and hence the predicted value of the corresponding flux density. The possible remedy, this time, is to have a different mathematical model which enables the scalar potential U to vary along the edge, whilst still ensuring that the current density at the edge is parallel to it. This requires that $\overline{H}$ = -grad U should be replaced by $\overline{H}$ = $\overline{T}$ −grad U, where $\overline{T}$ is the electric vector potential.[44,58]

In Fig.5.6 the correlation of measured and predicted flux densities for the secondary member SEC2 has been shown. The predicted vertical component of flux density (Bz) along the plane AA is higher than the measured value outside the U-core, and lower inside the U-core. This can be mainly attributed to those errors arising in the measurement of flux density and discussed in Sec.4.3. The difference can be reduced, however, by taking necessary precautions during the construction of the machine so as to enable easy and accurate location

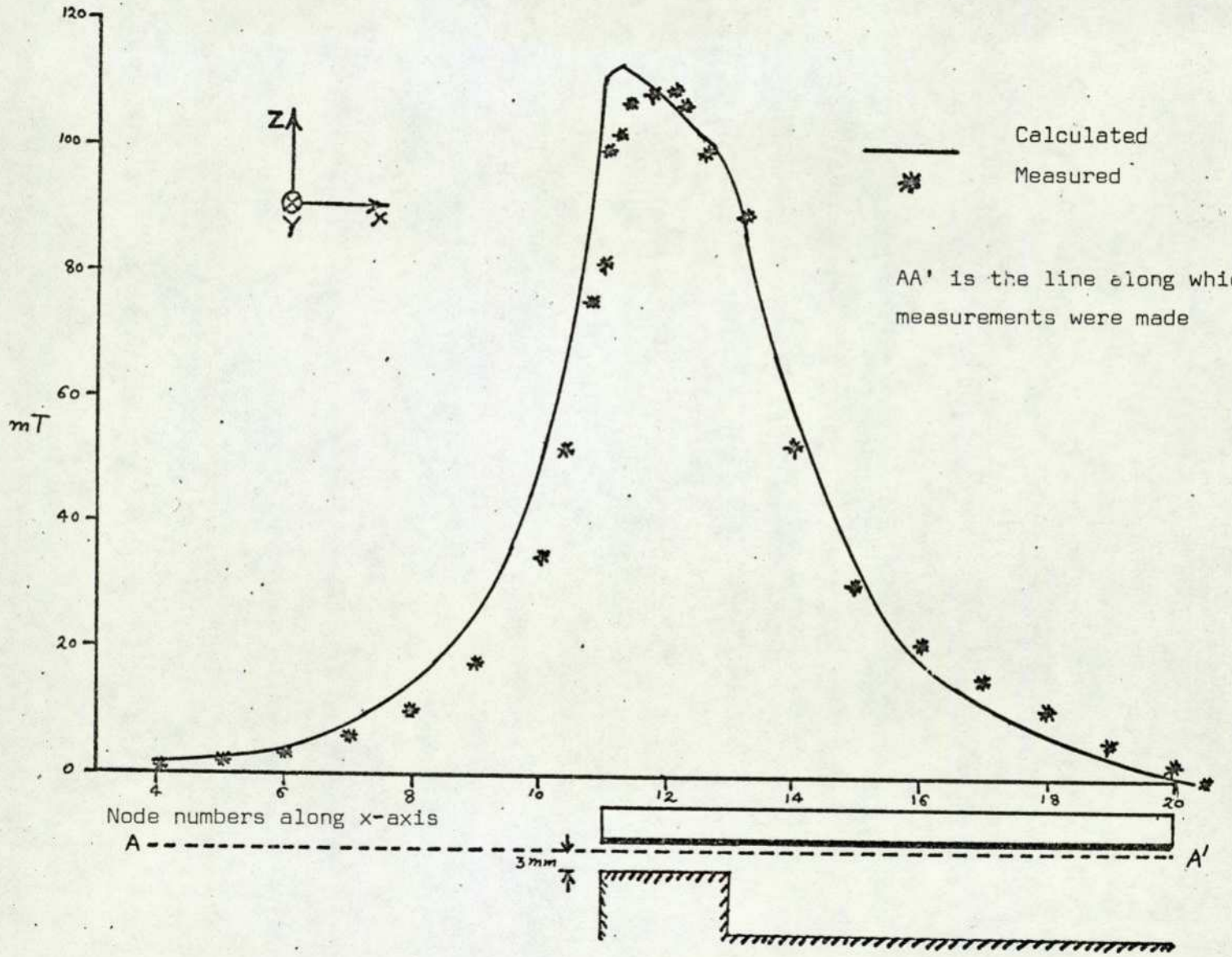

Fig.5.5 Vertical component of flux density (B_z) along x-axis
Case: Secondary SEC1

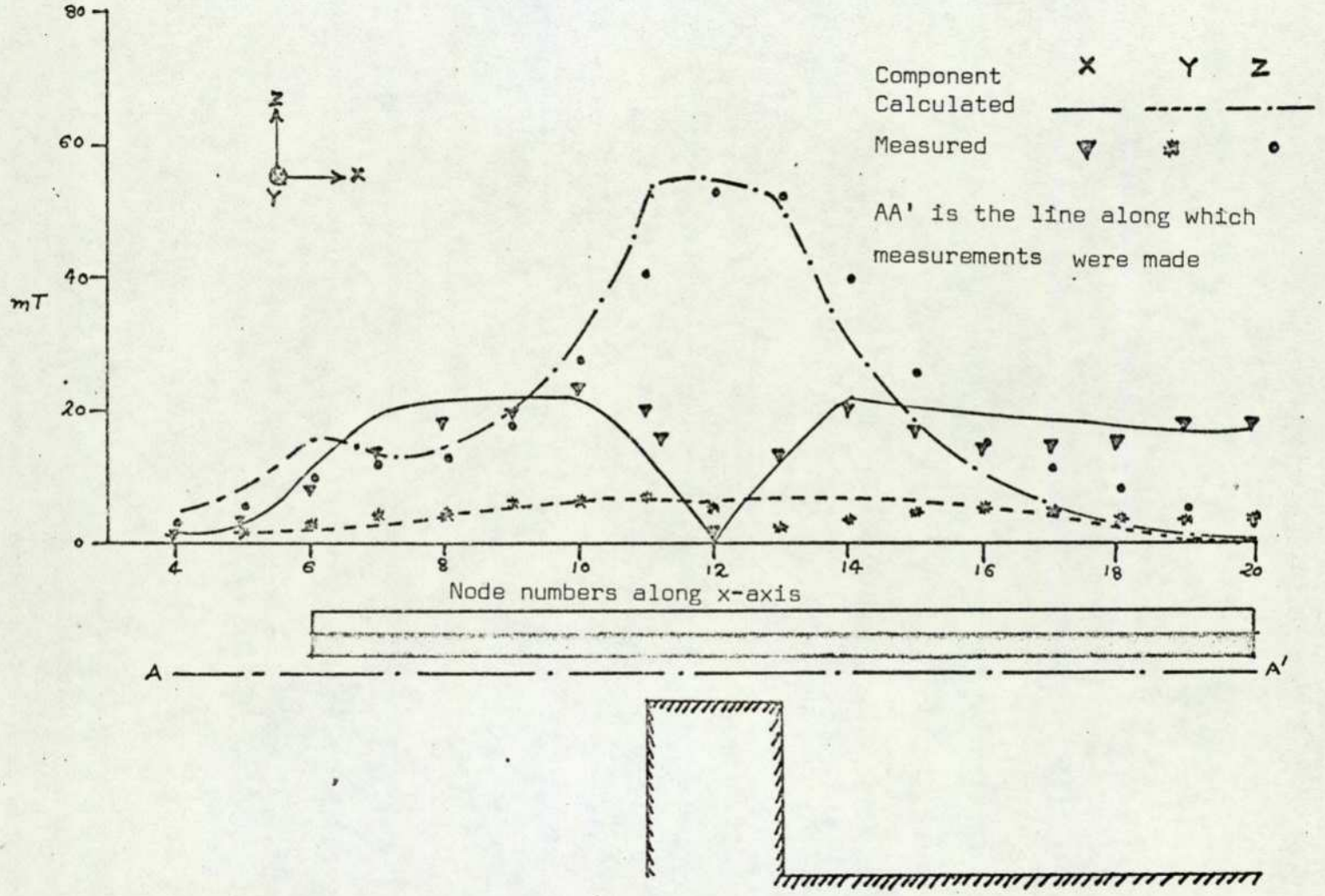

Fig.5.6 Variation of flux densities along x-axis for secondary SEC2

of a particular node in space. This applies also, of course, to the other components Bx and By.

The prediction and measurement of flux densities under dynamic conditions poses greater problems. For verification a node has been selected 5mm outside the U-core along the X-axis. Fig 5.7 shows the predicted and measured components of flux density during motoring and regenerative braking conditions. The transverse component of flux density (B_x) does not change appreciably from a slip of 2.0 to a slip of zero and the correlation is reasonably good.

The vertical component (B_z), however, shows considerable discrepancy both during motoring and braking operation. The predicted values are higher than those found by measurements at low slips (less than 0.6 p.u.) and lower at high slips. However, whereas in the region of braking (slip between 2.0 and 1.0) the difference between measured and predicted values remains fairly constant, that in the region of motoring (slip between 0.6 and zero) the measured value does not change but the predicted value keeps rising and therefore so does the difference between the two. The possible reason for this may be attributed to saturation taking place in the backing solid iron. Although the flux density incident on the backing iron is very low (about 40 mT) circulating eddy currents can nevertheless cause saturation of the surface layer and therefore violate the assumption made in Chapter 3. One remedy to this problem is to construct a laminated backing iron

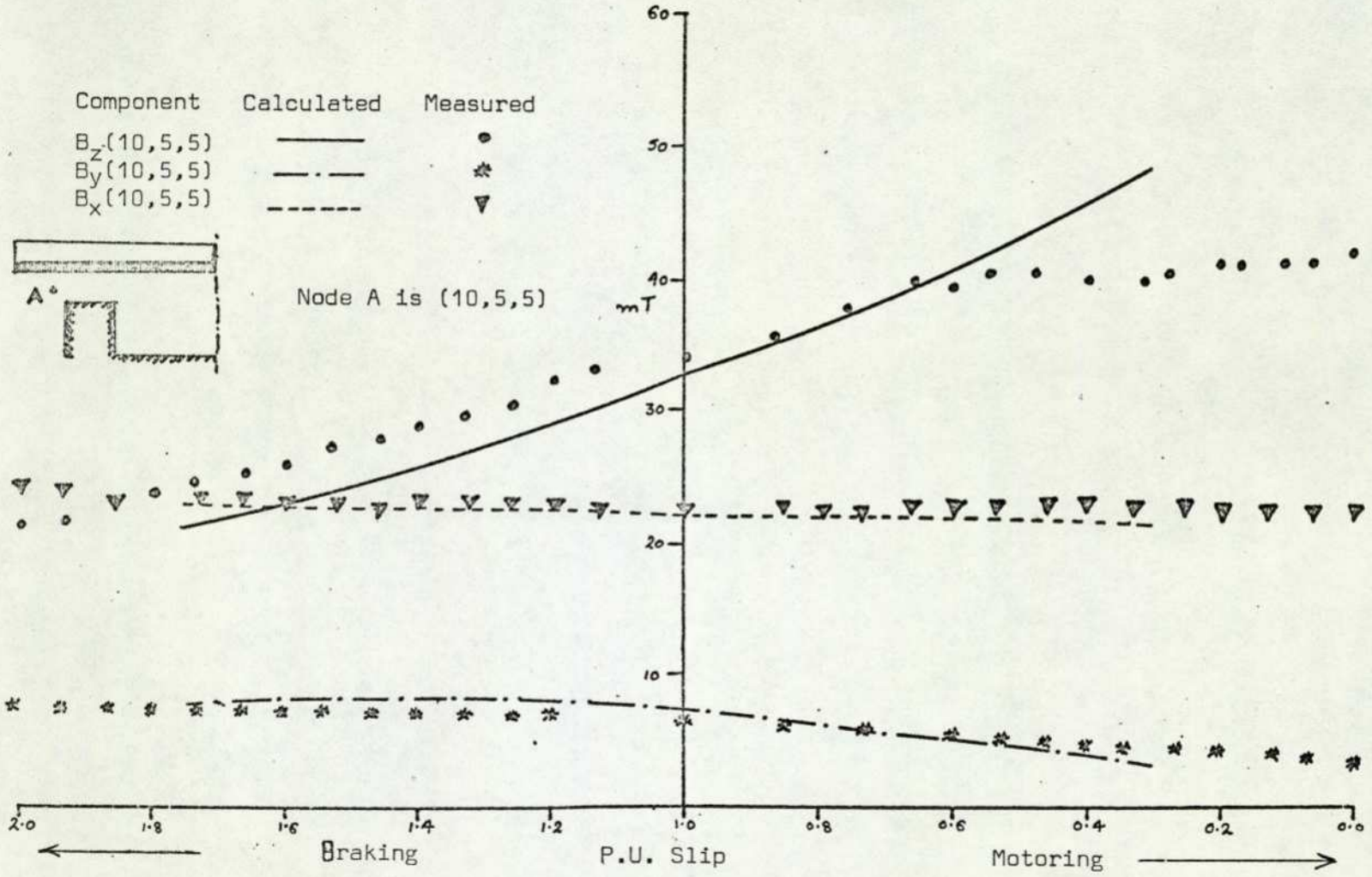

Fig.5.7 Variation of flux density near a tooth (at node A) during motoring and braking operation

of the same dimension radial as the aluminium plate under consideration, or, better, to include the effect of saturation in the backing iron in the computer programme [59].

The variation with respect to speed of the measured and predicted longitudinal component of flux density (B_y) has the same general trend, although the measured value is lower than that predicted theoretically during braking and higher during high speeds. This may be due to two reasons, first, that the backing iron is not laminated as is assumed in the model and secondly, incorrect positioning of the search coil.

In the next section the forces calculated by making use of the calculated flux densities are compared with those measured on the BTFCM under dynamic conditions.

5.4 LONGITUDINAL AND VERTICAL FORCES

In Sec.5.3 the correlation between the predicted and measured components of the flux density during motoring and braking conditions, has been discussed. The correlation is not very good, particularly at high speeds, especially for the vertical component (B_z) which forms the major part of the total flux in the air gap. The forces predicted by using these components of flux densities and Maxwell's stress tensor, as discussed in Chap.3, have been compared with those measured on the BTFCM in Fig.5.8.

As expected from the correlation of the vertical component of flux density in Sec.5.3, there is a considerable discrepancy in the predicted and measured vertical forces. The measured attractive forces are always higher than those predicted

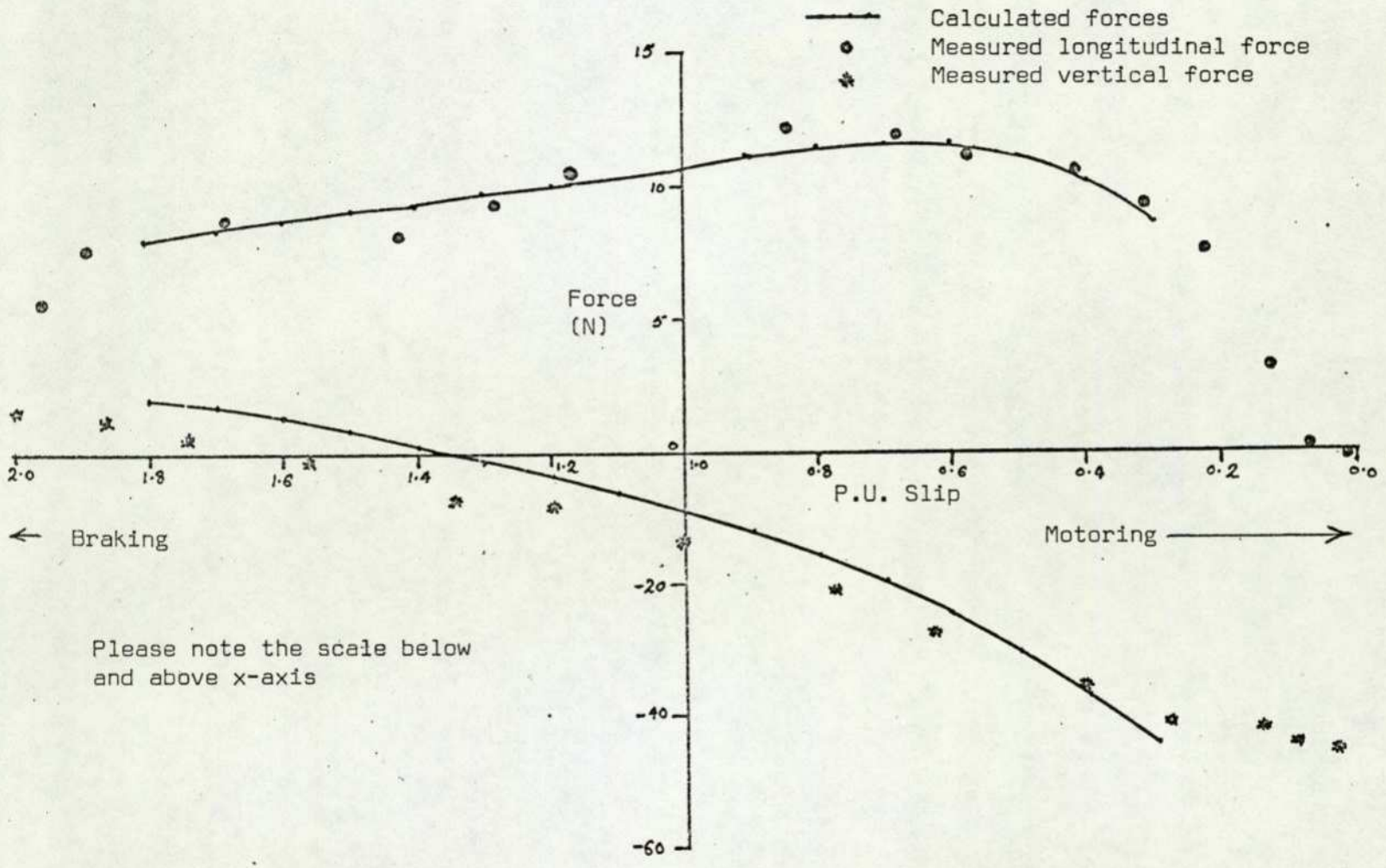

Fig.5.8 Variation of longitudinal and vertical forces during motoring and braking operation

except at high speeds where the measured ones remain fairly constant but the predicted ones keep increasing. This is primarily because in the numerical model discussed in Chap.3, the permeability of the backing iron has been assumed infinite throughout which may not be true at high speeds for reasons mentioned in Sec.5.3.

The measured and predicted longitudinal (or propulsive) forces, however, show a reasonable correlation in Fig.5.8. This is because the measured component By is higher than that predicted at high speeds and therefore the reduction in component B_z is partially compensated in the eqn.3.47.

The correlation of measured and predicted flux densities and forces in Sections 5.3 and 5.4 verify the numerical model proposed in Chap.3. These computed results, based on this model, have been plotted in two- and three-dimensions, in Sec.5.5, to study their distribution along the length of the machine.

5.5. TWO- AND THREE-DIMENSIONAL PLOTS OF COMPUTED MAGNETIC SCALAR POTENTIAL, FLUX DENSITIES, CURRENT DENSITIES AND FORCE DENSITIES

The correlation of flux densities and forces and suggestions for improving it further were discussed in Sec.5.3 and 5.4. In this section some of the two- and three-dimensional plots are presented to show the MSP, current density, flux density and force density distribution in the BTFCM.

Figs. 5.9 and 5.10 show the effect of the width of the secondary members on the MSP distribution in the x-z plane. Curves orthogonal to these MSP contours are the field lines, and they indicate that the flux density is more uniform in the case of secondary SEC2 than of SEC1. In Fig.5.11 MSP has been plotted in the air-gap for two pole pitches. The plots show ripples along the length of the machine. These ripples are due to the discontinuities in the primary member and justify the use of three dimensional analysis.

The three components of flux density in the air-gap are shown in Figs.5.12 to 5.14 for secondary SEC2 at slip 1.0. The transverse component (B_x) distribution remains fairly constant along the length of the machine along a line passing through the centre points of each U-core. The plot also shows maximum variation near the outer and inner edges of each limb. This sudden change results in a high gradient of B_x along the x-axis and therefore a high lateral force density as shown later in Fig.5.18(a).

The longitudinal and vertical components show maximum variation taking place along a line passing through the centre points of each limb of the U-core. The minimum variation in

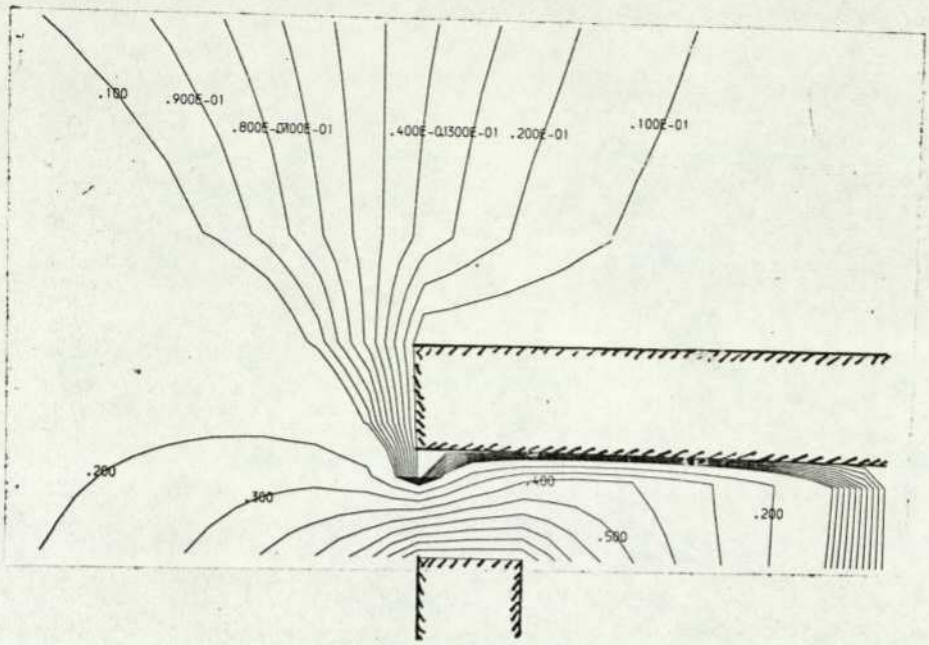

(a) Imaginary component. Contour 1.0 corresponds to MSP of 551.1A

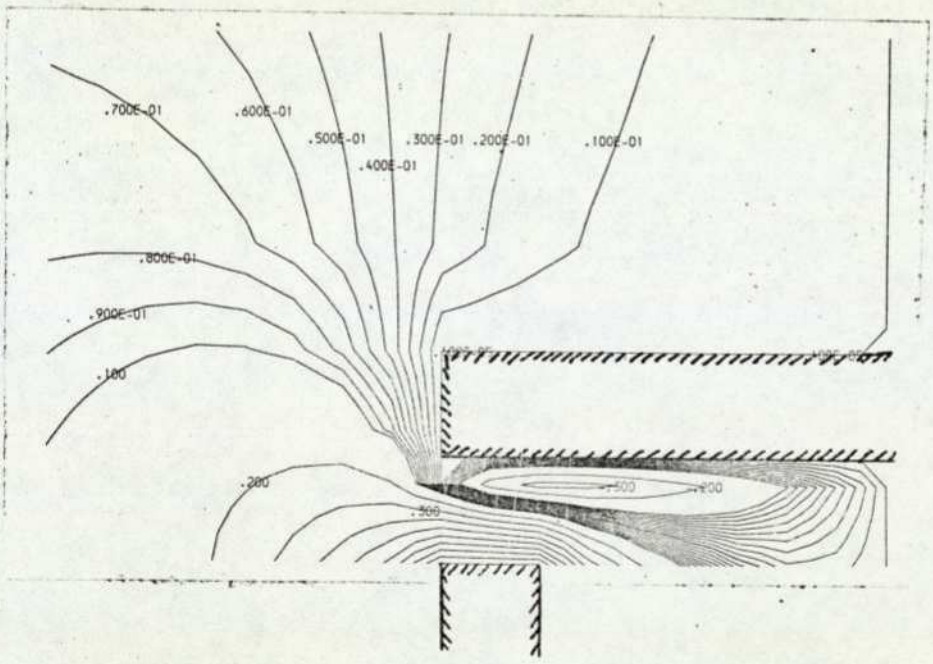

(b) Real component. Component 1.0 corresponds to MSP of 318.2A

Fig.5.9 MSP distribution in x-z plane for secondary SEC1 (the flux distribution is orthogonal to these contours)

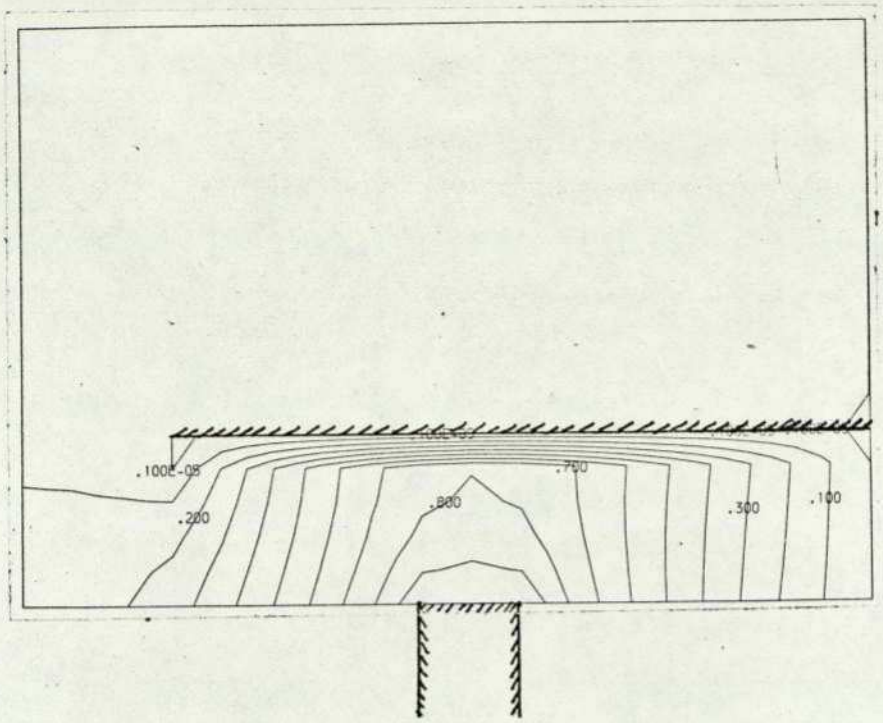

(a) Imaginary component. Contour 1.0 corresponds to MSP of 551.1A

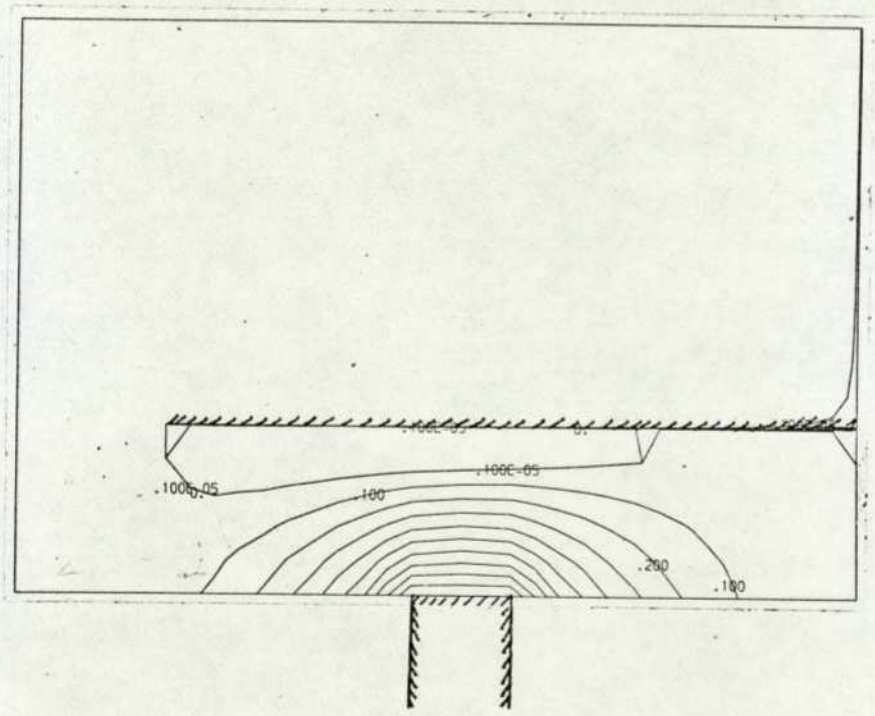

(b) Real component. Contour 1.0 corresponds to MSP of 318.2A

Fig.5.10 MSP distribution in x-z plane for secondary SEC2 (the flux distribution is orthogonal to these contours)

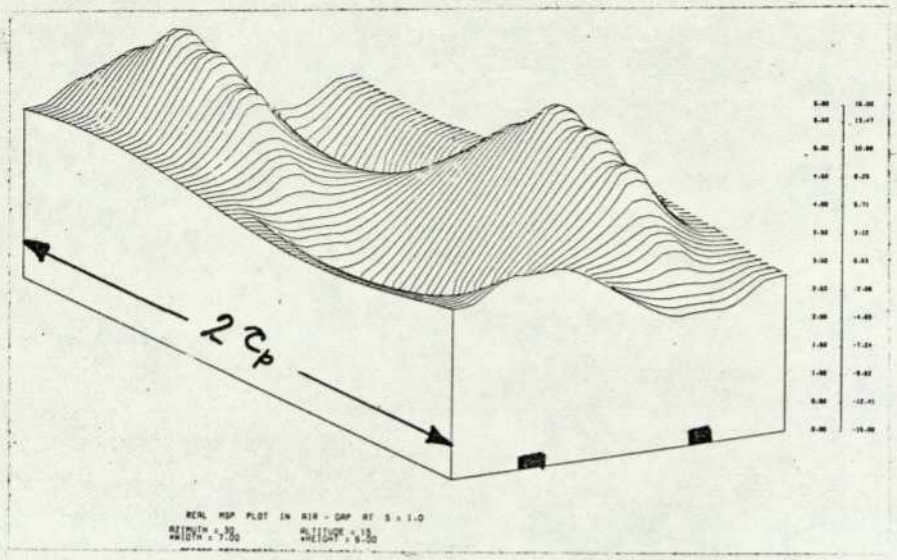

(a) Imaginary component. Normalising constant = 51.6A

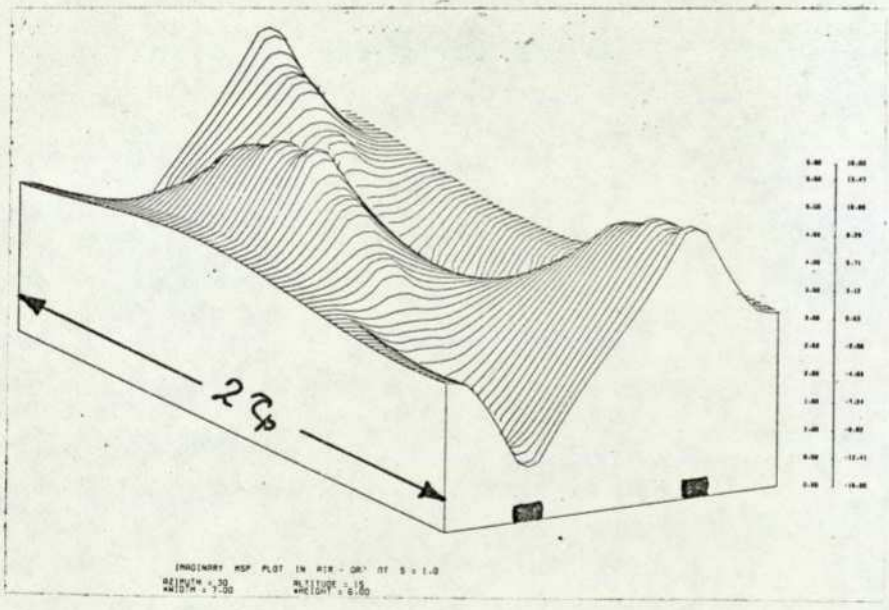

(b) Real component. Normalising constant = 51.1A

Fig.5.11 MSP distribution in x-y plane in the air-gap for two pole pitches. Secondary : SEC2. Slip = 1.0p.u.

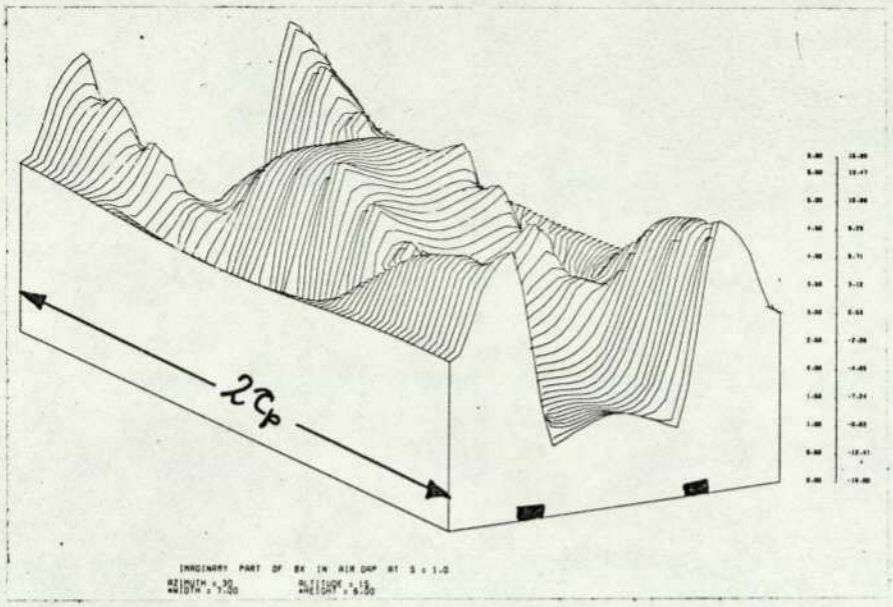

(a) Imaginary component. Normalising constant = 2.25mT

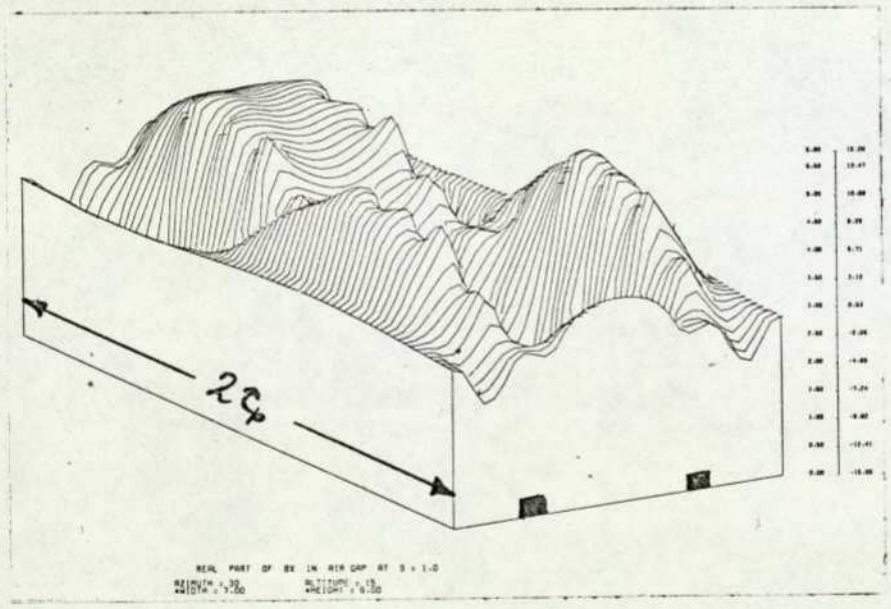

(b) Real component. Normalising constant = 2.12mT

Fig.5.12 Transverse component of flux density (B_x) distribution in x-y plane in the air-gap for two pole pitches. Secondary : SEC2. Slip = 1.0p.u.

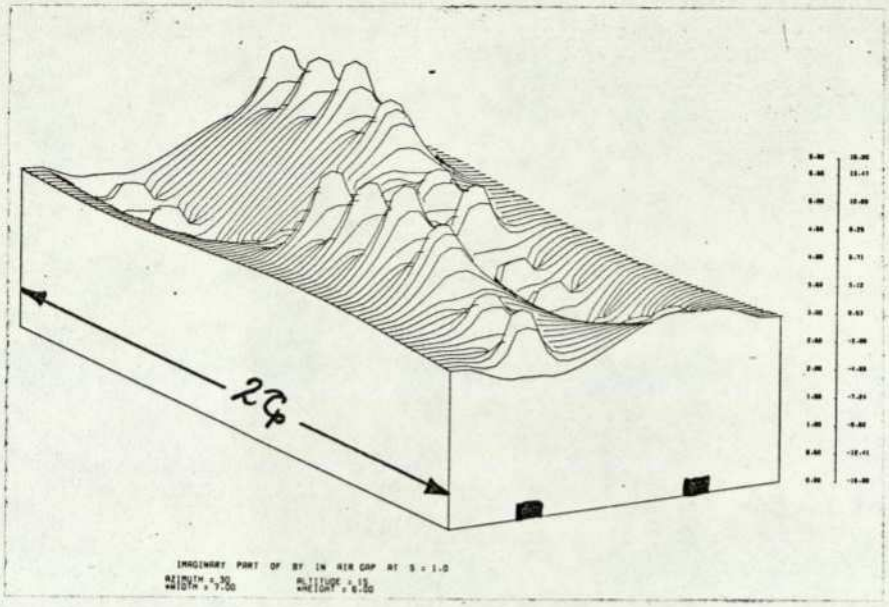

(a) Imaginary component. Normalising constant = 1.45mT

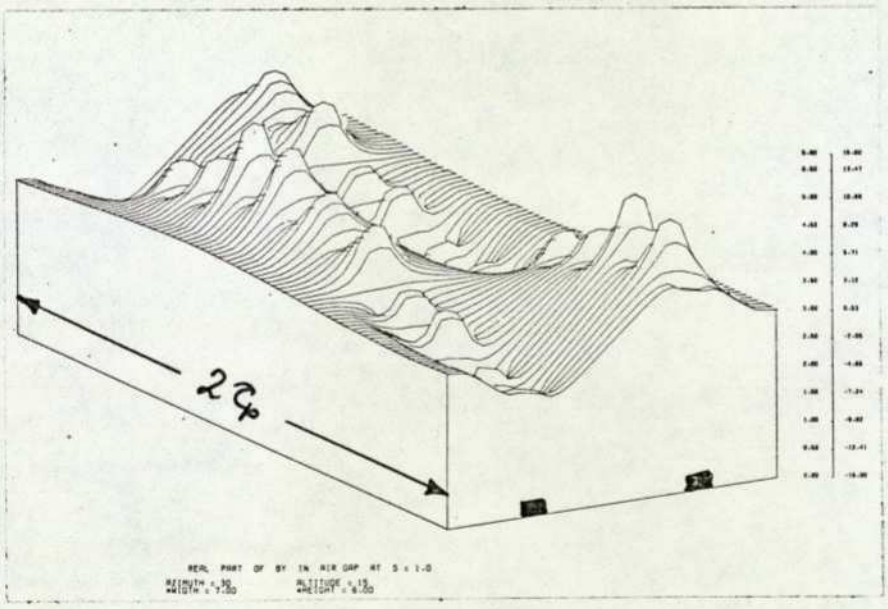

(b) Real component. Normalising constant = 1.50mT

Fig.5.13 Longitudinal component of flux density (B_y) distribution in x-y plane in the air-gap for two pole pitches. Secondary :SEC2. Slip = 1.0p.u.

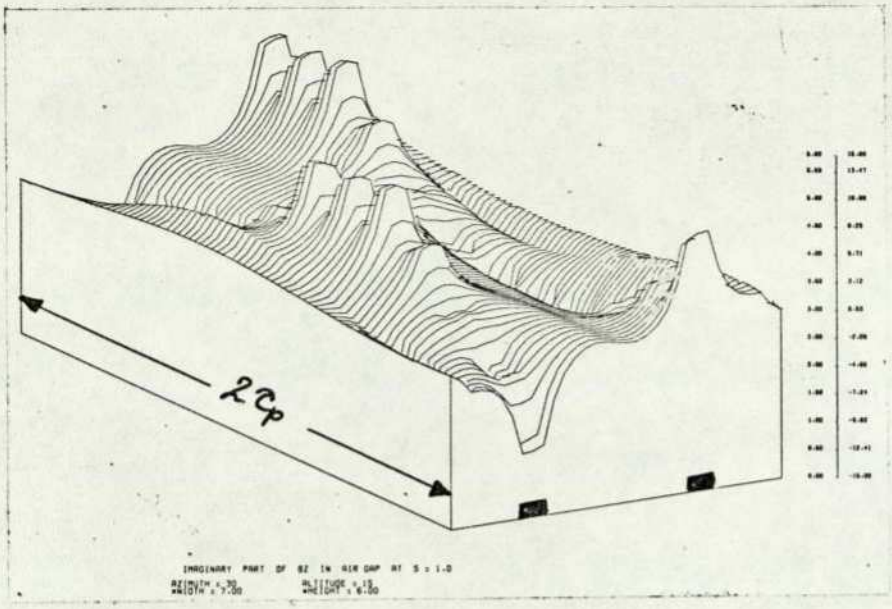

(a) Imaginary component. Normalising constant = 5.06mT

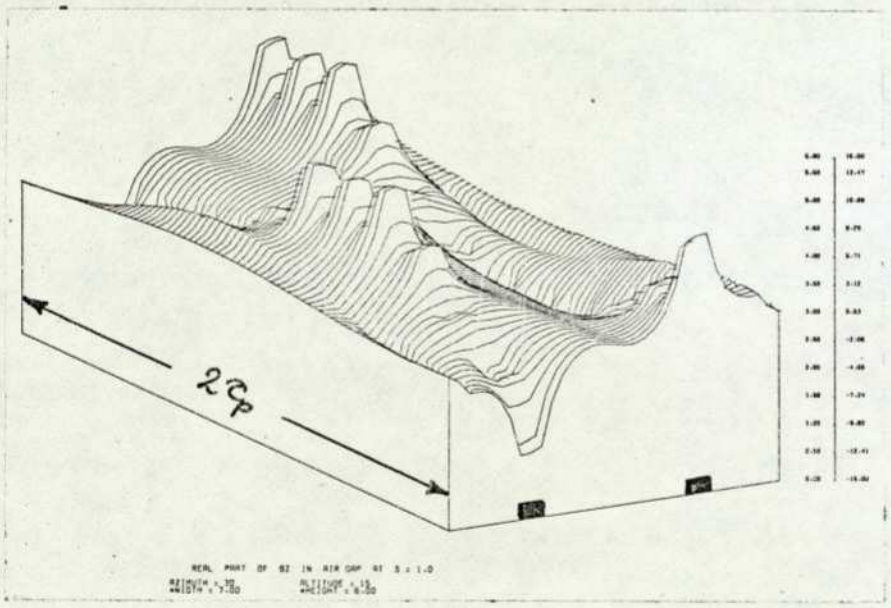

(b) Real component. Normalising constant = 5.49mT

Fig.5.14 Vertical component of flux density (B_z) distribution in x-y plane in the air-gap for two pole pitches. Secondary : SEC2. Slip = 1.0p.u.

each case is in the centre of the U-core, contrary to that of the transverse component. The corresponding force densities, as shown in Fig.5.18, therefore have their maxima in the centre of the teeth. Plots shown in Fig.5.13 and 5.14 also indicate a higher ripple along the length of the machine and a fairly uniform value along the width of the U-core limbs, as pointed out earlier with reference to Fig.5.9 and 5.10, with maxima for Bz lying in the centre of a tooth and that for By in the centre of a slot.

Figs.5.15 and 5.16 show the current density distribution in the secondary conducting sheet members SEC1 and SEC2 for a slip of unity. As pointed out earlier, the current density distribution has a higher concentration along the edges of secondary member SEC1 than it has for SEC2. Also the normalising constant is higher in the case of SEC2 because of the decrease in the secondary resistance due to the increase in the width of the plate. This would, obviously, increase the forces produced. In Figs.5.15 and 5.16 the zero contours lying between two poles have been plotted curved instead of straight lines. This is so because whereas the conducting sheet considered in the calculations has a circular geometry and hence so has the node mesh, for plotting purposes the node mesh has been assumed rectangular. Thus, if the plots are bent suitably to represent the current density distribution in the circular disc, the curved lines will naturally become radially straight lines.

In Fig.5.17 the current density distribution in the secondary SEC2 has been plotted in three dimensions in order

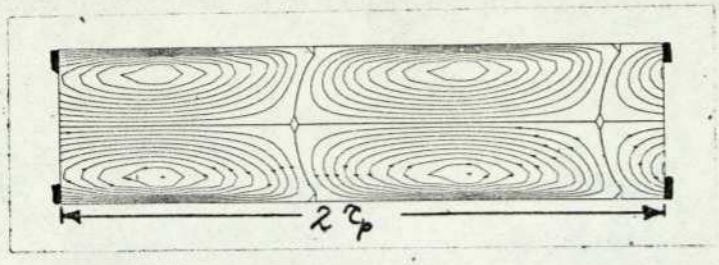

(a) Imaginary component. Contour 1.0 corresponds to 268.96

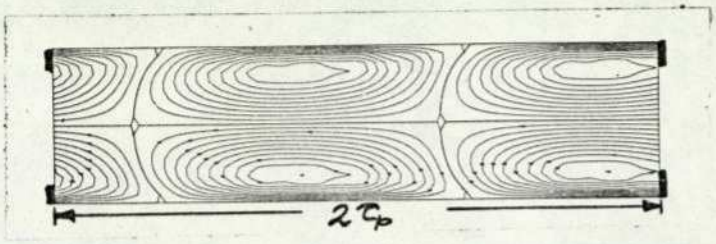

(b) Real component . Contour 1.0 corresponds to 255.18

Fig.5.15 Current density distribution in the secondary aluminium plate. Secondary : SEC1. Slip = 1.0p.u.

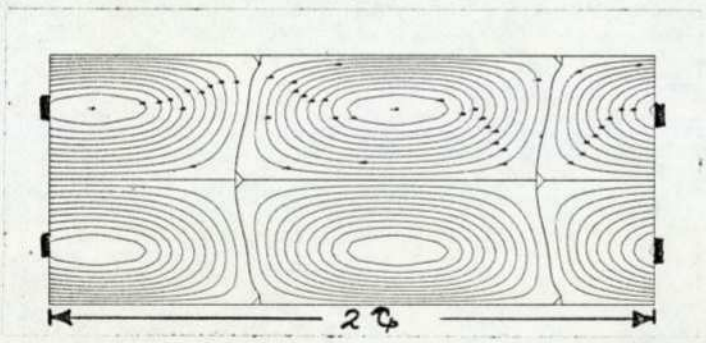

(a) Imaginary component. Contour 1.0 corresponds to 480.2

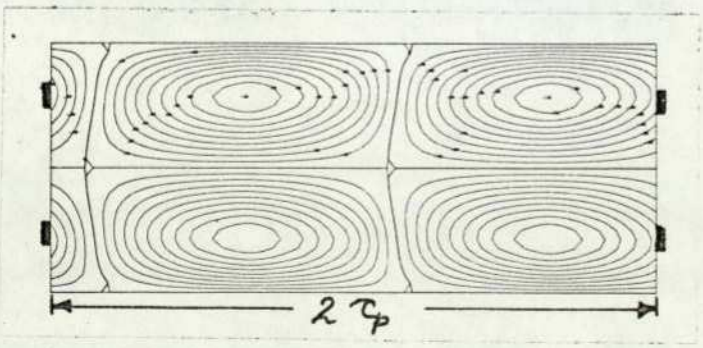

(b) Real component. Contour 1.0 corresponds to 499.67

Fig.5.16 Current density distribution in the secondary aluminium plate. Secondary :SEC2. Slip = 1.0p.u.

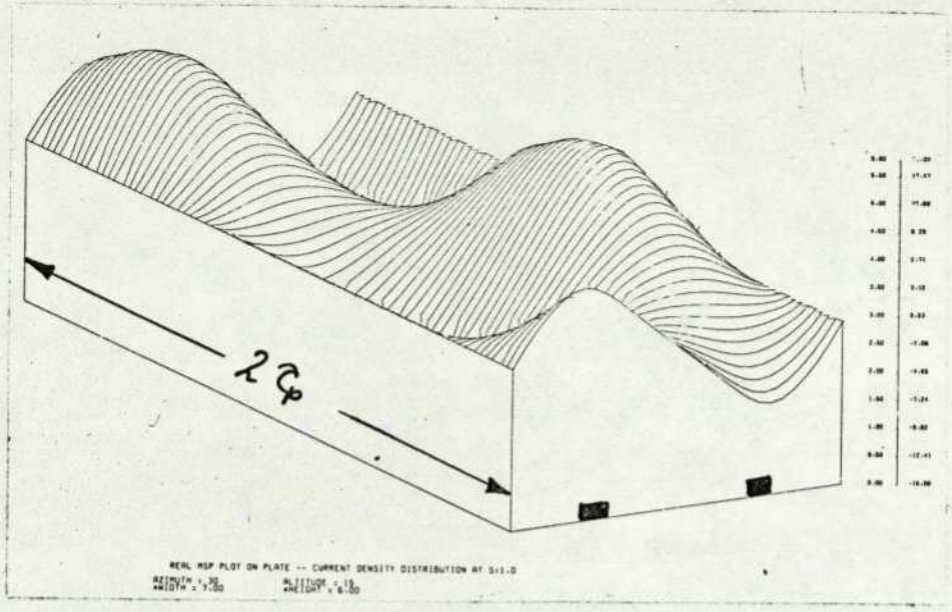

(a) Imaginary component. Normalising constant = 43.9

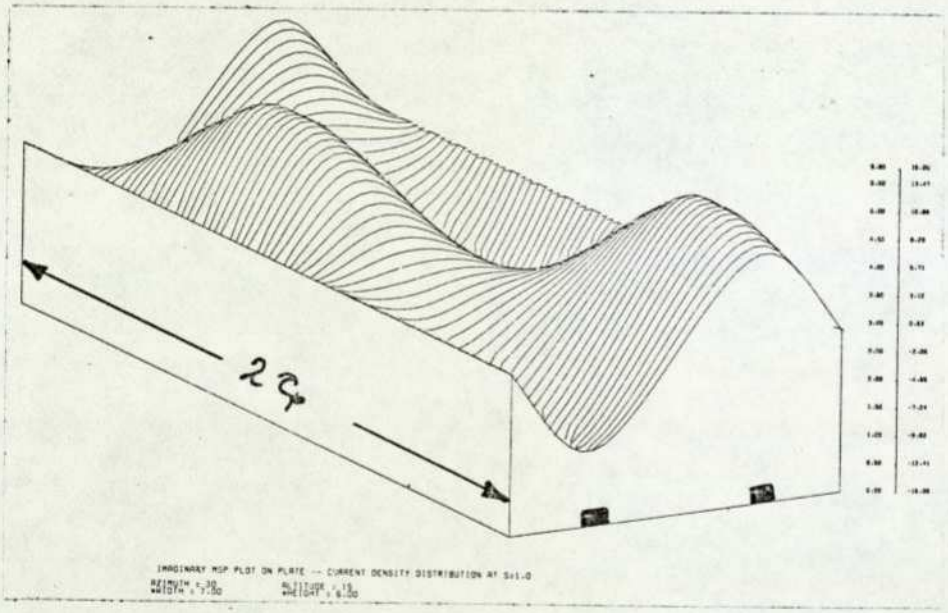

(b) Real component. Normalising constant = 45.3

Fig.5.17 Three-dimensional current density distribution in the secondary aluminium plate for two pole pitches. Secondary :SEC2. Slip = 1.0p.u.

to study the variation in the x-y plane. It is interesting to note that the ripple which was present in the diagram of Fig.5.11, for a plane very near to the surface of the plate has diminished considerably for a plane lying on the surface of the conducting plate. This is probably because the plate currents have a greater effect than have the energising currents on the flux density at the plate surface than happens at any other plane in the air gap away from the plate.

In Fig.5.18 the force density distribution calculated in the air-gap has been plotted. This on integration gives the total force but it is not the true stress distribution in the plate. To obtain a true stress distribution on the plate would require calculation of the magnetic stress tensor on the plate surface. This is often difficult, as indicated in Chap.3. The plots in Fig.5.18, however, suggest investigations into techniques of calculating stresses in the plate (which may not be required to be of uniform thickness along the width of the track, as seen from Fig.5.18(c)). Further discussions on the force density plots of Fig.5.18 have been made in the following section.

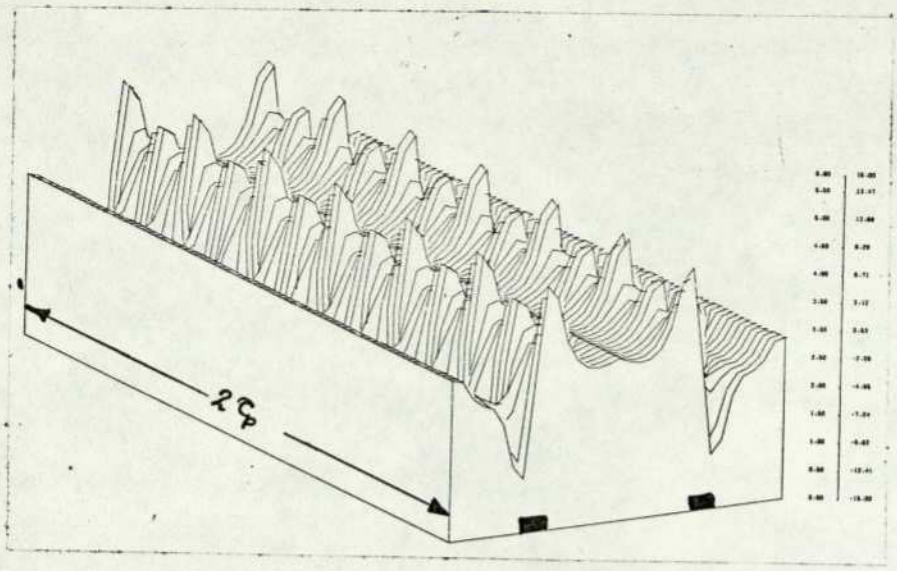

(a) Lateral guidance force density. Normalising constant = 50.2N/m^2

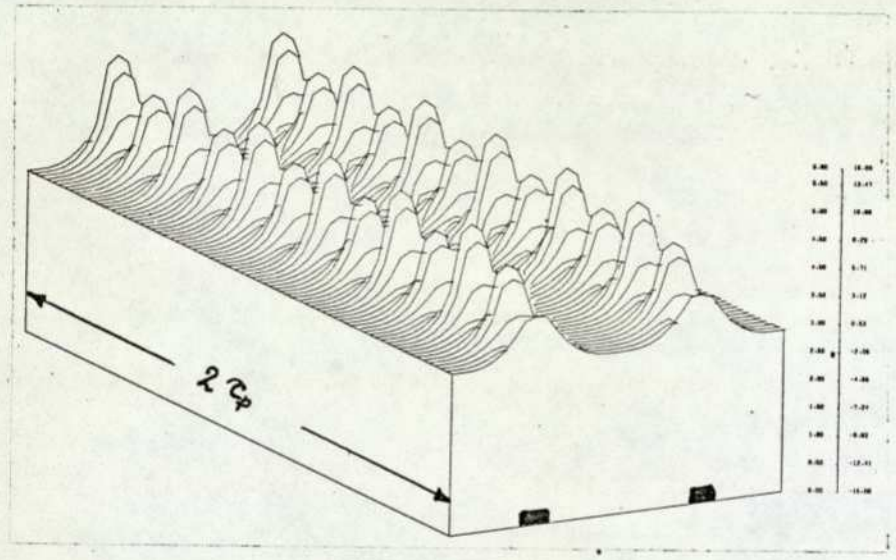

(b) Tractive force density. Normalising constant = 53.5N/m^2

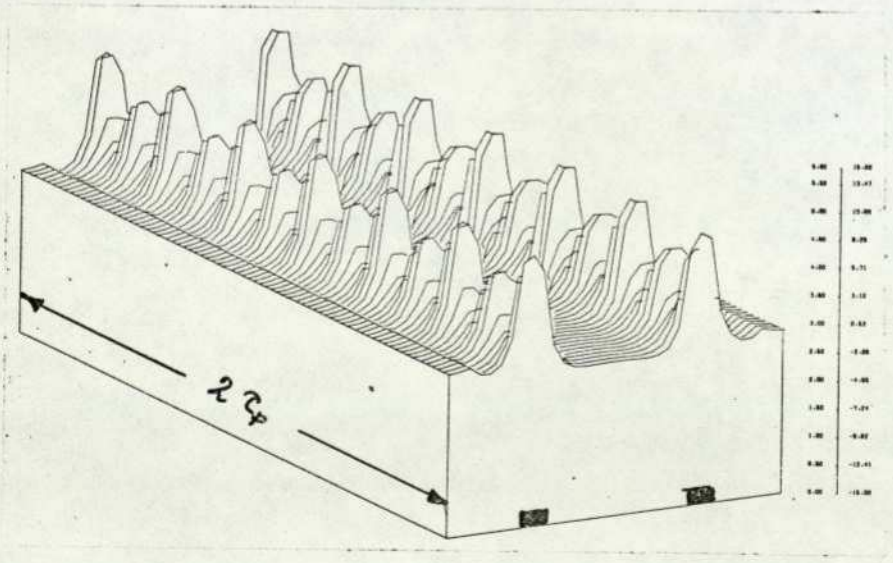

(c) Normal force density. Normalising constant = 115N/m^2

Fig.5.18 Force density distribution calculated in the air-gap.
(This is not true stress distribution in the plate.)

Secondary : SEC2. Slip = 1.0p.u.

5.6 DISCUSSION

In this chapter the flux densities and forces as obtained from the analysis of Chap.3 have been compared with those measured on the BTFCM. The correlation has been shown both under standstill and dynamic conditions and methods of improving the correlation are also discussed. Two- and three-dimensional plots of computed MSP, flux density, current density and force density distributions in the air gap region have been shown. They give a better understanding of the distribution of individual components and suggest means of improving the device.

The prime objective of the present work has been to obtain force characteristics similar to those described in Fig.1.2. The discussions on the computed results, presented in this chapter, are therefore mainly for the purpose of interpreting these results so as to deduce possibilities of obtaining the force characteristics described in Fig.1.2.

The force density plots shown in Fig.5.18 are for a case when the secondary member is placed symmetrically above the primary member, as shown in Fig.5.2. For this reason, as expected, plots are symmetrical about the centre of the primary member U-cores. The lateral guidance force density is zero on the centre of each limb of U-cores. It rises to a positive peak on the inner edge and a negative peak on the outer edge of the U-core limbs. In the event of the lateral displacement of the secondary member above the primary member from the symmetrical arrangement, the lateral guidance force density

distribution will re-distribute itself such as either to tend to keep the secondary member on the primary member or to tend to displace it still further. This will, of course, depend upon the displacement, the speed of operation, the operating 'entrefer' and, above all, on the configuration and design of the primary and secondary members.

The distribution of the tractive force density (as shown in Fig.5.18(b)) and the normal force density (as shown in Fig.5.18(c)) have their peaks on the centre of the U-core limbs. The normal force density changes sign outside the U-core limbs but the magnitude is low and therefore the resultant normal force, obtained after integrating over the surface discussed in Chap.3, remains attractive. Thus for levitation purposes the device requires, as expected, lesser iron surfaces and higher current carrying surfaces, in the primary and secondary members, facing each other. For traction purposes, however, as seen from Fig.5.18(b)), the requirements for obtaining high tractive force are opposite to those just mentioned for levitation purposes, viz. the increase in the iron surfaces for the same operating 'entrefer' and flux density. This is so because the device under discussion has a dominating vertical component of flux density (Bz). However, if the device is made such that the longitudinal and transverse components of flux density are relatively higher, then it might be possible (by suitable design) to obtain good levitation force together with high tractive and lateral guidance forces. The relative magnitudes of tractive and lateral guidance forces can then be controlled by suitably selecting the relative magnitudes of longitudinal and transverse components of flux

density. The arrangement thus will have resultant high-tangential and low-normal components of flux density in the space between the primary and the secondary members - a situation contrary to that in conventional rotary motors and the attraction type of electromagnet. This would increase the ampere-conductor loading in the device, for a 50Hz operation, and would be, naturally, the price paid for good levitation and lateral guidance forces for the same tractive force.

In the following chapter an improved model has been discussed for a secondary member consisting of a thick conducting sheet backed by iron which is partially saturated due to the eddy currents (discussed earlier in Sec.5.3).

CHAPTER 6

CHAPTER 6 MOTION OF A THICKER CONDUCTING PLATE WITH ITS BACKING IRON CARRYING EDDY CURRENTS

6.1. INTRODUCTION

In Chapter 3 the finite difference equations in terms of magnetic scalar potential were described for the motion of secondary members consisting of a thin conducting sheet backed by unsaturated iron, and in Chapter 5 the predicted results were compared with those measured on the BTFCM. The assumption of unsaturated iron implies that it is laminated such that the saturation does not occur due to eddy currents in the backing iron and the laminated stack is thick enough to carry flux from one pole to the other without saturating the iron. However, in practice a solid backing iron is used, for economic reasons, and this means that in effect it will be worked at or near saturation levels because the circulating eddy currents in the iron surface prevent the flux from penetrating into the backing iron and hence the saturation of a thin surface layer takes place. Thus the solid backing iron cannot be considered as infinitely permeable in the mathematical model, as was done in Chapter 3. In this chapter an improved mathematical model has been introduced to take into account the eddy current condition in the solid backing iron.

The saturation of only a thin surface layer of the solid backing iron mentioned above also implies that it would be wasteful to use other than a thin iron sheet equal to twice the surface layer depth, but as the speed increases, the depth of the layer increases as it is frequency (and therefore, slip) dependent. The iron sheet is then too thin and being saturated, is ineffective in carrying all the flux and so a significant proportion of it emerges as a leakage flux at the far side of the iron sheet. Under these conditions, the thin iron sheet is unsuitable as a backing medium. It follows, then, that the backing iron must have a certain minimum thickness for it to be effective over a fairly wide range of slip. However, instead of a single plate of iron, two thinner plates having a total thickness equal to that of the single plate is even more effective. Indeed, it is shown in this chapter that a composite backing iron, consisting of two mild steel plates having a thickness of only two thirds that of

a single plate is much more effective in preventing the flux from escaping from the other surface. This is important in connection with a transport system as a major cost of such a system is the track.

Another point, too, is that the aluminium plate used in practice will be thicker than the thin sheet considered in Chapter 3, and for the sake of completeness it is essential to modify the mathematical model to take this into account also. In thicker aluminium plates the electric vector potential $\overline{T}$ is not constant throughout the thickness of the conducting plate and therefore the plate cannot be modelled by a very thin plating of conducting material on the surface of the backing iron as discussed in Chapter 3. In this chapter an improved mathematical model is presented for modelling thicker aluminium conducting sheet.

6.2 MODELLING A THICKER CONDUCTING PLATE IN AN ALTERNATING FIELD

The behaviour of a conducting sheet, when eddy currents are induced in it due to an alternating field, depends to a large extent on the ratio of the sheet thickness (t) and the depth of penetration (d) at the operating frequency for that sheet material. This $\frac{t}{d}$ ratio decides the variation in the current density from one surface of the conducting sheet to the other. When the ratio is small, such that the variation in the current density with respect to the depth is negligible, the currents along x and y directions (and passing through elementary widths dy and dx respectively) are given by

$$I_x = J_x.t.dy, \text{ and}$$
$$I_y = J_y.t.dx, \qquad 6.1$$

and the respective components of surface current densities are given as

$$K_x = J_x t$$
$$K_y = J_y t \qquad 6.2$$

where J_x and J_y are current densities along x and y directions respectively, and t is the thickness of the conducting sheet.

However, when the $\frac{t}{d}$ ratio is larger the current density changes from one surface of the conducting sheet to the other. The surface current density is, therefore, obtained by integrating the current density across the conducting sheet thickness.

It should here be stressed that the thickness of the plate is such that, whilst allowing for a change in both magnitude and angle of the current density within the plate, it is still sufficiently thin for the direction of the current density to remain unaffected. The complexity of trying to allow for thicker plates than this can be seen by considering such works as that of Stoll [68]. In practice, this is no severe limitation since cost considerations alone prohibit the use of thicker plates than that considered here.

Assuming the material of the conducting sheet to be linear and homogeneous, the surface current densities (from Appendix F) are given by

$$K_x = \frac{\lambda}{2} \left[J_{bx} + J_{tx} \right]$$

$$K_y = \frac{\lambda}{2} \left[J_{by} + J_{ty} \right] \qquad 6.3$$

where suffixes b and t denote the bottom and the top surfaces of the conducting sheet, and

$$\lambda = \frac{1}{\gamma} \tanh (\gamma t) \qquad 6.4$$

$$\text{where } \gamma = \frac{1 + j}{2d} \quad \text{and} \quad d = \sqrt{\frac{2}{\omega \sigma \mu}} \qquad 6.5$$

Therefore,

$$\gamma t = \left(\frac{1 + j}{2}\right) \frac{t}{d} = \frac{t}{2d} + j \frac{t}{2d} \qquad 6.6$$

Comparing eqns. 6.2 and 6.3, λ can be defined as the 'effective thickness' which corresponds to the thickness of an equivalent conducting sheet in which the current density is made to be constant in magnitude and phase angle through the depth and equal to the average of the current densities on the bottom and the top surfaces of the original conducting sheet (eqn.6.3). Thus from eqn.6.4

$$t_{(\text{effective})} = \frac{1}{\gamma} \tanh (\gamma t) \qquad 6.7$$

For $\frac{t}{2d} < 0.2$, $\tanh (\gamma t) \simeq \gamma t$ (within 2 per cent)

and therefore

$$t_{(\text{effective})} \simeq \frac{1}{\gamma} \cdot \gamma t \simeq t \qquad 6.8$$

This corresponds to the case when the variation of current density through the depth of the conducting sheet is negligible and the $\frac{t}{d}$ ratio for the condition quoted with regard to eqn.6.8 is 0.4.

On the other hand, when

$\frac{t}{2d} > 3.3$, $\tanh (\gamma t) \simeq 1.0$ (within 2 per cent) and

therefore

$$t_{(\text{effective})} \simeq \frac{1}{\gamma} \simeq 2d \angle -45^{\circ} \qquad 6.9$$

and the $\frac{t}{d}$ ratio is 6.6, the assumption being that the current is (very closely) confined to layers parallel to the flat faces of the plate. So for $0.2 < \frac{t}{2d} < 3.3$ the effective thickness varies from t to $\sqrt{2}d \angle -45^{o}$ in accordance to eqn.6.7

The conducting sheets used in the present work have a $\frac{t}{d}$ ratio equal to or less than 0.225, which is less than 0.4 and therefore the representation of the conducting sheet, so far, by a thin plating on the surface of the backing iron in the mathematical model is valid. However, when the thickness is large, such that the $\frac{t}{d}$ ratio is greater than 0.4, the conducting sheet requires an improved modelling. One way of doing it is to express the effective thickness of the conducting sheet by eqn.6.7 and the surface current density by eqns. 6.2 and 6.3. However, in doing so the same current is put in a small section (in the form of a very thin plating on the iron surface) and therefore the corresponding current density $\bar{J}$ increases. This can be expressed analytically by the following expression [67]

$$K = \lim_{\substack{\bar{J}\to\infty \\ t\to 0}} \bar{J}\, t_{(\text{effective})} \qquad 6.10$$

$$(\text{effective})$$

where $\bar{J} = \hat{a}_x J_x + \hat{a}_y J_y$ 6.11

$$\bar{K} = \hat{a}_x K_x + \hat{a}_y K_y$$

It follows from eqn.6.10 that representing a thick plate by an infinitesimally thin layer in the mathematical model creates a current-free space which increases with the plate thickness. The error caused by the creation of this current free space is similar to the discretisation error in a finite difference method, and it becomes severe when the internode spacing (h) in the numerical model is comparable with the conducting plate thickness(t). This problem can,however, be overcome by describing the thick conducting sheet in a suitable multi-layer model as discussed below. This way of representing a conducting sheet in the

mathematical model is particularly useful when the material is non-linear like partially saturated solid iron. Each layer can then be given a different permeability and thereby approximate the varying degree of saturation within each layer of the model. This, of course, applies to thin as well as thicker sheets. The modelling of very thick sheets ($\frac{t}{d} > 1.0$, say) by a multilayer system, however, assumes that the current distribution does not deviate substantially from the simple one associated with thin plates.

6.2.1 Multi-layer model

When the field problem is solved in terms of magnetic scalar potential, the current density distribution in the conducting sheet is expressed as a curl of the electric vector potential ($\overline{T}$). So far, in Chapter 3 and in this chapter, the electric vector potential has been assumed not to vary with depth within the sheet because in the BTFCM only thin conducting sheets were used. In thicker conducting sheets, however, the electric vector potential changes with the depth and therefore, as discussed above, the sheet cannot be replaced in the mathematical model by a very thin plating on the surface of the backing iron. Instead, the thick conducting sheet can be represented by a number of thin conducting slices such that the electric vector potential in each slice is uniform through its thickness. In effect, all the slices taken together are then equivalent to a 'laminated-conducting-plate'. A four-layer model developed for a thick conducting sheet is now presented, and it can be incorporated in the computer programme developed so far, when the occasion arises.

Fig.6.1 shows a secondary member comprising a thick conducting sheet that has been sliced into four. The modelling of slice 1 is similar to that for the thin conducting sheet. As slices 2, 3 and 4 are not backed by iron, each must be modelled as an 'isolated conducting sheet'[47] where the magnetic scalar potential of nodes on each side of the slice are evaluated simultaneously. In Chapter 3 the network molecule for a general node on an isolated conducting sheet was described and the equations obtained for nodes lying on each side. However, when the nodes lie at an edge of the slice, their network molecule and the corresponding equations are different. This is so because the edge of each slice forms a line on one side of which the currents are zero and on the other side non-zero. Since the plate is not connected electrically to anything else, the total current flow through the section is zero, and therefore the condition $T_z = 0$ at each edge is satisfied. This implies that the magnetic scalar potentials at the edge nodes on the top and bottom surfaces of slice 2,3 and 4 are equal, and so they can be replaced by a single node for each

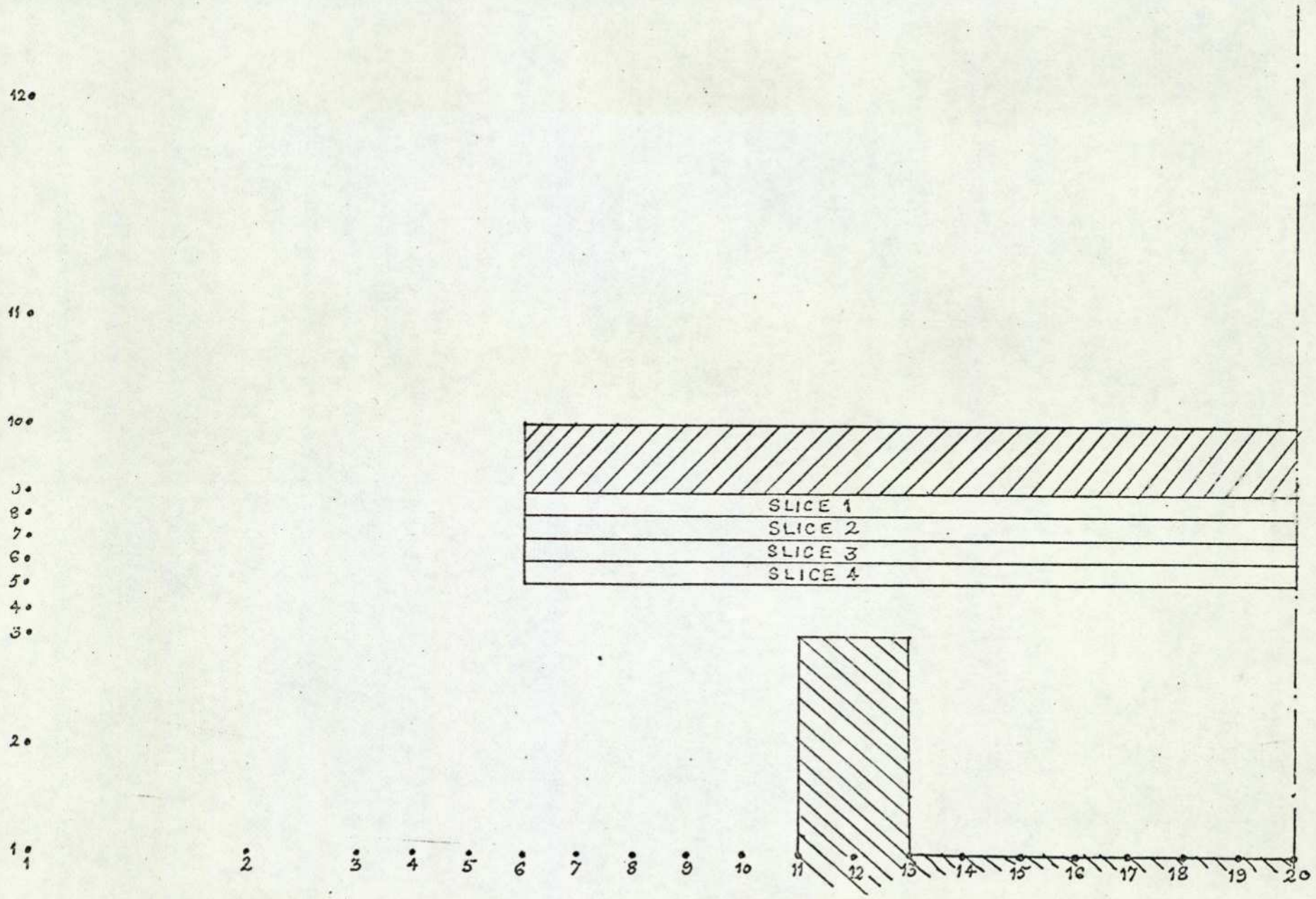

Fig.6.1 Description of the four slices of the thick conducting sheet for the mathematical model

slice as shown in Fig.6.2. On applying the continuity condition at node 'O' in Fig.6.2, the finite difference equation for the edge nodes is

$$\frac{\omega C_{m1}}{2}(U_{1T} - U_o) + \frac{\omega C_{m1}}{2}(U_1 - U_o) + \omega C_{m2}(U_2 - U_o)$$

$$+ \omega C_{m3}(U_3 - U_o) + \omega C_{m5}(U_5 - U_o) + \omega C_{m6}(U_6 - U_o) = 0 \qquad 6.12$$

where $\omega = 2\pi f$,

C_{m1}, C_{m2}, C_{m3}, C_{m5} C_{m6} are magnetic capacitances, and U's are magnetic scalar potentials at the nodes described in Fig.6.2.

Thus the multi-layer magnetic network model, for a thick conducting sheet, on the basis of the foregoing discussions is as drawn in Fig.6.3. The thick conducting sheet has been divided into four slices and it has been modelled for the case when it is backed by solid iron, which carries eddy currents and is saturated as a direct consequence of these eddy currents. The representation of eddy currents and saturation (as a direct consequence of these eddy currents) in the solid iron is discussed in Sec.6.4.

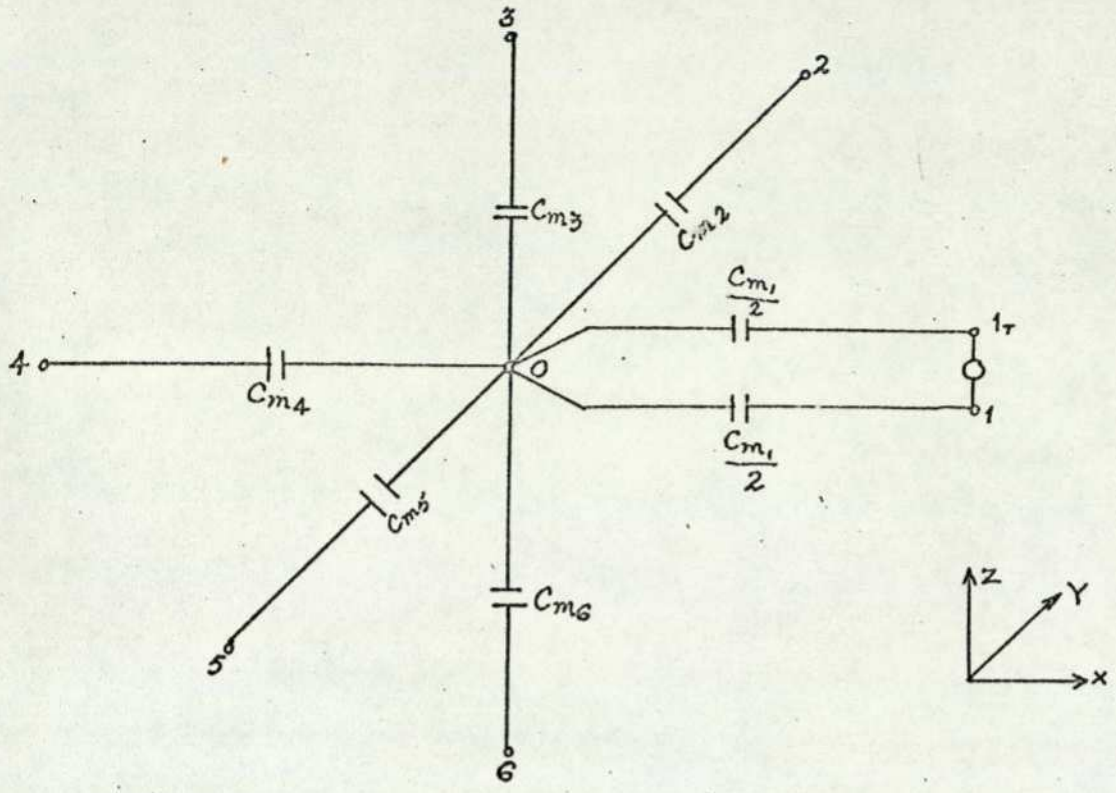

Fig.6.2 Network molecule for nodes lying at the edge of a slice

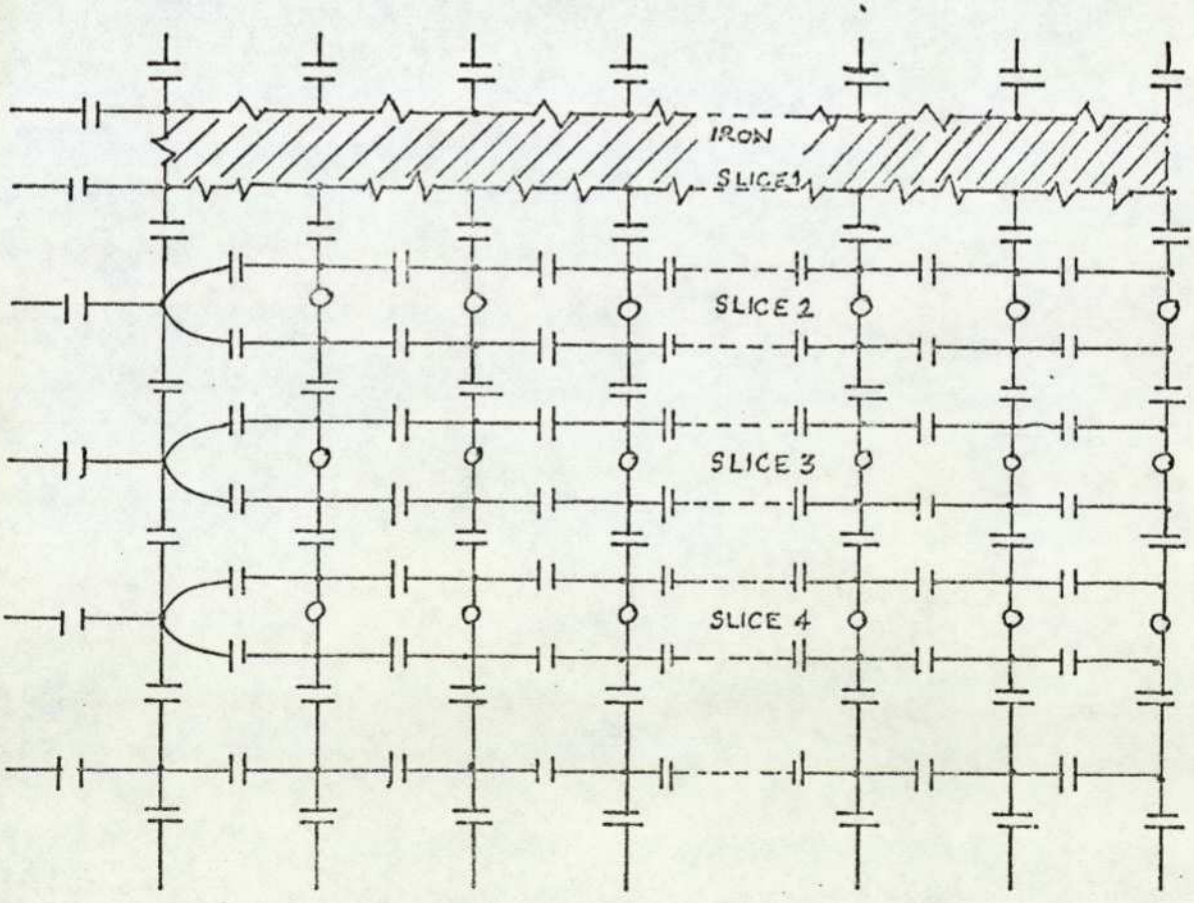

Fig.6.3 Network model for a four layer model of a thick conducting sheet

6.3 FLUX PENETRATION IN SOLID BACKING IRON BEHIND ALUMINIUM REACTION RAIL

The use of solid backing iron, instead of the laminated type, is desirable from both the cost and the mechanical strength points of view. Its use, however, makes the prediction of flux densities and forces produced difficult primarily because in the analysis the backing iron cannot be assumed infinitely permeable even when the flux density normal to the iron surface is low. This is so because the alternating flux after meeting the solid iron surface induces in it eddy currents, which tend to prevent the main flux from penetrating into the iron beyond a saturated layer close to the iron surface. Any further increase in the incident flux increases the layer thickness since the flux density in the layer can have only a small increase beyond the saturation level. The effect of this behaviour of the solid backing iron in an alternating field on the mathematical model is dealt with in the next section.

Another aspect of the cost consideration is that the thickness from the magnetic circuit point of view, should be just sufficient to carry the flux from one pole to the next whilst being thick enough, if necessary, to ensure mechanical rigidity. This is so with solid iron because, as can be seen from Fig.6.4[66], most of the flux is confined to a saturated layer close to the iron surface. Thus there is a region A in the backing iron which remains virtually flux-free. It reduces with the thickness of backing iron and for a good design becomes small but sufficient to accommodate any increase in flux beyond the designed limit. If the iron thickness is reduced beyond this limit the flux at B, pushing out of the top surface, increases rapidly. This was also observed during an experimental investigation into the behaviour of three types of backing iron (described in Fig.6.5). The backing iron BI3 was laminated in a direction normal to that of the flux flow and during each study the entrefer and the primary excitation were kept constant. The presence of flux at B was studied, for each type of backing iron, by measuring normal flux density along x-x above their top surfaces. These have been plotted in Fig 6.6. For comparison the flux density at location C has also been recorded.

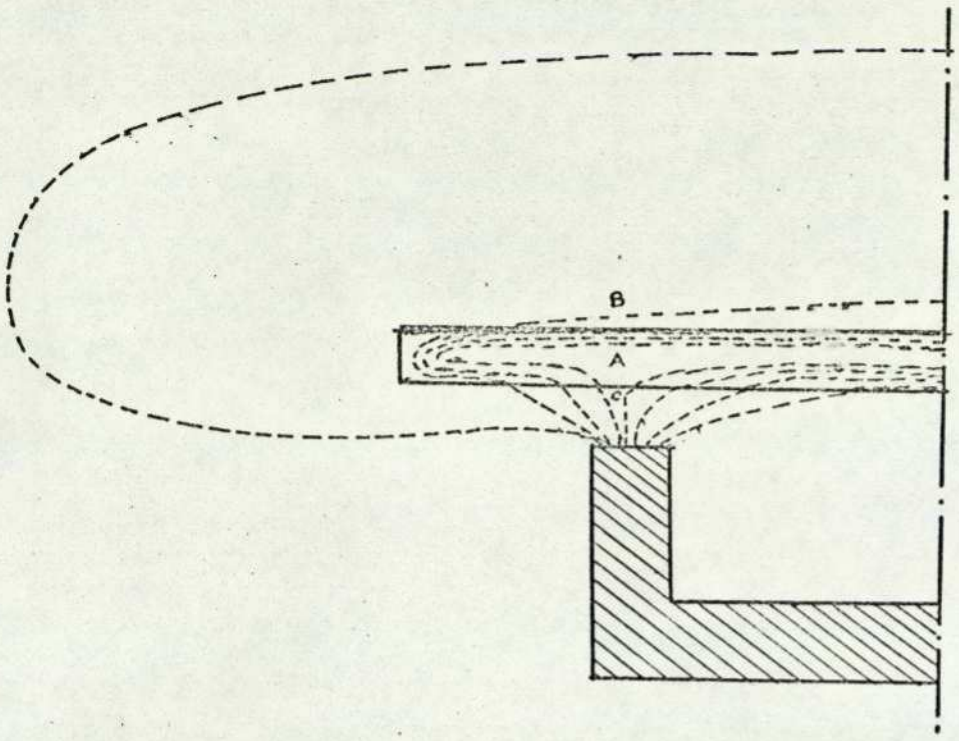

Fig.6.4 Flux distribution around a solid iron in an alternating field

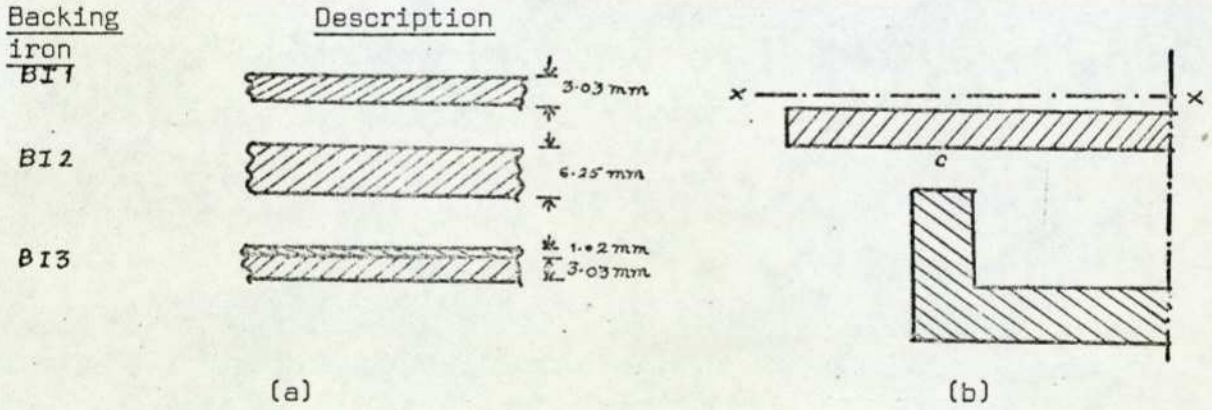

Fig.6.5 Backing iron arrangements used in the study and the line x-x along which normal flux densities were measured

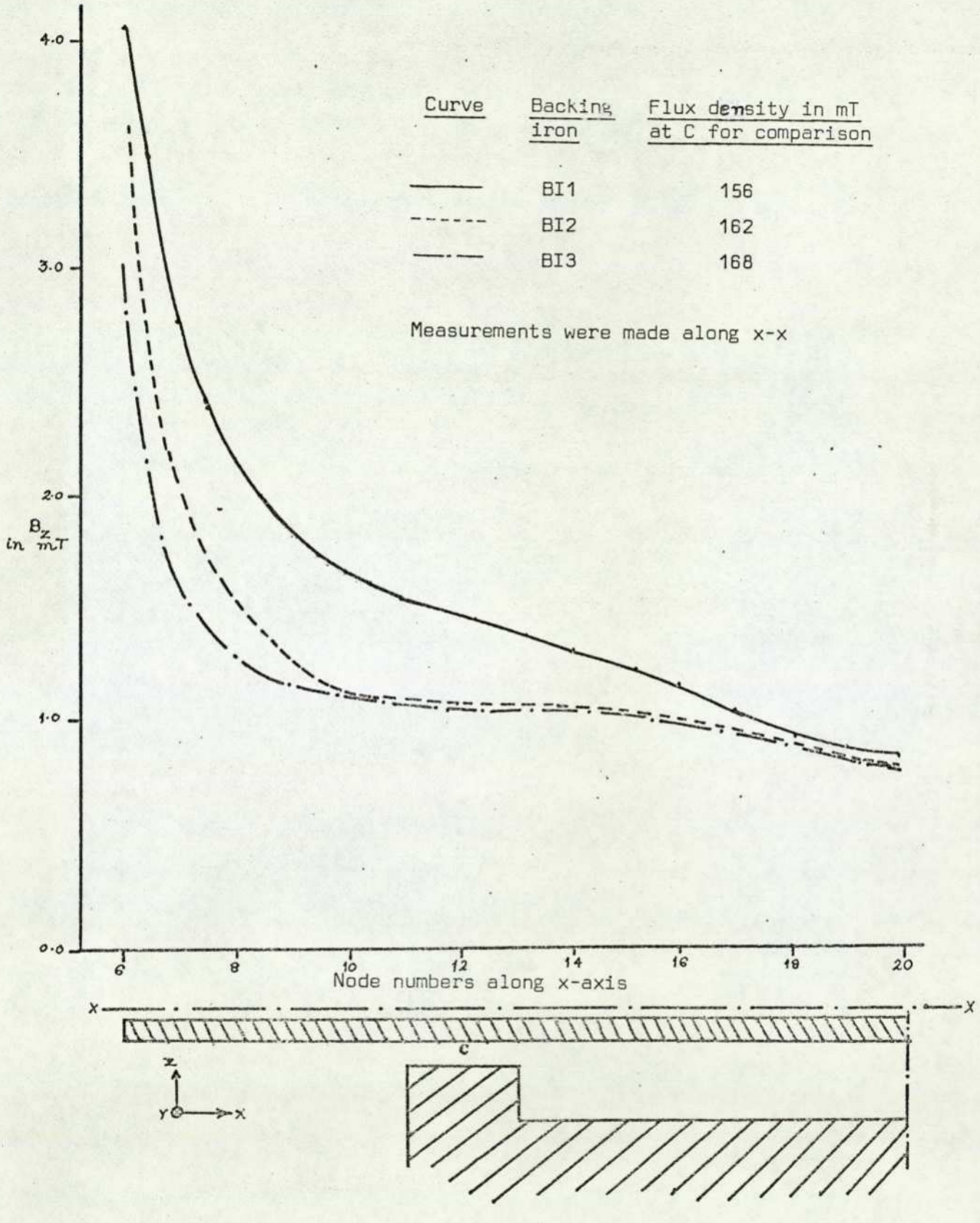

Fig.6.6 Z-component of flux desity along line x-x

From Fig.6.6 it is evident that the solid backing iron behaves in the manner discussed earlier with regard to the flux distribution within it as given in Fig.6.4. The product of conductivity and relative permeability of solid backing iron is typically 1000MS/m (for $100 < \mu_r < 200$ and $5 < \sigma_i < 10$ MS/m), and this gives a depth of penetration at 50Hz of 2.25 mm. Therefore, for a negligible flux free region A the backing iron thickness should be at least 4.5mm for the assumed conductivity and relative permeability of the iron. The thickness of the backing iron BI1 is less than, whilst that of BI2 is greater than this desirable minimum. Therefore, the flux at B is larger in the case of BI1.

However, although BI3 is thinner than BI2, the flux at B is actually less than the case for BI2. This arises because BI3 is a composite plate and, therefore, some of the flux in the bottom plate of BI3, when reaching the interface between the two plates, is allowed to penetrate into the interior of the composite plate as shown in Fig.6.6(a). So less flux actually passes round to the back surface of the composite plate and therefore less flux leaves it to pass into the air.

From the foregoing discussion, a selection of a suitable thickness of the solid backing iron involves, amongst others, a compromise between the amount of flux at B, coming out of the top surface of the backing iron, and its thickness. Further, the flux density at location C in each case was of the same order and, therefore, Fig.6.6 indicates a possible saving in the total iron thickness by using a composite backing iron of the type BI3 described in Fig.6.5, provided there is adequate mechanical rigidity.

The above experimental study and discussions also conclude that the flux paths around the secondary backing iron are as drawn in Fig.6.4. In the following section the effect of flux penetration in a solid backing iron in an alternating field has been modelled mathematically. The computed flux paths presented in Sec.6.6 have been obtained using the mathematical model described in Sec.6.4 and the resulting plots given in Fig.6.14 show similarity to those drawn in Fig.6.4.

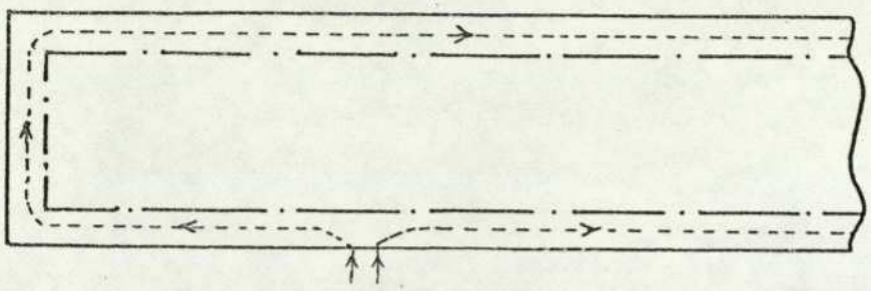

(a) Single solid iron plate

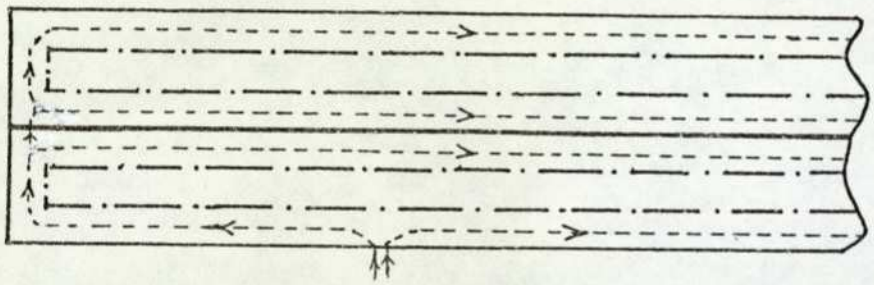

(b) Composite solid iron plate

Fig.6.6(a) Difference in flux paths in a single solid plate and a composite plate backing iron

6.4 MATHEMATICAL MODEL OF EDDY CURRENTS AND SATURATION (AS A CONSEQUENCE OF EDDY CURRENTS) AT THE SURFACE OF THE BACKING IRON

When an alternating flux strikes against an iron surface its penetration into the iron can be classified into three modes [65]. In Fig.6.7 these modes of flux penetration are shown for laminated and solid iron. As is evident from the experimental results of Sec.6.3 and also Fig.6.7, only a mode 2 flux penetration takes place in solid iron. This mode of penetration, like that for the mode 3 flux is quite different from the type of penetration associated with mode 1 flux in that these modes are intimately related to the eddy currents in the plate. The mode 1 flux, however, is not related to eddy currents and it also does not give rise to a power loss of the nature important in this study. The power loss (both hysteresis and eddy current) associated with the mode 1 flux, as discussed in undergraduate magnetic circuit problems even when present (e.g. in the U-cores) is negligible. The mode 2 flux, associated with the solid iron, after entering the plate turns to run parallel to the surface either to the left or right as shown in Fig.6.4 at point C. This is so because the eddy currents induced in the iron surface due to the alternating flux striking against it, prevent the flux from penetrating much beyond the depth of penetration (d), the iron within the depth being saturated. Thus, the flux in the mode 2 flux penetration is confined to surface layers and, therefore, the solution can be obtained by simply considering the conditions at the surface. This can be done in a magnetic network model by describing the properties of these surfaces by a single layer of nodes where the internode magnetic impedance is given by [65]

$$Z_{im} = (1-j)\sqrt{\frac{\sigma_i}{2\omega\mu_i}} \qquad 6.13$$

where σ_i and μ_i are the tangential conductivity and permeability of the backing iron, and

$\omega = 2\pi f$, where f is the frequency of operation.

The magnetic impedance given by eqn.6.13 is in parallel with the magnetic impedance due to the surrounding space to account for the tangential field. When this iron surface is behind a conducting sheet the effective magnetic impedance is

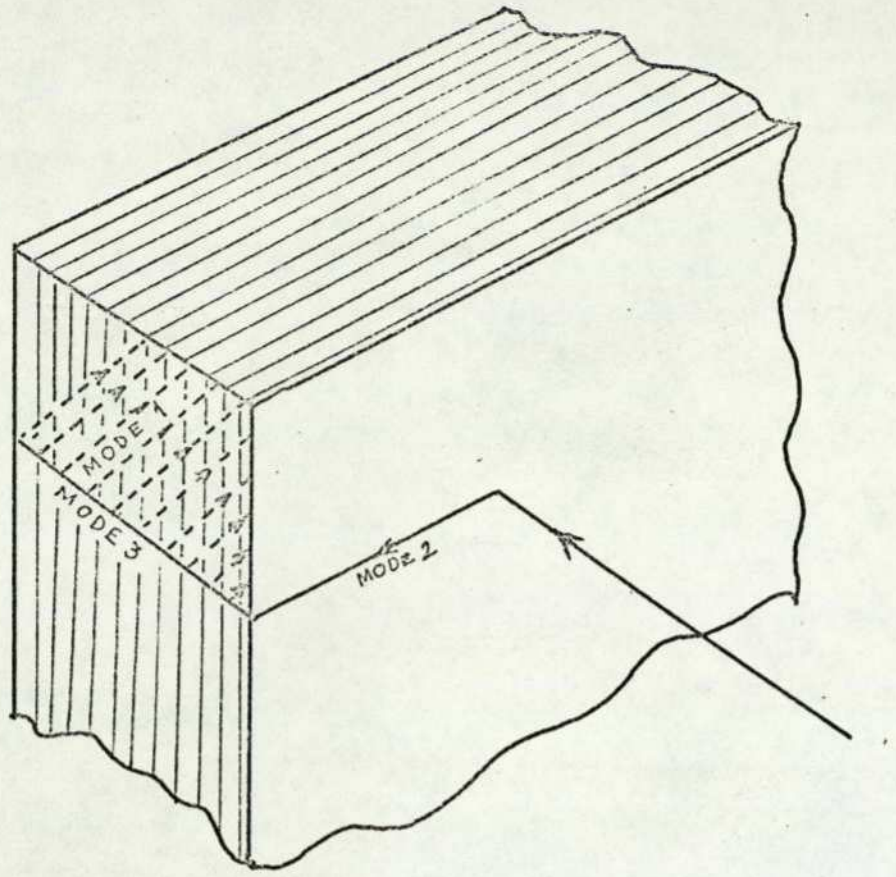

(a) Laminated iron

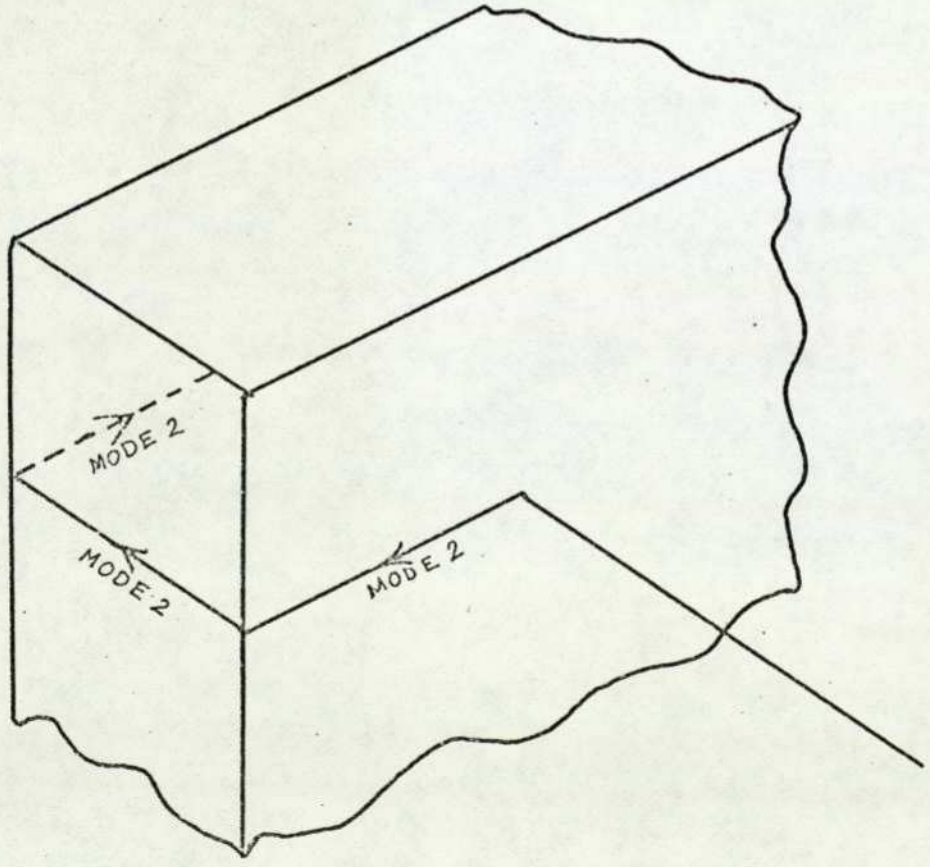

(b) Solid iron

Fig.6.7 Flux penetration modes in laminated and solid iron

represented by connecting in series the magnetic impedance due to the backing iron and that due to the conducting sheet. (This is so because electrically the conducting sheet and the backing iron are connected in parallel.) The combined magnetic impedance also has a component due to the surrounding space to account for the tangential flux. Thus the network model for the secondary member (consisting of thin conducting sheet backed by a solid iron which carries eddy currents) can be described by Fig. 6.8. In the network model no account has been made of the iron beneath the iron surface since, as pointed out earlier, it carries no flux. This also implies that the magnetic scalar potential in this region is constant throughout, the most probable value of the magnetic scalar potential being zero because the line of symmetry, between the two limbs of the U-core, also lies in this region.

6.4.1 Description of the network model

The network model drawn in Fig.6.8 is different from that used in Chapter 3 especially at the top surface and at the edges of the secondary member. The magnetic impedance of the bottom surface, which also contains an aluminium conducting sheet, has now become $(Z_p + Z_i)$ to account for the eddy currents in the backing iron. Similarly, for the top surface, which has no aluminium plate, the magnetic impedance is given by Z_i alone. The network molecules for nodes lying in the bottom surface and in the top surface (except those lying at the edges) of the secondary member are given in Fig.6.9(a) and (b) respectively.

In Chapter 3, the magnetic scalar potential of nodes lying at the edges of the secondary member were kept constant at zero value, because of the assumption that the currents exist only in the aluminium sheet. However, when the eddy currents in the solid backing iron are also taken into consideration, the situation becomes such that the currents at the edges can now find a closed path as described in Fig.6.10(a). Thus, zero constant value magnetic scalar potential condition, along the edges of the secondary member, is no longer necessary. Instead the

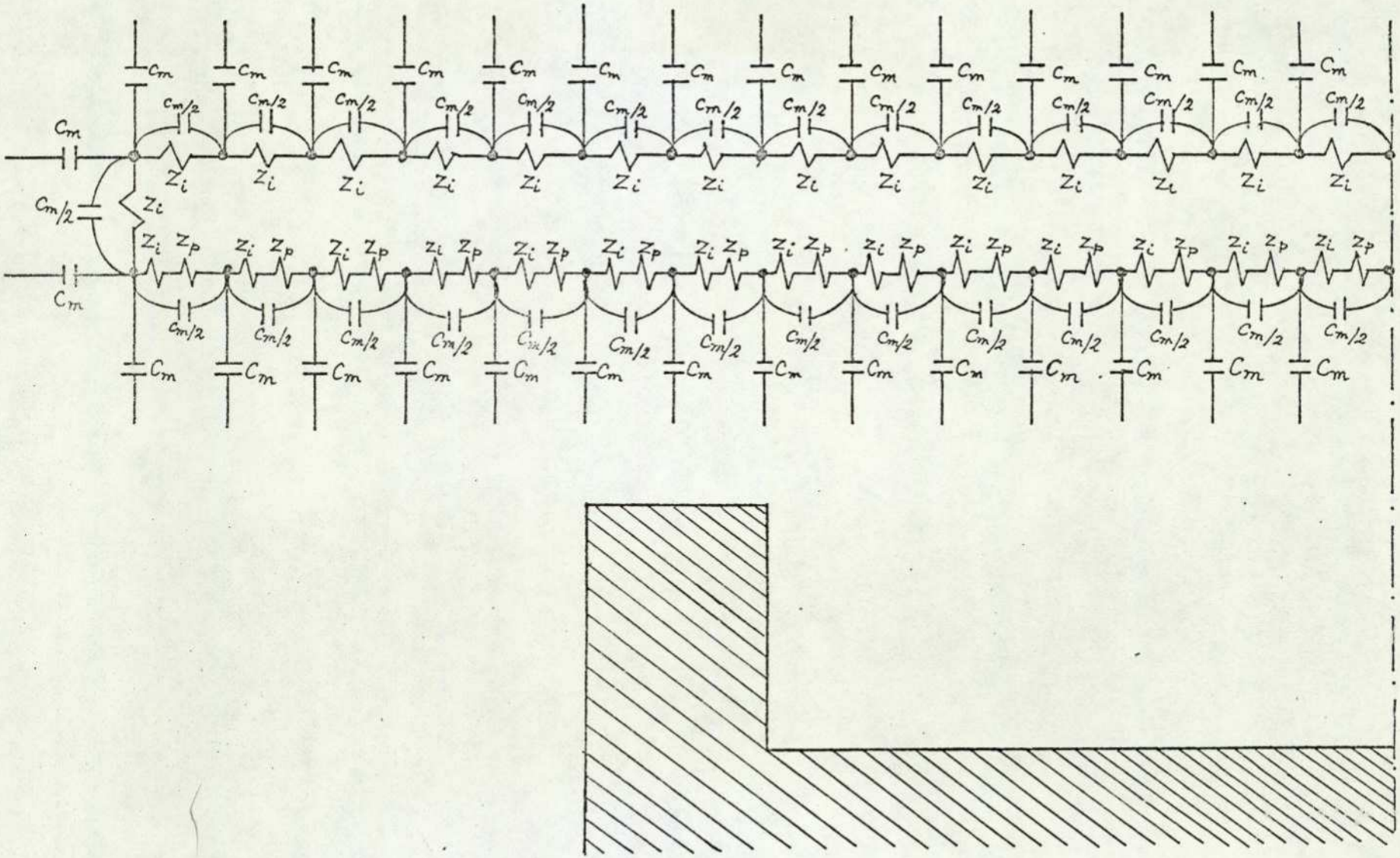

Fig.6.8 Network model for a secondary member consisting of a thin aluminium sheet backed by a partially saturated (due to eddy currents) solid iron

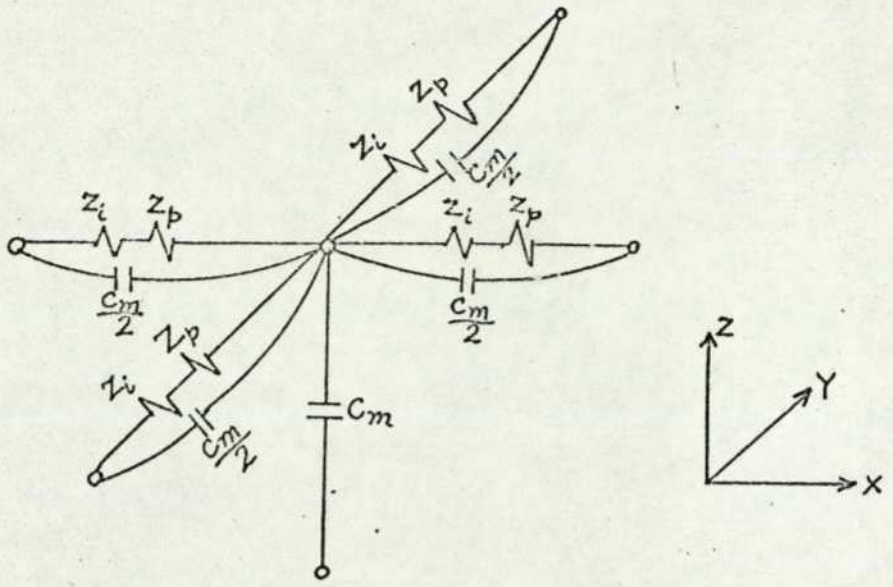

(a) Nodes on the bottom surface

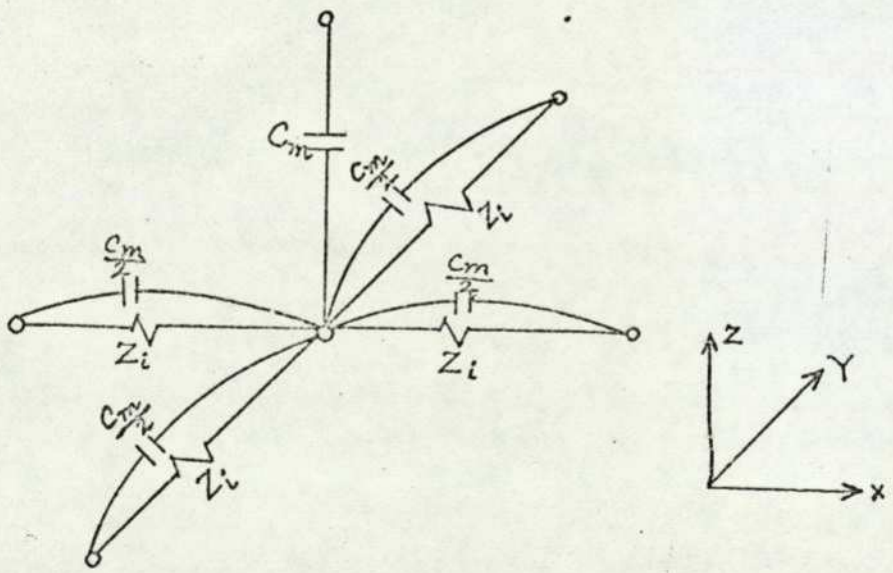

(b) Nodes on the top surface

Fig.6.9 Network molecule for nodes lying on the bottom surface and on the top surface (except at the edges) of the secondary member

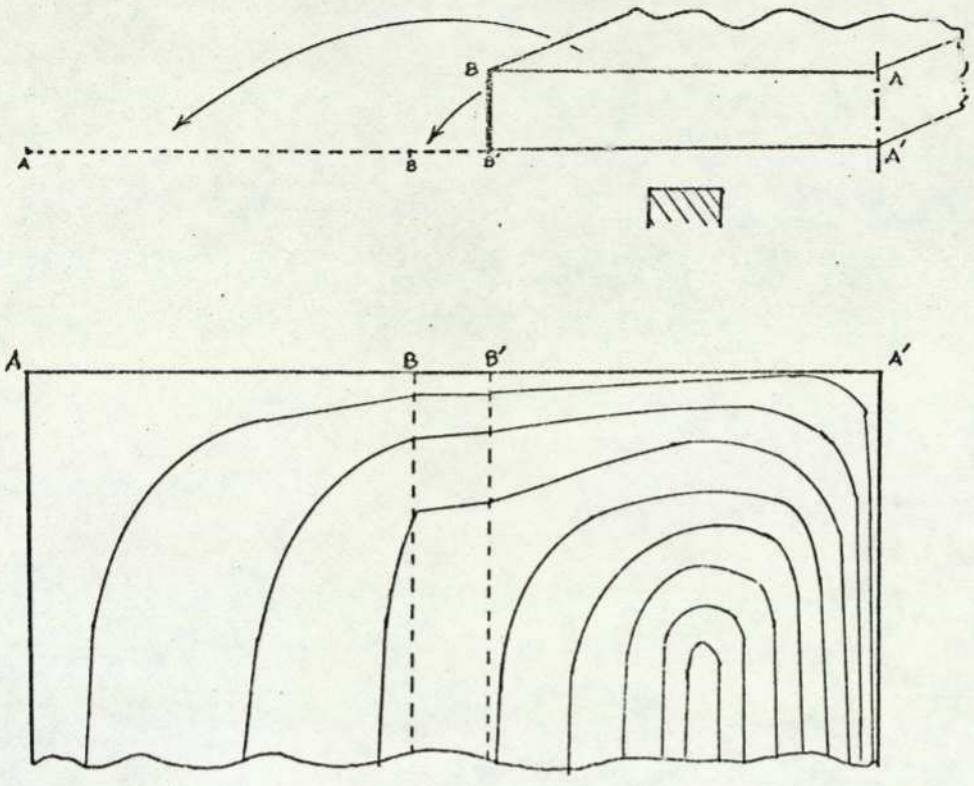

(a) Currents in the developed surface of the secondary member

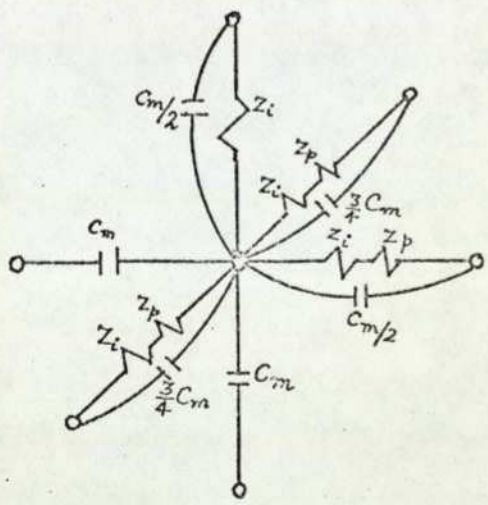

(b) Bottom surface

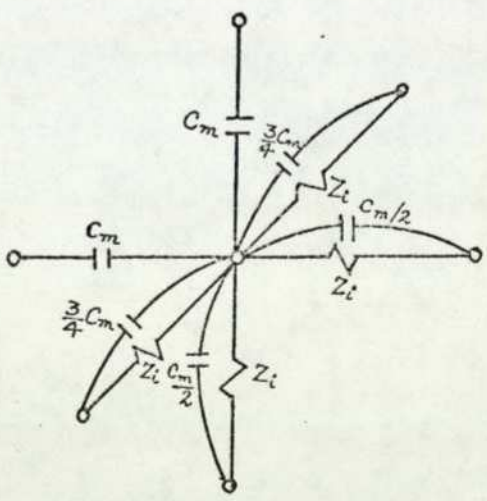

(c) Top surface

Fig.6.10 Network molecules for nodes lying at the edge of the secondary member

magnetic scalar potential at these edge nodes can be obtained by solving appropriate network molecules described by Fig.6.10(b).

6.5 ACCOUNTING FOR SPEED EFFECT IN SOLID IRON

Fig.6.8 gives the network model of a secondary member consisting of a thin conducting sheet backed by a solid backing iron, the latter being partially saturated as a direct consequence of the eddy currents due to the alternating flux. When this secondary member moves in the alternating field, the flux striking against the secondary member surface changes with respect to time not only because of the alternating nature of the flux but also because of the spatial variation. These two variations of flux density ($\overline{B}$) with respect to time can be expressed as

$$\nabla \times \overline{E}_{ac} = -\dot{\overline{B}} = -\frac{\partial \overline{B}}{\partial t} = -\alpha \overline{B} \qquad 6.14$$

and, for a constant speed motion,

$$\nabla \times \overline{E}_{\text{motion}} = \nabla \times \overline{v} \times \overline{B} = -v_y \frac{\partial \overline{B}}{\partial y} = -\beta \overline{B} \qquad 6.15$$

where $\alpha = \frac{1}{\overline{B}} \cdot \frac{\partial \overline{B}}{\partial t}$, and 6.16

$$\beta = \frac{v_y}{B} \cdot \frac{\partial \overline{B}}{\partial y} \qquad 6.17$$

Therefore, the net $\nabla \times \overline{E}$ due to variation in $\overline{B}$ with respect to time, as seen by the secondary member, is given as

$$\nabla \times \overline{E} = \nabla \times \overline{E}_{ac} + \nabla \times \overline{E}_{\text{motion}}$$

$$= -(\alpha + \beta)\, \overline{B} \qquad 6.18$$

The current density distribution in the secondary member is given by

$$\overline{J} = -\sigma \overline{E} \qquad 6.19$$

Taking the curl of both sides and substituting for $\nabla \times \overline{E}$ from eqn.6.18

$$\nabla \times \overline{J} = -\sigma (\nabla \times \overline{E}) = -\sigma(\alpha + \beta)\overline{B} \qquad 6.20$$

taking the curl of both sides of eqn.6.20, and substituting $\nabla \times \overline{B} = \mu J$ and assuming constant μ, we obtain

$$\nabla^2 \overline{J} = \mu\sigma(\alpha + \beta)\, \overline{J} \qquad 6.21$$

where $\nabla.\bar{J}$ has been assumed zero because ρ is zero within the conductor.

Writing

$$\mu\sigma(\alpha+\beta) = 4\gamma^2 \qquad 6.22$$

eqn. 6.21 becomes

$$\nabla^2\bar{J} = 4\gamma^2\bar{J} \qquad 6.23$$

giving a diffusion equation similar to eqn. F.4. For a homogeneous and linear medium, the surface current density is

$$\bar{K} = \frac{\lambda}{2}(\bar{J}_b + \bar{J}_t) \qquad 6.24$$

where $\bar{K}$, $\bar{J}_b$ and $\bar{J}_t$ are defined in Appendix F, and

$$\lambda = \frac{1}{\gamma}\tanh(\gamma t) \qquad 6.25$$

where γ is given by eqn.6.22 and t is the thickness of the conducting sheet.

Thus from eqns. 6.24 and 6.25 the effective thickness of the conducting sheet is obtained as below. When the conducting sheet is thin, such that $\frac{t}{2d}$ <0.2 then from eqn.6.24 (where $\tanh(\gamma t)\simeq\gamma t$ for $\frac{t}{2d}$ <0.2)

$$t_{(\text{effective})} \simeq \frac{1}{\gamma}\gamma t$$

or

$$t_{(\text{effective})} \simeq t. \qquad 6.26$$

When the conducting sheet is thick such that $\frac{t}{2d}$ >3.3, $\tanh(\gamma t)\simeq 1.0$ and

$$t_{(\text{effective})} \simeq \frac{1}{\gamma} \simeq 2\sqrt{\frac{1}{\mu\sigma(\alpha+\beta)}}$$

again assuming currents parallel to the surface of the conducting sheet. Further, when the normal component of the field varies from a maximum just outside the surface to zero under the surface layer (as shown in Fig.6.4) the current density likewise diminishes from a maximum at the surface to zero at the far side of the surface layer.

For a homogeneous and linear medium, the surface current density (from eqn. 6.24 by putting $\bar{J}_t = 0$) is given as

$$\bar{K} = \frac{\lambda}{2} \bar{J}_b \quad , \qquad 6.28$$

from which, for a small d, the effective thickness is given by

$$t_{(effective)} = \frac{\lambda}{2} \simeq \sqrt{\frac{1}{\mu\sigma(\alpha + \beta)}} \qquad 6.29$$

The surface magnetic impedance, in each case, is obtained by multiplying the surface conductivity (σ)by the effective thickness. Thus (see Appendix G)

$$Z_m = \sigma t_{(effective)} \quad . \qquad 6.30$$

which is like that for the aluminium plate used in the present work, where the magnetic impedance is given by

$$Z_{ma} = \sigma_a t_a \qquad 6.30(a)$$

and the suffix a stands for "aluminium plate".
However, in the case of solid iron the eddy currents are confined to the surface layer and they vary from a maximum on the surface to zero beyond the layer, and therefore, on the assumption that the behaviour of iron is linear and that the saturation remains constant, the effective thickness is given by eqn.6.29 and the corresponding magnetic impedance is

$$Z_{mi} = \sigma_i \sqrt{\frac{1}{\sigma_i \mu_i (\alpha + \beta)}}$$

$$= \sqrt{\frac{\sigma_i}{\mu_i (\alpha + \beta)}} \qquad 6.31$$

where α and β are given by eqns.6.16 and 6.17, and suffix i stands for iron.

If the variation of $\bar{B}_{ac}$ with respect to time is defined as

$$\bar{B}_{ac} = \bar{B}o_{ac} \exp(j\omega t) \qquad 6.32$$

where the real part is implied and it is assumed that the time

harmonics in the primary excitation are zero, then

$$\alpha = \frac{\dot{\bar{B}}_{ac}}{\bar{B}_{ac}} = j\omega \quad . \qquad 6.33$$

Further, for the purpose of defining the surface impedance of the solid iron, if it is assumed that the variation of $\bar{B}$ with respect to y is

$$\bar{B} = \bar{B}_{Cy} \exp\left(- j\frac{\pi y}{\tau_p}\right) \qquad 6.34$$

where again only the real part is implied, then

$$\beta = \frac{\nabla x \bar{v} x \bar{B}}{\bar{B}} = \frac{v_y \frac{\partial \bar{B}}{\partial y}}{\bar{B}}$$

or,

$$\beta = v_y \left(-j\frac{\pi}{\tau_p}\right) \quad . \qquad 6.35$$

The velocity at which the secondary member is moving can be expressed in terms of the synchronous velocity (v_s) as

$$v_s = (1-s)\, v_s \qquad 6.36$$

$$\text{where} \quad s = \text{slip} = \frac{v_s - v_y}{v_s} \qquad 6.37$$

$$\text{and} \quad v_s = 2\tau_p f \quad . \qquad 6.38$$

Substituting eqns.6.36 and 6.38 in eqn6.35 gives

$$\beta = 2\tau_p f\,(1-s)\left(-j\frac{\pi}{\tau_p}\right)$$

or,

$$\beta = -\,j\,(1-s)\omega \qquad 6.39$$

where,

$$\omega = 2\pi f \quad .$$

Therefore, by substituting the values of α and β (obtained in eqns.6.33 and 6.39 on the basis of the assumptions discussed above) in eqn.6.31 the magnetic impedance for the solid iron is

given as

$$Z_{mi} = \sqrt{\frac{\sigma_i}{\mu_i(j\omega - (1-s)j\omega)}}$$

$$= \sqrt{\frac{\sigma_i}{js\omega\mu_i}} .$$

or,

$$Z_{mi} = (1-j)\sqrt{\frac{\sigma_i}{2s\omega\mu_i}} \quad . \qquad 6.40$$

The magnetic impedance given by eqn.6.40 for solid iron accounts for the motion but assumes a sinusoidal variation of $\bar{B}$ with respect to the direction of motion. This assumption is only for the purpose of calculating the surface magnetic impedance of iron. The spatial harmonics are still taken into account during motion by solving the network model described in Fig.6.8 by making use of the approach described in Chapter 3.

6.6 RESULTS OF IMPROVED MODELLING

In Chapter 3 the eddy currents in the solid backing iron were neglected and in Chapter 5 the flux densities and forces calculated with this assumption were compared with those measured on the BTFCM. In this chapter an improved mathematical model has been developed to take into account the eddy currents and the resulting saturation in the solid iron. The magnetic impedance of the thin conducting sheet, below the backing iron, has been shown to remain unchanged with speed whereas the magnetic impedance of the solid iron changes with speed and is effected by the presence of spatial harmonics. Expressions have been derived to account for these effects in Sec.6.5 where, as a first approximation and only for the purpose of estimating the magnetic impedance of iron, the spatial harmonics were neglected. However, these harmonics can be accounted for by deriving β as given in eqn.6.17 after a set number of iterations.

Although the aluminium conducting sheet has been modelled (as in Chapter 3) as a thin sheet, a method has been presented and criteria established in Sec.6.4 for modelling thicker conducting sheets and this was applied to justify the use of a thin plate model for the BTFCM.

In this section the computed results of the improved modelling described above, are discussed.

6.6.1 Flux density at standstill

a) Magnitudes The three components of the flux density have been plotted separately in Fig.6.11 and Table 6.1 distinguishes the curves. The effect of the inclusion of eddy currents and saturation in the backing iron is such that the z-component of flux density is reduced all along the transverse direction x-x. This reduction arises because the eddy currents in the solid iron produce a flux that opposes the main flux thereby reducing the normal component of flux density. The effect of lowering the bottom boundary (to make the U-core limb its actual height of 50 mm) is small so far as the magnitude of B_z is concerned. It has, however, a considerable effect on the

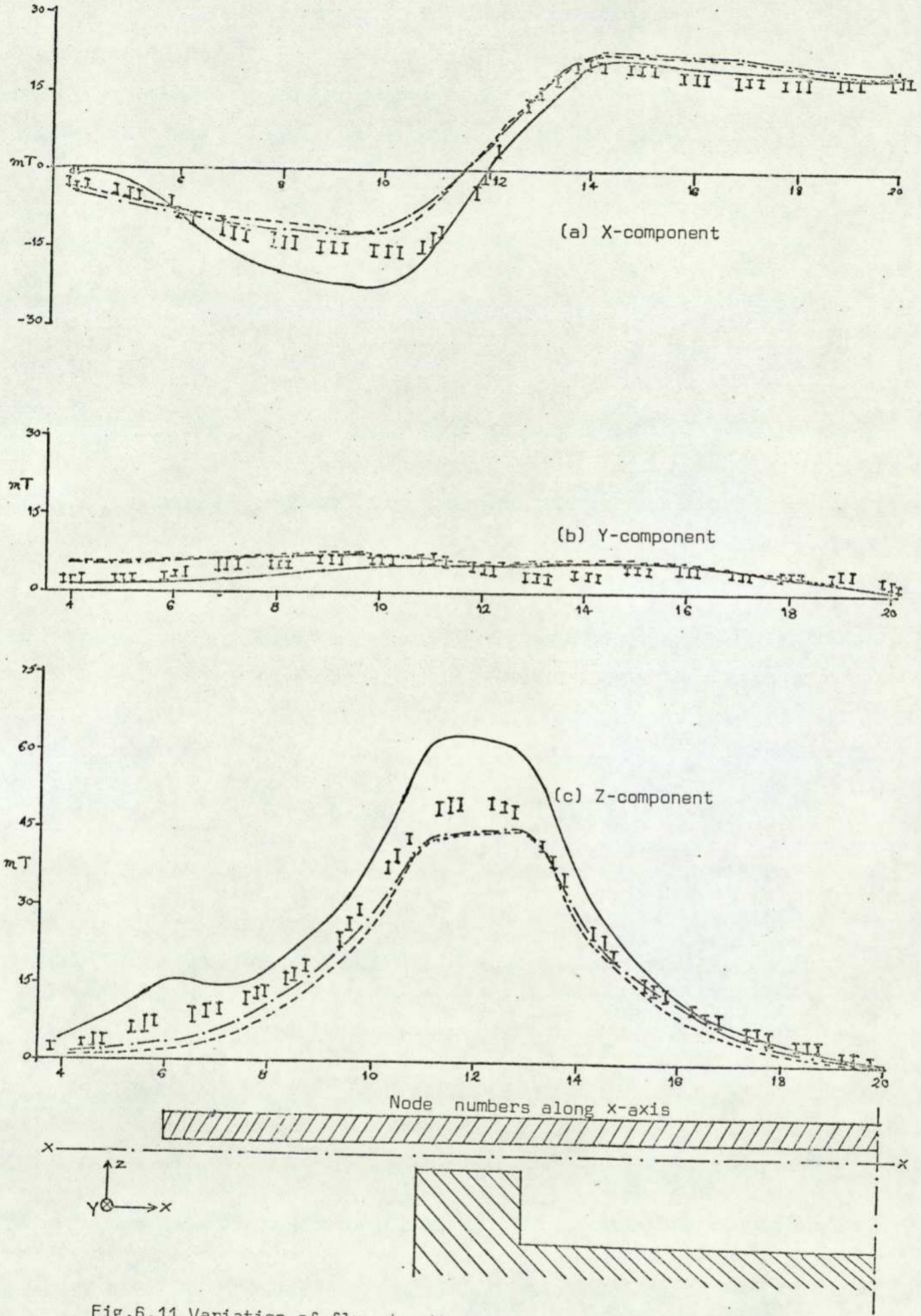

Fig.6.11 Variation of flux density along x-x

Table 6.1

Description of curves in Fig.6.11

Number	Description	Details
1	———	Eddy currents and saturation in the solid backing iron neglected
2	- - - - - - - -	Eddy currents and saturation in the solid backing iron considered
3	—·—·—·—	
2	- - - - - - - -	U-core limb considered 20mm high
3	—·—·—·—	U-core limb considered 50mm high
	I	Measured flux density

phase angle as shown in Fig.6.12 and discussed later.

The measured values of the z-component of flux density lie between those computed by using the mathematical model in which the eddy currents in the backing iron are ignored, and in the model in which they are considered. In the latter model, the saturation in the solid backing iron (as a direct consequence of the eddy currents) has been assumed to be uniform everywhere over the iron surface so as to allow a constant permeability to be adopted and thereby simplify the programming. In actual fact, however, the permeability of the iron is dependent on the tangential H, and since this is not uniformly distributed, the permeability must necessarily change from point to point over the iron surface. The variation in the tangential H just outside the iron surface in the BTFCM can be seen particularly from Fig.6.11(a) which, on changing the scale of the vertical axis (because the permeability is that of space) shows that $|H_x|$ varies from 0 to 16kA/m. Thus the non-uniformity in tangential H just outside the iron surface gives rise to a non-uniform saturation in the backing iron, and this can be accounted for by deriving the appropriate Z_{mi} for each node. This would, obviously, be the next step in improving the mathematical model further and this is suggested for further work in Sec.7.2. This, however, cannot be undertaken lightly for the present programme is particularly demanding in both computer storage capacity and mill time.

The computed x and y components of flux densities outside the U-core limb are greater when the eddy current condition in the backing iron is included in the mathematical model, than when it is not. This again is due to the field of the eddy currents opposing the incident flux, thereby increasing the tangential fluxes. The computed curves for tangential components of flux densities, for conditions with and without eddy currents in the solid backing iron, lie on the opposite sides of the measured flux densities along x-x outside the U-core. Along x-x on the inner side of the U-core, however, the inclusion of eddy currents in the mathematical model has not changed the y-component of flux density, although it increases the magnitude of the x-component of flux density. At the inner side of the U-core along x-x, the computed x-component of flux density (for conditions with and without eddy currents in the solid backing iron) remains fairly constant, but the measured values exhibit a small drop between node numbers 14 and 17, and are lower than the calculated values between node numbers 13 and 20. The maximum discrepancy between the calculated and measured x-component of flux density is between node numbers 16 and 17, and it is respectively 18 per cent and 11 per cent for those mathematical models which account for, and which do not account for the eddy currents in the solid backing iron. The causes for this discrepancy may, most likely, be due to an inaccurate orientation of the search coil at nodes lying along x-x in the inner side of the U-core as explained in Chapter 4, and due to the assumption of a constant permeability at all nodes on the iron surface.

(b) Phases

The variation along x-x of the phase angle of the 2-component of flux density is shown in Fig.6.12, the curves being distinguished in Table 6.2. The inclusion in the mathematical model of the eddy current condition in the solid backing iron and the various boundary conditions at z=o have a distinct effect on the phase angle when compared with curve 1 in Fig.6.12. Curves 2 and 3 and curves 4 and 5 are for U-core limb 20 mm and 50 mm high respectively. Each set is for a flux-line and a zero-potential boundary condition at z=o and, as is evident from Fig.6.12, each set is above and below the measured phase angles (except inside the U-core where, although curves 2 and 3 and likewise curves 4 and 5 merge, they differ somewhat from the measured values). Also the set of curves corresponding to a U-core limb length of 50 mm are nearer to the measured phase angles. This improvement arises because 50 mm distance corresponds to the height of the U-core limb in the BTFCM although only 20 mm of each limb carries primary excitation winding. At first sight it would seem that the 30 mm part of the U-core limb which is winding-free would not play a significant role and therefore the height of the U-core limb may be taken as 20 mm so reducing the number of nodes in the numerical model and hence the computing time. Although this may be true so far as magnitudes are concerned it is not so when considering phase angles as demonstrated in Fig.6.12 where it is clear that the curve 2 lies more closely to the measured values than any other curve. Consequently this extended leg length has been adopted in subsequent programming when studying the effect of speed, as discussed in the next section.

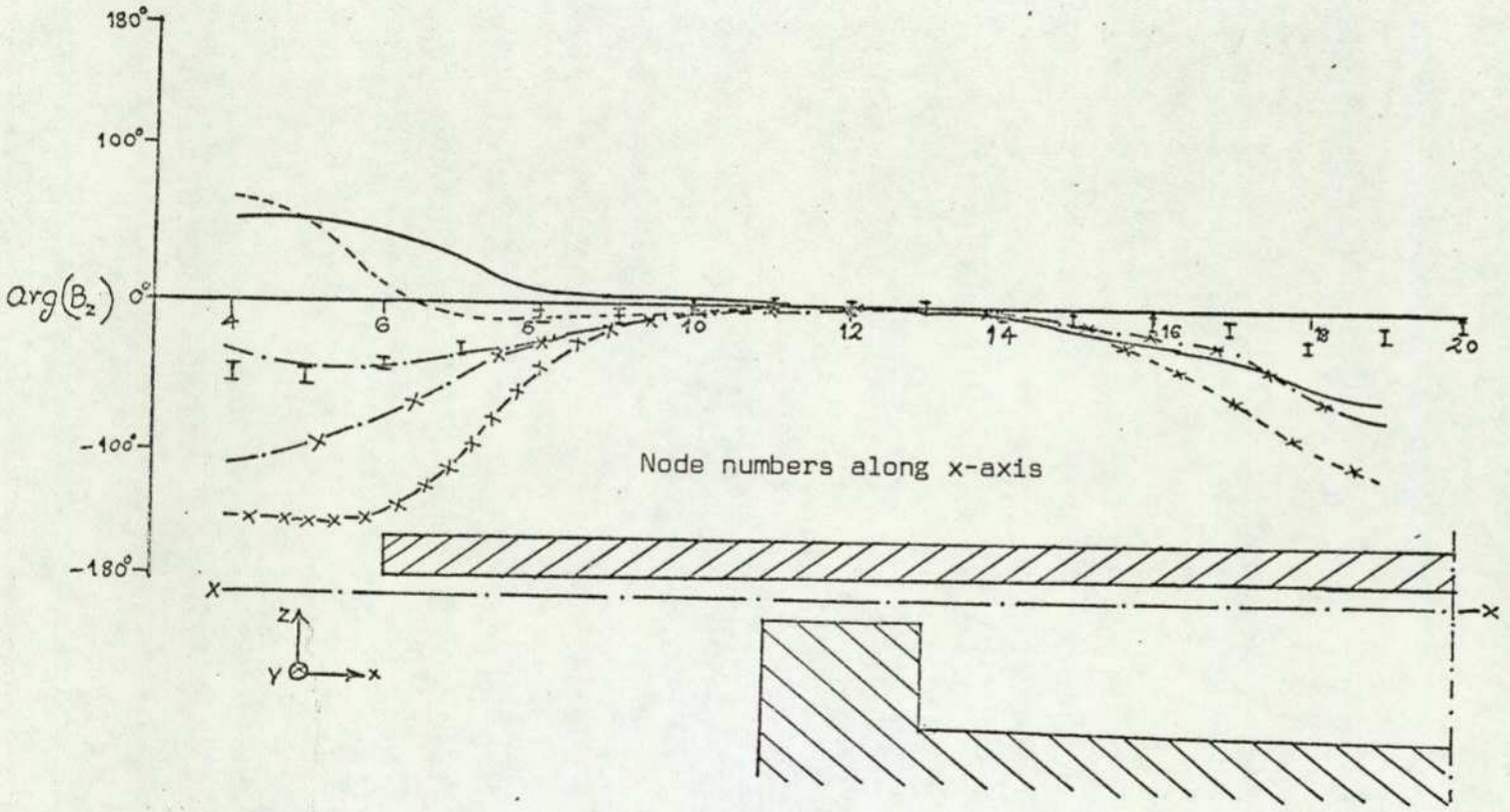

Fig.6.12 Variation of arg(B_z) along x-x

Table 6.2

Description of curves in Fig.6.12

Number	Description	Details
1	————	Eddy currents and saturation in the solid backing iron neglected
2	– – – – – – – – –	Eddy currents and saturation in the solid backing iron considered
3	–×–×–×–×–	
4	—·—·—·—·—	
5	—·—×—·—×	
2	----------	U-core limb considered 20mm high
3	—×—×—×—×—	
4	—·—·—·—	U-core limb considered 50mm high
5	—·—×—·—	
2	– – – – – – – –	Flux line boundary condition at z=0 plane
4	—·—·—·—	
3	—×—×—×—	Zero potential boundary condition at z=0 plane
5	—·— x —·—	
	I	Measured phase angle

(Reference in each case is node number 12 .)

6.6.2 Effect of Speed

In Sec.6.5 it was concluded that the effect of speed on the magnetic network model is such that the magnetic impedance for the solid iron is given by eqn.6.40 and that for the thin conducting sheet by eqn.6.30. The computer programme based on this new network model, using these magnetic impedances to represent the secondary member, is used as outlined in Chapter 3, to obtain the MSP distribution at various speeds. This MSP distribution, as before, is then used for calculating the flux densities and forces. The computed results are plotted in Fig.6.13 and the curves are distinguished in Table 6.3.

The inclusion in the mathematical model of the eddy current condition in the solid backing iron is such that the normal component of flux density (i.e. B_z) is lower at all speeds when compared with those obtained by ignoring the eddy currents in the solid iron. This reduction in the z-component of flux density has been attributed, in Sec.6.6.1, to the additional secondary flux (produced as a result of eddy currents in the solid iron) which opposes the main flux. The tangential components of flux density (i.e. B_x and B_y) are likewise changed significantly at all speeds when the eddy current conditions in the solid backing iron are included in the mathematical model. This is again because of the eddy-current reaction as mentioned in Sec.6.6.1. In the main, the curves 4 in Fig.6.13(a) for Bx, By and Bz, are closer to the measured values and, therefore, the inclusion of eddy current conditions in the solid backing iron improves the mathematical model.

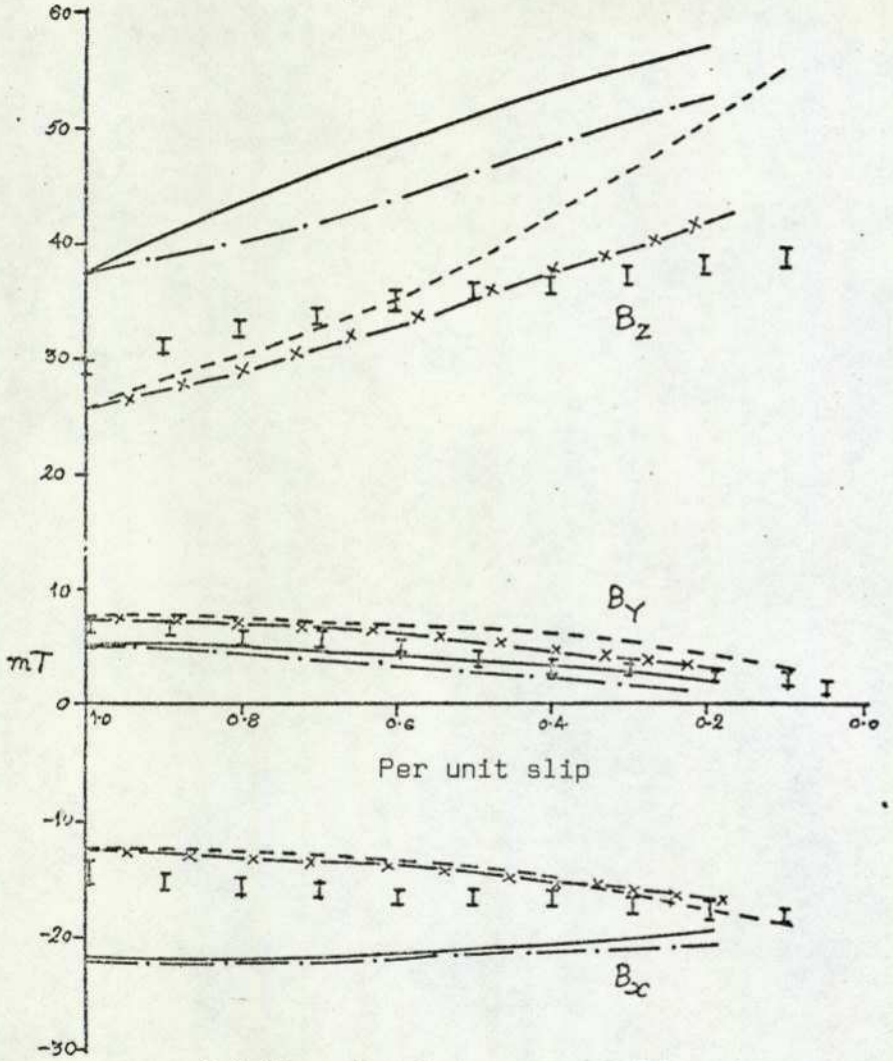

(a) Flux density

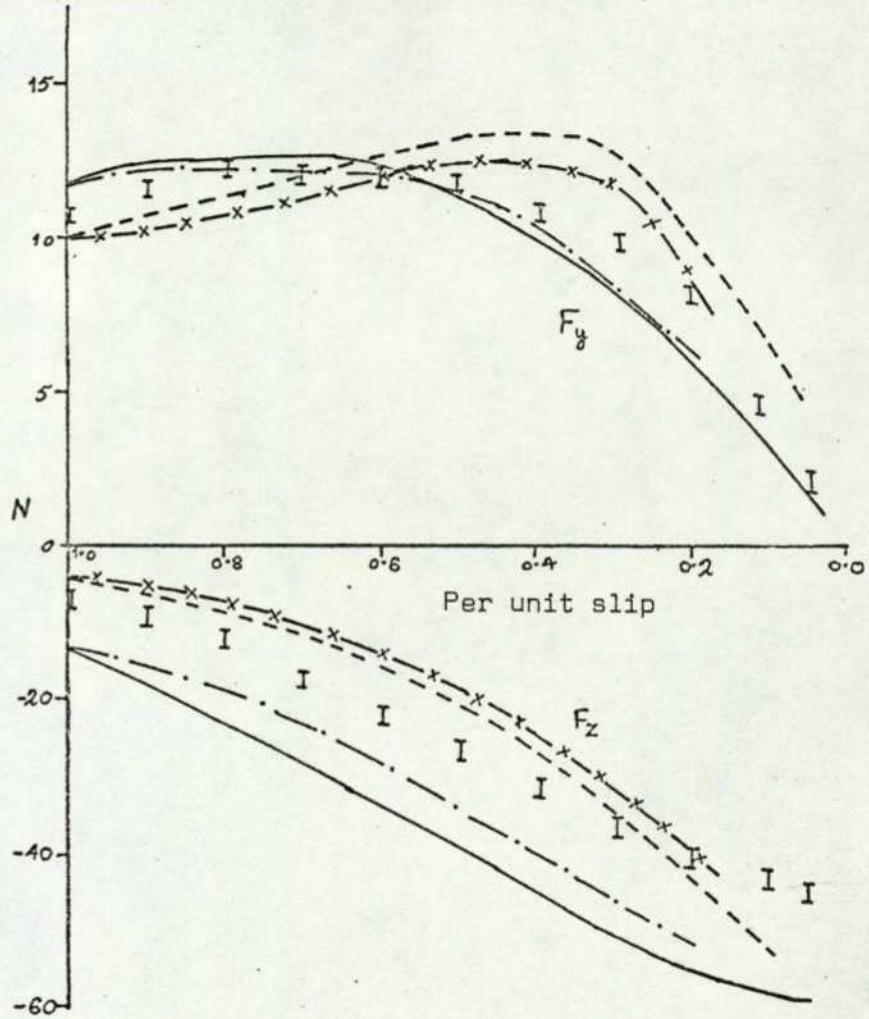

(b) Forces

Fig.6.13 Variation of flux density and forces with respect to speed

Table 6.3

Description of curves in Fig.6.13

Number	Description	Details
1 2	————	Eddy currents and saturation in the solid backing iron neglected
3 4	- - - - - - - - -	Eddy currents and saturation in the solid backing iron considered
1 3	————	Spatial harmonics neglected in the calculation of the MSP distribution
2 4	—·—·—·—	Spatial harmonics considered in the calculation of the MSP distribution
	I	Measured flux density and force

The flux density in Fig.6.13(a) are at a node (10,5,5) described below.

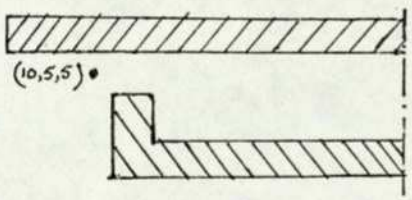

The effect of the modified mathematical model on the force versus speed characteristic is depicted in Fig.6.13(b). Examining this in the same way as the torque-speed characteristic of an induction machine, the inclusion of the eddy current condition in the form of Z_{mi} is such that, so far as the variation of the propulsive force (F_Y) with speed is concerned, the secondary member appears to have an effective resistance lower than is the case when the eddy currents (and the resulting saturation) in the solid backing iron are neglected. The consideration of spatial harmonics, by using the method described in Chapter 3, in the secondary member is, as expected, such that the propulsive force becomes less than that obtained without taking into account the spatial harmonics. This approach, however, does not account for the effect of spatial harmonics on Z_{mi} as pointed out earlier in Sec.6.5, although this can be done by defining β (in eqn.6.17) at each node. The influence of its inclusion in the mathematical model will have an effect on the F_Y versus speed characteristic particularly at high speed and will, therefore, improve the correlation of measured and computed forces in the region of 0.3 p.u. slip in Fig.6.13(b). The discrepancy between the measured and computed force F_Y in the region of 0.8 p.u. slip may be due to the use of a fixed permeability all over the secondary backing iron. The development of a variable permeability model is referred to later in Sec.7.2.

The effect of the modified mathematical model on the variation of the normal force (F_Z) with speed is similar to that described for the variation of F_Y with speed. The eddy currents in the solid backing iron increase the total current in the secondary member for the same primary excitation, as compared with the case when eddy currents are present only in the aluminium conducting sheet. This causes a corresponding reduction in B_Z (as discussed earlier) and therefore the attraction force also reduces (as eqn.3.48 indicates) for the same primary excitation . In Fig.6.13(b) the normal forces calculated by neglecting and by considering eddy currents (and the resulting saturation) in the solid backing iron lie on either side of the measured normal forces. These measured forces

are closer to those calculated by using the mathematical model in which the eddy currents in the solid backing iron are taken into account, although there is some discrepancy at low and high slips. The discrepancy at high slips is most probably due to the use of a uniform permeability throughout the iron surface. This can be overcome by defining permeability at each node on the iron surface, depending upon the prevailing tangential field conditions. At low slips, however, the computed forces would come closer to the measured ones when β (given by eqn.6.17) is also defined at each node to account for the spatial harmonics for defining Z_{mi} (by eqn.6.31). Also at very low slips the depth of penetration would become large, approaching half the thickness of the backing iron, in which case the surface impedance modelling of the backing iron will not be valid. This, therefore, requires a corresponding modification in the computer programme for establishing the criteria for finding out when the model becomes invalid and then switching over to the thick or thin sheet model, described in Sec.6.2, as the case may be. The improvement in correlation at low slips is expected because the inclusion of harmonics in defining Z_{mi} would effectively increase the eddy currents in the secondary member, and this would lower the computed B_z and F_z in Fig.6.13 (a) and (b) respectively. The method of including these two suggestions for improving the mathematical model further has been discussed later. In the following sub-section the effect of improvements in the mathematical model made in this chapter, and the effect of speed on the MSP distribution around the secondary member and on the current distribution in the secondary member, are presented in the form of computer plots.

6.6.3 MSP distribution and current density distribution plots

In Fig.6.14 the flux distribution around the secondary member has been shown for conditions in the mathematical model when eddy currents in the solid backing iron (and the resulting saturation) are both neglected and, alternatively, included. Fig.6.14(b) is comparable with Fig.6.4 which was drawn earlier to illustrate discussions in Sec.6.3. The effect of including eddy currents in the solid backing iron is, as expected, such that the flux pushed around on the other side of the secondary member increases, as shown in Fig.6.14.

The plots presented in Fig.6.15 are comparable to the current density distribution plot drawn earlier in Sec.6.4 (Fig.6.10). In this the surface of the secondary member has been "developed" (i.e. laid out in a two-dimensional form) for the convenience of plotting and the original secondary member can be re-formed by bending the plot along the dotted lines (in Fig.6.15(b)). When this is done the current density distrbution along the edges (between B and C) and on the other side of the solid backing iron (between A and B) will be obtained. The current density distribution (between A and B) on the other side of the solid backing iron indicates that a significant percentage of current does flow on the top surface of the solid backing iron.

In Fig.6.16, the magnetic scalar potential plots, described earlier in Fig.6.14, have been presented for high and low slips for the mathematical models in which the eddy current condition in the solid backing iron is both neglected and considered. The flux lines are orthogonal to the constant MSP lines and, therefore, Fig.6.16 shows the effect of speed on the flux distribution around the secondary member for both the mathematical models. As expected, and indicated later in Fig.6.17, the eddy currents in the secondary member decrease with the decrease in slip and, therefore, more flux enters the iron from the bottom surface to find its path to the opposite pole, instead of being diverted around to the other side of the secondary member. This has been illustrated better in Fig.6.16(b)).

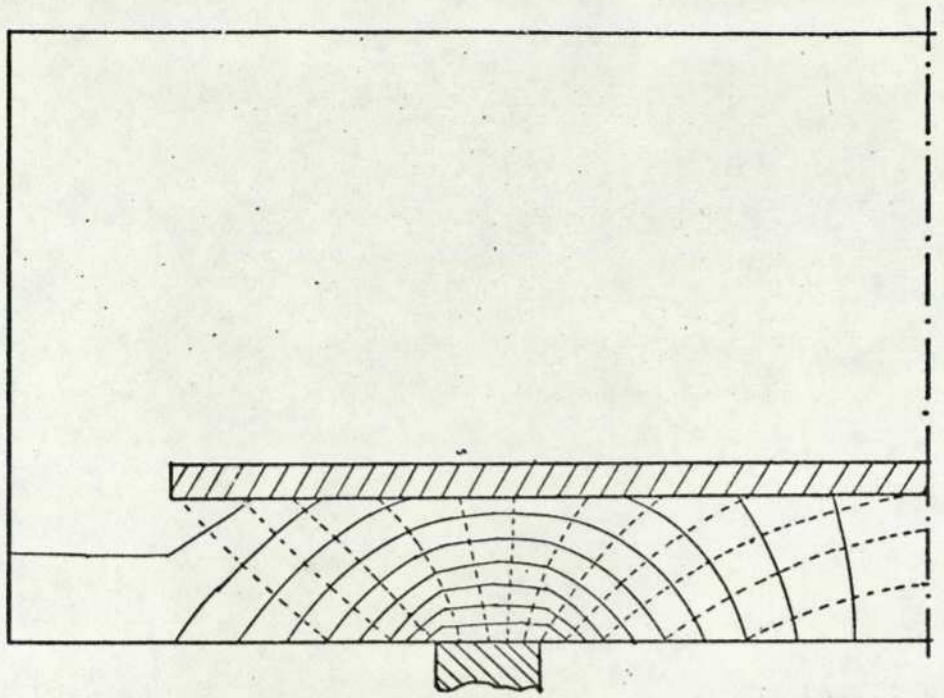

(a) Eddy current condition in the backing iron neglected

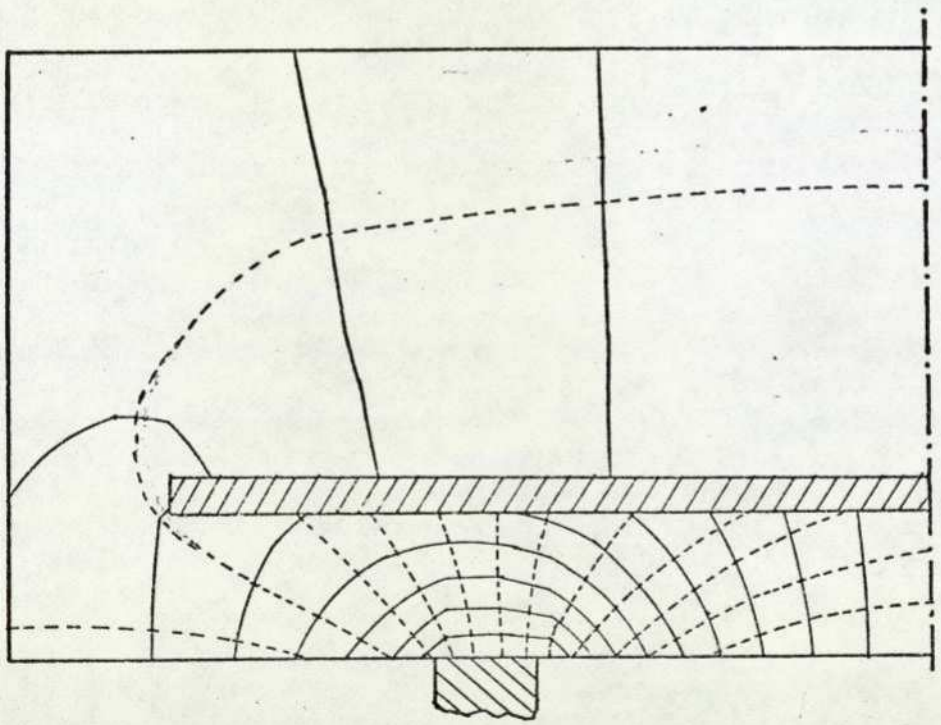

(b) Eddy current condition in the solid backing iron considered

Fig.6.14 Flux distribution around the secondary member of the BTFCM

(——— Equipotential lines, ------- Equi-flux lines)

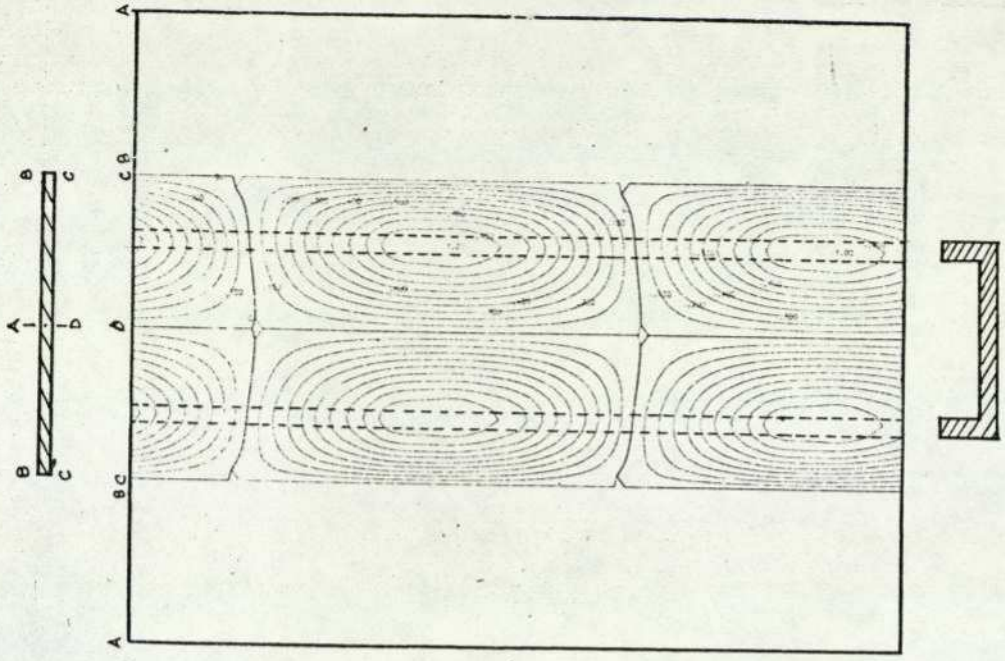

(a) Eddy current condition in the backing iron neglected

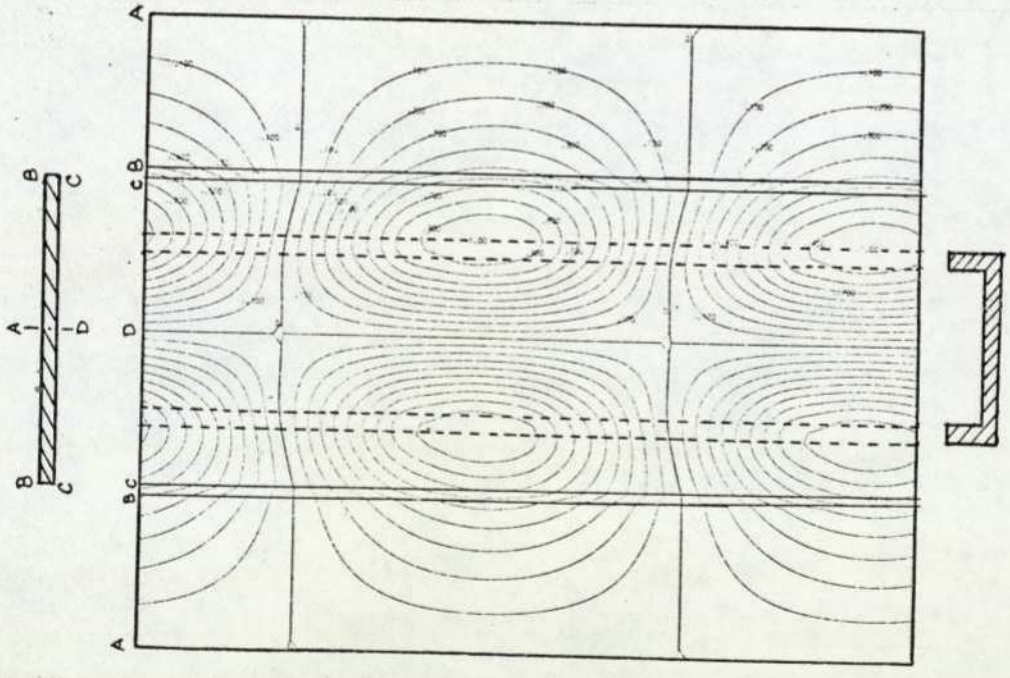

(b) Eddy current condition in the solid backing iron considered

Fig.6.15 Eddy current distribution in the developed secondary member of the BTFCM at 1.0 p.u. slip

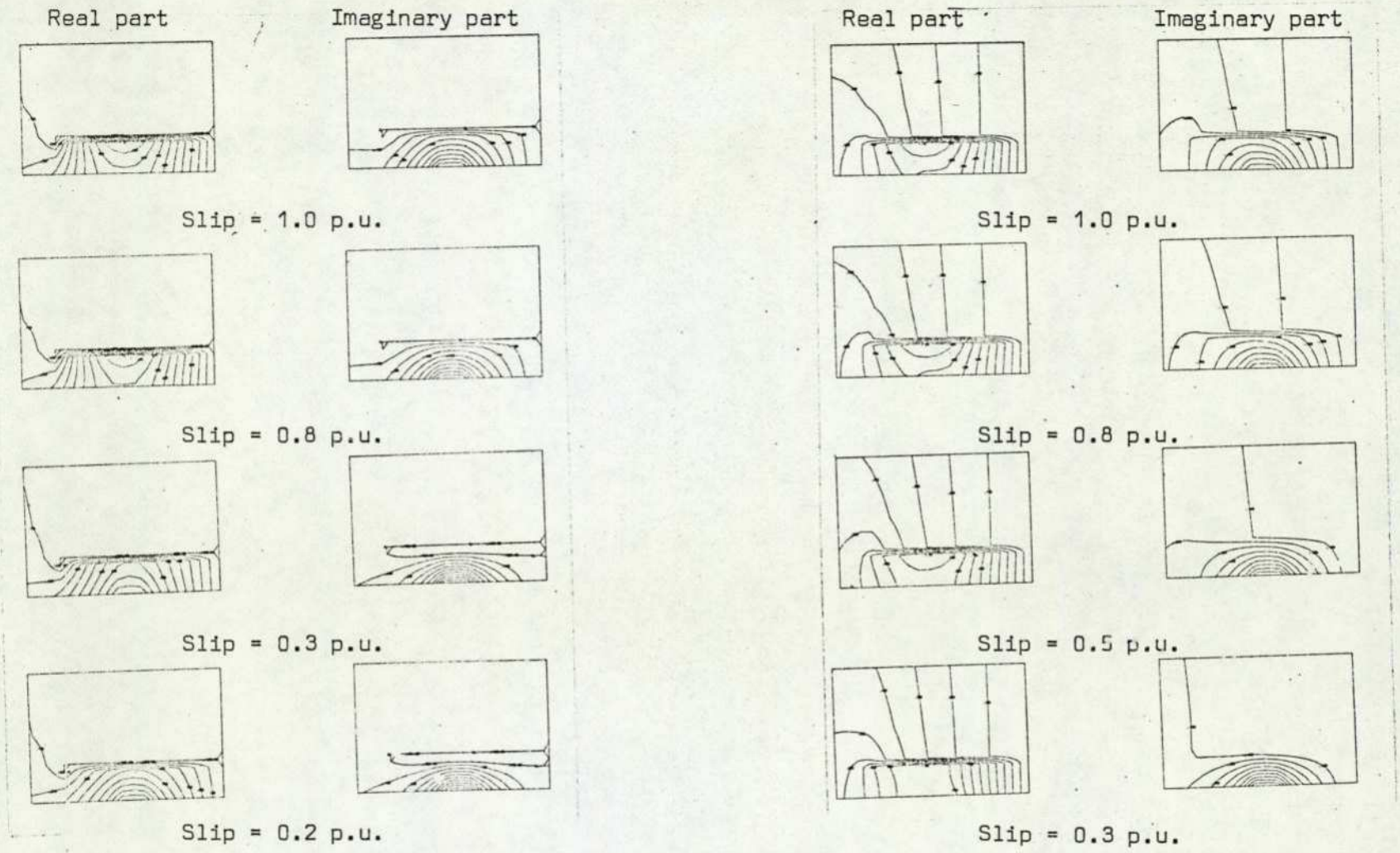

(a) Eddy current condition in the backing iron neglected

(b) Eddy current condition in the solid backing iron considered

Fig.6.16 Effect of speed on the MSP distribution around the secondary member of the BTFCM

In Fig.6.17 the effect of speed on the surface current density distribition in the secondary member is shown for both the mathematical models. The plots are similar to those described in Fig.6.15, and the speed has two significant effects on them. The first is the relative movement with speed of poles formed in the secondary member with respect to the poles of the primary member. This is expected and is indicated in both Fig.6.17(a) and (b), because the plots have been obtained at the same instant of time and at the same location in space with respect to the primary member. The second significant effect of speed on the current density distribution plots is the significant change in the shape of the eddy current loops. As the speed increases some 'rings' are formed within a pole pitch indicating the presence of locally-circulating eddy currents. This happens at high speeds because as the speed increases the eddy currents in the secondary member due to the primary alternating flux decreases and that due to the spatial harmonics becomes comparable and therefore 'rings' are formed corresponding to the individual U-core limbs. The primary member has six U-cores per pole pitch and this gives rise to six corresponding 'rings' in the secondary member which can be counted in the plots for high speeds. In Fig.6.18 the current density distribution plots obtained at 0.2 p.U. slip for both the mathematical models have been enlarged to show the 'ring' formation. The plot for the modified mathematical model (given by Fig.6.18(b)) is a little suspect because in this case the convergence was not quite as good as usually obtained. The plots, however, do show the odd shapes of the current density distribution in the conducting sheet attributable to the sharp discontinuities in the primary U-core limbs. The effect of spatial harmonics is therefore allowed, by the reduced eddy current reaction, to increase at high speeds. This 'ring' formation leads to additional losses in the secondary member, and, therefore, it is necessary to design the primary member and its windings to smooth out the spatial variation of the flux density (see Fig.6.19).

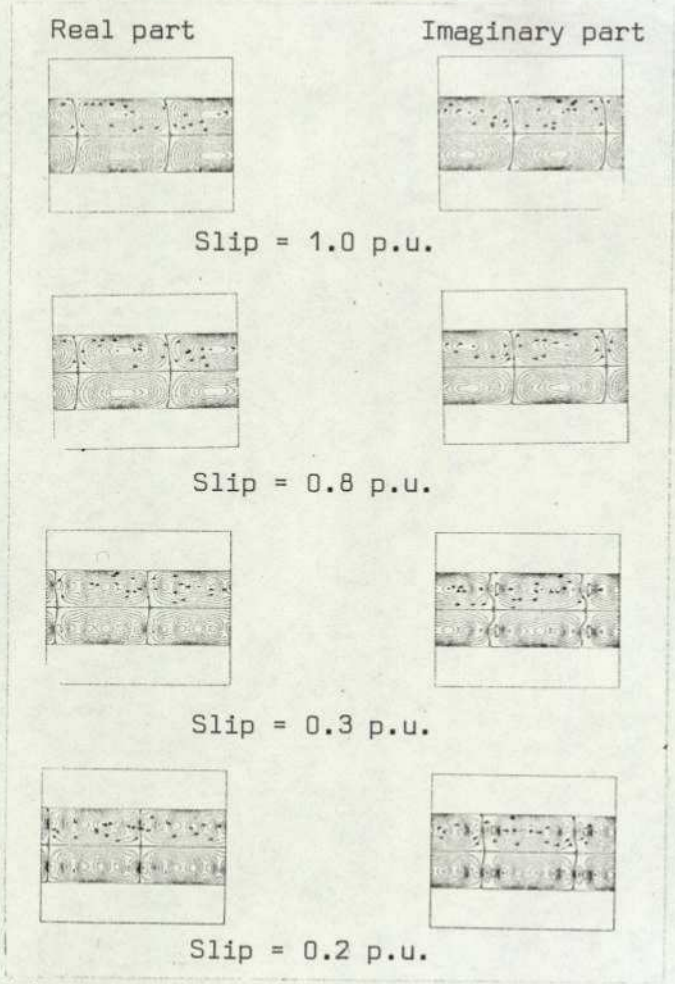

(a) Eddy current condition in the backing iron neglected

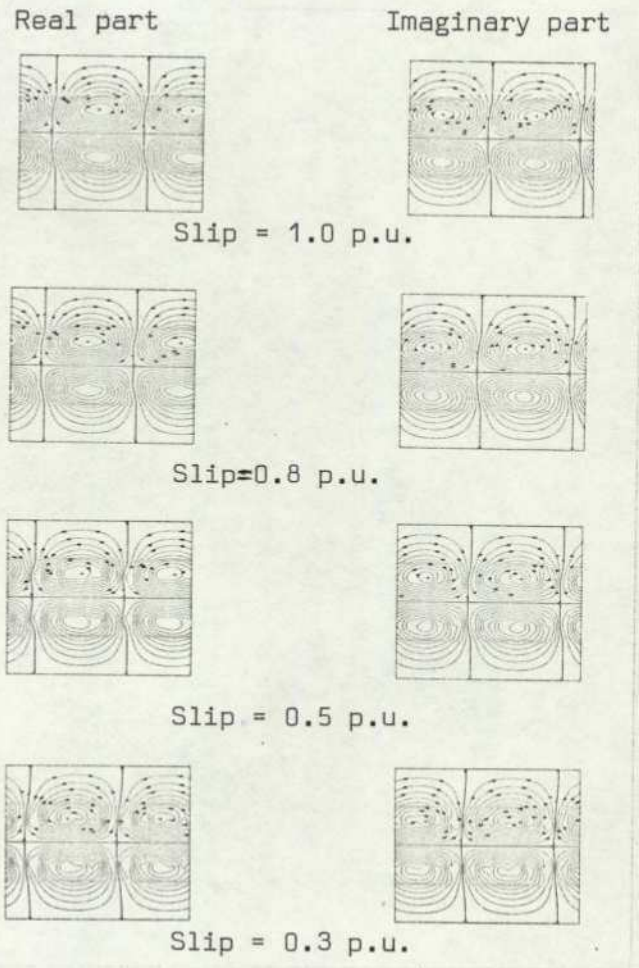

(b) Eddy current condition in the solid backing iron considered

Fig.6.17 Effect of speed on the current density distribution in the secondary member of the BTFCM

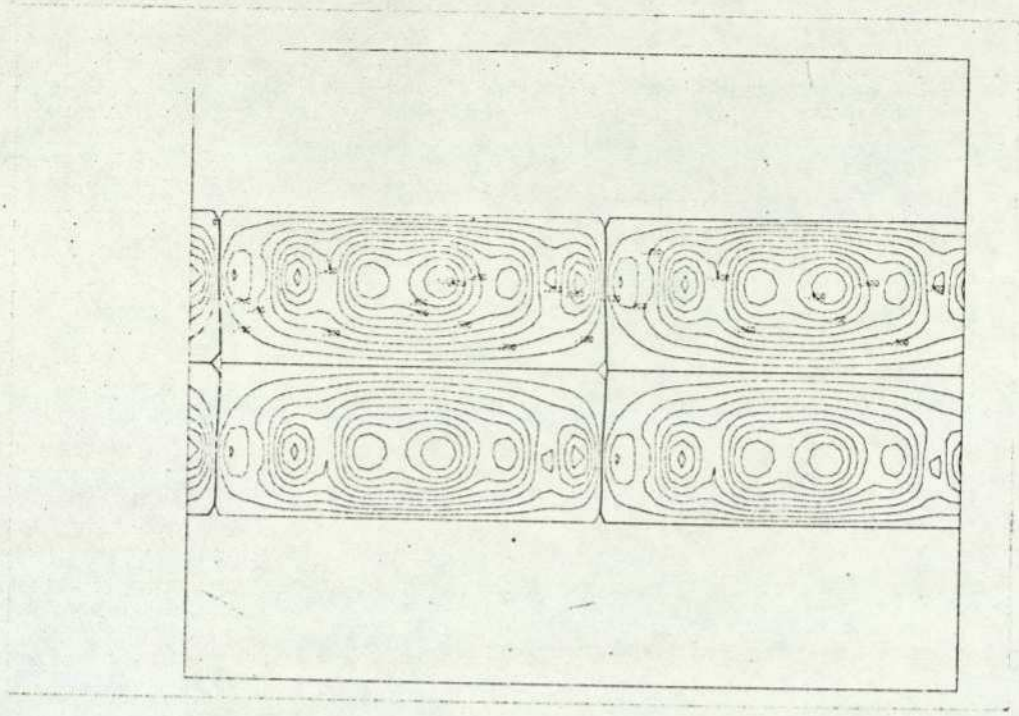

(a) Eddy current condition in the backing iron neglected

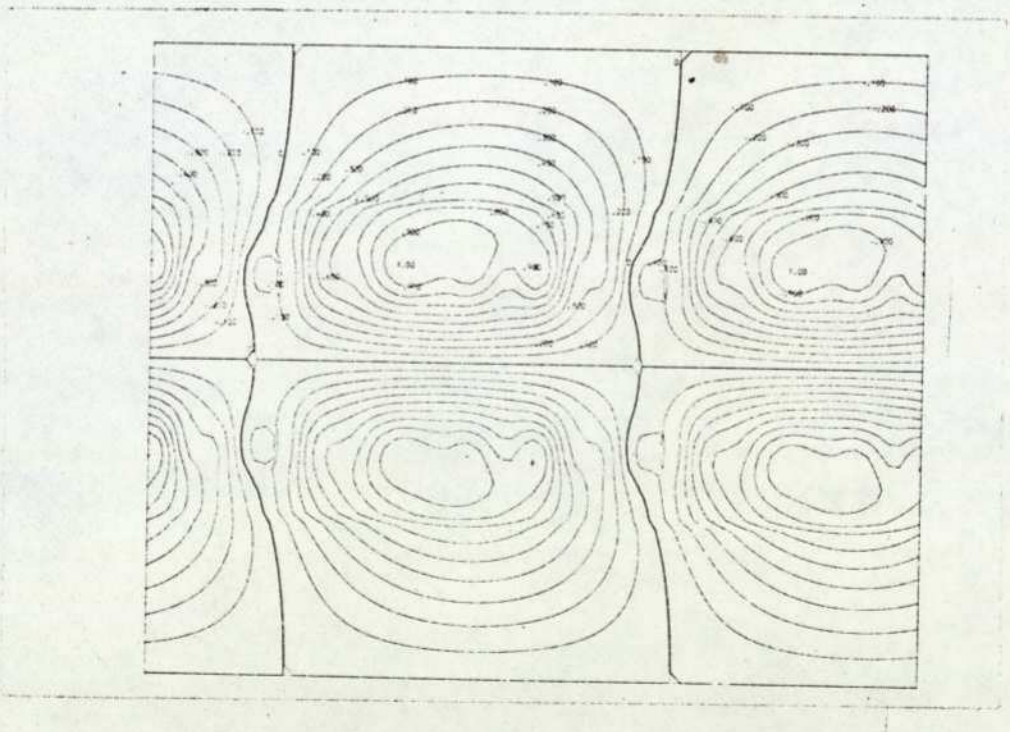

(b) Eddy current condition in the solid backing iron considered

Fig.6.18 'Ring' formation in the eddy current distribution diagrams at 0.2 p.u. slip

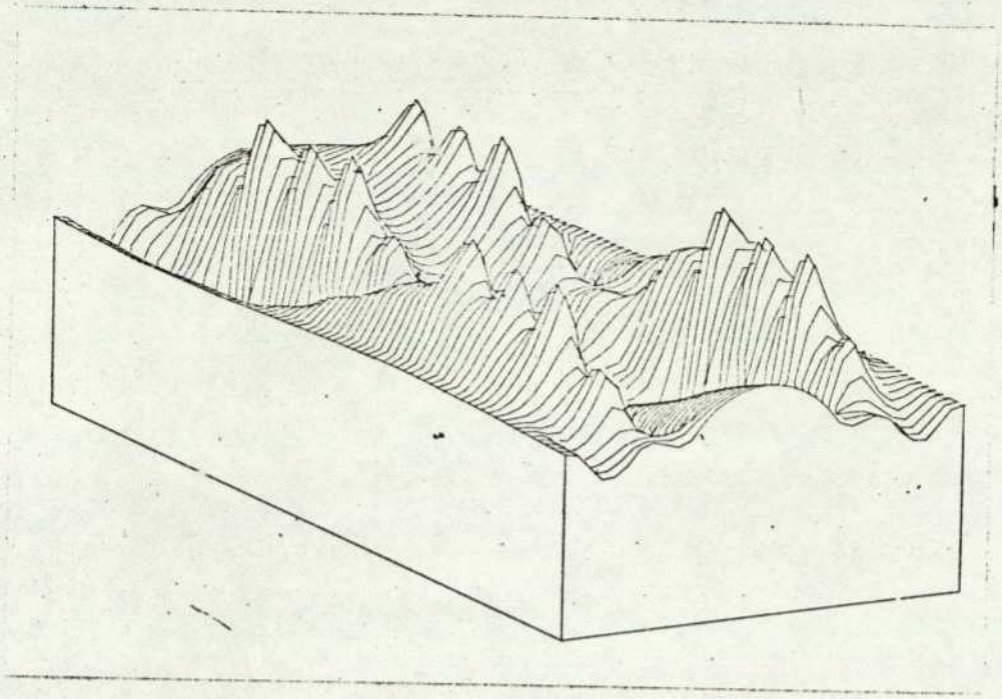

(a) Real part of the x-component of flux density
Maximum corresponds to 1.91 mT

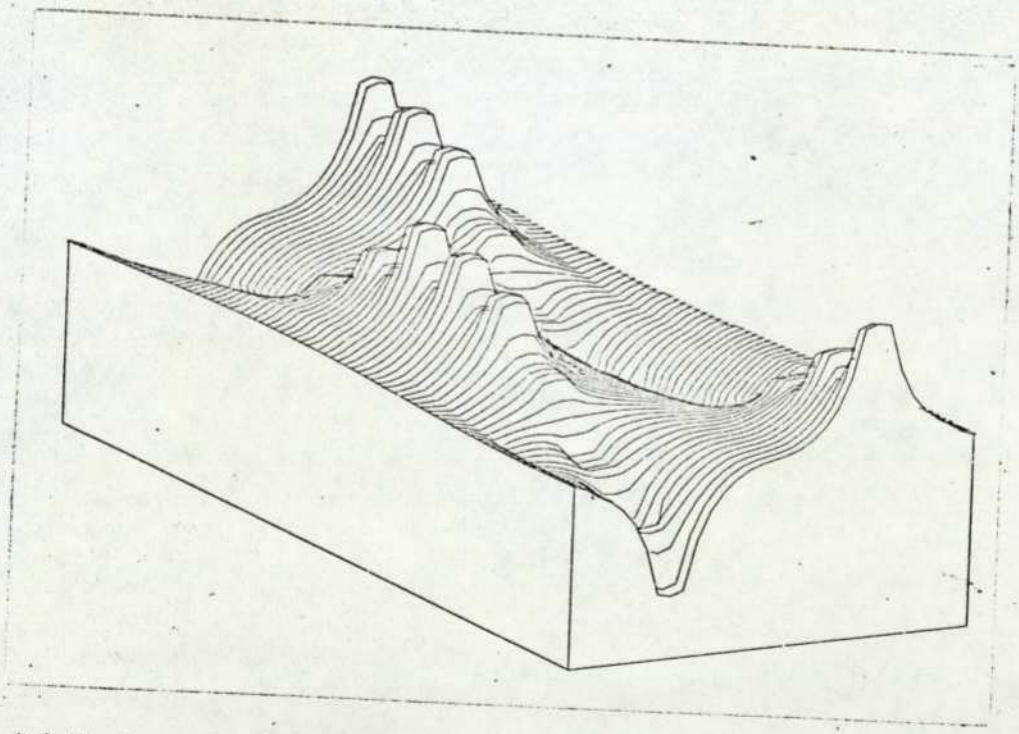

(b) Real part of the z-component of flux density
Maximum corresponds to 7.85 mT

Fig.6.19 Spatial variation of flux density at 0.3 p.u. slip

8./ DISCUSSION

In this chapter a modified mathematical model has been discussed to account for the eddy currents and the resulting saturation in the solid backing iron and also to model thicker conducting sheets. The criteria have been established in Sec.6.4 for using the latter. It has also been shown by using the same criteria that the aluminium conducting sheet used in the present work can be represented by a thin sheet model. The effect of speed on the surface magnetic impedance of the backing iron has been described by β in eqn.6.17 and, as a first approximation for the purpose of defining Z_{mi} only, it has been defined by eqn.6.35 for the case when the variation of flux density is sinusoidal with respect to the direction of motion (i.e. $\bar{y}$). The computed flux densities and forces at various speeds have been compared in Sec.6.6 with those measured on the BTFCM, and it has been found that by using the improved mathematical model the correlation between measured and computed results has in general improved. Possible reasons for the remaining discrepancy have been discussed and further modifications in the mathematical model for the purpose of minimising this discrepancy in the results have been suggested. These suggestions and general conclusions drawn from the work reported in this thesis are dealt with in the next chapter.

CHAPTER 7

CHAPTER 7 CONCLUSIONS AND RECOMMENDATIONS FOR FURTHER WORK

7.1 CONCLUSIONS

In the foregoing chapters of this thesis an approach was described towards understanding and developing transverse flux machines. For the purpose of predicting flux densities and hence the forces in the machine a "three-dimensional computer programme" was developed on the lines of discussions given in Chapters 2,3 and 6. A listing of this computer programme has been given in Appendix H. In Chapter 3 the mathematical model was developed and in Chapter 5 it was tested by correlating the calculated flux densities and forces with those measured on the BTFCM (described in Chapter 4) during standstill, motoring and braking conditions. In addition the computed results were plotted in two-and three-dimensional diagrams to show the distribution of various components of flux density, current density and force density in the machine. These diagrams are useful particularly in appreciating the effects of modifications in the material and shape of the secondary member, and the effect of modifications in the mathematical model (as shown in Chapter 6).

In the mathematical model of Chapter 3 the solid backing iron was considered as infinitely permeable and computed results, on the basis of this assumption, were compared in Chapter 5 where it was found that the correlation was not good particularly at low slips. This was thought to be, most probably, due to the assumption made that the solid backing iron is infinitely permeable. In Chapter 6 it was shown that flux at even low flux densities (about 40mT) when they strike against the solid backing iron surface give rise to circulating eddy currents which prevent the flux from penetrating into the solid iron and therefore saturate the surface layer. The eddy currents in the solid backing iron and the resulting saturation due to the alternating flux and due to the motion of the secondary member, have been defined by the surface magnetic impedance as in eqn.6.40. The aluminium conducting sheet was modelled (as in Chapter 3) as a thin sheet, although a method has been presented and criteria established in Sec.6.4 for modelling thicker conducting sheets.

These criteria were also applied to justify the use of thin plate model for the BTFCM. In Sec.6.5 it was also shown by eqn.6.30(4) that for a thin plate model the magnetic impedance is independent of the speed at which the secondary member moves. The computed results of this improved mathematical model and those computed without accounting for the eddy current condition in the solid backing iron were compared (in Sec.6.6) with those measured on the BTFCM. It was shown that, in general, the measured flux densities and forces lie between the computed results of these two mathematical models, and they are closer to those obtained by using the improved mathematical model. The possible reasons for the discrepancies between the measured and computed results, and the necessary modifications in the mathematical model for minimising these discrepancies were also discussed in Sec.6.6. In Sec.7.2 these modifications are further discussed, and their implementation suggested for further work in this field.

In Chapter 6 it was pointed out that the backing iron behind the aluminium reaction rail, for economic reasons, should be solid rather than laminated (for preventing the flow of eddy currents in it). However, when the backing iron is solid the surface layers get saturated because of eddy currents produced by the alternating flux striking against the surface, and this would imply that it is wasteful to use solid iron thicker than the thin layer carrying the flux. But since the thickness of this thin layer is dependent on the penetration depth it would increase with the speed (as shown in Sec.6.5) and therefore the required thickness of the solid backing iron may then be considerable. However, as was shown in Sec.6.3, the use of a composite backing iron consisting of two mild steel plates can be more effective than a single mild steel plate of thickness greater than one-and-a-half times the total thickness of the composite backing iron, thereby resulting in a saving of backing iron. This is an important consideration in developing a viable transport system because the major cost involved in such a system is in the track. Thus, on the basis of the results of analysis, it is clear that a composite backing iron (like BI3, in Fig.6.5, which can be of the cheapest mild steel) behind the aluminium reaction rail is well worth while.

An important concept of 'effective thickness' was described and used in Chapter 6 for introducing the speed term β (as in eqn.6.17) in the expression for the magnetic impedance. Thus eqn.6.31 gives the magnetic impedance for a case when the flux striking against the solid backing iron surface changes with respect to time both because of the alternating nature of the primary excitation and also because of the motion of the secondary member in a magnetic field which is non-uniform along the direction of motion. The latter, in fact, accounts for the spatial harmonics as well because β is defined at a particular node numerically in the computer programme by using the flux density at the surrounding nodes.

The most attractive feature of the approach, discussed in Chapters 3 and 6 and used in the present work, is that it

suits the basic philosophy of special purpose electromagnetic devices [22,56,61,62], particularly during their development stages. This is because the approach can take into account the less common geometries and discontinuities present in special purpose electromagnetic devices, which depend more on the application than on criteria like efficiency, powerfactor and cost. The approach appears to have a clear advantage over other analytical approaches (discussed in Chapter 2) for cases when it becomes extremely difficult to define the resulting primary magnetomotive forcing function by using one or more known mathematical functions to solve the field equations analytically within existing boundary conditions. It is also difficult to consider secondary members whose electrical and magnetic properties vary along the length and width of the machine. On the contrary, however, the approach discussed in Chapters 3 and 6 accounts for the magnetic and electric properties of the surrounding space for evaluating the potential at every node. Only the surrounding nodes are used in the calculation at any one time and therefore the effects of variations in the material properties and shape of the electromagnetic device can be easily included, so long as the general equation includes the facilities necessary to account for the changes taking place. This feature, incidentally, takes care of the problem of accounting for the spatial harmonics as well, which are necessarily included.

As mentioned earlier, the approach is useful particularly during the development stages of an electromagnetic device, when the development engineer can modify the shape and dimensions of the device on an on-line console and see the effect immediately of modifications in the form of two- and three-dimensional plots of flux densities and forces by using suitable computer programmes stored in the computer library. His experience can then be used to frame suitable equivalent circuits for the simpler and routine design and analysis in the design department. In fact, the whole approach forms a stepping stone to the

development of the three-dimensional engineering necessary in the design, development and analysis of electromagnetic devices. The approach may also be found useful for educational purposes where flux density and forces can be calculated quite easily by the method adopted in Chapters 3 and 6 and their verification shown on the BTFCM or any other similar machine developed for this purpose. This can, obviously, lead to greater confidence in the field approach for the analysis of electromagnetic field problems.

7.2 RECOMMENDATIONS FOR FURTHER WORK

In this thesis an approach to the design of electromagnetic devices (especially unusual electric machines) was discussed in Chapter 3 and the calculated flux densities and forces of such a machine were correlated in Chapter 5 with those measured on the BTFCM under standstill, motoring and braking conditions. The correlation and especially the discrepancies between calculation and test were discussed in Chapter 5. In Chapter 6 it was shown that the discrepancies were, most likely, due to the assumption made in Chapter 3 that the backing iron is infinitely permeable and carries no eddy currents, and, therefore, these conditions were incorporated in an improved mathematical model. The computed results were shown closer to those measured on the BTFCM as compared to those which were computed without accounting for the eddy current condition in the solid backing iron.

In Chapter 6 some first order assumptions were made to simplify the mathematical model, and in Sec.6.6 it was shown that most of the remaining discrepancies between calculation and test are due to these assumptions. In this section some proposals for further work are made. They are for the purpose developing the mathematical model further in order to deal with the first order assumptions made in Chapter 6 for improving the efficiency of the computer programme and for dealing with certain other important aspects of the problem.

(a) Two assumptions were made in the improved mathematical model, described and used in Chapter 6.

(i) The secondary backing iron has a constant permeability everywhere irrespective of the tangential H just outside the iron surface.

(ii) The flux density varies sinusoidally with respect to the direction of motion (i.e. y) for the purpose of defining Z_{mi} in eqn.6.40.

As a further improvement in the mathematical model, these two assumptions can be circumvented by calculating the permeability and β (given by eqn.6.17) at each node by making use of the MSP distribution around that node. This would require two sub-routines, one for calculating the permeability at that node by using the magnetisation curve (actual or approximated) for the backing iron material, and the other for calculating β by using eqn.6.17 and the magnetic scalar potentials at the surrounding nodes.

(b) The problem of convergence becomes extremely severe at low slips. This may be due to the violation of the surface impedence model for solid backing iron at low slips (as pointed out in Sec.6.6.2) and, therefore, a corresponding improvement in the computer programme is required for establishing the criteria for finding out when the model becomes invalid and for switching over to the thick or thin sheet models, described in Sec.6.2, as the case may be. Further, the incorporation of suggestion (a) above would increase the compution and, therefore, for any further work it is essential that suitable techniques are developed for causing a quick convergence of the iteration matrix. This effort will be worth while particularly when the number of nodes in the mathematical model will have to be increased for the purpose of incorporating the suggestions given under (c) to (f) below.

(c) The circular geometry of the primary and secondary members of the BTFCM was adapted in order to eliminate entry and exit effects. Also, the lateral forces cancel out for the same reason. However, these will be present when the transverse flux machine is used in truly linear form for HSGT applications and therefore, the inclusion of these features in the mathematical model is another important area for further work.

(d) Dynamic movement in the lateral and vertical directions including pitch, yaw and roll will be a common occurrence in a practical application. Therefore, knowledge of the effects of these on the lateral and vertical stiffnesses is essential, and forms a vital study for showing the viability of any such proposed transport system. Such a study can also incorporate the effects on the lateral and vertical stiffnesses of bending the secondary conducting plate along its edge [63].

(e) The three-dimensional model used in this thesis may then be supplemented by the above proposals and also a thermal circuit added to take account of the three-dimensional heat flow in the machine. This will enable a systems approach to be used in the development of machines for particular applications.

(f) The experience to be gained from the recommended work may be further extended and suitable equivalent circuits devised for routine use in design offices. The possible form of the complete equivalent circuit may incorporate one separate equivalent circuit (linked with others) for each force. This can then be used to devise a suitable hybrid process of design analysis and optimisation for the electromagnetic device [42,60].

7.3 GENERAL CONCLUSION

It is hoped that the approach reported in this thesis together with the results of the recommendations made in Sec.7.2 may lead to the possibility of designing and costing such special purpose electromagnetic devices as the transverse flux linear induction machine. The approach, described in Chapter 6, for including the eddy currents in the secondary solid backing iron (and the resulting saturation) is general so far as the secondary member is concerned and, therefore, it should be useful in the analysis of machines other than transverse flux type as well.

REFERENCES

REFERENCES

1. Freeman, E.M. and Lowther, D.L.: 'Normal force in single sided linear induction motors', Proc. IEE, 1973, 120, (12), pp 1499-1506.
2. Matsudaira, T.: 'How high can train speed be increased ?', Japanese Railway Engineering, Tokyo, June, 1966.
3. 'Advanced ground transport', report published by Science Research Council, State House, High Holborn, London, Oct. 1975.
4. Porter, J.: 'Non-contact suspension systems as alternatives to the wheel', TRRL Report LR517, 1972.
5. Ellison, A.J. and Bahmanyar, H: 'Contact-free propulsion and suspension systems for future high-speed surface guided vehicles', International Hovering Craft, Hydrofoil and Advanced Transit Systems Conference, 13-16 May, 1974, Brighton, Sussex.
6. Ellison, A.J. and Bahmanyar, H.: 'Surface-guided transport systems of the future', Proc. IEE, Nov. 1974, 121, (IIR), IEE Reviews.
7. Bliss, D.S.: 'The evolution of tracked air-cushion vehicle', Hovering Craft and Hydrofoil, 1970, 9, (11 and 12), pp 17-48 and 6-39.
8. Jaywant, B.V. and West, J.C.: British Patent No. 1165704.
9. Polgreen, G.R.: 'Railways with magnetic suspension', The Engineer, 25 Oct., 1968, pp 632-636.

10. Polgreen, G.R.: 'The ideal magnet - fully controllable permanent magnets for power transport', Electronics and Power, Jan. 1971, pp 31-34.

11. Geary, P.J.: 'Magnetic and electric suspensions', SIRA Research Report p 314, 1964.

12. Rhodes, R.G. and Eastham, A.R.: 'Magnetic suspension for high speed trains', Hovering Craft and Hydrofoil, 1971, II, (3), pp 12-26.

13. 'A new system for magnetic levitation', Rutherford Laboratory (S.R.C.) and Culham Laboratory (U.K. Atomic Research Authority) CR 7676.

14. Earnshaw, S.: 'On the nature of the molecular forces which regulate the constitution of the luminiferous ether', Cam. Phil. Soc. 1842, 7, pp 97-112.

15. Braunbeck, W.: 'Freischwebende Körper im elektrischen und magnetischen feld', Z. Phys., 1939, 112, pp 753-763. Culham Laboratory Translation, CTO/1181(Draft)

16. Bevir, M.K.: 'The stability of electromagnetic levitation system for solid bodies', UKAEA Culham Laboratory, Culham Laboratory Preprint CLM-P, 458.

17. Wormell, R.: 'Electricity in the service of man', Cassell and Co. Ltd., London (1896).

18. Andreé, H.: French Patent No. 361098 (1905) and German Patent No. 181014 (1904).

19. Kemper, H.: German Patent No. 643316 (1934).

20. Laithwaite, E.R., Eastham, J.F., Bolton, H.R. and Fellows, T.G.: 'Linear Motors with transverse flux', Proc. IEE, 1971, 118, (12), pp 1761-1767.

21. Eastham, J.F. and Alwash, J.H.: 'Transverse flux tubular motors', ibid, 1972, 119, (12), pp 1709-1718.

22. Eastham, J.F. and Laithwaite, E.R.: ' Linear motor topology', ibid, 1973, 120, (3), pp 337-343.

23. White, D.C., Thornton, R.D., Kingsley, C., and Navon, D.H.: 'Some problems related to electric propulsion', report prepared for the U.S. Department of Commerce, Contract C-85-65, Nov. 1966.

24. Bolton, H.: 'The design of special purpose induction machines', Ph.D. thesis, Imperial College, London, 1971.

25. Chahal, J.S.: 'Some aspects of a transverse flux linear induction motor design, suitable for high speed applications', Conference on Linear Electric Machines, IEE Conf. Pub. No. 120, 21-23, Oct., 1974, pp 161-166.

26. Barwell, F.T.: Personal communication.

27. Binns, K.J. and Lawrenson, P.J.: 'Analysis and computation of electric and magnetic field problems', Pergman Press, Oxford, 1963.

28. Vitkovitch, D.: 'Field analysis - experimental and computational methods', D. Van Nostrand Co. Ltd., London, 1966.

29. Cook, David M.: 'The Theory of the Electromagnetic Field', Prentice-Hall, INC, Englewood Cliffs, New Jersey, 1975.

30. Carpenter, C.J.: 'Finite-element network models and their application to eddy-current problems', Proc. IEE 1975, 122, pp 455-462.

31. Southwell, R.V.: 'On relaxation methods, a mathematics for engineering science', Proc. Roy. Soc. A., 1945, 184, p 253

32. Ehrlich, L.W.: 'Monte Carlo solutions of boundary-value problems', J.Ass. Comp.Mach., 1959, 6, (2), p 204.

33. Erdelyi, E.A., Ahmad, S.V., and Hopkins, R.E.: 'Nonlinear theory of synchronous machine on-load', IEEE Trans., 1966, PAS85, pp 792-801.

34. Young, D.: 'Modern mathematics for the engineer' McGraw Hill, 1961

35. Forsythe, E.G. and Wasow, R.W.: 'Finite difference methods for partial differential equations', John Wiley & Sons, 1960.

36. Ehrenborg, Jöns and Sigdell, Jan-Erik: 'Magnetic eddy current fields calculated by complex over-relaxation', Ericsson Technics, 1963, (1), pp 31-56.

37. Stoll, R.L.: 'Solution of linear steady-state eddy current problems by complex successive over-relaxation', Proc. IEE, 1970, 117, pp 1317-1323

38. Sharples, K.O.: Personal communication, 1975.

39. Crandall, S.H.: 'Engineering analysis', McGraw-Hill, New York, 1956.

40. Smith, G.D.: 'Numerical solution of partial differential equations', Oxford, 1965, pp 65-78

41. Young, D.: 'Iterative methods for solving partial difference equations of elliptic type', Trans. Amer. Math. Soc., 1954, 76, pp 92-111.

42. Mahendra, S.N.: 'Computer-aided analysis and optimisation of three phase squirrel cage induction motor design', M.Sc.(Eng.) Dissertation, Banaras Hindu University, India, 1972.

43. Sharma, M.A.: 'Computer-aided analysis of three dimensional electromagnetic field problems as applied to the design of electrical machinery', The Journal of the Institution of Engineers, India, 1974, 54, (EL4), pp 105-111.

44. Carpenter, C.J.: 'Computation of magnetic fields and eddy currents', 5th Int. Conf. on Magnet Technology, Rome, April 1975. pp 147-158

45. Carpenter, C.J., Djurovic, M.: 'Three-dimensional numerical solution of eddy currents in thin plates', Proc. IEE, 1975, 122, (6), pp 681-688.

46. Carpenter, C.J.: 'Theory and application of magnetic shells', ibid, 1967, 114, (7), pp 995-1000.

47. Carpenter, C.J.: 'Three-dimensional stray-loss problems', Imperial College, 1972.

48. Dorn, William S. and McCracken, Daniel D.: 'Numerical methods with Fortran IV case studies', John Wiley and Sons, Inc., New York, 1972.

49. Carpenter, C.J.: 'Surface integral methods of calculating forces on magnetised iron parts', Proc. IEE , Monograph 342, August 1959, 107C, p 19.

50. Carpenter, C.J.: 'Numerical solution of magnetic fields in the vicinity of current-carrying conductors', Proc. IEE, 1967, 114, (11) pp 1793-1800.

51. Lowther, D.A.: 'A study of the 3-axis forces in linear induction machines using electromagnetic scale models', Ph.D. thesis, Brighton Polytechnic, 1973.

52. Bolton, H.: Personal communication, 1974.

53. Bass, H.G.: 'Introduction to engineering measurements', McGraw Hill Publishing Co. Ltd., London, 1971.

54. Coutts, J.A.: Personal Communication, 1974.

55. Halford, A.J.: Personal communication, 1974.

56. Mahendra, S.N.: 'Linear oscillating induction machines', M.Sc. (Eng.) Project, Banaras Hindu University, India, 1972.

57. Freeman, E.M.: Lowther, D.A. and Laithwaite, E.R.: 'Scale model of linear induction motor', Proc. IEE, 1975, 122, (7), pp 721-726.

58. Carpenter, C.J., and Locke, D.H.: ' Numerical models of three-dimensional end winding arrays', Proc. COMPUMAG Conf. on Computation of Magnetic fields, Oxford, April 1976, pp 47-55.

59. Carpenter, C.J., Sharples, K.O. and Djurovic, M.: 'Heating in transformer cores due to radial leakage flux - Part 2', Proc. IEE (to be published)

60. Rajsekar, G., Bhattacharyya, M. and Mahendra, S.N.:'Computer-aided design of three-phase squirrel cage induction modors - Design technique, Hybrid process and Optimisation', The Journal of the Institution of

Engineers (India), Electrical Engineering, Dec. 1974, 55, (EL2), pp 42-50.

61. Bhattacharyya, M. and Mahendra, S.N.: 'Self-oscillating single phase linear motor', ibid, Feb. 1975, 55, (EL3), pp 134-138

62. Bhattacharyya, M. and Mahendra, S.N.: 'Switchless undulating motor for shuttle propulsion', RDOEI Seminar Record, 'Industrial Machines and their control', Nov. 1971, pp 28-1 to 28-8. Bhopal, India.

63. Eastham, J.F. and Laithwaite, E.R.: 'Linear induction motor as 'electromagnetic rivers'',Proc. IEE, 1974, 121, (10), pp 1099-1108.

64. Laithwaite, E.R.: 'Electromagnetic rivers', Elect. Eng. (Melb.), 51, (4), 1974, pp 11-15.

65. Carpenter, C.J.: 'Theory of flux penetration into laminated iron cores and associated losses', Proc. IEE (to be published).

66. Carpenter, C.J. and Lowther, D.A.:'Losses due to transverse fluxes in laminated iron cores', Conference on Advances in Magnetic Materials, London, 1976, pp 37-40.

67. Naussbaum, A.:'Field theory', Charles E. Merrill Books, Inc., Columbus, Ohio, 1966.

68. Stoll, R.L.: 'Approximate formula for the eddy-current loss induced in a long conductor of rectangular cross-section by a transverse magnetic field', Proc. IEE, 1969, 116, (6), pp 1003-1008.

APPENDICES

APPENDIX A PROPERTIES OF SECOND ORDER PARTIAL DIFFERENTIAL EQUATIONS

The general form of a second order partial differential equation involving two independent variables may be stated as

$$A\frac{\partial^2 \psi}{\partial x^2} + B\frac{\partial^2 \psi}{\partial x \partial y} + C\frac{\partial^2 \psi}{\partial y^2} + D\frac{\partial \psi}{\partial x} + E\frac{\partial \psi}{\partial y} + F\psi + G = 0 \qquad \text{A.1}$$

where ψ is the dependent variable and x and y are the independent variables. If the coefficient A to G are functions of x and y only, the equation is said to be linear. In non-linear equations they also depend on ψ or its derivative. The value of these coefficients determine[39] the type of equation and hence the method of solution. The important parameter

$$\lambda = B^2 - 4AC \qquad \text{A.2}$$

decides eqn.A.1 to be elliptic, parabolic or hyperbolic according to whether λ is negative, zero or positive.

The elliptic equations normally occur in equilibrium problems, whereas the parabolic and hyperbolic types occur in propagation problems. A distinction between equilibrium and propagation problems can be made in terms of the type of conditions applied at the boundaries of the solution domain. In an equilibrium problem the domain is closed and the boundary conditions are prescribed around the entire boundary: such a problem is often said to be the boundary value type.

The Laplace's equation in three dimension Cartesian co-ordinate system is given by

$$\frac{\partial^2 \psi}{\partial x^2} + \frac{\partial^2 \psi}{\partial y^2} + \frac{\partial^2 \psi}{\partial z^2} = 0 \qquad \text{B.1}$$

Consider an asymmetrical star with the node under consideration '0' and surrounding nodes 1,2,3,4,5 and 6.

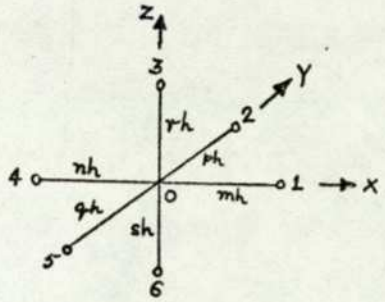

The internode spacing between node '0' and surrounding nodes is mh,ph,rh,nh,qh and sh respectively. In a symmetrical case

$$m = n = p = q = r = s = 1 \qquad \text{B.2}$$

At any point x, on the line parallel to the x-axis passing through the point '0', the potential ψ can be expressed as

$$\psi = \psi_0 + \left(\frac{\partial \psi}{\partial x}\right)_0 \cdot (x - x_0) + \frac{1}{2!} \cdot \left(\frac{\partial^2 \psi}{\partial x^2}\right)_0 \cdot (x - x_0)^2 + \frac{1}{3!} \left(\frac{\partial^3 \psi}{\partial x^3}\right)_0 \cdot (x - x_0)^3 + \left(\frac{\partial^4 \psi}{\partial x^4}\right)_0 \cdot (x - x_0)^4 + \cdots \qquad \text{B.3}$$

The potential at nodes 1 and 4 can be obtained by substituting $x = x_0 - mh$ and $x = x_0 - nh$ respectively. Thus

$$\psi_1 = \psi_0 + mh \cdot \left(\frac{\partial \psi}{\partial x}\right)_0 + \frac{m^2 h^2}{2!}\left(\frac{\partial^2 \psi}{\partial x^2}\right)_0 + \frac{m^3 h^3}{3!}\left(\frac{\partial^3 \psi}{\partial x^3}\right)_0 + \frac{m^4 h^4}{4!}\left(\frac{\partial^4 \psi}{\partial x^4}\right)_0 + \cdots \qquad \text{B.4}$$

$$\psi_4 = \psi_0 - nh \cdot \left(\frac{\partial \psi}{\partial x}\right)_0 + \frac{n^2 h^2}{2!}\left(\frac{\partial^2 \psi}{\partial x^2}\right)_0 - \frac{n^3 h^3}{3!}\left(\frac{\partial^3 \psi}{\partial x^3}\right)_0 + \frac{n^4 h^4}{4!}\left(\frac{\partial^4 \psi}{\partial x^4}\right)_0 + \cdots \qquad \text{B.5}$$

The sum of n - times eqn.B.4 and m - times eqn.B.5 on simplifaction yields

$$n\psi_1 + m\psi_4 = (m+n)\psi_0 + \frac{h^2}{2!}mn(m+n)\left(\frac{\partial^2\psi}{\partial x^2}\right)_0 + \frac{h^3}{3!}mn(m^2-n^2)\left(\frac{\partial^3\psi}{\partial x^3}\right)_0 + \frac{h^4}{4!}mn(m^3+n^3)\left(\frac{\partial^4\psi}{\partial x^4}\right)_0 + \cdots\cdots\cdots \quad B.6$$

Ignoring terms containing higher power of h, eqn.B.6 may be re-written as,

$$n\psi_1 + m\psi_4 = (m+n)\psi_0 + \frac{h^2}{2!}mn(m+n)\left(\frac{\partial^2\psi}{\partial x^2}\right)_0$$

Or

$$\left(\frac{\partial^2\psi}{\partial x^2}\right)_0 = \frac{1}{h^2}\left[\frac{2\psi_1}{m(m+n)} + \frac{2\psi_4}{n(m+n)} - \frac{2\psi_0}{mn}\right] \quad B.7$$

In a similar manner expressions can be written for $\left(\frac{\partial^2\psi}{\partial y^2}\right)_0$ and $\left(\frac{\partial^2\psi}{\partial z^2}\right)_0$ as

$$\left(\frac{\partial^2\psi}{\partial y^2}\right)_0 = \frac{1}{h^2}\left[\frac{2\psi_2}{p(p+q)} + \frac{2\psi_5}{q(p+q)} - \frac{2\psi_0}{pq}\right] \quad B.8$$

and,

$$\left(\frac{\partial^2\psi}{\partial z^2}\right)_0 = \frac{1}{h^2}\left[\frac{2\psi_3}{r(r+s)} + \frac{2\psi_6}{s(r+s)} - \frac{2\psi_0}{rs}\right] \quad B.9$$

Substituting eqns.B.7 to B.9 in eqn. B.1 yields after simplifying,

$$\frac{2\psi_1}{m(m+n)} + \frac{2\psi_2}{p(p+q)} + \frac{2\psi_3}{r(r+s)} + \frac{2\psi_4}{n(m+n)} + \frac{2\psi_5}{q(p+q)} + \frac{2\psi_6}{s(r+s)} - 2\psi_0\left(\frac{1}{mn} + \frac{1}{pq} + \frac{1}{rs}\right) = 0 \quad B.10$$

And for a symmetrical case, from eqns.B.2 and B.10

$$\psi_1 + \psi_2 + \psi_3 + \psi_4 + \psi_5 + \psi_6 - 6\psi_0 = 0 \quad B.11$$

or

$$\sum_{n=1}^{6}(\psi_n - \psi_0) = 0 \quad B.12$$

APPENDIX C CALCULATION OF COMPLEX OPTIMUM ACCELERATION FACTOR

An effective criterion, for investigating the convergence of the successive over relaxation (S.O.R.) scheme, is the study of the error vector after N iterations defined as,

$$\bar{e}^N = \bar{\psi} - \bar{\psi}^N \qquad \text{C.1}$$

where $\bar{\psi}$ is the true complex potential matrix,

$\bar{\psi}^N$ is the complex potential after N number of iterations

Eqn.C.1 can be expressed in the form (40)

$$\bar{e}^N = \sum_{s=1}^{N-2} k_s \lambda_s^N \bar{\nu}_s \qquad \text{C.2}$$

where k_s are constants,

λ_s are eigenvalues,

$\bar{\nu}_s$ are eigenvectors, and,

s = 1,2,3...., n-2,(n being number of nodes in finite difference grid).

An essential condition for S.O.R. method to converge is that the eigenvalues must live within a 'unit circle'(37) i.e., the absolute value of the dominant eigenvalues (the spectral radius) should be less than unity.

In practice it is difficult to find λ_s for a complex matrix using eqn.C.2. It's approximate value, however, can be obtained by integrating the error or residual over the iteration matrix and taking the ratio of its values at two successive iterations. Thus, the dominant eigenvalue is

$$\lambda \simeq \frac{R^N}{R^{N-1}} \qquad \text{C.3}$$

where $R^N = \sum_{1}^{n} (\text{Residual})_i$ C.4

Therefore, the critical eigenvalue (μ) can be found using Young's [41] equation.

$$(\lambda + \alpha_{old} - 1)^2 = \lambda \alpha_{old} \mu^2 \qquad C.5$$

$$\mu = \sqrt{\frac{(\lambda + \alpha_{old} - 1)^2}{\lambda \alpha_{old}^2}} \qquad C.6$$

And, using Stoll's [37] formula, the optimum acceleration factor is,

$$\alpha_b = \frac{2}{1+\sqrt{1-\mu^2}} \qquad C.7$$

where $\sqrt{1-\mu^2}$ is the factor determined on the basis of the convergence taking place. Let us define a factor.

$$C_f = \sqrt{1-\mu^2} \qquad C.8$$

such that after substituting eqn.C.6 in eqn.C.8 we have,

$$C_f = 1 - \frac{(\lambda + \alpha_{old} - 1)^2}{\lambda \alpha_{old}^2} \qquad C.9$$

Therefore, the optimum acceleration factor for the next set of iterations, in terms of the old acceleration factor and the dominant eigenvalue of the iteration matrix, is

$$\alpha_b = \frac{2}{1+\sqrt{C_f}} \qquad C.10$$

On substituting eqn.C.9 in eqn.C.10 and simplifying we have,

$$\alpha_b = \frac{2\alpha_{old}\sqrt{\lambda}}{\alpha_{old}\sqrt{\lambda} + \sqrt{(1-\lambda)\{\lambda - (\alpha_{old}-1)^2\}}} \qquad C.11$$

where λ is defined by eqn.C.3 and α_{old} is the old acceleration factor.

The new accleration factor (α_{new}), however, should be less than the optimum defined by eqn.C.11 [37], and Carre has suggested an empirical formula for estimating $\alpha_{new(real)}$ as,

$$R_e(\alpha_{new}) = R_e(\alpha_b) - F\{2 - R_e(\alpha_b)\} \qquad C.12$$

where F= 0.25 Re denotes the real part.

In complex S.O.R., therefore, eqn.C.12 can be applied to alter the real part of α_b while keeping the imaginary part unaltered. The value of F= 0.2 has been found to be more appropriate for 2-dimensional eddy-current problem involving both conducting and non-conducting regions [37]. The advantage of a lower value of F is that, while still seeking the optimum factor, the solution progresses using a factor that is closer to that optimum. This is important especially with large problems, where the optimum may never be reached during the course of the solution, but because it proceeds with factors close to the optimum, there is a greater possibility of quicker convergence.

APPENDIX D CURRENT-SHEET AND FLUX-SHEET EQUIVALENTS FOR A MAGNETISING WINDING

A magnetising winding can be replaced by its equivalent current-sheet and flux-sheet such that the field outside the winding is still the same. The field inside it may also be determined but, more often, it is the surrounding field that is desired for analysing the behaviour of the electromagnetic device. Obtaining the current sheet and the flux sheet is easily achieved by taking advantage of the knowledge that the electric and magnetic properties of the winding are equivalent to two linked networks. These networks can be replaced by equivalent branch sources by 'tearing'[45] the networks apart in any arbitrary way and inserting into each of the magnetic branches an m.m.f. equal to the amount of current which intersects it. The m.m.f. generators are then replaced by flux generators by using Norton's theorem and hence the flux-sheet and current-sheet are obtained.

However, when a core is not uniformly wound or has a number of coils carrying different currents, the same principle applies for each uniformly wound portion. The current sheet will be composed of several sheets, one for each winding and the variation of m.m.f. along the composite sheet will show the separate contributions of the windings. As before, flux sheets will exist along the end faces of the windings, and where two windings occur with their end faces close together, the corresponding flux sheets will naturally be in close proximity. It often happens that these flux sheets pass through the same set of nodes, and in such cases these sheets will combine into a single sheet.

As an example, consider two windings carrying different currents, though having the same number of turns N. In this example, the adjacent end faces of the windings are separated by a distance equal to one node spacing. If the currents are $I_1\angle\theta_1$ and $I_2\angle\theta_2$ respectively, the equivalent current sheet and flux sheet are as shown in Fig.D.1. The current sheet distribution is given by:

$$C_s = NI_1\angle\theta_1\left(\frac{y}{a}\right) \qquad \text{for } 0<y<a \qquad \text{D.1(a)}$$

$$C_s = NI_1\angle\theta_1 \qquad \text{for } a<y<b \qquad \text{D.1(b)}$$

$$C_s = NI_1\angle\theta_1 + NI_2\angle\theta_2\left(\frac{y-b}{c-b}\right) \qquad \text{for } b<y<c \qquad \text{D.1(c)}$$

and the flux sheet distribution by

$$F_{s1} = NI_1\angle\theta_1\left(\frac{x}{w}\right)\left(\frac{1}{\mu\mu_0}\cdot\frac{a}{w}\right) \qquad \text{D.2(a)}$$

$$F_{s2} = NI_2\angle\theta_2\left(\frac{x}{w}\right)\left(\frac{1}{\mu\mu_0}\cdot\frac{c-b}{w}\right) \qquad \text{D.2(b)}$$

where w,a,b,c,x and y are explained in Fig.D.1(a), μ_0 is the permeability of the free space, and μ is the relative permeability of the medium.

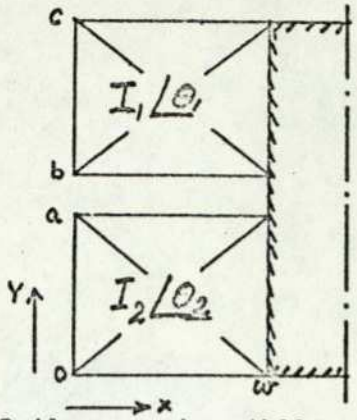

(a) Coils carrying different currents

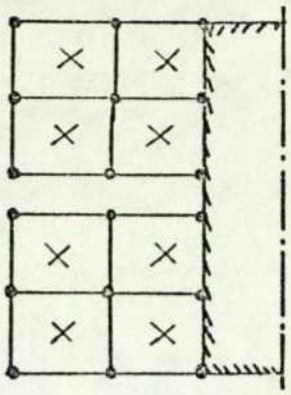

(b) Winding replaced by equivalent mmf(x) in meshes

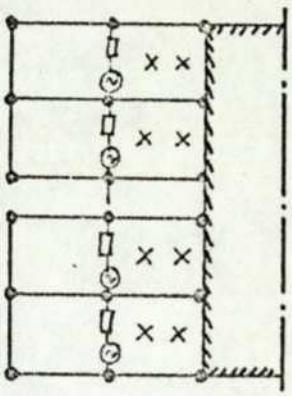

(c) 'Tearing' across the walls of the mesh resulting in mmf generators (⌀)

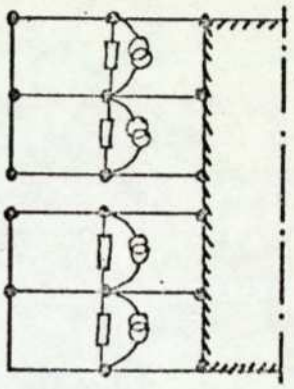

(d) Equivalent flux generators from Norton's theorem

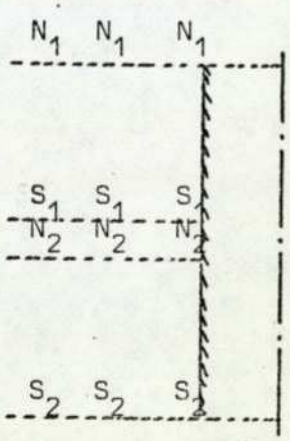

(e) Equivalent flux-sheets for each coil shown in (a) above

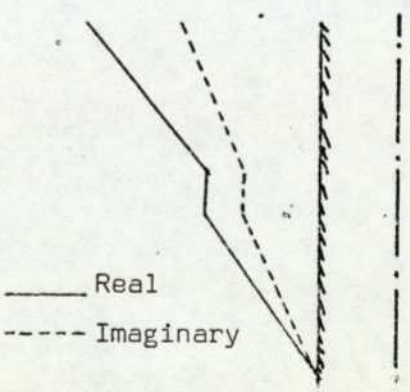

(f) Equivalent resultant current-sheet due to coils shown in (a) above

Fig.D.1 Flux-sheet and current-sheet for two rectangular coils carrying non-equal currents. The directions shown are instantaneous ones.

APPENDIX E DERIVATION OF MAXWELL'S SECOND STRESS TENSOR

The derivation of Maxwell's stress-energy tensor has been discussed in many standard text books on electromagnetic fields. Of the four vectors, three are for stresses and together they form Maxwell's stress tensor. This stress tensor has two distinct components, one (consisting of electric field stresses) is known as the 'first stress tensor', and the other (consisting of magnetic field stresses) is called the 'second stress tensor'. It is the 'second stress tensor' that is of direct interest and it has been derived below.

Neglecting the surface charge and displacement currents, the Maxwell's equations can be expressed as

$$\nabla \times \bar{E} = -\frac{\partial \bar{B}}{\partial t} \qquad \text{E.1}$$

$$\nabla \times \bar{B} = \mu \bar{J} \qquad \text{E.2}$$

$$\text{div}\bar{B} = 0 \qquad \text{E.3}$$

$$\text{div}\bar{E} = 0 \qquad \text{E.4}$$

Further, the cross-product of $\bar{B}$ with eq.E.2 yields,

$$(\nabla \times \bar{B}) \times \bar{B} = \mu \bar{J} \times \bar{B} \qquad \text{E.5}$$

whose left-hand side can be expressed as,

$$(\nabla \times \bar{B}) \times \bar{B} = \bar{a}_x \left(B_z \frac{\partial B_x}{\partial z} - B_z \frac{\partial B_z}{\partial x} - B_y \frac{\partial B_z}{\partial x} + B_y \frac{\partial B_x}{\partial y}\right) + \bar{a}_y \left(-B_z \frac{\partial B_z}{\partial y} + B_z \frac{\partial B_y}{\partial z} + B_x \frac{\partial B_y}{\partial x} - B_x \frac{\partial B_x}{\partial y}\right) + \bar{a}_z \left(B_y \frac{\partial B_z}{\partial y} - B_y \frac{\partial B_y}{\partial z} - B_x \frac{\partial B_x}{\partial z} + B_x \frac{\partial B_z}{\partial x}\right) \qquad \text{E.6}$$

For further derivations only the x - component of eqn.E.6 has been considered thus:

$$\{(\nabla \times \bar{B}) \times \bar{B}\}_x = B_x \frac{\partial B_x}{\partial x} + B_z \frac{\partial B_x}{\partial z} - B_z \frac{\partial B_z}{\partial x} - B_y \frac{\partial B_y}{\partial x} + B_y \frac{\partial B_x}{\partial y} - B_x \frac{\partial B_x}{\partial x} \qquad \text{E.7}$$

which on simplification becomes,

$$\{(\nabla\times\bar{B})\times\bar{B}\}_x = \frac{\partial}{\partial x}(B_x^2 - \frac{1}{2}B^2) + \frac{\partial}{\partial y}(B_x B_y) + \frac{\partial}{\partial z}(B_x B_z) \qquad \text{E.8}$$

where $$|B|^2 = B_x^2 + B_y^2 + B_z^2 \qquad \text{E.9}$$

Similarly, the y- and z- components of eqn.E.6 may be solved and the three together may be expressed as divergence of a tensor which is defined as,

$$T^m = \frac{1}{\mu\mu_r}\begin{vmatrix} (B_x^2 - \frac{1}{2}|B|^2) & B_x B_y & B_x B_z \\ B_y B_x & (B_y^2 - \frac{1}{2}|B|^2) & B_y B_z \\ B_z B_x & B_z B_y & (B_z^2 - \frac{1}{2}|B|^2) \end{vmatrix} \qquad \text{E.10}$$

where T^m is the magnetic stress tensor and is also known as Maxwell's second stress tensor.

Thus eqn.E.5 may be re-written as,

$$\bar{J}\times\bar{B} = \text{div}T^m \qquad \text{E.11}$$

where JxB has the dimension of force per unit volume

Therefore, the total force on any enclosed volume may be obtained by taking volume integral of eqn.E.11,i.e.,

$$\bar{F} = \iiint(\bar{J}\times\bar{B})dv = \iiint \text{div}T^m dv \qquad \text{E.12}$$

Using divergence theorem, eqn.E.12 can be re-written as

$$\bar{F} = \iint(T^m\bar{n})da \qquad \text{E.13}$$

where n is a unit vector normal to the surface on which the force is being determined.

APPENDIX F EFFECTIVE THICKNESS OF A CONDUCTING SHEET

The current density distribution in a conducting sheet due to an alternating field is given by

$$\bar{J} = \sigma \bar{E} \qquad F.1$$

Taking the curl of both sides and substituting $\nabla \times \bar{E} = -\dot{\bar{B}}$ yields for a sinusoidal variation of $\bar{B}$ with respect to time

$$\nabla \times \bar{J} = -\sigma \dot{\bar{B}} = -j\sigma\omega\bar{B}. \qquad F.2$$

Taking the curl of both sides again in eqn. F.2 and substituting for $\nabla \times \bar{B} = \mu \bar{J}$ (assuming constant μ)

$$\nabla \times \nabla \times \bar{J} = -j\omega\mu\sigma\bar{J}$$

or $$\nabla^2 \bar{J} = j\omega\mu\sigma\bar{J} \qquad F.3$$

assuming that $\nabla . \bar{J}$ is zero because $\rho = o$ within the conductor. Replacing $j\omega\sigma\mu$ [for convenience later] by $4\gamma^2$, eqn. F.3 becomes

$$\nabla^2 \bar{J} = 4\gamma^2 \bar{J}. \qquad F.4$$

Eqn. F.4 is the diffusion equation for $\bar{J}$ in the conducting sheet. Assuming a z-axis normal to the plane of the conducting sheet, the current density through the depth can be given by

$$\bar{J} = \bar{C}\, e^{-2\gamma z} + \bar{D}\, e^{2\gamma z} \qquad F.5$$

where $\bar{C}$ and $\bar{D}$ are functions of x and y only. They are also vectors since $\bar{J}$ is, and along the depth of the conducting sheet for constant values of x and y, they become fixed vectors having values that do not change with z.

Consider a z = o plane in the middle of the sheet, such that at the top surface $z = \frac{t}{2}$ and at the bottom surface $z = -\frac{t}{2}$ (where t is the thickness of the conducting sheet). Then the current densities at the two surfaces are

$$\bar{J}_b = \bar{C}\, e^{\gamma t} + \bar{D}\, e^{-\gamma t} \quad \text{at } z = -\tfrac{t}{2} \qquad F.6$$

and $$\bar{J}_t = \bar{C}\, e^{\gamma t} + \bar{D}\, e^{\gamma t} \quad \text{at } z = \tfrac{t}{2}$$

These current densities are wholly tangential and it is assumed that $J_z = o$, and therefore, as mentioned earlier, $\bar{C}$ and $\bar{D}$ also have zero z-components. Thus the general form of the eqn. F.5 describing the current density in a thick conducting sheet is

$$\bar{J} = \hat{a}_x J_x + \hat{a}_y J_y \qquad \text{F.7}$$

On solving eqn.F.6, constants $\bar{C}$ and $\bar{D}$ are given as

$$\bar{C} = \frac{1}{e^{2\gamma t} - e^{-2\gamma t}} \cdot \left[\bar{J}_b e^{\gamma t} - \bar{J}_t e^{-\gamma t} \right]$$

$$\bar{D} = \frac{1}{e^{2\gamma t} - e^{-2\gamma t}} \cdot \left[\bar{J}_t e^{\gamma t} - \bar{J}_b e^{-\gamma t} \right] \qquad \text{F.8}$$

The currents along x and y directions in the conducting sheet passing through small areas dydz and dxdz respectively are given by

$$dI_x = J_x \, dydz = dK_x . dy \qquad \text{F.9}$$

$$dI_y = J_y \, dxdz = dK_y . dx$$

where dK_x and dK_y are components of surface current density $d\bar{K}$ along x and y directions respectively.

From eqn.F.9 the surface current density in the conducting sheet along the x and y directions is obtained by integrating eqn.F.5 between the two surfaces. Thus

$$K_x = \int_{\text{bottom}}^{\text{top}} J_x dz \qquad \text{F.10}$$

and

$$K_y = \int_{\text{bottom}}^{\text{top}} J_y dz$$

where J_x and J_y are given by eqns.F.5 to F.7.

On integrating, eqn.F.10 becomes

$$K_x = \frac{\lambda}{2} (J_{bx} + J_{tx})$$

$$K_y = \frac{\lambda}{2} (J_{by} + J_{ty}) \qquad \text{F.11}$$

where $\lambda = \frac{1}{\bar{\gamma}} \tanh(\gamma t)$. $\qquad$ F.12

APPENDIX G EFFECTIVE THICKNESS APPROACH FOR DEFINING SURFACE MAGNETIC IMPEDANCE

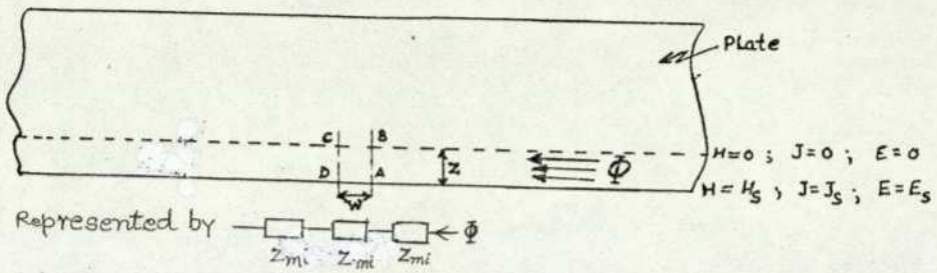

Fig. G.1

Consider an elementary section of the plate having a width w small enough for H_s not to vary significantly along it. From Ampere's circuital relation

$$\oint_L \bar{H}.\bar{ds} = I \qquad \text{G.1}$$

and when applied to an elementary area ABCD

$$H_s w = w \int_0^z \bar{J} dz. \qquad \text{G.2}$$

Substituting the solution of eqn.F.10 in eqn.G.2 for conditions given in Fig.G.1 we have

$$H_s = J_s \frac{\lambda}{2} . \qquad \text{G.3}$$

Define $\frac{\lambda}{2}$ as $t_{(effective)}$ as in eqn.6.29 gives

$$H_s = J_s \, t_{(effective)} \qquad \text{G.4}$$

Also from Ohm's law

$$J_s = \sigma E_s \qquad \text{G.5}$$

therefore the surface magnetic impedance from eqns.G.4 and G.5 is

$$Z_{mi} = \frac{H_s}{E_s} = \sigma t_{(effective)} \qquad \text{G.6}$$

APPENDIX H COMPUTER PROGRAMME

In Chapters 2,3 and 6 an approach has been outlined and the finite difference equations have been discussed for obtaining the MSP distribution, flux density and forces in the BTFCM. Based on these discussions and the flow diagram given in Fig.3.5 a computer programme has been developed. The main sections of this computer programme are given below and its listing is given in Fig.H.1.

(a) Initialisation of 3-dimensional MSP and flux sheet matrices to zero. (Between card numbers 33 and 44.)

(b) Description of the primary member by current sheet and flux sheet. This section requires an input data for defining the phase and magnitude of currents on the overhang and in the slot in conformity with the discussion in Appendix D. (Between card numbers 45 and 169.)

(c) Description of the secondary member properties in terms of the magnetic impedance between nodes lying on its surface. The equations for the magnetic impedance have been discussed in Chapters 3 and 6. The BTFCM has a circular geometry and the internode spacing between the nodes in all the directions is non-uniform. This has been accounted in the computer programme between card numbers 186 and 360.

(d) Check for convergence and termination of the programme. In this section the criteria used for the termination of the computer programme are

i. the highest residual is less than a pre-set value (the programme has converged),

ii. the number of iterations is greater than a pre-set value (the programme has not fully converged and considered to be taking too much time. The results are printed out and examined to see if they are meaningful.)

iii. the highest residual is greater than a pre-set value (the programme has diverged).

The relevant cards are between card numbers 475 and 536.

(e) Iteration of the 3-dimensional MSP matrix. This is done by successive over-relaxation using Carré-Stoll acceleration technique as discussed in Appendix C. After a set number of

iterations, depending upon the covergence behaviour of the iteration matrix, a new acceleration factor is calculated (see Appendix C). The choice of the number of iterations after which a new acceleration factor should be calculated, and the amount by which it should be modified depend upon the problem in hand. These two decisions are critical especially for calculations involving motion of the secondary member. This is so because the effect of the primary flux on the secondary member due to motion is opposite of that due to the alternating nature of the primary excitation. At low slips the former becomes large and comparable to the latter, and their interaction often leads to an inaccurate estimation of the convergence rate and therefore the new acceleration factor. One way of overcoming this problem is to use the three dimensional matrix of the MSP distribution for the slip at which the programme has converged successfully, as the starting point and then reduce the p.u. slip from the initial to the final value in steps (say 100) followed by convergence at the final slip. (Between card numbers 430 and 433, and the subroutine ACCNEW.)

(f) Calculation of flux density and forces. The method of calculating these quantities has been discussed in Chapter 3 and the integration (to obtain the forces) has been done by using the subroutine SIMPR based on Simpson's rule. (Between card numbers 538-708.)

```
      PROGRAM TDN(INPUT,OUTPUT,TAPE1=INPUT,TAPE6=OUTPUT,TAPE8,TAPE9,
     1TAPE10,TAPE11,TAPE12)
      INTEGER PP,P
      DIMENSION        FX(37),FY(37),FZ(37),XF(33),YF(33),ZF(33)
      DIMENSION PP(8),P(6)
      DIMENSION HHY(20),A0(20),HYY(36)
      DIMENSION A1(20),A2(20),A3(10),A4(20),A5(20),A6(10)
      COMPLEX          C1(20),C2(20),C3(20),C4(20),C5(20),C6(20),C0(20)
      COMPLEX C1T(20),C2T(20),C3T(20),C4T(20),C5T(20),C6T(20),C0T(20),
     1         PCIRT,PCIMT
      COMPLEX ZMT,PC,PCIP,PCIM
      COMPLEX U(21,43,10),TA(20,42,3)
      COMPLEX A(6),B,TAU(6),DECRT
      COMPLEX AMPP,EPSLN,UNULL,RESOL,GREAT,ACCL,ACCL0
      COMPLEX B1(20),B2(20),B3(20),B4(20),B5(20),B6(20),B0(20)
      COMPLEX B1T(20),B2T(20),B3T(20),B4T(20),B5T(20),B6T(20),B0T(20),
     1         PCT
      COMPLEX CC1,CC2,CC3,CC4,CC5,CC6,CC0 ,UNITJ
      DIMENSION AM(6),BP(6)
      COMPLEX UPEED,UPIES,UNPEE
      COMPLEX ENTA,ENTY,ENTZ,ENTT
      COMMON/TDCSP/U,TA
      LEVEL 2, U,TA
CCC   ...|....1....|....2....|....3....|....4....|....5....|....6....|....7x
      IN80=1
      IL80=20
      JL80=5
      JR80=41
      KB80=1
      KT80=6
      KT80N=10
CCC   ...|....1....|....2....|....3....|....4....|....5....|....6....|....7x
C     I N I T I A L I S A T I O N
      DO 11 II=IB80N,IL80N
      DO 11 JJ=JL80N,JR80N
      DO 11 KK=KB80N,KT80N
      IF (KK.GT.3) GO TO 10
      TA(I,JJ,KK)=(0.0,0.0)
   10 CONTINUE
      U(II,JJ,KK)=(0.0,0.0)
      GO TO 11
   11 CONTINUE
CCC   ...|....1....|....2....|....3....|....4....|....5....|....6....|....7x
C     DEFINE R.M.S. VALUE OF PHASE CURRENT.
      ARMS=3.0
C     DEFINE MAXIMUM VALUE OF PHASE CURRENT.
      AMP=3.0
      AMP=4.0
      AMP=SQRT(2.0)*ARMS
C     GENERAL DISCRIPTION .
      H=0.005
      H2=2.*0.005
      HH=H*H
      HH2=H2*H2
      FREQ=50.
      PI=4.*ATAN(1.0)
      OMEGA=2.*PI*FREQ
      T=0.0
      PUNCT=4.*PI/(10.**7)
C     STUDY NUMBER 0 NSDY .
      NSDY=1
      WRITE (6,14)NSDY
   14 FORMAT (20X,*CALCULATIONS FOR STUDY NUMBER *,I10,//)
CCCC  ...|....1....|....2....|....3....|....4....|....5....|....6....|....7x
CCCC  ...|....1....|....2....|....3....|....4....|....5....|....6....|....7x
C     THE FOLLOWING PROGRAM IS FOR  THREE PHASE EXCITATION IN STATOR
C     WINDING. THE CONNECTIONS ARE MADE AS FOLLOWS O (+R)-R1,(+B)-O1,(-Y
C     THE CURRENTS IN THE SLOTS O    TOP LAYER   -B+R+R-Y-Y+B+B
C                                    BOTTOM LAYER   +R-Y-Y+B+B-R-R
CCCC  ...|....1....|....2....|....3....|....4....|....5....|....6....|....7x
CCCC  ...|....1....|....2....|....3....|....4....|....5....|....6....|....7x
CCC   ...|....1....|....2....|....3....|....4....|....5....|....6....|....7x
C     DEFINE FUNDAMENTAL SIX  CURRENTS OF MODEL FOR CORE UNDER STUDY.
      DO 12 JJJ=1,7
      JSTAT=(JJJ-1)*6+1
      JS1BP=(JJJ-1)*6+6+1
      JT=(JJJ-1)*6+3+1
      IF (JJJ.EQ.1) JSTAT=5
      IF(JJJ.EQ.7) JSTBP=41
      READ (1,1)  (PP(N),N=1,6)
      READ (1,1)  (P(N),N=1,6)
    1 FORMAT (6I2)
      DO 13  N=1,6
      THETA=2.*PI*P(N)/3.
      AMPR=PP(N)*AMP*COS(OMEGA*T+THETA)
      AMPI=PP(N)*AMP*SIN(OMEGA*T+THETA)
      AMPP= CMPLX(AMPR,AMPI)
      A(N)=60.*ARMS*P/4.
   13 CONTINUE
C     DEFINE THE TA'S FOR FLUX SHEET .  JRJSTAT  .
      JRJSTAT
C     FOR I=10
      I=10
      TA(I,J,3)= 2.80*A(1)+3.00*A(2)              +0.35*A(4)
      TA(I,J,2)=-2.80*A(1)-3.20*A(2)+4.00*A(3)+2.00*A(4)
      TA(I,J,1)=          -0.40*A(2)-4.00*A(3)-2.35*A(4)
C     FOR I=9
      I=9
      TA(I,J,3)= 1.6*A(1)+3.35*A(2)
      TA(I,J,2)=-1.6*A(1)-2.05*A(2)+4.0*A(3)+0.5*A(4)
      TA(I,J,1)=          -0.40*A(2)-4.00*A(3)-0.60*A(4)
C     FOR  I  =  8
      I=8
      TA(I,J,3)= 0.6*A(1)+2.65*A(2)
      TA(I,J,2)=-0.6*A(1)-2.20*A(2)+2.05*A(3)
      TA(I,J,1)=          -0.35*A(2)-2.85*A(3)
C     FOR  I  =  7
      I=7
      TA(I,J,3)=          1.45*A(2)
      TA(I,J,2)=         -1.20*A(2)+1.25*A(3)
      TA(I,J,1)=         -0.25*A(2)-1.25*A(3)
C     FOR  I  =  6
      I=6
      TA(I,J,3)=(0.0,0.0)
```

Fig.H.1 The computer programme

```
      TA(I,J,2)=(0.0,0.0)
      TA(I,J,1)=(0.0,0.0)
C     FOR  I  =  12
      I=12
C     FOR J=J
      TA(I,J,3)= 1.00*A(1)
      TA(I,J,2)=-1.00*A(1)                          -3.00*A(5)
      TA(I,J,1)=                                     3.00*A(5)
C     FOR J=J+1
      TA(I,J+1,3)= 2.00*A(1)
      TA(I,J+1,2)=-2.00*A(1)                        -2.00*A(5)
      TA(I,J+1,1)=                                   2.00*A(5)
C     FOR J=J+2
      TA(I,J+2,3)= 3.00*A(1)
      TA(I,J+2,2)=-3.00*A(1)                        -1.00*A(5)
      TA(I,J+2,1)=                                  1.00*A(5)
C     FOR  I  =  11
      I=11
C     FOR J=J
      TA(I,J   ,3)=TA(I+1,J   ,3)+TA(I-1,J   ,3)+1.20*A(1)+0.10*A(4)
      TA(I,J   ,2)=TA(I+1,J   ,2)+TA(I-1,J   ,2)-1.20*A(1)+1.10*A(4)
      TA(I,J   ,1)=TA(I+1,J   ,1)+TA(I-1,J   ,1)          -1.20*A(4)
C     FOR J=J+1
      TA(I,J+1,3)=TA(I+1,J+1,3)+TA(I-1,J+1,3)+1.20*A(1)+0.10*A(4)
      TA(I,J+1,2)=TA(I+1,J+1,2)+TA(I-1,J+1,2)-1.20*A(1)+1.10*A(4)
      TA(I,J+1,1)=TA(I+1,J+1,1)+TA(I-1,J+1,1)          -1.20*A(4)
C     FOR J=J+2
      TA(I,J+2,3)=TA(I+1,J+2,3)+TA(I-1,J+2,3)+1.20*A(1)+0.10*A(4)
      TA(I,J+2,2)=TA(I+1,J+2,2)+TA(I-1,J+2,2)-1.20*A(1)+1.10*A(4)
      TA(I,J+2,1)=TA(I+1,J+2,1)+TA(I-1,J+2,1)          -1.20*A(4)
C     DEFINING  TA'S  AND  U'S  .J=JSTAT,JSTOP  .
      DO 21 J=JSTAT,JSTOP
      ICON=10
C     DEFINING TA'S FOR FLUX SHEET .  J=JSTAT,JSTOP .
      DO 22 K=1,3
      DO 22 I=6,ICON
      TA(I,J,K)=TA(I,JSTAT,K)
   22 CONTINUE
      IF (J.LT.JT) GO TO 21
C     DEFINING U'S FOR THE CURRENT SHEET .  J=JT,JT+2 .
      DO 15 I=11,13
      U(I,J   ,1)=(0.0,0.0)
      U(I,J   ,2)=4.4*A(2)+4.0*A(3)+3.5*A(4)
      U(I,J   ,3)=4.0*A(1)+4.0*A(2)+4.0*A(3)+4.0*A(4)
   15 CONTINUE
      GO TO 21
   21 CONTINUE
   12 CONTINUE
C     REVERSAL OF TA'S AND U'S ON THE OTHER SIDE OF U-CORE LIMB .
      DO 30 K=1,3
      DO 30 J=JLBON,JRBON
      DO 30 II=6,11
      I=24-II
      TA(I,J,K)=TA(II,J,K)
   30 CONTINUE
C     CARDS CONTAINED WHITHIN ' GO TO 110 ' HAVE BEEN REMOVED .
CCC   ...1.........2.........3.........4.........5.........6.........7.
```

```
C     ITERATION  DETAILS .
      MITER=200
CCC   ...1.........2.........3.........4.........5.........6.........7.
      ACCL=(1.6,0.005)
CC    ...1.........2.........3.........4.........5.........6.........7.
      EPSAE=1.6D0*9.3*100.*AMP*0.0001*0.001
      EPSIM=1.6/9.3/100.*AMP*0.0001*0.001
      EPSAE=500.*EPSAE
      EPSIM=500.*EPSIM
      EPSLN=CMPLX(EPSAE,EPSIM)
CCC   ...1.........2.........3.........4.........5.........6.........7.
      SLIP=0.8
      SLIP=SLIP
      SLIP=1.0
CCC   ...1.........2.........3.........4.........5.........6.........7.
      UNIT=(0.0,1.0)
C     DEFINE CONDUCTIVITY OF PLATE  0  SIGMA
      SIGMA=10.0*8/2.8
C     DEFINE THICKNESS OF PLATE  0  TP
      TP=0.00186
CCC   ...1.........2.........3.........4.........5.........6.........7.
C     DETAILS OF BACKING IRON
C     THICKNESS OF BACKING IRON  0 TBI
C     CONDUCTIVITY               0  SIGMI
C     PERMEABILITY               0  PUIRN
C   LAMINATED IRON THICKNESS =0.01364       SOLID IRON THICKNESS = 0.001
      TBI=0.0129
      TBI=0.00193
      TBI=0.00225
      SIGMI=3.0*10.**6
      PUIRN=200.*PUN01
C     MAGNETIC IMPEDANCES DUE TO ALUMINIUM PLATE (ZMA) AND
      ZMA=SIGMA*TP
      N=A
C     THICKNESS OF PLATE   BACKING IRON  0  HS2
C     TBI  TO BE IGNORED FOR THIN SHEET MODEL.
      HS2=TBI
      HS=HS2/2.0
      HS=TBI
CC    ...1.........2.........3.........4.........5.........6.........7.
C     DEFINING HHY(I) AND AD(I) FOR MODEL ONE .
      HX=H
      HX=HX+DX
      HZ=H/2.
      HHZ=HZ-HZ
      DO 120 I=1,36
      IF (I.GT.2) GO TO 121
      IF (I.EQ.1) DX=32.65
      IF (I.EQ.2) DX=30.65
      GO TO 122
  121 DX=29.65-(I-3)*0.5
  122 HY=2.*PI*DX/(100.*6.*48.)
      HHY(I)=HY
      IF (I.GT.20) GO TO 120
      HHY(I)=HY+HY
      HXP=H
      HXM=H
```

Fig.H.1 (Continued) The computer programme

```
            IF (I.EQ.1) HXP=4.*H
            IF (I.EQ.1) HXM=4.*H
            IF (I.EQ.2) HXP=2.*H
            IF (I.EQ.2) HXM=4.*H
            IF (I.EQ.3) HXM=2.*H
            A1(I)=2./(HXP*(HXP+HXM))
            A2(I)=1.-A1(I)
            A4(I)=2./(HXM*(HXP+HXM))
            A5(I)=A2(I)
  120   CONTINUE
            DO 124 K=1,10
            HZP=H
            HZM=H
            IF (K.LE.3) HZM=2.*H
            IF (K.LT.3) HZP=2.*H
            IF (K.LE.2) HZM=10.*H
            IF (K.LT.2) HZP=10.*H
C     LENGTH OF AIR-GAP FOR THIS STUDY IS SET AT 10 MM.
            GAP=0.010
            HGAP=GAP/4.
            IF (K.GE.3.AND.K.LT.7) HZP=HGAP
            IF (K.GT.3.AND.K.LE.7) HZM=HGAP
            IF (K.EQ.7) HZP=HS
            IF (K.EQ.8) HZM=HS
            IF (K.EQ.8) HZP=2.*H
            IF (K.EQ.9) HZM=2.*H
            IF (K.EQ.9.OR.K.EQ.10) HZP=4.*H
            IF (K.EQ.10) HZM=4.*H
            A3(K)=2./(HZP*(HZP+HZM))
            A5(K)=2./(HZM*(HZM+HZP))
  124   CONTINUE
CCC     ***1*********2*********3*********4*********5*********6*********7**
  170   CONTINUE
C     SATURATED BACKING IRON (ZMI)
            ZMI=(1.-UNITJ)*(SQRT(SIGMI/(2.*SLIP*OMEGA*PUI0N)))
            WRITE (6,115)
  115   FORMAT (//,30X,'COEFICIENTS FOR THE NODES ON SECONDARY PLATE AT ST
           1NDSTILL',//,4X,'I',13X,'B1(I)',17X,'B2(I)',17X,'B4(I)',17X,'B6(I
           2)',17X,'B0(I)',20)
            HZ=HGAP
            HHZ=HZ*HZ
            DO 123 I=6,20
            HY=HYY(I)
            HYM=HYY(I-1)
            VOL=HX*HY*HZ
            PC=OMEGA*PUNIT*VOL*(ZMA+ZMI)
            B1(I)=HX/HY*UNITJ*(PC/(2.*HHX))
            B2(I)=HY/HX*(UNITJ*(PC/(2.*HHY(I))))
            B3(I)=0.0,0.0
            B4(I)=HX/HYM*UNITJ*(PC/(2.*HHX))
            B6(I)=B2(I)
            B5(I)=UNITJ*(PC/HHZ)
            IF (I.NE.6) GO TO 116
            B2(I)=HY/HX*UNITJ*(3.*PC/(4.*HHY(I)))
            B4(I)=UNITJ*(PC/HHX)
            B5(I)=B2(I)
            PC=PC*HS*ZMI/(HZ*(ZMA+ZMI))
            B3(I)=HS/HY*UNITJ*PC/(2.*H*S)
  116   CONTINUE
            B0(I)=B1(I)+B2(I)+B3(I)+B4(I)+B5(I)+B6(I)
            VOLT=HX*HY*2.*H
            PCT=OMEGA*PUNIT*VOLT*ZMI
            B1T(I)=HX/HY*UNITJ*(PCT/(2.*HHX))
            B2T(I)=HY/HX*(UNITJ*(PCT/(2.*HHY(I))))
            B3T(I)=UNITJ*PCT/(4.*H*S)
            B4T(I)=HX/HYM*UNITJ*(PCT/(2.*HHX))
            B5T(I)=B2T(I)
            B6T(I)=0.0,0.0
            IF (I.NE.6) GO TO 117
            B2T(I)=HY/HX*UNITJ*(3.*PCT/(4.*HHY(I)))
            B4T(I)=UNITJ*(PCT/HHX)
            B5T(I)=B2T(I)
            B6T(I)=B3T(I)
  117   CONTINUE
            B0T(I)=B1T(I)+B2T(I)+B3T(I)+B4T(I)+B5T(I)+B6T(I)
            WRITE (6,130) I,B1T(I),B2T(I),B4T(I),B3T(I),B0T(I)
            WRITE (6,130) I,B1(I),B2(I),B4(I),B6(I),B0(I)
  130   FORMAT (3X,I3,2X,10(2X,1PE9.2))
  123   CONTINUE
CC      ***1*********2*********3*********4*********5*********6*********7**
C CALCULATION OF CONSTANTS FOR SPEED EFFECT.
  160   CONTINUE
            UPLE=0.0,0.0
            UPEE=0.5,0.0
            WRITE (6,145) SLIP
  145   FORMAT (//,20X,'CONSTANTS FOR THE NODES ON SECONDARY PLATE TO ACCO
           1UNT FOR THE SPEED EFFECT   SLIP = ',F6.3,
           1       /,4X,'I',13X,'C1(I)',17X,'C2(I)',17X,'C4(I)',17X,'C6(I)
           2',17X,'C0(I)',20)
            DO 140 I=6,19
            IP=I+1
            IM=I-1
            VOL=HX*HYY(I)*HZ
            PC=OMEGA*PUNIT*VOL*(ZMA+ZMI)
            PCIP=PC*HYY(IP)/HYY(I)
            PCIM=PC*HYY(IM)/HYY(I)
            C1(I)=PCIP/(2.*HHX)
            C2(I)=PC/(2.*HHY(I))
            C3(I)=0.0,0.0
            C4(I)=PCIM/(2.*HHX)
            C5(I)=C2(I)
            C6(I)=PC/HHZ
            IF (I.NE.6) GO TO 146
            C2(I)=3.*PC/(4.*HHY(I))
            C4(I)=PC/HHX
            C5(I)=C2(I)
            PC=PC*HS*ZMI/(HZ*(ZMA+ZMI))
            C3(I)=PC/(2.*H*S)
  146   CONTINUE
            C0(I)=C1(I)+C2(I)+C3(I)+C4(I)+C5(I)+C6(I)
            VOLT=HX*HYY(I)*2.*H
            PCT=OMEGA*PUNIT*VOLT*ZMI
            PCIPT=PCT*HYY(IP)/HYY(I)
            PCIMT=PCT*HYY(IM)/HYY(I)
```

Fig.H.1 (Continued) The computer programme

```
      C1T(I)=PCIPT/(2.*HHO
      C2T(I)=PCT/(2.*HYY(I))
      C3T(I)=PCT/(4.*RRW)
      C4T(I)=PCIPT/(2.*HHO
      C5T(I)=C2T(I)
      C6T(I)=0.1/3.0
      IF (I.NE.6) GO TO 147
      C6T(I)=3.*PCT/(4.*HYY(I))
      C4T(I)=PCT*HHX
      C5T(I)=C2T(I)
      C6T(I)=C3(I)
  147 CONTINUE
      COT(I)=C1T(I)+C2T(I)+C3T(I)+C4T(I)+C5T(I)+C6T(I)
      WRITE (6,150) I,C1T(I),C2T(I),C4T(I),C5T(I),COT(I)
      WRITE (6,150) I,C1(I),C2(I),C4(I),C6(I),CO(I)
  150 FORMAT (3X,I3,2X,10(2X,1PE9.2))
  140 CONTINUE
CC    ...1.........2.........3.........4.........5.........6.........7..
C     ITERATIONS START
      ITER=0
  299 ITER=ITER+1
      GREAT=0.0/0.0
      GRAT=REAL(GREAT)
      GRATI=AIMAG(GREAT)
      JTT=1
      DO 210 JJ=JL80N,JR80N
      J=JJ
      IF (MOD(ITER,2).NE.1) J=46-JJ
      JP=J+1
      JM=J-1
      JTT=JTT+1
      JTP=1
      IF (JTT.EQ.2) JTP=2
      IF (JTT.EQ.5) JTP=2
      IF (JTT.EQ.7) JTP=2
      IF (JTT.EQ.7) JTT=1
      DO 210 KK=KSPUN,KT80N
      K=KK
      IF (MOD(ITER,2).NE.1) K=1-KK
      KP=K+1
      KM=K-1
      IF (K.EQ.KT80N) KP=K
      DO 210 II=IC80N,IC80N
      I=II
      IF (MOD(ITER,2).NE.1) I=21-II
      IP=I+1
      IM=I-1
      IF (I.EQ.IC80N) GO TO 210
      IF (I.EQ.IP80N) IM=IP
      IF (J.EQ.JL80N) U(I,JM,K)=-U(I,40,K)
      IF (J.EQ.JR80N) U(I,JP,K)=-U(I,6,K)
      IF (I.GE.6.AND.K.GE.7.AND.K.LE.8) GO TO 231
CC    ...1.........2.........3.........4.........5.........6.........7..
C  CALCULATION AT NODES OTHER THAN SECONDARY MEMBER
      ROS=A1(I)+A2(I)+A3(K)+A4(I)+A5(I)+A6(K)
      IF (K.GT.2) GO TO 220
      IF (JTP.EQ.3.AND.K.EQ.KB80N.AND.I.GE.11) GO TO 210
      IF (JTP.EQ.2.AND.I.GE.11.AND.I.LE.13) GO TO 210
      IF (K.EQ.KB80N) KM=KP
      UNEW=(A1(I)*U(IP,J,K)+A2(I)*U(I,JP,K)+A3(K)*U(I,J,KP)
     1     +A4(I)*U(IM,J,K)+A5(I)*U(I,JM,K)+A6(K)*U(I,J,KM)
     2     +A6(K)*TA(I,J,K))/ROS
      GO TO 200
  220 UNEW=(A1(I)*U(IP,J,K)+A2(I)*U(I,JP,K)+A3(K)*U(I,J,KP)
     1     +A4(I)*U(IM,J,K)+A5(I)*U(I,JM,K)+A6(K)*U(I,J,KM))/ROS
      GO TO 200
CC    ...1.........2.........3.........4.........5.........6.........7..
C  CALCULATION AT NODES ON THE SECONDARY MEMBER
  231 CONTINUE
      UPEED=(0.0,0.0)
C     CALCULATION OF SPEED EFFECT O UPEED
      IF (SLIP.EQ.1.0) GO TO 235
      JP2=J+2
      JP3=J+3
      IF (J.NE.JL80N) GO TO 232
      U(I,JP2,K)=U(I,38,K)
      U(IP,JM,K)=U(IP,40,K)
      U(IM,JM,K)=-U(IM,40,K)
      U(I,JM,KM)=U(I,40,KM)
      U(I,JM,KP)=U(I,40,KP)
  232 IF (J.NE.JR80N) GO TO 234
      U(I,JP2,K)=U(I,7,K)
      U(IP,JP,K)=U(IP,6,K)
      U(IM,JP,K)=-U(IM,6,K)
      U(I,JP,KM)=U(I,6,KM)
      U(I,JP,KP)=U(I,6,KP)
  234 IF (J.EQ.40) U(I,JP2,K)=-U(I,6,K)
      FACTP=1.0
      RATIO=FLOAT(ITER)/100.0
      FACTB=SLIP*3.-3.*SLIP-SLIP**3+SQRT(RATIO)
      IF (ITER.LT.100) FACTB=(1.-FACTB)/(1.-SLIP)
      IF (K.EQ.7) GO TO 233
      CC1=                    C1T(I)*U(IP,JP,K)-U(IP,JM,K))
      CC2=                    C2T(I)*U(I,JP2,K))
      CC3=                    C3T(I)*U(I,JP,KP)-U(I,JM,KP))
      CC4=                    C4T(I)*U(IM,JP,K)-U(IM,JM,K))
      CC5=                   +C5T(I)*U(I,JP2,K))
      CC6=                    (0.0,0.0)
      IF (I.EQ.6) CC6=       C6T(I)*U(I,JP,KM)-U(I,JM,KM)
      CCG=                    COT(I)*U(I,JP,K)-U(I,JM,K))
      UPEED=FACTP*(18./PI)*(1.-SLIP)*(CC1+CC2+CC3+CC4+CC5+CC6-CCG)
     1     /BOT(I)
      GO TO 235
  233 CONTINUE
      CC1=                    C1(I)*U(IP,JP,K)-U(IP,JM,K))
      CC2=                    C2(I)*U(I,JP2,K))
      CC3=(0.0,0.0)
      IF (I.EQ.6) CC3=       C3(I)*U(I,JP,KP)-U(I,JM,KP))
      CC4=                    C4(I)*U(IM,JP,K)-U(IM,JM,K))
      CC5=                   -C5(I)*U(I,JP2,K))
      CC6=                    C6(I)*U(I,JP,KM)-U(I,JM,KM))
      CCG=                    CO(I)*U(I,JP,K)-U(I,JM,K))
      UPEED=FACTR*(18./PI)*(1.-SLIP)*(CC1+CC2+CC3+CC4+CC5+CC6-CCG)/BO(I)
  235 CONTINUE
```

Fig.H.1 (Continued) The computer programme

```
      IF (K.EQ.7) GO TO 236
C     CALCULATIONS ON THE TOP SURFACE OF THE BACKING IRON.
      UNULL=(B1T(I)*U(IP,J,K)+B2T(I)*U(I,JP,K)+B3T(I)*U(I,J,KP)
     1      +B4T(I)*U(IM,J,K)+B5T(I)*U(I,JM,K)+B6T(I)*U(I,J,KM))/B0T(I)
     2      -UPEED
      GO TO 240
  236 CONTINUE
C     CALCULATIONS ON THE BOTTOM SURFACE OF THE BACKING IRON WITH THE
C     CONDUCTING SHEET.
      UNULL=(B1(I)*U(IP,J,K)+B2(I)*U(I,JP,K)+B3(I)*U(I,J,KP)
     1      +B4(I)*U(IM,J,K)+B5(I)*U(I,JM,K)+B6(I)*U(I,J,KM))/B0(I)
     2      -UPEED
      IF (I.EQ.14.AND.J.EQ.7.AND.K.EQ.7) UPEES=UPEED
      IF (I.EQ.14.AND.J.EQ.7.AND.K.EQ.7) UNPEE=UNULL-UPEES
  200 RESDL=UNULL-U(I,J,K)
      U(I,J,K)=U(I,J,K)+ACCL*RESDL
      CALL RESDU (I,J,K,IRESL,JRESL,KRESL,RESDL,GREAT,GRATR,GRATI)
  210 CONTINUE
CCC   1234567890123456789012345678901234567890123456789012345678901234567890
C     TERMINATION CRITERION
      MTERM=1
      ALREA=ALOG10(ABS(GRATR))
      ALIMA=ALOG10(ABS(GRATI))
      IF (ITER.GT.3) GO TO 281
      L=ITER
      TPU(L)=CMPLX(0.0,0.0)
      DO 282 I=IOBGN,ICBGN
      DO 282 J=JOBGN,JCBGN
      DO 282 K=KOBGN,KCBGN
  282 TPU(L)=TPU(L)+U(I,J,K)
      GO TO 285
  281 L=4
      TPU(L)=CMPLX(0.0,0.0)
      DO 283 I=IOBGN,ICBGN
      DO 283 J=JOBGN,JCBGN
      DO 283 K=KOBGN,KCBGN
  283 TPU(L)=TPU(L)+U(I,J,K)
      DO 284 L=1,4
  284 TPU(L-1)=TPU(L)
      DECRT=(TPU(3)-TPU(2))/(TPU(2)-TPU(1))
      IF (GRATR.LE.EPSRO) MTERM=MTERM+1
      IF (GRATI.LE.EPSIM) MTERM=MTERM+1
      IF (MOD(ITER+10,NE.1) GO TO 295
      WRITE (6,280) ITER,GREAT,ALREA,ALIMA,DECRT
  280 FORMAT(1H ,10X,*SITUATION AFTER*,2X,I3,2X,*ITERATIONS*//
     1           25X,*GREATEST   RESIDUAL POTENTIAL  IS*,2(3X,1PE12.5)/
     2           25X,*LOGS OF REAL AND IMAGY PARTS ARE*,2(3X,1PE12.5)/
     3           25X,*DECREMENT OF TOTAL POTENTIAL  IS*,2(3X,1PE12.5)//)
      IF (ITER.LT.10) GO TO 295
      IF (MTERM.EQ.3) GO TO 260
      CALL ACCNEW (DECRT,ACCL)
  295 CONTINUE
C     CHECK FOR TERMINATION
      IF (ITER.GT.MITER) GO TO 290
      IF (CABS(GREAT).GT.10000.) WRITE (6,998) ITER,IRESL,JRESL,KRESL,
     U                                         GREAT,UPEES
  998 FORMAT (1HO,10X,*THE PROGRAMME HAS DIVERGED AFTER*,2X,I3,2X,
     1           *ITERATIONS*//,
     1           25X,*MAXIMUM RESIDUAL OCCURS AT I =*,I3,3X,*J =*,I3,
     2                                                3X,*K =*,I3,//,
     3           25X,*GREATEST RESIDUAL IS     = *,2(3X,1PE8.2),//,
     4           25X,*SPEED EFFECT AT (14,7,7) = *,2(3X,1PE8.2),////)
      IF (CABS(GREAT).GT.10000.) GO TO 999
      GO TO 260
CCC   1234567890123456789012345678901234567890123456789012345678901234567890
  290 CONTINUE
      WRITE (6,293) ITER,IRESL,JRESL,KRESL,UPEES
  293 FORMAT(1HO,10X,*SOLUTION  AFTER*,2X,I3,2X,*ITERATIONS*//
     1           25X,*MAXIMUM RESIDUAL OCCURS AT I =*,I3,3X,*J =*,I3,
     2                                                3X,*K =*,I3,//,
     3           25X,*SPEED EFFECT AT (14,7,7) = *,2(3X,1PE8.2),////)
C     WRITING OF U'S AND CALCULATION OF FLUX DENSITIES 0 CARDS EXCLUDED.
      WRITE (6,281) ((REAL(U(I,11,K)),K=1,10),I=1,20)
      WRITE (6,281) ((AIMAG(U(I,11,K)),K=1,10),I=1,20)
      WRITE (6,281) ((REAL(U(I,17,K)),K=1,10),I=1,20)
      WRITE (6,281) ((AIMAG(U(I,17,K)),K=1,10),I=1,20)
  281 FORMAT (/////,20(10(2X,1PE8.2)/))
      WRITE (6,282) ((REAL(U(I,J,7)),I=6,19),J=5,41)
      WRITE (6,282) ((AIMAG(U(I,J,7)),I=6,19),J=5,41)
  282 FORMAT (/////,37(14(1X,1PE8.1)/))
CC    1234567890123456789012345678901234567890123456789012345678901234567890
CC    12345678901234567890123456789012345678901234567890123456789012345678901234
C     FLUX DENSITY CALCULATIONS
CC    12345678901234567890123456789012345678901234567890123456789012345678901234
      PU60T=PUMAT/60
      PU60R=PUREAL/60
      K=5
  310 CONTINUE
      DO 320 MM=1,3
      WRITE (6,330) K
  320 FORMAT (/////,40X,*FLUX DENSITY CALCULATIONS 3.750 MM. BELOW SLOT
     1NOMAY PLANE O  K=*,I2,/,50X,21H(RAISED  BY  SECONDARY.)
      DO 350 JJ=5,16,5
      WRITE (6,317) JJ,JJ+1,JJ+2,JJ+3,JJ+4,JJ+5
  317 FORMAT (///,3X,6(5X,*J =*,I2,5X),/)
      IF (MM.EQ.1) WRITE (6,341)
      IF (MM.EQ.2) WRITE (6,342)
      IF (MM.EQ.3) WRITE (6,343)
  341 FORMAT (2X,1HI,1X,6(4X,5HBXMG,5X,4HBXPH,3X))
  342 FORMAT (2X,1HI,1X,6(4X,5HBYMG,5X,4HBYPH,3X))
  343 FORMAT (2X,1HI,1X,6(4X,5HBZMG,5X,4HBZPH,3X))
      DO 300 I=4,20
      IP=I+1
      IM=I-1
      JX=0
      JJ=JJ+5
      DO 301 J=JJ,JJ5
      JP=J+1
      JM=J-1
      KP=K+1
      KM=K-1
      JX=JX+1
      IF (MM.EQ.1) GO TO 346
      IF (MM.EQ.2) GO TO 347
```

Fig.H.1 (Continued) The computer programme

```
      IF (MM.EQ.3) GO TO 348
  346 CONTINUE
CC    ...1....2....3....4....5....6....7..
C     CALCULATIONS FOR X - COMPONENT .
  575 PUH=PUNIT/H2
      IF (I.EQ.20) U(IP,J,K)=-U(IM,J,K)
      IF (I.EQ.2) U(I-1,J,KP)=U(IM,J,KP)
      IF (I.LE.3) GO TO 349
      B=PUH*(U(IM,J,K)-U(IP,J,K))
  580 GO TO 350
  349 IF (I.EQ.2) PUH=PUH/3.
      IF (I.EQ.3) PUH=PUH/1.5
      B=PUH*(U(IM,J,K)/2.-U(IP,J,K))
      PUH=PUNIT
  585 GO TO 350
  347 CONTINUE
CC    ...1....2....3....4....5....6....7..
C     CALCULATIONS FOR Y - COMPONENT .
      IF (J.EQ.5) U(I,4,KP)=-U(I,40,KP)
  590 IF (J.EQ.5) U(I,4,K)=-U(I,40,K)
      IF (J.EQ.41) U(I,42,KP)=-U(I,5,KP)
      IF (J.EQ.41) U(I,42,K)=-U(I,5,K)
      PUH=PUNIT/(2.*HYY(I))
      B=PUH*(U(I,JM,K)-U(I,JP,K))
  595 GO TO 350
  348 CONTINUE
CC    ...1....2....3....4....5....6....7..
C     CALCULATIONS FOR Z - COMPONENT .
      PUH=PUNIT/(2.*H2)
  600 B=PUH*(U(I,J,KM)-U(I,J,KP))
      GO TO 350
CCC   ...1....2....3....4....5....6....7..
  350 BM(JX)=CABS(B)
      BR(JX)=400.
  605 IF (.NOT.(AIMAG(B).EQ.0.AND.REAL(B).EQ.0.))
     1BR(JX)=57.2957795*ATAN2(AIMAG(B),REAL(B))
  301 CONTINUE
      WRITE (6,316) I,((BM(JX),BR(JX)),JX=1,6)
  316 FORMAT (1X I2,6(2X,1PE9.2,1X,1PE9.2))
  610 300 CONTINUE
      K=K+1
      IF (K.EQ.5) GO TO 310
CCC   ...1....2....3....4....5....6....7..
CCC   ...1....2....3....4....5....6....7..
  615 C     F O R C E   D E S I T Y   C A L C U L A T I O N S
      H2Z=2.*HZ
      H2XH=2.
      TFX=0.0
      TFY=0.0
  620 TFZ=0.0
      K=5
      KP=K+1
      KM=K-1
      DO 600 III=4,36
  625 I=III
      IF (I.EQ.20) GO TO 600
      H2Y=2.*HYY(III)
```

```
      USIGN=1.0
      IF (III.GT.20) I=40-III
  630 IF (III.GT.20) USIGN=-1.0
      IP=I+1
      IM=I-1
      IF (I.EQ.20) U(IP,J,K)=-U(IM,J,K)
      IF (I.EQ.20) U(I,JM,K)=(0.0,0.0)
  635 DO 640 J=5,41
      JP=J+1
      JM=J-1
      JJ=J-4
      ENTX=-U(IP,J,K)+U(IM,J,K))/H2X
      ENTY=-U(I,JP,K)+U(I,JM,K))/H2Y
  640 ENTZ=-U(I,J,KP)+U(I,J,KM))/H2Z
      ENTT=ENTX*ENTY
      ENTX=USIGN*ENTX
      ENTY=USIGN*ENTY
      ENTZ=USIGN*ENTZ
  645 ENTT=USIGN*ENTT
      FX(JJ)=0.5*REAL (PUNIT*ENTZ*CONJG(ENTX))
      FY(JJ)=0.5*REAL (PUNIT*ENTZ*CONJG(ENTY))
      FZ(JJ)=0.5*REAL (0.5*PUNIT*(ENTZ*CONJG(ENTZ)-ENTT*CONJG(ENTT)))
  650 640 CONTINUE
C  EVALUATION OF FORCES FXT, FYT, FZT  ALONG THE WIDTH OF THE MACHINE.
      JF=37
      JF=36
      I=III
      II=I-3
  655 HGY=H2Y/2.
C  INTEGRATE FOR X- COMPONENT OF FORCE.
      CALL SIMPR(FX,JE,JF,HGY,FXT)
      XF(I)=FXT
C  INTEGRATE FOR Y- COMPONENT OF FORCE.
  660 CALL SIMPR(FY,JE,JF,HGY,FYT)
      YF(I)=FYT
C  INTEGRATE FOR Z- COMPONENT OF FORCE.
      CALL SIMPR(FZ,JE,JF,HGY,FZT)
      ZF(I)=FZT
  665 C  OUTPUT OF FORCES  ALONG THE WIDTH OF THE MACHINE.
      WRITE (6,820) I,FXT,I,FYT,I,FZT
  820 FORMAT (3X,'LATERAL FORCE AT I=',I3,4X,1PE9.2,5X,'TRACTIVE FORCE A
     1T I=',I3,4X,1PE9.2,5X,'VERTICAL FORCE AT I=',I3,4X,1PE9.2,/)
  670 800 CONTINUE
C  OUTPUT OF TOTAL FORCES PER POLE-PITCH.
      XF(17)=0.0
      XF(17)=(XF(16)+XF(18))/2.0
      YF(17)=0.0
  675 YF(17)=(YF(16)+YF(18))/2.0
      ZF(17)=0.0
      ZF(17)=(ZF(16)+ZF(18))/2.0
      INTE=1
  680 660 CONTINUE
      IF=17
      IF (INTE.EQ.2) IF=33
      IL=16
      IF (INTE.EQ.2) IL=32
      HGX=H
```

Fig.H.1 (Continued) The computer programme

```
      CALL SIMPR(XF,IF,IL,HGX,TFX)
      CALL SIMPR(YF,IF,IL,HGX,TFY)
      CALL SIMPR(ZF,IF,IL,HGX,TFZ)
      IF (INTE.EQ.1) WRITE (6,835) TFX,TFY,TFZ
      IF (INTE.EQ.2) WRITE (6,836) TFX,TFY,TFZ
835   FORMAT(//,20X,*ALONG OUTER CIRCLE PER POLE*,/,
     1          ,5X,*LATERAL FORCE  = *,1PE9.2,* NEWTONS*
     2          ,10X,*TRACTIVE FORCE = *,1PE9.2,* NEWTONS*
     3          ,10X,*VERTICAL FORCE = *,1PE9.2,* NEWTONS*,/)
836   FORMAT (//,20X,*ALONG OUTER AND INNER CIRCLE PER POLE*,/,
     1          ,5X,*LATERAL  FORCE = *,1PE9.2,* NEWTONS*
     2          ,10X,*TRACTIVE FORCE = *,1PE9.2,* NEWTONS*
     3          ,10X,*VERTICAL FORCE = *,1PE9.2,* NEWTONS*,/)
      INTE=INTE+1
      IF (INTE.EQ.2) GO TO 860
      TFXM=8.*TFX
      TFYM=8.*TFY
      TFZM=8.*TFZ
      WRITE (6,837) TFXM,TFYM,TFZM
837   FORMAT (//,20X,*TOTAL FORCES PRODUCED IN THE MACHINE*,/,
     1          ,5X,*LATERAL  FORCE = *,1PE9.2,* NEWTONS*
     2          ,10X,*TRACTIVE FORCE = *,1PE9.2,* NEWTONS*
     3          ,10X,*VERTICAL FORCE = *,1PE9.2,* NEWTONS*,/)
995   CONTINUE
      STOP
      END
```

```
      SUBROUTINE ACCNEW(DECRT,ACCL)
CC    ...1....2....3....4....5....6....7*
C ADAPTED FROM R. L. STOLL'S PAPER IN PROC IEE ,VOL    , 1970, PP
CC    ...1....2....3....4....5....6....7*
      COMPLEX DECRT,ACCL,CURRN,OPTIM
      DECABS=CABS(DECRT)
      OLACM= REAL(ACCL)
      OLACI=AIMAG(ACCL)
      UPPER=1.0
      BOTTOM=(OLACM-1.0)**2
      CORRN=1.0-(DECABS+ACCL-1.0)**2)/(ACCL*ACCL*DECRT)
      OPTIM=2.0/(1.0+CSQRT(CORRN))
      ACCL=1.0+2.0*(OPTIM-1.0)/(OPTIM*(3.0-OPTIM))
      WRITE (6,240) OPTIM,ACCL
240   FORMAT(1H ,19X,*THE CALCULATED OPTIMUM FACTOR IS*,2(3X,F8.5,4X)/
     1          20X,*THE  NEW ACCLERATION FACTOR  IS*,2(3X,F8.5,4X)//)
      RETURN
      END
```

```
      SUBROUTINE SIMPR(FF,JE,JF,HGY,FFT)
C  SUBROUTINE SUBPROGRAMME FOR SIMPSON'S RULE.
      DIMENSION FF(37)
C  APPLY SIMPSON'S RULE.
      FT=0.0
      DO 850 J=2,JF,2
850   FT=FT+FF(J-1)+4.*FF(J)+FF(J+1)
      FFT=FT*HGY/3.
      RETURN
      END
```

```
      SUBROUTINE RESDU(I,J,K,IRESL,JRESL,KRESL,RESDL,GREAT,GRATR,GRATI)
CC    ...1....2....3....4....5....6....7*
C  THIS SUBROUTINE FINDS THE VALUES AND LOCATION OF MAXI. RESDU. - GREAT.
C  FOR USE AS A 2-D SUBROUTINE, PUT I,J OR K = 1 AS APPROPRIATE IN MAIN
C                                NO OTHER CHANGES ARE REQUIRED.
C  INTERPRETATION OF THE SUBROUTINE ARGUMENTSO
C        I,J,K      LOCATION OF ARBITRARY NODE WITH REFERENCE TO AN
C                   ORTHOGONAL COORDINATE SYSTEM.
C        RESDL      RESIDUAL POTENTIAL AT ARBITRARY NODE.
C        IRESL,JRESL,KRESL
C                   LOCATION OF NODE WHERE THE RESIDUAL CURRENTLY HAS
C                   ITS MAXIMUM MAGNITUDE.
C        GREAT      CURRENT MAXIMUM MAGNITUDE.
C  ADAPTED FROM SUBROUTINE SPRESD WRITTEN BY MR. K.O. SHARPLES.
CC    ...1....2....3....4....5....6....7*
      COMPLEX RESDL,GREAT
C  TAKE MAXIMUM VALUE OF THE RESIDUAL AND COMPARE WITH CURRENT MAXIMUM
      RESAB=CABS(RESDL)
      GAIAB=CABS(GREAT)
      IF (RESAB.LE.GAIAB) GO TO 400
C  REPLACE OLD MAXIMUM BY NEW MAXIMUM.
      GRATR=ABS( REAL(RESDL))
      GRATI=ABS(AIMAG(RESDL))
      GREAT=CMPLX(GRATR,GRATI)
C  STORE LOCATION OF MAXIMUM RESIDUAL.
      IRESL=I
      JRESL=J
      KRESL=K
400   CONTINUE
      RETURN
      END
```

Fig.H.1 (Continued) The computer programme

PUBLICATION